

Finite Element Model of the Thermal Profile During Submerged Arc Welding with One and Two
Electrodes

by

Alexandre J. L. LECOANET

A thesis submitted in partial fulfillment of the requirements for the degree of

Master of Science

in

Chemical Engineering

Department of Chemical and Materials Engineering
University of Alberta

Abstract:

The submerged-arc welding (SAW) process is used extensively in the manufacturing of pipes. The heat flow introduced by the welding operation has a significant impact on the properties of both the weld metal and the heat affected zone (HAZ).

The work presented in this thesis aims to develop a numerical heat flow model to predict the temperature profile in piece welded using SAW as a function of the welding parameters. Measurement were done using instrumented thermocouples during an operation of SAW with one electrode. The models were then compared to the measurements and a sensitivity analysis was carried out on the density, the specific heat, the parameter called “ f_r ” in the double ellipsoid model, and the Neumann boundary condition.

The three models used are a point source model giving results similar to Rosenthal’s results, a model using a double ellipsoid heat source with constant thermal properties, and a model using a double ellipsoid heat source with varying thermal properties. The presence of the thermocouples linked to the data acquisition system used in the experiment disturbed the weld but workable data were still extracted. Then the comparison between the measurement and the simulations showed that the most accurate model is the one using a double ellipsoid heat source with varying thermal properties. It predicts well the heating and the cooling phases of all the temperature profiles recorded but it predicts the peak well only for the thermocouples located around 12 mm from the center of the plate closer it overestimates the peak.

The sensitivity analysis showed that the most sensitive parameters are the thermal properties. It also showed that the parameter called “ f_r ” in Goldak’s approach is sensitive. The Neumann boundary condition is not a sensitive parameter. Also when measurements are done using thermocouples close to the knowing the exact location of the thermocouples is crucial.

Preface:

This thesis is an original work by Alexandre J. L. LECOANET. No part of this thesis has been previously published.

Acknowledgments:

For their guidance I would like to thank Professor Hani HENEIN and Professor Douglas IVEY. Dr. Barry WISKEL was of precious help for this work in general and the experiments especially. The members of the Advanced Materials and Processing Laboratory group also helped me throughout my work and for that I thank them.

I would like to thank Joel PEPIN for his help for the development of the statistical model used in this work to determine the bead shape of the weld. Also, Stephen KENNY and Jason SZARKOWICZ helped me a lot to conduct the experiments.

The pictures of the cross-sections analyzed here as well as some of the measurements done on them were done by David ROSE and I thank him for his time.

I want to thank Les DEAN and Walter BODDEZ for their help in designing the instrumentation of the welds.

I would like to give special thanks for their sponsorship, Evraz Inc. NA, Trans-Canada Pipelines, Enbridge, Alliance Pipelines, UT Quality, and the Natural Science and Engineering Research Council (NSERC) of Canada.

Table of contents:

Abstract:	ii
Preface:	iii
Acknowledgments:	iii
Acronyms and symbols:	xix
Acronyms:	xix
Symbols – Latin alphabet:	xx
Symbols – Greek alphabet:	xxi
1. Introduction:	1
2. Literature review:	4
2.1. Welding:	4
2.1.1. Definitions:	4
2.1.2. Welding history:	4
2.1.3. Submerged arc welding:	5
2.2. Variables:	8
2.2.1. Overview of the variables involved:	9
2.2.2. Input variables and their effect on the output ones:	10
2.2.3. Additional considerations for tandem SAW:	14
2.3. Steel:	15
2.4. Pipelines:	15
2.4.1. General overview:	15
2.4.2. The reasons behind the choice of micro-alloyed steel for pipelines:	16
2.4.3. Pipeline manufacturing:	17
2.5. Simulation:	20
2.5.1. Analytical solutions:	21

2.5.2. Numerical methods:	24
2.6. Frame of the present work:	28
3. Simulation:.....	30
3.1. Governing equations:	30
3.2. Point source on a semi-infinite body:	32
3.2.1. Single point source:.....	32
3.2.2. Two point sources:.....	41
3.3. Mixed boundary conditions:	45
3.3.1. Geometry:	45
3.3.2. Boundary conditions considered:.....	46
3.3.3. Results:.....	48
3.3.4. Conclusions:.....	51
3.4. Double ellipsoid source:	51
3.4.1. Presentation of the source and geometry:	52
3.4.2. Boundary conditions:	56
3.4.3. Numerical transient calculations:.....	56
3.4.4. Simulation with constant thermal properties:	57
3.4.5. Simulation with temperature dependent thermal properties:	59
3.4.6. Simulation with two sources:.....	61
3.5. Conclusions:.....	65
4. Instrumented welds:	66
4.1. Bead on plate weld:.....	69
4.1.1. Bead shape analysis:	69
4.1.2. Welding stability:.....	69
4.1.3. Conclusions:.....	70

4.2. Weld on machined plate without thermocouples:.....	70
4.2.1. Bead shape analysis:	71
4.2.2. Welding stability:.....	74
4.2.3. Conclusions:.....	75
4.3. Weld with type B and type K thermocouples:.....	75
4.3.1. Bead shape analysis:	75
4.3.2. Welding stability:.....	78
4.3.3. Temperature profiles:.....	78
4.3.4. Conclusions:.....	81
4.4. Weld with only type K thermocouples:.....	82
4.4.1. Bead shape analysis:	82
4.4.2. Welding stability:.....	84
4.4.3. Temperature profiles:.....	85
4.4.4. Conclusions:.....	88
4.5. Conclusions:.....	88
5. Comparison between simulation and experiments:.....	90
5.1. General presentation:	90
5.2. Comparison for each thermocouple:.....	92
5.2.1. R1KbZ1:	92
5.2.2. R1KbZ3:	93
5.2.3. R2KbZ1:	94
5.2.4. R2KbZ2:	95
5.2.5. R2KaZ1:.....	96
5.2.6. R2KaZ2:.....	98
5.2.7. Conclusions:.....	99

5.3. Sensitivity analysis:	100
5.3.1. Density and specific heat:	101
5.3.2. Thermal conductivity:	102
5.3.3. F_f parameter:	103
5.3.4. Mixed boundary condition coefficient:	104
5.3.5. Effects of the uncertainties on the location of the thermocouples:	105
5.3.6. Conclusions on the sensitivity of the studied parameters:	108
5.4. Conclusions:	109
6. Conclusions and future work:	111
6.1. Conclusions of this work:	111
6.2. Future developments:	113
References:	115
Appendices:	122
A. Statistical Analysis Results:	122
A.1. Wire feed speed:	122
A.2. Reinforcement area:	123
A.3. Maximum reinforcement height:	125
A.4. Bead width:	126
A.5. Penetration area:	128
A.6. Maximum penetration depth:	130
B. Statistical Analysis of Wire Feed Speed During Submerged Arc Welding:	134
B.1. Abstract:	134
B.2. Introduction:	135
B.3. Inputs:	136
B.4. Methods used:	137

B.5. Implementation:	141
B.6. Results & Discussion:	143
B.7. Insignificant variables:	148
B.8. Link with properties:	148
B.9. Conclusions:	150
B.10. Acknowledgements:	151
B.11. Symbols and Acronyms:	152
B.12. Data used for processing:	153
C. Thermo-physical properties:	155
C.1. Constant thermo-physical properties:.....	155
C.2. Thermo-physical properties varying with the temperature:	155
D. Additional information on the experiments:	170
D.1. Temperature profiles:	170
D.2. Output of the welder:	181
E. Bead shape measurements:.....	196

Tables:

Table 3.1: Input parameters used for the simulation.....	36
Table 3.2: Parameters used to calculate the dimensions of the source presented in Figure 3.18.	56
Table 4.1: Parameters used for the experiments.	66
Table 4.2: Summary of the four different welds performed and their results.....	68
Table 4.3: Average values and standard deviations of the parameters given by the welder reported along with the intended values.	70
Table 4.4: Main bead shape parameters measured from the cross-sections.	74
Table 4.5: Average values and standard deviations for the parameters given by the welder along with the intended values.	74
Table 4.6: Main bead shape parameters measured from the cross-sections.	78
Table 4.7: Average values and standard deviations of the parameters given by the welder reported along with the intended values.	78
Table 4.8: Main bead shape parameters measured from the cross-sections.	84
Table 4.9: Average values and standard deviations of the parameters given by the welder reported along with the intended values.	85
Table 5.1: Position of different thermocouples in the plane (z,y). Parameters Dz and Dy are the ones shown in Figure 5.1.....	91
Table 5.2: Strengths and weaknesses of the three models compared with measurements.	99
Table A.1: Half-width of the confidence intervals for the regression of the reinforcement area.	123
Table A.2: Half-width of the confidence intervals for the regression of the maximum reinforcement height.	125
Table A.3: Half-width of the confidence intervals for the regression of the bead width.	127
Table A.4: Half-width of the confidence intervals for the regression of the penetration area. ..	129
Table A.5: Half-width of the confidence intervals for the regression of the penetration area. ..	131
Table B.1: Range in variables for analysis.	137
Table B.2: Half width of the confidence intervals, for the significant variables.	143
Table B.3: List of symbols and acronyms used (Latin alphabet).	152
Table B.4: List of symbols and acronyms used (Greek alphabet).	152
Table B.5: Data utilized.	153

Table E.1: Bead shape parameters measured on the cross-sections. 196

Table of figures:

Figure 2.1: Schematic representing what happens during a SAW operation with one electrode. This schematic is adapted from [17] with the permission of ASM international.....	7
Figure 2.2: Schematic representing the differences between DCEN and DCEP. Inspired by [11].	13
Figure 2.3: Electrical signal changes corresponding to changes in offset Inspired by [11].	13
Figure 2.4: Electrical signal changes corresponding to changes in balance. Inspired by [11].	14
Figure 2.5: Example of uneven strain encountered by pipelines.....	16
Figure 2.6: UOE pipe forming steps. Based partly on work referenced in [7].	18
Figure 2.7: Simplified schematic of ERW pipe forming process. Based partly on work referenced in [7].	19
Figure 2.8: Simplified schematic of spiral weld pipe forming process. Based partly on work referenced in [7].....	20
Figure 2.9: Diameters available for different pipe making processes [7].....	20
Figure 2.10: Gaussian distribution from Eagar and Tsai. Welding Journal, (December, 1983), © American Welding Society [40].	23
Figure 2.11: Representation of a double ellipsoid volumetric source with the power distribution along the welding direction. Reproduced from [50] with permission of Springer.....	27
Figure 2.12: Heat source for twin-wire SAW. Reproduced from the work of Sharma et al [52] with permission of Taylor & Francis.....	28
Figure 3.1: Generic geometry used for the simulation. Any geometry used here is a variation of this one.....	32
Figure 3.2: Schematic of the geometry used to obtain Rosenthal's solution using FEM.	35
Figure 3.3: Mesh used to obtain the temperature profile in Figure 3.4.	36
Figure 3.4: Temperature profile obtained using the point source.....	37
Figure 3.5: Percentage of difference between Rosenthal's solution and the temperature profile available in Figure 3.4.	38
Figure 3.6: Mesh generated when a hemisphere, 0.1 mm in radius, is removed from the geometry at the position of the point source.....	39
Figure 3.7: Temperature profile generated using a spherical irregularity at the surface.	40

Figure 3.8: Difference of the temperature profile reported in Figure 3.7 with Rosenthal's solution when a hemispherical irregularity is introduced.....	40
Figure 3.9: Mesh used to simulate two point sources separated by 23mm.....	43
Figure 3.10: Temperature profile obtained with two point sources.....	43
Figure 3.11: Difference with Rosenthal's solution of the temperature profile when two spherical irregularities are used.....	44
Figure 3.12: Geometry and mesh used for a point source and mixed boundary conditions.....	46
Figure 3.13: Heat flux calculated using two different methods for the boundary conditions. The blue curve corresponds to the addition of Equation (3.15) and Equation (3.16). The red dashed curve corresponds to the heat flux calculated using Equation (3.17).....	48
Figure 3.14: Boundary conditions used in the both cases studied. a) corresponds to the first case, while b) corresponds to the second one.....	49
Figure 3.15: Temperature profiles generated by the two cases considered in this work.....	50
Figure 3.16: Comparison of the temperature profiles obtained for both cases considered in this work.....	50
Figure 3.17: Schematic of the geometry used for one double ellipsoidal source simulation.....	55
Figure 3.18: Close up of the double ellipsoidal source with the parameter notations characterizing the source.....	55
Figure 3.19: Geometry and boundary conditions used for the simulation with one double ellipsoidal source.....	57
Figure 3.20: Mesh used to carry out the calculations with a single double ellipsoidal source and fixed thermal properties. 74,161 tetrahedral elements were used.....	58
Figure 3.21: Temperature profile generated with a double ellipsoidal source and an input current of 700 A and an input voltage of 32 V.....	59
Figure 3.22: Temperature profile generated using a double ellipsoid source and varying thermal properties.....	60
Figure 3.23: Percentage of difference between the temperature profiles generated using fixed and varying thermal properties.....	61
Figure 3.24: Geometry used for the simulation with two double ellipsoid sources. On this schematic the different boundary conditions used are noted.....	62
Figure 3.25: Mesh used to carry out the calculations with two double ellipsoidal sources.....	63

Figure 3.26: Temperature profile generated using a two double ellipsoid source and varying thermal properties.....	64
Figure 4.1: Picture of the BOP weld.....	69
Figure 4.2: Geometry of the machined plates.....	71
Figure 4.3: Description of the plate in place for welding, with the positions of the thermocouples.....	71
Figure 4.4: Image of the weld performed on the machined plate without thermocouples.....	72
Figure 4.5: Polished and etched cross-sections taken at different thermocouple positions along the welding direction. The blue line is 5 mm long.....	73
Figure 4.6: Image of the weld performed with 8 thermocouples embedded in the plate.....	76
Figure 4.7: Polished and etched cross-sections taken at the different positions of the thermocouples along the welding direction. The blue line is 5 mm long.....	77
Figure 4.8: Superposition of the raw data obtain for R1KaZ1 (red line) and the processed data (black circles). The treated data were reported as discreet circles, at a rate of one every 0.2 s, for legibility sake.....	79
Figure 4.9: Superposition of the raw data obtain for R2KaZ1 (red line) and the processed data (black circles). The treated data were reported as discreet circles, at a rate of one every 0.2 s, for legibility sake.....	80
Figure 4.10: Signals for three Kb thermocouples. The black points corresponds to zone 1, the red ones to zone 2 and the blue ones to zone 3. The time display was manipulated to superimpose the three graphs.....	81
Figure 4.11: Instrumented weld produced with only 6 type K thermocouples embedded.....	83
Figure 4.12: Polished and etched cross-sections taken at the different positions of the thermocouples along the welding direction. The blue line is 5 mm long.....	84
Figure 4.13: Superposition of the three temperature profiles recorded by the Kb thermocouples. The black curve corresponds to zone 1. The red one to zone 2 shifted 9 s to the left and the blue plot shows the temperature for zone 3 shifted 18 s to the left.....	86
Figure 4.14: Superposition of the three temperature profiles recorded by the Ka thermocouples. The black curve corresponds to zone 1 with. The red one corresponds to zone 2 shifted 9 s to the left and the blue plot shows the temperature for zone 3 shifted 18 s to the left.....	87
Figure 5.1: Example of line on which the calculated temperature profile is extracted.....	90

Figure 5.2: Experimental temperature profile for R1KbZ1 along with temperature profiles generated by a point source (green), a double ellipsoid source with constant properties (blue) and a double ellipsoid source with varying thermal properties (red). 93

Figure 5.3: Experimental temperature profile for R1KbZ3 along with temperature profiles generated by a concentrated heat source (green), a double ellipsoid source with constant properties (blue) and a double ellipsoid source with varying thermal properties (red)..... 94

Figure 5.4: Experimental temperature profile for R2KbZ1 along with temperature profiles generated by a concentrated heat source (green), a double ellipsoid source with constant properties (blue) and a double ellipsoid source with varying thermal properties (red)..... 95

Figure 5.5: Experimental temperature profile for R2KbZ2 along with temperature profiles generated by a concentrated heat source (green), a double ellipsoid source with constant properties (blue) and a double ellipsoid with varying thermal properties (red). 96

Figure 5.6: Experimental temperature profile for R2KaZ1 along with temperature profiles generated by a concentrated heat source (green), a double ellipsoid source with constant properties (blue) and a double ellipsoid source with varying thermal properties (red). The cyan line corresponds to 800°C the magenta one corresponds to 500°C. 97

Figure 5.7: Experimental temperature profile for R2KaZ2 along with temperature profiles generated by a concentrated heat source (green), a double ellipsoid source with constant properties (blue) and a double ellipsoid with varying thermal properties (red). 98

Figure 5.8: Distribution of the scaled sensitivity coefficient for density..... 102

Figure 5.9: Distribution of the scaled sensitivity coefficient for thermal conductivity. 103

Figure 5.10: Distribution of the scaled sensitivity coefficient for the f_f coefficient in the double ellipsoid source. 104

Figure 5.11: Distribution of the scaled sensitivity coefficient for the mixed boundary coefficient. 105

Figure 5.12: Temperature profile measured by R2KbZ1 (black circles). The other two curves are the profiles extracted assuming two different positions for the thermocouple. The thermocouple was assumed to be at the specified location for the blue curve while for the red curve its position was determined by measurements..... 106

Figure 5.13: Temperature profile measured by R2KaZ1 (black circles). The other two curves are the profiles extracted assuming two different positions for the thermocouple. The

thermocouple was assumed to be at the specified location for the blue curve while for the red curve its position was determined by measurements.....	107
Figure A.1: Parity plot representing the calculated reinforcement area against the measured one. The black curve is the function "y=x".	124
Figure A.2: Parity plot representing the calculated maximum reinforcement height against the measured one. The black curve is the function "y=x".	126
Figure A.3: Parity plot representing the calculated bead width against the measured one. The black curve is the function "y=x".	128
Figure A.4: Parity plot representing the calculated penetration area against the measured one. The black curve is the function "y=x".	130
Figure A.5: Parity plot representing the calculated maximum penetration depth against the measured one. The black curve is the function "y=x".	132
Figure A.6: Schematic illustrating the difference between a BOP weld (left) and a beveled one. The green parts corresponds to the material added during the operation while the red ones corresponds to the material melted.	133
Figure B.1: Schematic description of the algorithm used.	142
Figure B.2: Parity plot representing the output according to the model versus the real measured one. The black curve is the function "y=x".	144
Figure B.3: Schematic showing the effect of the polarity on the melting of both the base metal and the electrode. Inspired by [11].	146
Figure B.4: Schematic explaining how the balance effects the electrical signal. Inspired by [11].	147
Figure B.5: Schematic explaining how the offset effects the electrical signal. Inspired by [11].	147
Figure B.6: Schematic explaining how the semi-penetration ratio can help characterize a weld. Inspired by [11].	149
Figure B.7: Effect of the semi-penetration ratio on the average SSCVN fracture energy for two different currents.....	150
Figure C.1: Density as a function of temperature given by Thermo-Calc [®] for the bulk material and a maximum step size of 0.5 K.	158
Figure C.2: Color legend of the phases present as a function of temperature.	159

Figure C.3: Zoom on the parts of the density curves where a change in evolution is witnessed.	160
Figure C.4: Evolution, with the temperature, of the derivative of the enthalpy with respect to the temperature in J/g.K using a maximum step-size of 0.5 K.....	162
Figure C.5: Evolution of the thermal conductivity with the temperature in solid phase.....	163
Figure C.6: Evolution of the thermal conductivity with the temperature according to the program of the MAP (blue) and according to Miettinen (black line). The red and the green points are part of the calculation for Miettinen's approach.....	164
Figure C.7: Thermal conductivity in the liquid as predicted using the Wiedemann-Franz-Lorenz law.....	167
Figure C.8: Thermal conductivity computed using Equation (C.11).....	168
Figure C.9: Thermal conductivity computed using Equation (C.12) and an Amix of 5.....	169
Figure D.1: Temperature profile recorded by the thermocouple KbZ1. The red line corresponds to 600°C.....	171
Figure D.2: Temperature profile reported by the thermocouple KaZ1. The red line corresponds to 1450°C.....	171
Figure D.3: Temperature profile recorded by the thermocouple KbZ2. The red line corresponds to 600°C.....	172
Figure D.4: Temperature profile reported by the thermocouple KaZ2. The red line corresponds 1450°C.....	173
Figure D.5: Temperature profile recorded by the thermocouple KbZ3. The red line corresponds to 600°C. The blue one corresponds to 700°C.....	174
Figure D.6: Temperature profile reported by the thermocouple KaZ3. The red line corresponds 1450°C.....	175
Figure D.7: Temperature profile recorded by the thermocouple KbZ1. The red line corresponds to 600°C.....	176
Figure D.8: The black curve corresponds to the temperature profile recorded by the thermocouple KbZ1. The blue one corresponds to the temperature profile generated with 8 thermocouples with a shift of 11.5s to the left. The red one corresponds to 600°C.....	176
Figure D.9: Temperature profile recorded by the thermocouple KaZ1 after smoothing. The red line correspond to 900°C.....	177

Figure D.10: Temperature profile recorded by the thermocouple KbZ2 after smoothing. The red line corresponds to 600°C.....	178
Figure D.11: Temperature profile recorded by the thermocouple KaZ2. The red line corresponds to 900°C.	178
Figure D.12: Temperature profile recorded by the thermocouple KbZ3. The red line corresponds to 600°C.	179
Figure D.13: The black curve corresponds to the temperature profile recorded by the thermocouple KbZ3. The blue one corresponds to the temperature profile generated with 8 thermocouples and with a shift of 11.5s to the left. The red one corresponds to 600°C.....	180
Figure D.14: Temperature profile recorded by the thermocouple KaZ3. The red line corresponds to 900°C.	181
Figure D.15: Current recorded by the welder during the BOP experiment. The red line corresponds to the mean value (700 A) and the two green ones correspond to the mean plus or minus the standard deviation (2.47 A).	182
Figure D.16: Voltage evolution throughout the BOP experiment. The red line corresponds to the mean (31.9 V) and the green line corresponds to the mean plus or minus the standard deviation (0.53 V).....	183
Figure D.17: The black stars represent the recorded evolution of the WFS during the BOP experiment. The red line shows the mean (32.9 mm/s) and the green ones represent the mean plus or minus the standard deviation (0.70 mm/s). The blue stars correspond to the WFS calculated from the method presented in Appendix A and the recorded current. The black line corresponds to the WFS calculated using the aim current (32.2 mm/s). It is under the lower green line.	184
Figure D.18: Evolution of the current during the welding operation carried out on a machined plate with no thermocouples embedded. The red line corresponds to the average (700 A), the green lines to the mean plus or minus the standard deviation (2.46 A).	185
Figure D.19: Evolution of the voltage during the welding operation carried out on machined plate with no thermocouples embedded. The red line corresponds to the average (32 V), the green lines to the mean plus or minus the standard deviation (0.50 V).	186
Figure D.20: The black stars represent the recorded evolution of the WFS for a weld performed on a machined plate without thermocouples. The red line shows the mean (33.9 mm/s) and the	

green ones represent the mean plus or minus the standard deviation (0.90 mm/s). The blue stars correspond to the WFS calculated from a formula obtained via regression using the recorded current and the black line corresponds to the WFS calculated using the aim current (32.2 mm/s).....	187
Figure D.21: Evolution of the current during the welding operation carried out with eight thermocouples embedded. The red line corresponds to the average (701 A), the green lines to the mean plus or minus the standard deviation (4.27 A).....	189
Figure D.22: Evolution of the voltage during the welding operation carried out with eight thermocouples embedded. The red line corresponds to the average (32.2 V), the green lines to the mean plus or minus the standard deviation (0.60 V).....	190
Figure D.23: The black stars represent the recorded evolution of the WFS during the experiment with eight thermocouples. The red line shows the mean (32.7 mm/s) and the green ones represent the mean plus or minus the standard deviation (1.43 mm/s). The blue stars correspond to the WFS calculated from a formula obtained via regression using the recorded current and the black line corresponds to the WFS calculated using the aim current (32.2 mm/s).....	191
Figure D.24: Evolution of the current during the welding operation carried out with six thermocouples embedded. The red line corresponds to the average (701 A), the green lines to the mean plus or minus the standard deviation (3.94 A).....	193
Figure D.25: Evolution of the voltage during the welding operation carried out with six thermocouples embedded. The red line corresponds to the average (31.7 V), the green lines to the mean plus or minus the standard deviation (1,19 V).....	194
Figure D.26: The black stars represent the recorded evolution of the WFS during the experiment with six thermocouples. The red line shows the mean (34.9 mm/s) and the green ones represent the mean plus or minus the standard deviation (2.13 mm/s). The blue stars show the values of the WFS calculated by using the current recorded. The black one shows the WFS calculated with the aim parameters only (32.2 mm/s).....	195

Acronyms and symbols:

In this chapter are listed the acronyms and symbols used within the present thesis.

Acronyms:

AC:	Alternating current
AWS:	American welding society
B:	Balance (%)
BOP:	Bead on plate
BW:	Bead width (mm)
CFD:	Computational welding dynamic
DC:	Direct current
DCEN:	Direct current electrode positive
DCEN:	Direct current electrode negative
ERW:	Electric resistance welding
F:	Frequency (Hz)
FEM:	Finite element method
HAZ:	Heat affected zone
HI:	Heat input (J/mm)
I:	Current (A)
MAP:	Materials algorithms project
MIG:	Metal inert gas
O:	Offset (%)
PA:	Penetration area (mm ²)
PD:	Penetration depth (mm)
PDE:	Partial derivative equation
RA:	Reinforcement area (mm ²)
RH:	Reinforcement height (mm)
RMS:	Root means square
SAW:	Submerged arc welding
TMCP:	Thermo-mechanically controlled processing

TS:	Travel speed (mm/s)
V:	Voltage (V)
WFS:	Wire feed speed (mm/s)

Symbols – Latin alphabet:

a_{xf} :	Semi-axis of the front ellipsoid in the double ellipsoid model in the welding direction (mm)
a_{xr} :	Semi-axis of the rear ellipsoid in the double ellipsoid model in the welding direction (mm)
b_y :	Semi-axis of the double ellipsoids in the double ellipsoid model in “y” direction (mm)
C_p :	Specific heat (J/(kg.K))
c_z :	Semi-axis of the double ellipsoids in the double ellipsoid model in “z” direction (mm)
f_f :	Fraction of the heat source inputted in the front source in Goldak’s model
f_r :	Fraction of the heat source inputted in the rear source in Goldak’s model
h :	Heat transfer coefficient (W/(m ² .K))
h_{comb} :	Heat transfer coefficient used for the mixed boundary condition (W/(m ² .K))
k :	Thermal conductivity (W/(m.K))
l_x :	Length of the geometry in the welding direction used for the simulation and the experiments (cm)
l_y :	Length of the geometry in “y” direction used for the simulation and the experiments (cm)
l_z :	Length of the geometry in “z” direction used for the simulation and the experiments (cm)
P :	Power (w)
q_{conv} :	Heat flux lost by convection (W/m ²)
q_{comb} :	Heat flux lost by convection and radiation calculated using h_{comb} (W/m ²)
q_{rad} :	Heat flux lost by radiation (W/m ²)
Q :	Power density (W/m ³)
t :	Time (s)
$t_{8/5}$:	Time required for a point to go from 800°C to 500°C (s)
T :	Temperature (K) or (°C)
$T_{measured}$:	Temperature measured by the thermocouples during the experiments (°C)
T_{ps} :	Temperature profile generated using the point heat source (°C)

$T_{\text{ellipsoid}}$:	Temperature profile generated using the double ellipsoid heat source with constant thermal properties ($^{\circ}\text{C}$)
$T_{\text{ellipsoid-CT}}$:	Temperature profile generated using the double ellipsoid heat source with varying thermal properties ($^{\circ}\text{C}$)
T_{θ} :	Scaled sensitivity coefficient of parameter θ (K)
T_{∞} :	Infinite temperature which corresponds to the ambient temperature (293.15 K)
v :	Travel speed (m/s)

Symbols – Greek alphabet:

δ :	Offset used for the computation of the derivative used in the sensitivity analysis
ε :	Emissivity 0.9
θ :	Refers to the parameter studied in the sensitivity analysis
θ_0 :	Value of θ used in the simulations
ρ :	Density (kg/m^3)
σ :	Stefan-Boltzmann constant $5.670367 \cdot 10^{-8}$ ($\text{W}/(\text{m}^2 \cdot \text{K}^4)$)

1. Introduction:

Welding is a widespread technique used to join metallic materials. It has been known for centuries and its practice evolved throughout the ages giving a wide range of different processes. However, the most common types of welding are arc welding processes, where an electric source is used to produce an electric arc which melts the two pieces to be joined and sometimes also some metal is fed into the weld. It is a fast and reliable way to join two pieces of metal, making it interesting from a productivity perspective [1, 2]. For heavy industry, the submerged-arc welding (SAW) process is often used to weld large pieces of metals together. It is an arc welding process where a powder blanket is poured atop the plates where the welding takes place. It has numerous advantages over other welding processes regarding; for instance, safety and automation ease, but it has its limitations; for instance, it is not suited for vertical applications [3, 4].

A lot of different variables can be tuned during an arc welding process. This makes it a versatile process but also a complicated one to understand. The number of variables increases when studying the SAW [4, 5], as it is often automated and the presence of the flux opens new ways to act on the weld.

Most of the materials welded using SAW are steels. Steels are versatile as their alloying makes it possible to obtain many different properties. The main type of steel that is the focus of this thesis is micro-alloyed steels. These steels have good weldability and are comparatively cheap due to a low concentration of alloying elements, while displaying interesting properties. The special properties of these steels are mostly obtained via thermomechanical controlled processing (TMCP). During these operations the steel is heated up, hot rolled and controlled cooled to achieve its distinct properties [6].

One of the main domains of application of micro-alloyed steels is pipeline manufacturing. This is an industry which needs materials with good ductility and toughness. Also, the pipes are assembled on site which means that they must be easy to transport and to assemble. Micro-alloyed steels are materials of choice for this application as they are easily welded and have good strength to weight ratio [7]. Several processes are used to produce the pipes. One of the differentiating factors between these processes is the diameter of the pipes. Two main approaches exist for pipe manufacturing, continuous and discontinuous processes.

With all the tuning possibilities offered by the SAW operation and the pipeline manufacturing processes, it is impossible to grasp the effect that all, or even most, of these tuning factors have on the final product using only trial and error methods or experiments. It would take too much time and be too expensive. That is why simulation is important in the pipeline manufacturing industry and even more for industries using SAW [8]. The temperature profile of the welded piece is one of the key factors to assess the end result of a welding operation. For instance, the microstructure and mechanical stresses depend on the thermal history of the steel. The coupling between the energy equation and stress generation gives acceptable results [9]. A lot of work has been done on this subject. First, some analytical models were developed, which were soon supplanted by numerical methods that are more suited to handle non-linear problems due to the increase in computational power available for universities and industries. The main numerical method used to tackle this problem is the finite element method (FEM), which was initially designed to solve structural mechanics problems but was extended to other domains.

The focus of this work is to develop a reliable method to predict the temperature profile during an operation of SAW during the manufacturing of pipelines using the spiral-weld process with one or two electrodes. The FEM and COMSOL Multiphysics® were used. The model passed through several steps and some other results were used to test the adequacy of both the model and the software used to develop it. This then led to the development of an FEM based on Goldak's double ellipsoid model [10], where temperature dependent thermo-physical properties were considered. Also, the parameters used to determine the input parameters needed were determined by statistical analysis of some data previously generated by J. Pepin [11].

Several experiments were conducted using instrumented thermocouples on single wire SAW to collect data for model validation. Sets of matching machined plates were prepared with a bevel. On one side, three groups of three horizontal holes were drilled to insert the thermocouples. The three groups were the same and had three holes drilled at three different depths to insert two type K thermocouples and a type B thermocouple. Finally, the results of these experiments were compared to the model developed.

After the introduction a literature review is presented in chapter 2. This is followed by a chapter presenting the simulations done. The instrumented welds that were conducted are then discussed. After that, the models are compared to the measurements done using the instrumented welds. The

conclusions and the recommendations for future work are then reported. Finally the references are reported followed by the appendices.

2. Literature review:

In this chapter, work done previously on the main topics covered in this project is discussed as follows. The subject of welding is tackled first. Then, the variables used to describe a welding operation and how they affect the welding operation are presented. Afterward, the steel used in this project is described. As this project focuses on the welding of steel to manufacture pipes, an introduction to the pipeline industry is also presented. Finally, the way simulation of welding in general, and SAW in particular, evolved from the first attempts to the methods used currently is presented.

2.1. Welding:

In this section, welding and SAW are first defined. Then a quick look at the history of welding is outlined up to the development of the SAW process. The latter is addressed in more detail in the last part of the present section.

2.1.1. Definitions:

The American welding society (AWS) defines SAW as follows:

“Welding is defined as: A joining process producing coalescence of materials by heating them to the welding temperature, with or without the application of pressure or by the application of pressure alone, and with or without the use of filler metal.” [12]

“Submerged arc welding (SAW) is defined as: An arc welding process using an arc or arcs between a bare metal electrode or electrodes and the weld pool. The arc and molten metal are shielded by a blanket of granular flux on the workpieces. The process is used without pressure and with filler metal from the electrode and sometimes from a supplemental source (welding rod, flux, or metal granules).” [12]

2.1.2. Welding history:

Welding began around 2500 BC and consisted mostly of forging. Some minor improvements were emerged in 1800 when Alessandro Volta invented the battery. This gave the possibility to produce and store a much more versatile type of energy, electricity. Ten years later, Sir Humphry Davy discovered the electric arc, which produces a lot of heat on a small spot. This is ideal for welding.

It led the way to the invention of the first arc welding device in 1885 by De Benardos and Olszewski. [1, 2]

The SAW welding process was born in 1935 in an effort to automate an older welding process called shielded metal arc welding. This explains the connection between this process and the progress in automation technologies. [13]

2.1.3. Submerged arc welding:

After a general presentation of the process, several aspects of the SAW technology are discussed here. These aspects are the shielding of the arc, which is one of the specifics of this process, the productivity, which explains its wide usage in industry, the use of multiple electrodes in general and the tandem variant of the process in particular, and the interest of modelling this process. Finally, a summary of the strength and weaknesses of the process are given.

2.1.3.1. General overview:

SAW is an arc welding process with a consumable electrode. An electric arc is struck between a fusible electrode and the workpiece, which acts as the second electrode. This process differs from the others mainly by the presence of a layer of powder, called flux, on top of the workpiece where the weld is to be performed. This small change makes a big difference [3]. As the process is automated, it can operate safely using higher power than the other welding processes making it more productive.

Figure 1.1 shows a schematic of the process. The arc effectively travels through the flux and melts a part of the base metal as well as some of the electrode and some of the flux. The flux typically solidifies faster than the molten pool and shapes the fillet. The slag must eventually be removed to release the weld.

2.1.3.2. Shielding of the arc:

As stated before, the SAW process is an evolution of the shielded metal arc welding process and uses shielding of the arc too. This shield is achieved by the presence of the flux which protects the weld from the atmosphere and the water it contains. It plays an important role in the physical aspect of the fillet. It has a direct influence on the shape and compactness of the deposited metal as well

[3]. It also gives rise to a whole new range of possibilities as flux melting changes the composition of the weld.

From a safety point of view, the presence of the flux is beneficial as it blocks radiation and projections from the arc. It also retains a large amount of the toxic fumes [14], containing copper and manganese, which are responsible for “Metal Fume Fever” [15]. The fact that it is safer than most other welding operations makes it easier to automate, as less supervision is required.

2.1.3.3. Productivity:

This blanket of powder is also beneficial for productivity. In most welding processes a large amount of radiation is lost; here, radiation melts the flux which falls on top of the molten pool where it gives back the heat. Experiments by Christensen et al. show that between 91% and 99% of the total power provided to the system goes into the workpiece. For the sake of comparison, the values are between 66% and 85% for metal-arc welding of mild steel and between 66% and 69% for the metal inert gas (MIG) process on mild steel [16]. Being an automated process, much higher current can be used without compromising safety. This makes it possible to put more energy into the workpiece and, therefore, to increase the melting rate and thus the productivity. Higher travel speeds are, therefore, possible to achieve. For instance, according to [4] the SAW process is at least three times faster than stick-electrode welding. The high energy input, leading to the weld pool taking time to solidify as well as the presence of the flux, restrain the process to horizontal welding operations. Also, the presence of the flux *de facto* prevents the experimenter to see what is happening directly by using an infrared camera for instance.

2.1.3.4. Multiple electrodes:

To further improve productivity and avoid multiple passes, it is possible to use several electrodes [3]. Two main designs are used for two electrodes [4]. The first is called twin-wire SAW in which the two electrodes are connected to the same power source and the current splits between the wires according to Kirchhoff’s circuit laws. In the second one, called tandem SAW, each wire is connected to an independent power supply. The former is a rather inexpensive and quick way to increase the deposition of metal from the electrode, which is called the deposition rate, while the latter, in addition to the increase in deposition rate, enables the operator to fine tune the process. These methods can then be transposed to even more electrodes.

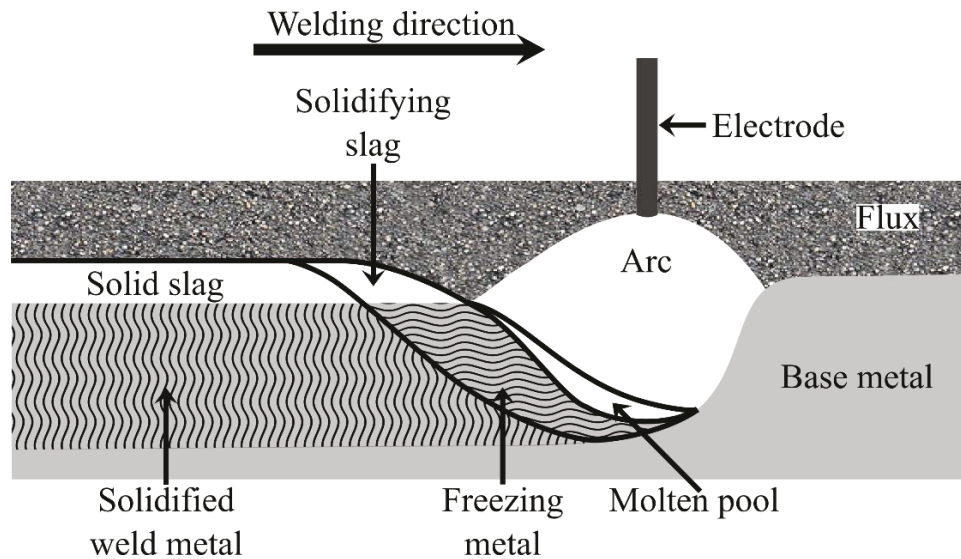


Figure 2.1: Schematic representing what happens during a SAW operation with one electrode. This schematic is adapted from [17] with the permission of ASM international.

2.1.3.5. Focus on tandem-wire SAW:

The tandem-wire SAW process, which is considered in this study, makes it possible to achieve different features with each electrode. The electrodes work in synergy. The first electrode is responsible for the penetration as the arc pressure pushes the molten metal backward [18]. The second electrode is responsible for the width of the weld and the deposition rate [14]. This assumes that the parameters have been set up correctly¹. This freedom also comes with the burden to find an operating window. Working out these parameters by trial and error only would be highly costly and can present some safety issues. The best way to reduce the number of experiments is to simulate the process.

2.1.3.6. Pros and cons of SAW:

To sum up, the advantages of this process are as follows [19, 20]:

- The deep penetration achieved by the process makes it possible to reach the same penetration depth as with other processes but, with a smaller bevel to be filled, which requires less metal addition.
- It is a rather safe process, as the flux stops radiation from the arc and most of the fumes.

¹ This will be developed in section 2.2.3.

- The process is highly productive as it can operate at high current and high travel speed.
- The flux can collect some contaminants from the molten pool and help produce better welds.
- For low-carbon steels it is possible to use inexpensive electrodes, which makes the process cheaper.
- The flux resting on the workpiece is less sensitive to the elements, like wind, which is an interesting aspect for semi-automatic SAW machines which can be used in the field.

This process also has its limitations [19, 20]:

- The handling of the flux requires more equipment than for other welding operations.
- Flux contamination can lead to porosity.
- The workpiece must be prepared with care and contaminants removed to achieve good welds.
- If multiple passes are required then the slag must be removed between each pass. This requires more work.
- The process cannot be used on plates tilted by more than 20%.
- The process can only be used on steel and some nickel alloys [3, 14]

This process is used in various heavy industries like structures, ship building, pipelines and many more. It is the ideal process to join large pieces of steel on an industrial scale.

2.1.3.7. Input from modelling:

SAW is an automated process widely used in plants, so it is difficult to see directly what happens; as such SAW is a domain in which industry is eager for modelling. Carrying out experiments to see what is happening during the process itself is costly and time consuming [21]. Modelling can help reduce the number of experiments and help in the decision making process. The development of better power supplies also increases the tuning possibilities and the complexity of the process.

2.2. Variables:

In the previous section the SAW process was presented. Here, the main variables used to describe this process are presented. First, the variables are listed. Then, the way the input variables, that can be fixed, affect the output ones, which characterize the resulting weld will be discussed. Finally,

the presence of a second electrode is discussed via the presentation of the difference in input parameters between the two electrodes of a tandem-wire SAW operation to produce a good weld.

2.2.1. Overview of the variables involved:

The capability to finely tune a considerable amount of variables during the SAW process is a double-edged sword as it makes the process more versatile and gives a lot of freedom to the operator on one hand. On the other hand, it means that it is hard to comprehend the effect of all the variables and their interactions as most of them are coupled. These variables for one wire SAW are:

- Current (I)
- Voltage (V)
- Travel speed (TS)
- Stickout
- Angle of the electrode (θ)
- Electrode diameter
- Polarity:
 - Direct current electrode positive (DCEP)
 - Direct current electrode negative (DCEN)
 - Alternating current (AC)
 - Frequency (F)
 - Balance (B)
 - Offset (O)

In addition to the input variables, there exists a number of output variables that are functions of the input ones. These variables are:

- Penetration depth (PD)
- Penetration area (PA)
- Reinforcement height (RH)
- Reinforcement area (RA)
- Bead width (BW)
- Heat affected zone parameters (HAZ)

Finally some variables can be considered either as input or as output. One of these is the wire feed speed (WFS), which is tuned so that the system operates at the chosen current and voltage.

2.2.2. Input variables and their effect on the output ones:

Here the influence of the input variables on the output ones is discussed.

2.2.2.1. Current:

Current represents the movement of positive electric charges, so it goes against the flow of electrons in metals. This is one of the parameters that can be changed by the operator. Current has a major influence on SAW. It is generally accepted that an increase in current increases the penetration depth [4, 5]. The effect of current on penetration in high current processes, such as SAW, can be explained by the plasma jet force which, at high current densities, creates a rapid flow directed downward in the plasma [22]. This force, therefore, creates a pressure on the surface of the molten pool, which pushes the liquid metal backward and reduces the layer of liquid between the arc and the base metal, which receives more energy from the plasma. The current is also responsible for Joule heating. Joule heating plays, in conjunction with the stickout, a role in the heating and melting of the electrode, which controls the WFS. An increase in current will tend to increase the melting rate and the bead height. [23, 24]. For the tandem SAW process the previous trends hold for the penetration and the reinforcement height [25]. The increase in current seems to increase the bead width, but the effect of current on the bead width is not simple and the square of the current can be shown to have a decreasing effect on the bead width (see Appendix A).

2.2.2.2. Voltage:

Voltage represents the driving force for the flow of electric particles (e.g., electrons and ions). It is responsible for the acceleration of electrons and the actual creation of the plasma. This variable is mostly responsible for the bead width; the higher the voltage, the wider the bead [4, 5, 26, 27]. This is due to the fact that the voltage is responsible for the arc length and as the arc grows in length it gets wider [22]. As a first approximation the arc can be considered conical.

2.2.2.3. Travel speed:

Travel speed is important for the productivity of the process, but also has an effect on the weld itself. When the travel speed increases, the bead width decreases [4, 5, 27]. For low travel speed,

however, the trend is reversed but one study reports that when travel speed increases, the bead width increases [26].

2.2.2.4. Heat input:

Current, voltage and travel speed have an effect on the process on their own, but sometimes their effect is not clear. This is explained by the fact that the three variables are strongly coupled. Electricity only flows due to a driving force. This is characterized by the power which is given by Equation (2.1) for DC and Equation (2.2) for AC. The subscript RMS, meaning root mean square, will be removed from now on for sake of simplicity, but when AC is considered, the values of the current and voltage corresponds to the RMS values.

$$P_{DC} = I \cdot V \quad (2.1)$$

$$P_{AC} = I_{RMS} \cdot V_{RMS} \quad (2.2)$$

The travel speed also changes the power effectively transferred to the workpiece as it is a measure of the time the arc (i.e., the heat source) stays above a given point. This is why heat input, HI, which takes travel speed into account via Equation (2.3), is widely used in welding.

$$HI = \frac{I \cdot V}{TS} \quad (2.3)$$

When the HI is used, the trends are much clearer [28]. As expected, an increase in HI produces an increase in all the bead shape parameters classically used to characterize a weld, i.e., reinforcement, penetration and bead width. An increase in HI also increases the deposition rate, which is important for productivity. On the other hand, a higher HI results in a wider HAZ, which is the weak point of the weld.

The HI is not enough to explain everything, but gives a good indication and can be used in addition to the first order variables. The HI is the first interaction variable used in statistical analysis. First order variables are the most important and account for most of the variation. This is an example of a case where an interaction term can be as significant as a first order one.

2.2.2.5. Stickout and electrode diameter:

The stickout [4] is the length of the electrode that is subjected to Joule heating. When the process stabilizes, the WFS is constant and the stickout is equivalent to the time a slice of the electrode is heated by Joule heating. Therefore, a higher stickout tends to result in a higher deposition rate, assuming the WFS stays constant. An increase in stickout also reduces the penetration depth as there is more liquid in the molten pool.

An increase diameter of the electrode will tend to decrease the WFS, if the other parameters are fixed. Indeed, the mass of material inputted is proportional to the WFS and the diameter of wire squared. So, for a larger diameter the same mass of matter will be inputted using a lower WFS than for a smaller diameter [23] (Appendix A).

2.2.2.6. Angle of the electrode:

According to some modeling studies, the angle of the electrode can influence the penetration depth by changing the flight of the molten metal droplets coming from the electrode. This ultimately more or less disturbs the flow patterns in the molten pool, based on the way the droplets fall in it [29].

2.2.2.7. Polarity:

The first thing to consider with polarity is whether the system uses DC or AC. Two types of DC exist, DCEP and DCEN. Figure 2.2 illustrates the differences between those two modes. DCEN mode tends to increase the melting rate of the electrode. Instead, the DCEP mode increases the melting rate of the base metal [30]. DC mode tends to give bead shapes that are easier to predict. AC polarity allows one to tune the time spent on a specific polarity (balance) as well as the difference between the current applied during the positive polarity part of the signal and the negative one (offset).

AC polarity finds its most common application in tandem SAW as it helps avoid arc blow between the two arcs as well as deviations of the plasma columns induced by the presence of another arc. AC polarity is mostly applied to the trail electrode to avoid disturbing the lead one. Also a higher voltage is often used on the trail electrode to produce a wider bead to cover the one produced by the lead electrode. Higher voltage is reported to make the arc more sensitive to the presence of

another arc. The lead electrode is often used to achieve penetration by digging in the molten pool. DCEP and high current are best suited for the lead electrode. [4, 31].

Figure 2.3 and 2.4 represent the electrical signal modulations corresponding respectively to a change in offset and a change in balance. When the balance increases, the process gets closer to a DCEP mode. A change in offset is equivalent to a change of current in DCEP and DCEN. For instance, when the offset increases an increase in melting rate occurs for the base metal while the melting rate of the electrode typically decreases.

Pepin [11] studied the effect of the waveform variables on the bead shape during SAW. His results confirm the trends outlined here.

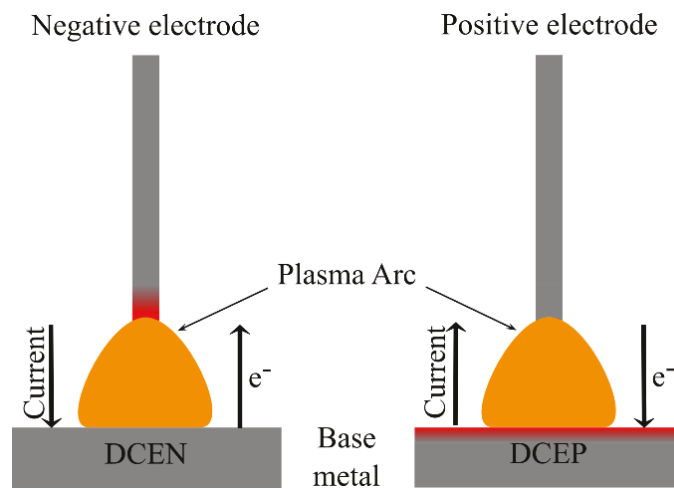


Figure 2.2: Schematic representing the differences between DCEN and DCEP. Inspired by [11].

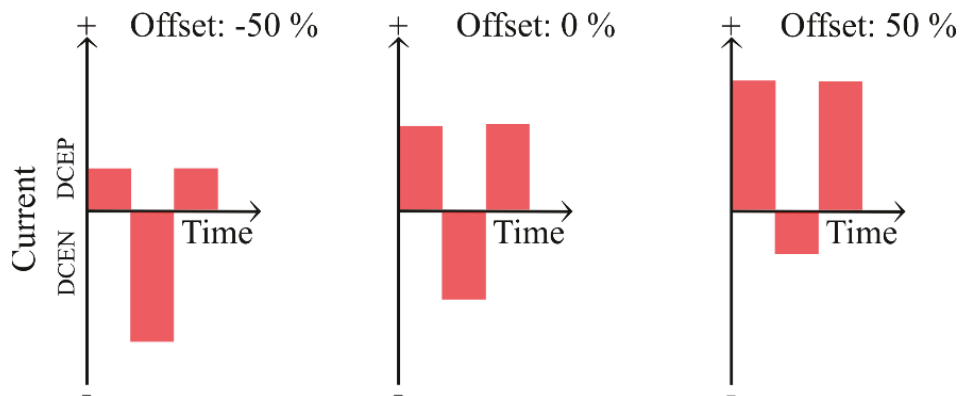


Figure 2.3: Electrical signal changes corresponding to changes in offset Inspired by [11].

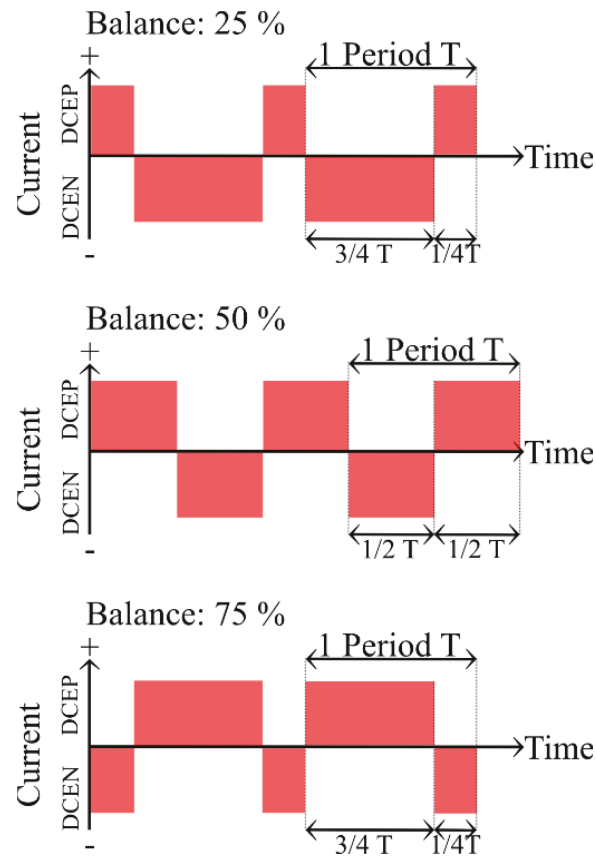


Figure 2.4: Electrical signal changes corresponding to changes in balance. Inspired by [11].

2.2.3. Additional considerations for tandem SAW:

For tandem SAW, the two electrodes can be operated with independent settings. Based on what has been developed previously, the best theoretical settings for tandem SAW are outlined:

Lead electrode:

- Polarity: DCEP, for improved penetration.
- Current: higher than that of the trail electrode to make sure the digging action of the lead electrode is not undermined by the pressure produced by the trail electrode.
- Voltage: lower than that of the trail electrode to make sure the trail electrode covers the width of the bead created by the lead electrode and thus avoids defects.
- Stickout: short, to avoid reducing penetration.

Trail electrode:

- Polarity: AC, to avoid arc interferences.
- Current: lower than the lead one.
- Voltage: higher than the lead one.
- Stickout: long, for a higher melting rate of the electrode.

The lead electrode achieves the penetration, while the trail one deals with the deposition rate and the bead width.

2.3. Steel:

Ferrous alloys are materials of high engineering interest [6]. Iron is widespread in the accessible part of earth's crust. It is relatively cheap to produce. It is one of the most recycled materials in the world. These alloys offer a lot of possibilities; their properties like ductility, strength, toughness,

Among the steels, the ones that are especially used for pipelines are referred to as micro-alloyed steels. Low carbon steels contain less than 0.25 wt% of carbon [6]. These steels feature good ductility and toughness as well as good weldability. In micro-alloyed steels, other alloying elements are used to increase the strength and the corrosion resistance. With their high strength-to-weight ratio, they are used in application where weight reduction is crucial. One example is the automotive industry, which is the first industry to use them, or in pipelines as more weight means more problems for the transportation and the assembly of the pipes [32]. They are also abrasion resistant, which is an asset when transporting bitumen with diluents, like in Alberta, such as sand, and impurities.

2.4. Pipelines:

The material considered in this project is a pipeline steel. Therefore, pipeline usage in general is discussed. Then the reasons for using micro-alloyed steels to construct pipelines are presented. Finally, the different processes used to produce steel pipelines are presented.

2.4.1. General overview:

Pipelines represent one of the most efficient ways to transport fluids at high flowrate. They are widely used for oil, gas and CO₂ transmission, onshore as well as offshore. With maritime transportation, pipelines are one of the two main ways to transport hydrocarbons. Hundreds of thousands of kilometers of pipelines are buried across the world [33]. Pipelines are more

environmentally friendly than ship transportation, as posing less of a threat in the case of failure, compared with wreckage of a ship. Pipelines are especially suitable for large countries like the U.S., Canada or Russia. They are widely used in Alberta where extracted bitumen is blended with diluent and transported via pipeline [34]. Some pipelines have been constructed under water but their construction requires significant investment.

2.4.2. The reasons behind the choice of micro-alloyed steel for pipelines:

The best material for onshore and offshore pipelines used to transport oil and gas is steel [7]. While the problem posed for offshore pipelines are well known, the problems encountered when building onshore pipelines are as big as for offshore ones. For instance, onshore pipelines are subjected to more displacement than one may think. These structures are required to stay underground for decades without breaking. However, the ground is moving. Pipelines built close to water streams of any type can end up in the stream due to erosion of the soil by the water. This will entirely change the stress distribution encountered by the pipe. Also, in some places the ground is frozen for several months, which can lead to uneven heaving of the ground and strain along the pipe [35]. For example, when frozen, soils consisting of sand tend to heave more soils containing mainly gravel; Figure 2.5 illustrates this effect. If pipelines are installed in regions with sand and gravel that are prone to freezing, the pipe will undergo cycles of stresses and strains which may lead to failure.

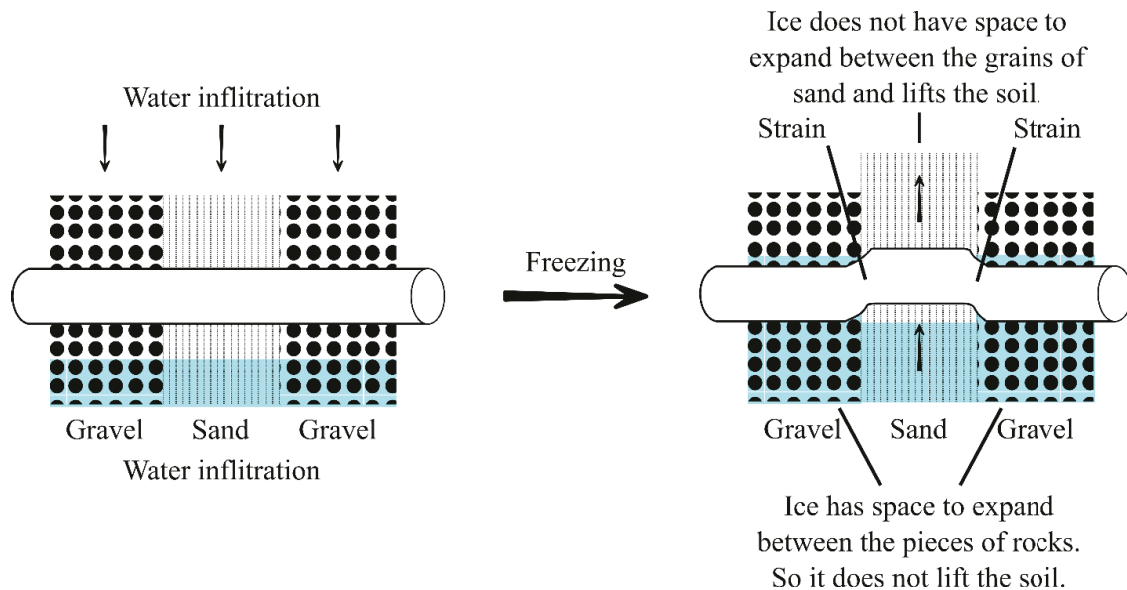


Figure 2.5: Example of uneven strain encountered by pipelines.

As such, pipes have to be made from a ductile and tough material. Also, the material must be able to sustain the pressure and stay in the ground for years without breaking. This implies high toughness, high strength and high corrosion resistance. It is impossible to build the entire pipeline from one single block, so smaller sections must be easy to assemble into larger pipes using SAW. All these issues considered together leads to micro-alloyed steels, which can be produced in large quantities at an affordable price.

2.4.3. Pipeline manufacturing:

Once the material used is determined, it must be fabricated into a pipe. Several processes are used based on the type of pipe being manufactured [7].

Here, two discontinuous pipe manufacturing processes are presented: seamless pipe manufacturing process and the UOE pipe manufacturing process. Then two continuous processes are discussed, the ERW process and the spiral weld process.

2.4.3.1. UOE pipes:

A discontinuous method which can process diameters between 40.64 cm (16 inches) and 162.56 cm (64 inches) is called UOE pipes. The letters “U”, “O” and “E” refer to the different steps of the process which are schematically represented in Figure 2.6. A steel plate is first formed into a “U” shape then is closed and welded into a cylinder using SAW. Finally, the cylinder is expanded from the inside to improve the roundness of the pipe. In this process, TMCP is done on the skelp prior to formation. However, the strain applied to the plate during forming can jeopardize the mechanical properties of the pipe [36]. To improve productivity, it is possible to produce pipes via continuous processes.

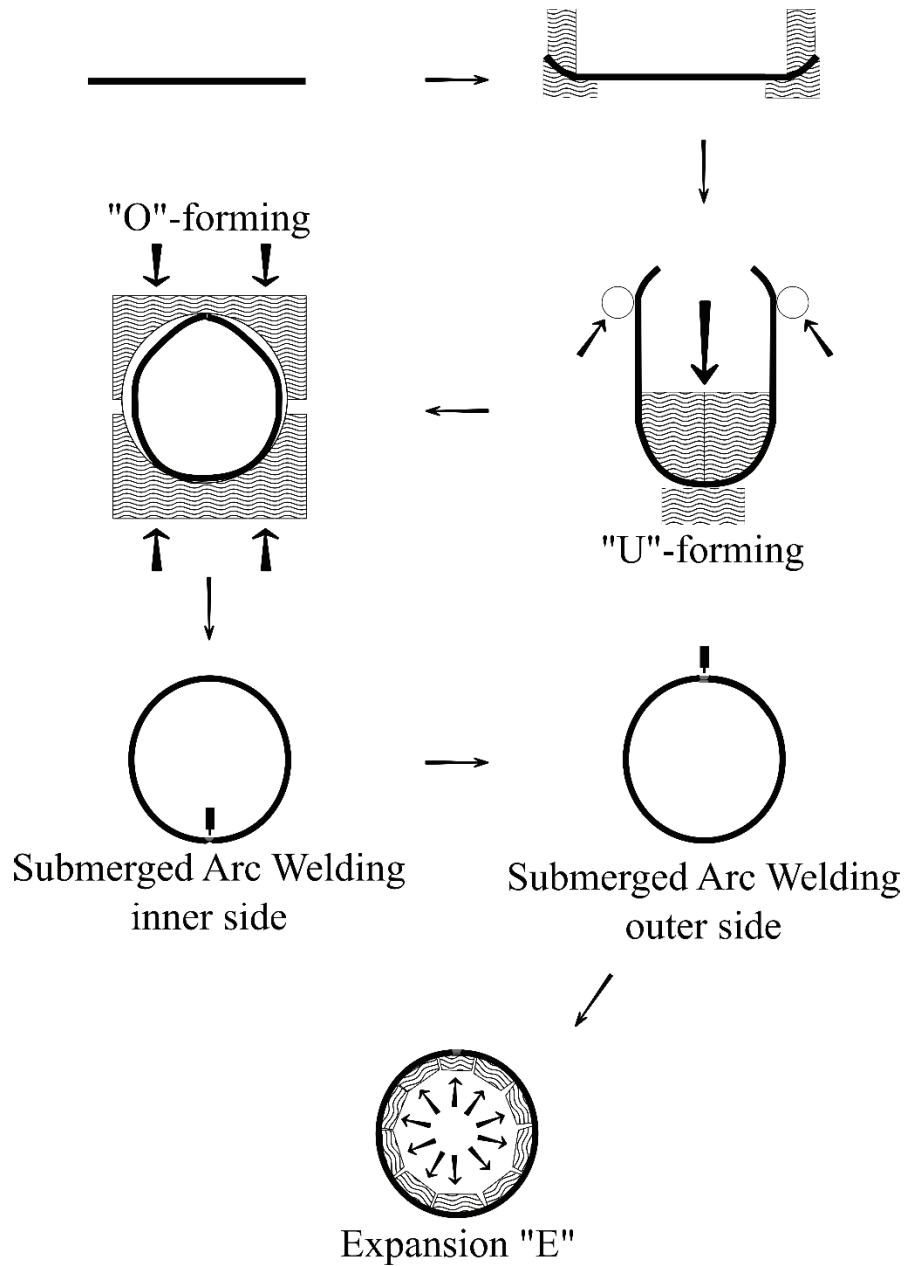


Figure 2.6: UOE pipe forming steps. Based partly on work referenced in [7].

2.4.3.2. Continuous processes:

Two examples of continuous processes are the electric resistance welding process (ERW), Figure 2.7, and the spiral welding pipe manufacturing process, Figure 2.8. ERW can produce pipes with diameters ranging from 6.0325 cm (2.375 inches) up to 60.96 cm (24 inches), making it a versatile process. The spiral welding process is especially used for large diameters between 50.8 cm (20 inches) and 254 cm (100 inches). These processes present some differences in terms of the wall

thickness of the pipes produced, but the diameters achievable for each process (Figure 2.9) depict well the complementarity of these processes.

The ERW process begins by uncoiling a steel coil. Then a succession of rolls bends the plate in the desired pipe width by progressively turning the plate into a cylinder. Finally the seam is welded using electric resistance.

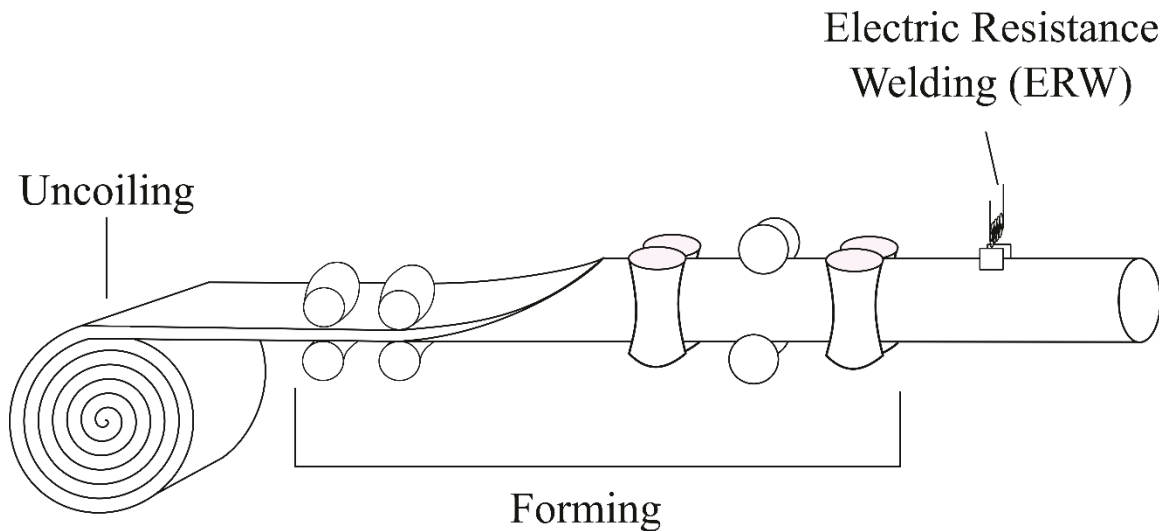


Figure 2.7: Simplified schematic of ERW pipe forming process. Based partly on work referenced in [7].

The spiral welding process begins by uncoiling coiled steel and feeding the plate at an angle with respect to the center of the pipe to be formed. Then several rolls bend the plate to form a spiral which is finally welded using SAW on both the inside and the outside surfaces. One of the key advantages of this process is the possibility to produce a wide range of diameters of pipes by just changing the angle at which the plate is presented and bent.

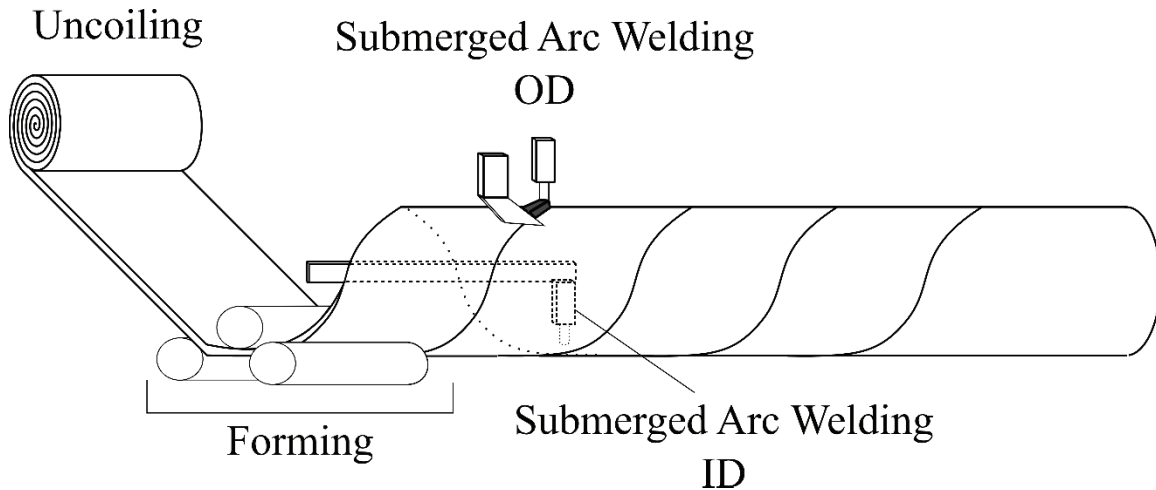


Figure 2.8: Simplified schematic of spiral weld pipe forming process. Based partly on work referenced in [7].

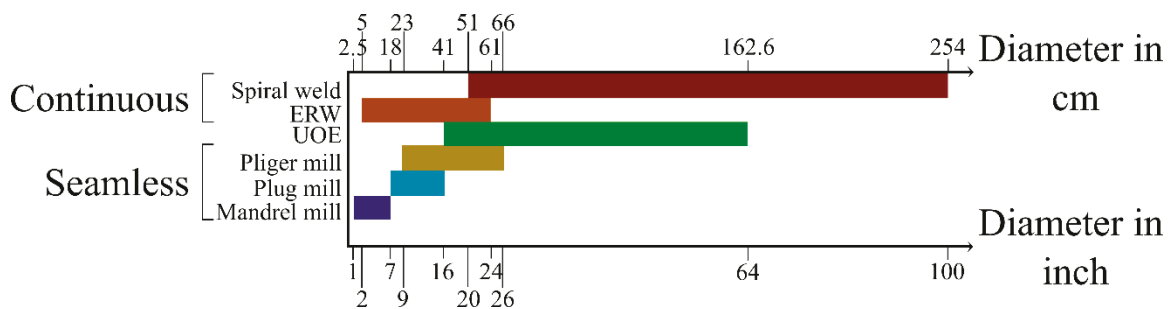


Figure 2.9: Diameters available for different pipe making processes [7].

2.5. Simulation:

As was shown above, welding of pipelines is an important process in both its manufacture and installation. ERW and spiral pipe are welded. Different ends of pipe are often welded together to make up a pipe of desired length. Finally, during installation pipe ends are welded together in the construction of a pipeline. These are termed girth welds. As the goal of this project is to simulate the temperature profile during an operation of SAW, so a review on what has been done previously on the subject is warranted. This section is divided into two parts. The first presents the analytical models proposed in the past and currently to simulate the welding process. The second presents the numerical models.

2.5.1. Analytical solutions:

Here the different approaches proposed to model the welding process analytically are reviewed. The first analytical solution put forward by Rosenthal [37] is discussed. Then an introduction of various thermal properties is presented. The use of distributed heat sources is also presented. After this first step showing the complexity of the heat source, an introduction to volumetric heat sources is discussed. This part ends with a short conclusion on the analytical solutions used in modeling welding.

2.5.1.1. Point source:

Rosenthal [37] proposed the first solution to the problem of determining the temperature profile during welding. His solution was an analytical model based on a moving point source and led the way to analytical modelling. His work provided a powerful tool to scientists and engineers who still use it to this day to quickly work out $t_{8/5}$, which is the time a point takes to go from 800°C to 500°C in the HAZ. This parameter gives insight into which phases are likely to appear in the weld. To come to a solution, assumptions have to be made as follows:

1. Thermophysical parameters are assumed to be constant (i.e. independent of temperature).
These properties include:
 - thermal conductivity, k ;
 - density, ρ ;
 - specific heat, C_p , and the latent heats for phase changes.
2. The speed at which the electrode moves is considered constant.
3. The power delivered by the heat source to the plate to be welded is constant and localized on a point.
4. A quasi-stationary state is assumed. This means that the temperature profile in the reference system of the moving source is considered constant.
5. The geometry is assumed to be semi-infinite.

Despite the number of constraining assumptions, Rosenthal has been able to develop an equation which agrees well with experiments, away from the vicinity of the heat source. This was proven, in part, by Christensen et al who published a paper in 1965 [16] comparing some experimental results with theoretical results derived from Rosenthal's solution. Their work showed surprisingly

good agreement, away from the source. The main problem with Rosenthal's approach is the fact that the source is considered to be concentrated on a point.

2.5.1.2. Varying thermal properties:

To improve the results given by analytical models, Malmuth [38] put forward an analytical method accounting for the latent heat. This method used dimensionless numbers. Among them one was the dimensionless velocity-power product. The method was limited by the fact that this dimensionless quantity was considered as going to zero for the mathematical developments. This approach improved the prediction of the penetration depth, but still some large discrepancies occurred and it was applicable to only a small number of cases. However, it showed that taking into account the latent heat of fusion as a reduction of the inputted power lead to overestimating the effect of the latent heat of fusion on the process. To take into account the change in material properties with temperature, it is possible to operate a linearization of the parameters. This method better predicts the temperature field; [39] however, this method still considers a semi-infinite body.

2.5.1.3. Heat source distributed on the surface:

The discrepancies mentioned above can be reduced by considering a distributed heat source which is a sum of point sources. This is what Eagar and Tsai [40] did in 1983 and they noticed a major improvement from Rosenthal's solution. An illustration of the heat flux distribution they used is shown in Figure 2.10. The solution agrees better with experimental data, but is more complex and therefore harder to utilize. These methods do not account for the transient temperature distribution. In 1997 Jeong and Cho [41] came up with an analytical solution for the transient temperature distribution in fillet arc welding. The results they obtained were in agreement with experiments. These models, despite being good for a wide array of welding processes, failed to account for the penetration. This is a problem, especially for deep penetration welding operations like SAW.

2.5.1.4. Volumetric distributed heat source:

In 2010, Ghosh and Chattopadhyaya [42] proposed an analytical solution for a general 3D double central conicoidal heat source. This enhanced the way to deal with penetration depth. Another study was done comparing the use of two conical volumetric distributed heat sources: a double ellipsoidal one and an oval one [43]. The geometry was still semi-infinite. They found that the best

heat source was the oval one, but to use it one needs to know the shape of the weld pool, which is hard to assess.

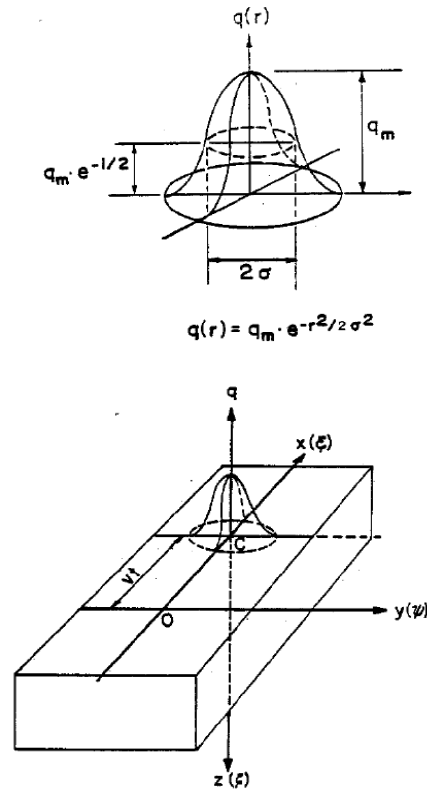


Figure 2.10: Gaussian distribution from Eagar and Tsai. Welding Journal, (December, 1983), © American Welding Society [40].

2.5.1.5. Conclusions on analytical models:

Analytical models have attracted interest in this field as they require less computational power and are, therefore, quicker in providing an answer. The problem is that even with all the progress made, they are constrained to problems which are close to linearity. This prevents one to account for the real evolution of the physical characteristics of the material with temperature. Some coupling, like the one between the temperature profile and the microstructure, must be put aside. On the other hand, the linearity of the problems they deal with makes it easier to consider multiple electrode welding, as any linear combination of solutions of a linear problem is also a solution of the problem. So, multiple wire solutions are just linear combinations of one wire solutions. To go further, numerical methods are required.

2.5.2. Numerical methods:

First, the reason why numerical methods were introduced later in the welding industry are presented here. Then, their application to the welding field is presented. In this project, the FEM is used, so a part of this section is dedicated to FEM. The dimensions used in the simulations are discussed. The use of more and more complex heat sources is addressed. The last two parts of this section concern the modelling of the weld pool and of multiple electrode processes.

2.5.2.1. Problems to overcome to use numerical methods:

The biggest hurdle to overcome for numerical analysis to become mainstream in the field of welding was computational power. Actually, such modelling can become extremely intricate. Nonlinearities, which require numerical analysis, make the convergence of the algorithms difficult and require a lot of computational power. That is why the first real numerical analysis did not emerge before the *1960s* [8].

2.5.2.2. Application of numerical methods to welding:

Initially, finite difference methods were used. They are easy to understand, but are not designed to be used for complex geometries, and the introduction of nonlinearities is not natural. The gain in momentum of numerical analysis coincides with the generalization of the FEM to handle partial differential equations (PDE) [44]. This happened between the *1950s* and *1970s*. This method is less intuitive, but makes the introduction of the complexity of the geometry more natural. Indeed, like all other numerical solutions, the reliability of the results obtained via FEM is dependent on the number of elements used. More specifically, the type of elements used matters [45]. Rosenthal's solution was reproduced using FEM [46, 47]. It was also demonstrated that, taken in an equivalent situation, FEM can give results close to the ones given by analytical solutions [48]. This means that this numerical method is suitable to the problem and, despite the approximations intrinsic to every numerical method, can give meaningful results.

2.5.2.3. Focus on the finite element method:

The FEM is a numerical method used to solve PDE, which fall into the boundary value problem denomination. This means that the problem is to seek a solution knowing the constraints on the boundaries of the domains to be solved. For most numerical methods, the system is broken into a network of discrete points. For FEM, not only are the points considered, but also the spaces

between them. In this method, the system is broken into smaller entities called elements containing some points and the space between them. From there, most numerical methods, like the finite difference method, approximate directly the solution on the nodes of the mesh by matrix manipulation and give, as a result, an array of scalars. FEM instead begins by postulating the shape of the evolution of the parameters desired around the point at which it is evaluated. Then the functions replace the values of the parameter in the PDE to be solved and the boundary conditions, if applicable. FEM gives an array of equations assembled in a matrix form. Then the solution is desired by carrying out a minimization on the error. To sum up, the system is considered as an assembly of smaller systems interacting with each other, whose behaviors can be assessed by a finite number of parameters.

This method is computationally costly but can handle complex problems. It can also be used for intricate geometries, which would be hard to deal with otherwise. FEM allows local changes to the scale of a single element. It can handle highly non-linear 3D systems. Finally, it is a more natural way of modelling a system as the points are not singled out and the parameters at each point are supposed to have a continuous effect on their surroundings. Some of the disadvantages of FEM are the fact that the precision of the results depend on the number of elements used, it approximates the behavior of the desired parameter across the elements using polynomials, which *de facto* introduce errors, and the nature of the elements must be well chosen to give good results [45].

2.5.2.4. Dimensions used in the simulation:

Simulations were restricted to 1D until the *1970s* [10], mainly because going from one dimension to higher ones increased the order of magnitude of elements needed exponentially. The first fully 3D analysis was carried out in 1986.

The welding process is inherently transient as the arc needs to be struck, then travel through the piece, and finally stop. The evolution of the welding source with time and its travel through space are widely neglected for industrial processes, like pipe manufacturing since the start and end of the pipes are cut and recycled as scrap to avoid defects. Instead, an Eulerian approach is often used, in which a quasi-steady state solution is desired in a moving reference system moving along with the source. This suppresses the issue of making the actual source move across the geometry.

It also makes it possible to reduce the geometry size as only a chunk of material around the source is taken into account. [37, 48].

2.5.2.5. Complexity of the heat source:

The first source used was a point source. It gives interesting results but soon the need for more precise results pushed for the development of better models.

The progression in the complexity of sources used to simulate the process follows the same logical trend as for analytical analysis. The first introduction of a Gaussian distribution is credited to Pavelic [10] in 1969. His approach was restricted to the surface of the workpiece where the heat flux was spread on a disc. A Gaussian distribution was then used in conjunction with FEM (Friedman 1975, 206-213). This improved the results close to the source. The approach was still not sufficient to correctly simulate deep penetration processes like SAW. To reach deep penetration processes, volumetric sources were used [49].

One of the best heat source models proposed, as of now, is the double ellipsoid put forward in 1984 by Goldak et al [50]. A representation of the power distribution and the source used in Goldak's model is available in Figure 2.11. It can account for many different situations and the other sources presented here turn out to be special cases of this one. It also gives reproducibly accurate results. This approach can also be extended to account for the welding of two dissimilar metals by choosing two different sets of double ellipsoids accounting for the nature of the two different metals [10]. To go a step further, Yadaiah and Bag came up with an egg-configuration heat source [51]. This integrates the shape difference between the front and the rear end of the source introduced by the double ellipsoid heat source, as well as new possibilities of shapes which could not be easily produced otherwise. The egg-shaped heat source is also a little bit more general, as the double-ellipsoid itself is a special case of this geometry. To determine the geometrical parameters for all these sources, experiments are required. Christensen's results [16] are still widely used for this purpose.

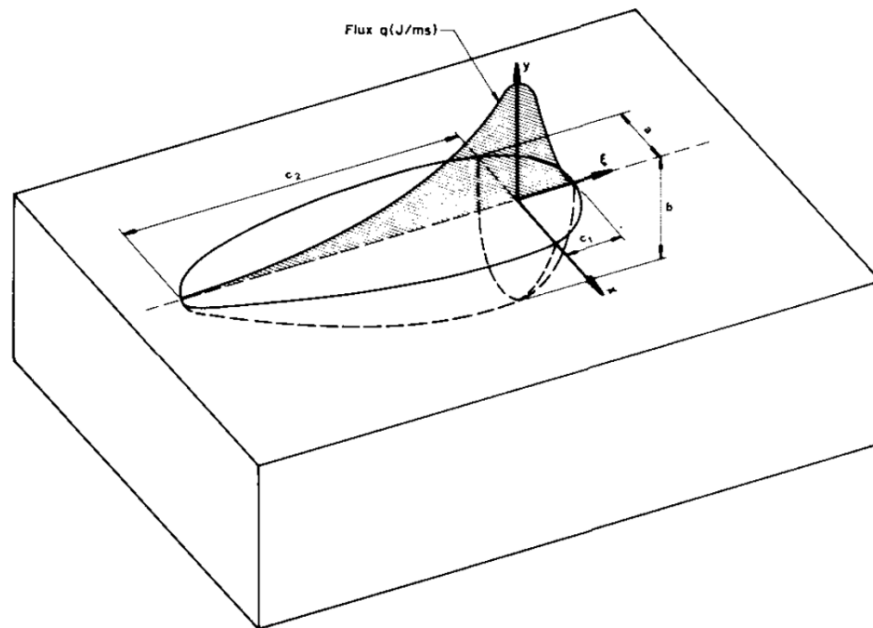


Figure 2.11: Representation of a double ellipsoid volumetric source with the power distribution along the welding direction. Reproduced from [50] with permission of Springer.

2.5.2.6. Modelling of the weld pool:

The next step is to take into account the movement in the weld pool itself. The problem for SAW is that the weld pool and the source are hidden during the process and direct measurements based on image analysis cannot be done. In 2013, Cho et al. [29] did some computational fluid dynamic (CFD) to model the stirring in the weld pool. The heat source dimension was dictated by measurements on the arc itself after it exited the flux. The plasma jet force, as well as the heat carried by the droplets from the electrode and the flux were considered separately. It showed good agreement with the experiments and determined that the angle the electrode makes with the vertical had an effect on the bead shape, especially the penetration.

2.5.2.7. Multiple electrodes:

Processes with more than one electrode have existed for years now. A superposition of several sources is often chosen to model these processes [52] (Figure 2.12). In 2014, Cho et al. [53] did some CFD calculations for tandem SAW taking the interactions of the two arcs into account. The

calculations showed correct agreement, but the top surface was different from the experiments and showed wavelike patterns. The bead shape did not match the one obtained experimentally. Therefore, the CFD approach has some merit, but is extremely costly in computational time and tends to deviate from the actual weld shape. As such, it does not seem to suit the needs of this project, even if it can provide information on what happens inside the weld pool which is not available for the other methods.

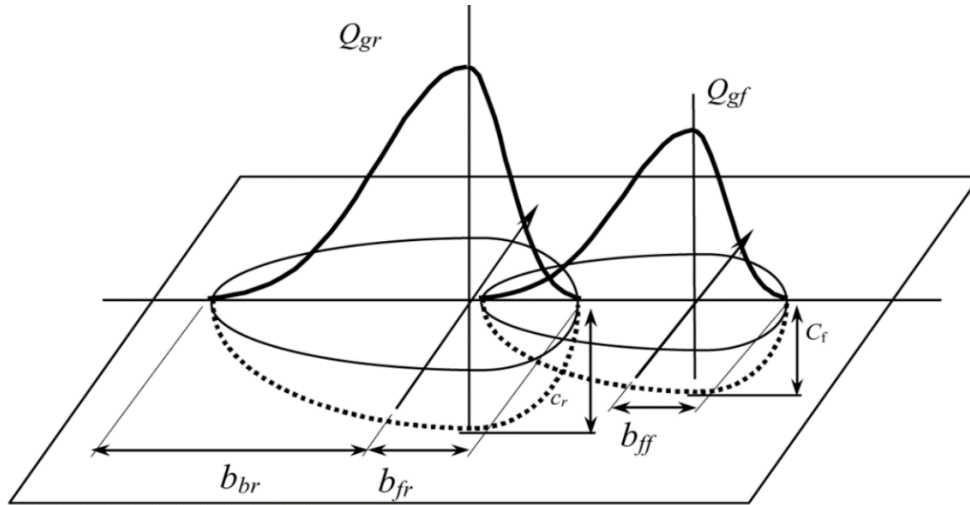


Figure 2.12: Heat source for twin-wire SAW. Reproduced from the work of Sharma et al [52] with permission of Taylor & Francis.

2.6. Frame of the present work:

Among the existing welding processes the one studied here is SAW. This process is used extensively in pipe manufacturing, especially it is at the centre of the spiral weld pipe manufacturing process. The parameters and properties used here were determined for this process. To simulate the temperature profile generated by different welding processes several approaches were developed. In the present work the simulation is done using FEM as it is the most versatile numerical method applicable to this process. The introduction of the heat source is crucial for the simulation of the temperature profile during a welding operation. The first source considered is the point source. It was used to obtain analytical solutions. Its use to obtain numerical solutions is studied here. Another heat source that is studied is the double ellipsoid heat source as it is the most versatile heat source that can be used with the data available. Some better sources exist but they require either the use of CFD or data that are hard to obtain, like the shape of the molten pool.

Taking the variation of the thermal properties with the temperature is also a way to improve the results obtained by simulation. Therefore, the use of such data is studied here.

After the presentation of the simulations their results are compared to measurement done using instrumented thermocouples.

3. Simulation:

The objective of this work is the development of a thermal model to predict temperature during SAW. The choice was made to tackle the problem via numerical analysis and the FEM. Also numerical analysis was done with the help of COMSOL Multiphysics® software.

Here the governing equations are first presented. Then the case of a point source supplying heat to a semi-infinite body is discussed. The mixed boundary condition is then introduced. This is followed by the presentation of a double ellipsoid volumetric heat source. Finally a conclusion on the simulation is proposed.

3.1. Governing equations:

To understand the work that has been done it is important to present the relevant equations used throughout this work. In this study fluid flow in the weld pool is not studied. Therefore, the welding system can be modelled assuming conductive heat transfer. The conductive heat equation can be written as follow [54, 55]:

$$\vec{\nabla} \cdot (k\vec{\nabla}(T)) + Q = \rho C_p \frac{\partial T}{\partial t} \quad (3.1)$$

If the thermal conductivity is assumed to be constant Equation (3.2).

$$k\vec{\nabla}^2 T + Q = \rho C_p \frac{\partial T}{\partial t} \quad (3.2)$$

Equation (3.1) is the one considered when varying thermal properties are considered while Equation (3.2) is used when the thermal properties are considered constant. In welding the operation never reaches steady state as the source is moving along a finite piece of material. For SAW the piece to be welded is often several meters long. Thus, the temperature profile in the vicinity of the source, viewed in the Cartesian² reference system of the source, can be considered as independent of time. This is the notion of quasi steady-state which will be used here to simplify

² The reference system is Cartesian, as it is in steady translational motion with respect to the observer's system which is considered Cartesian too. For a spiral weld the reference system is not strictly Cartesian but the deviations are neglected due to the slow speed and the typically large diameters of the welded pipes.

the calculations. In this case a change of variable is operated on the space variable along with the welding source movement. Here, it is arbitrarily called x , which is replaced by $X = x - vt$, where v is the travel speed and t is the time, to account for the movement of the reference system. Equation (3.1) becomes Equation (3.3) in the reference system (X, y, z, t) .

$$\vec{\nabla} \cdot (k\vec{\nabla}(T)) + Q = \rho C_p \left[\frac{\partial T}{\partial t} - v \frac{\partial T}{\partial X} \right] \quad (3.3)$$

Quasi steady-state is assumed in this reference system yielding Equation (3.4).

$$\vec{\nabla} \cdot (k\vec{\nabla}(T)) + Q + \rho C_p v \frac{\partial T}{\partial X} = 0 \quad (3.4)$$

As the new reference system is the only one used throughout the study, it will be denoted as (x, y, z, t) , even if the x should be upper case, for sake of simplicity.

If the thermal conductivity is considered constant in Equation (3.4) then it is possible to write Equation (3.5).

$$k\vec{\nabla}^2 T + Q + \rho C_p v \frac{\partial T}{\partial X} = 0 \quad (3.5)$$

The global equation is applied on different geometries which are all variations of the one displayed in Figure 3.1. More specific information will be given in the subsequent sections. The first thing highlighted in the picture is the fact that the direction of the “ x ” axis is opposite to the welding direction. Another important point is the fact that the source will always be applied on a part of the geometry and never on the entire geometry.

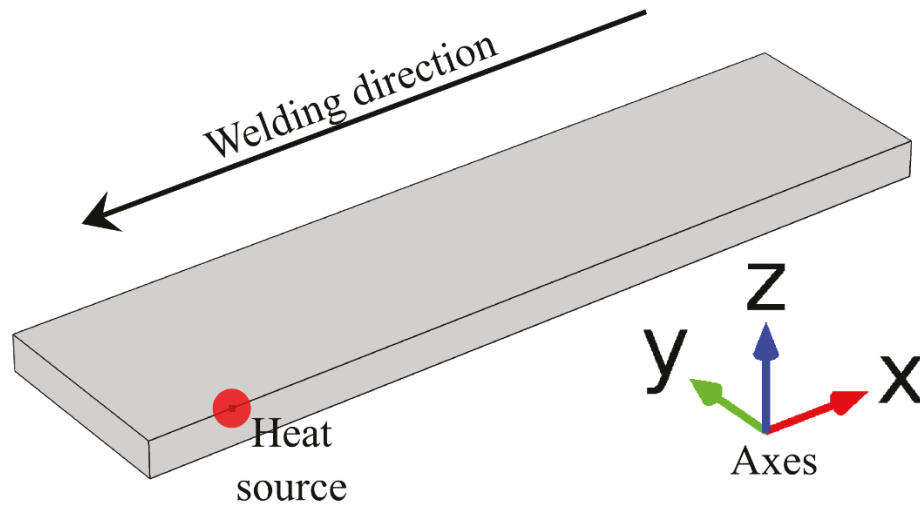


Figure 3.1: Generic geometry used for the simulation. Any geometry used here is a variation of this one.

3.2. Point source on a semi-infinite body:

The first attempt to simulate the temperature profile during welding was undertaken by Rosenthal in 1946. To build confidence in the software and to make a first step into the simulation, it is of interest to dwell on a semi-infinite body with point sources.

Here, a single point source applied to a semi-infinite body is considered. Then the extension of the problem to two point sources is presented.

3.2.1. Single point source:

First, Rosenthal's assumptions and results are presented. Then the way to obtain these results using COMSOL Multiphysics® is presented. After, an improvement on the point source, via a hemispherical surface source, is discussed. Finally, the conclusions drawn on the single point source are reported.

3.2.1.1. Rosenthal's assumptions and results:

Rosenthal's solution [37] is the first one that has been proposed. It gives interesting results [16] but is limited. As both its interests and limitations are well known, it is of interest to reproduce it using FEM software to check the reliability of the software as well as to go beyond the capabilities of the Rosenthal's solution alone.

After some mathematical developments, available in the original paper from Rosenthal [37], the following assumptions are made:

1. The variations in the physical parameters with temperature are ignored; these include, therefore Equation (3.2) is considered:
 - a. thermal conductivity k ;
 - b. density ρ ;
 - c. specific heat C_p and the latent heats of phase change.
2. The speed at which the electrode moves is considered constant.
3. The power delivered by the heat source to the plate to be welded is constant and localized at a point.
4. A quasi-stationary state is assumed. This means that the temperature profile in the reference system of the moving source is considered constant.
5. The geometry is assumed to be semi-infinite.

Rosenthal found solutions to the heat transfer equation in different cases. The solution for a semi-infinite body is available in Equation (3.6). One can notice a 2 in the denominator instead of a four. This is due to the fact that only half of the space is considered.

$$T = T_0 + \frac{P}{2\pi k} e^{-\lambda vx} \frac{e^{-\lambda vR}}{R} \quad (3.6)$$

where

$$R = \sqrt{x^2 + y^2 + z^2} \quad (3.7)$$

If the source is placed at the point $(x, y, z) = (0,0,0)$ and:

$$\lambda = \frac{C_p}{2k} \quad (3.8)$$

3.2.1.2. Rosenthal's temperature results using COMSOL Multiphysics®:

The biggest problem to be handled when trying to duplicate Rosenthal's solution with a numerical scheme is the fact that most of the numerical schemes cannot handle the notion of infinity. This is another strength of FEM. It uses elements to describe the space between these points. There exist a wide array of elements to choose from and it is possible to mix them. The default element type for heat transfer in 3D for COMSOL Multiphysics® is tetrahedral with quadratic shape functions. In addition to those elements, used for the main domain, infinite elements [56] were used to simulate the infinite stretch of the geometry assumed by Rosenthal. These elements use a different coordinate system scaled toward infinity in one direction when they are attached by a surface to a Cartesian domain.

The geometry used for this comparison is shown in Figure 3.2. The domains with infinite elements are the space with wavy patterns in Figure 3.2. As mentioned previously, the infinite elements used here are scaled toward one direction and the space between them must be a domain with the reference coordinate system in which the important calculations take place. Here the top surface is thermally insulated and a symmetry boundary condition is applied at the symmetry plane. The temperature is considered to be fixed at 293.15 K (20°C) on all other surfaces.

The FEM mesh used here is reported in Figure 3.3. It was produced by the FEM software. This is the first time a mesh is presented, so it is interesting to discuss briefly the way the mesh is generated in COMSOL Multiphysics®. First, one has to choose between user-controlled mesh and physics-controlled mesh. In this thesis only physics-controlled meshes were used. Then, one can choose whether the mesh should be coarse or fine. To do so, one has to choose among the nine possible levels which are labelled from "Extremely coarse" to "Extremely fine". The finer the mesh the more elements it contains. During the building of all the models presented in this thesis it was checked that when the mesh density was increased the solution was reaching an asymptote. In most cases here, except if otherwise is stated, the mesh was generated using the "Extremely fine" setting.

The mesh reported in Figure 3.3 is composed of 84,184 elements. The position of the heat source is highlighted in this figure. The mesh obtained is regular around the source, i.e., the element density does not change drastically around the source.

A depth of 1.34 cm corresponds to the thickness of some pipe and, in particular, the thickness of the material used for the experiments detailed in the next section. The length corresponds to the length of the samples used for experimental measurements. The width (y direction) is based on the fact that the temperature 7.5 cm from the weld is not high enough to generate any microstructural changes within the time it takes the source to travel through the length of metal considered here. The source is positioned at 80% of the length between the centre and the end of the top surface on the centerline. This is to allow some space before the source to prevent cooling from the boundary condition in front of the source, which would be physically wrong.

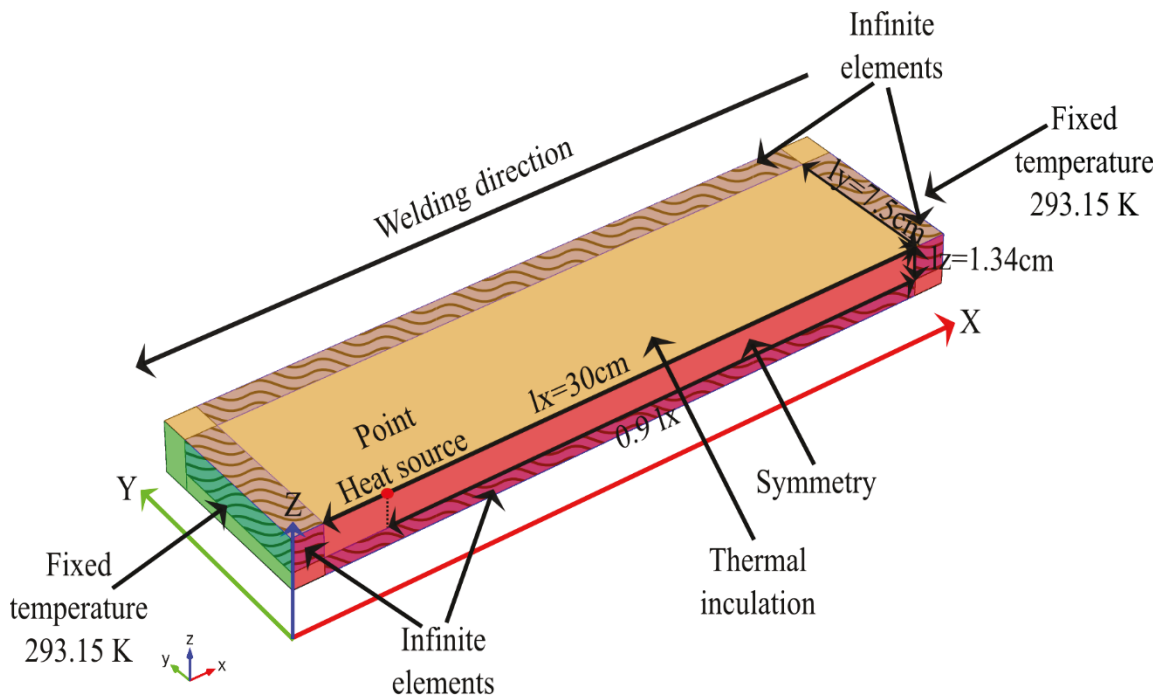


Figure 3.2: Schematic of the geometry used to obtain Rosenthal's solution using FEM.

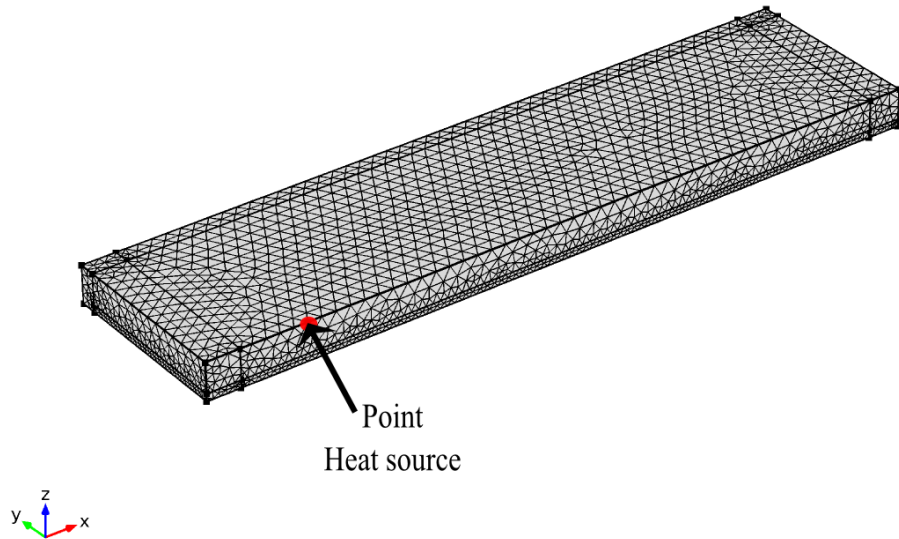


Figure 3.3: Mesh used to obtain the temperature profile in Figure 3.4.

To conduct the first calculation, constant thermal parameters have been selected. Also based on Pepin’s [11] work, the parameters reported in Table 3.1 were used.

Table 3.1: Input parameters used for the simulation.

Parameter	Value
Current (A)	700
Voltage (V)	32
Travel speed (mm/s)	8.9
Power (kW)	22.4
Heat input (kJ/mm)	2.517

Figure 3.4 shows the temperature profile obtained with a color range cropped at 1800 K to improve the legibility. Otherwise, the extremely high temperatures close to the source would make it difficult to draw any conclusions. A temperature of 1800 K has been chosen as it is close to the fusion temperature of different steels. A comparison with Rosenthal’s solution is available in Figure 3.5. When a comparison is made, the domains with infinite elements and the domains at the junctions are omitted, as the comparison does not apply because they represent infinity and the comparison is on a finite scale. The two temperature profiles compared here come from models.

Neither of the temperature profile can be considered better or more accurate. Therefore, Equation (3.9) is used for the comparison to give the same weight to the two temperature profiles,

$$ERR\% = 200 \cdot \left| \frac{T_{Rosenthal} - T_{FEM}}{T_{Rosenthal} + T_{FEM}} \right| \quad (3.9)$$

As shown in Figure 3.4 and 3.5, discrepancies are apparent. In Figure 3.5 the color scale was manually cropped by 50%. So, all errors above 50% will appear with the same color as 50%. This can be explained by the singularity of the point. This is shown in Rosenthal's solution, Equation (3.6), where there is a division by the distance from the point and thus a singularity at the point itself. In general, for this system, no temperature below the initial one, which is 293.15 K, should appear and here the lowest temperature is -8424 K. A temperature below 0 K is physically impossible but the domain presenting temperatures below 0 K is actually limited in space. A possible explanation for this is the use by the software of quadratic shape functions, which can go below the temperature of each point and the temperature gradient close to the source is close to infinity. The temperature profile in front of the source seems erratic, even with 84,184 elements, when it should show a shape close to a deformed ellipsoid. Therefore, to obtain acceptable results some improvements were done on the point heat source.

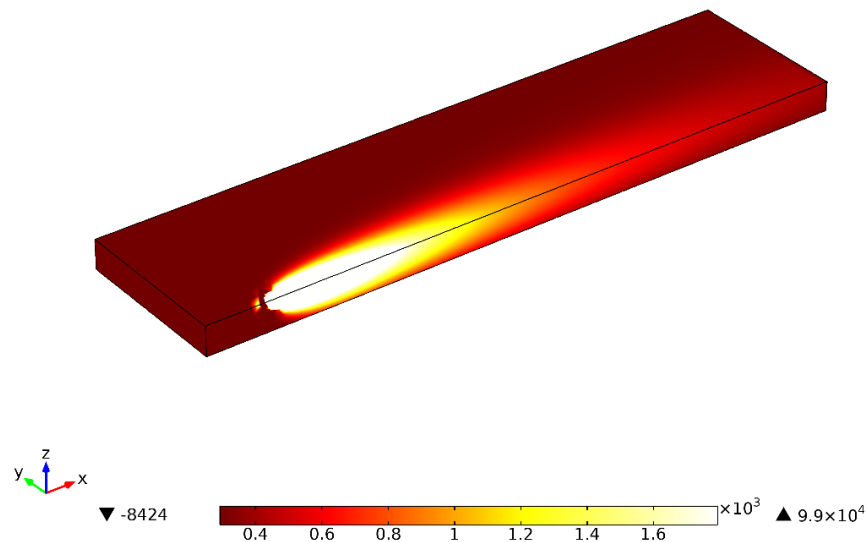


Figure 3.4: Temperature profile obtained using the point source.

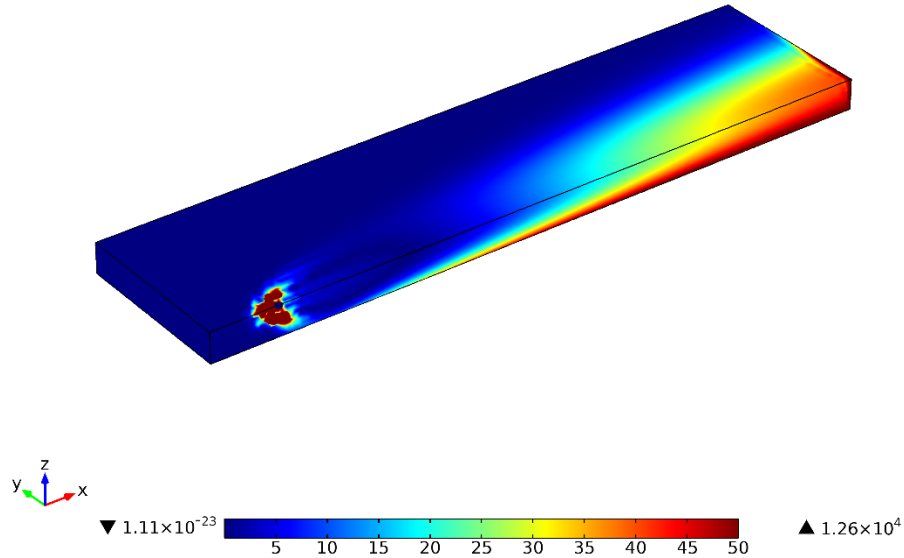


Figure 3.5: Percentage of difference between Rosenthal's solution and the temperature profile available in Figure 3.4.

3.2.1.3. Improvement on the point source - the hemispherical surface source:

This is mainly being shown as an introduction for a better way to introduce a point source. With a point source, the distribution of elements created by the meshing program is fairly even. The settings used are discussed in Section 3.1.2.1. This means that the element density is the same no matter how steep the temperature gradient. This is a problem that can only be overcome manually with this geometry.

A point source is a sphere with zero radius. To get an approximation of a point without singularity, it is possible to apply the entering flux on the surface of a small hemisphere removed from the surface of the geometry. Figure 3.6 gives more explanation and shows the mesh generated by the meshing program of COMSOL Multiphysics® when a 0.1 mm radius hemisphere is excavated from the geometry. The radius was fixed at 0.1 mm. The radius was determined by trying different radius from $1 \cdot 10^{-5}$ m to $1 \cdot 10^{-2}$ m [46]. It was determined that this radius is the one for which the difference with Rosenthal's solution is the smallest. The mesh available in Figure 3.6 was generated using the physics controlled extremely fine mesh setting of the software. This is the same setting as for Figure 3.3, but in this case 42,752 free tetrahedral elements were used instead of 84,148 without the irregularity. This irregularity produces an irregular mesh with a higher

element density close to the source. This is an improvement as the temperature gradients are steeper close to the source than further away; thus the need for more elements close to the source.

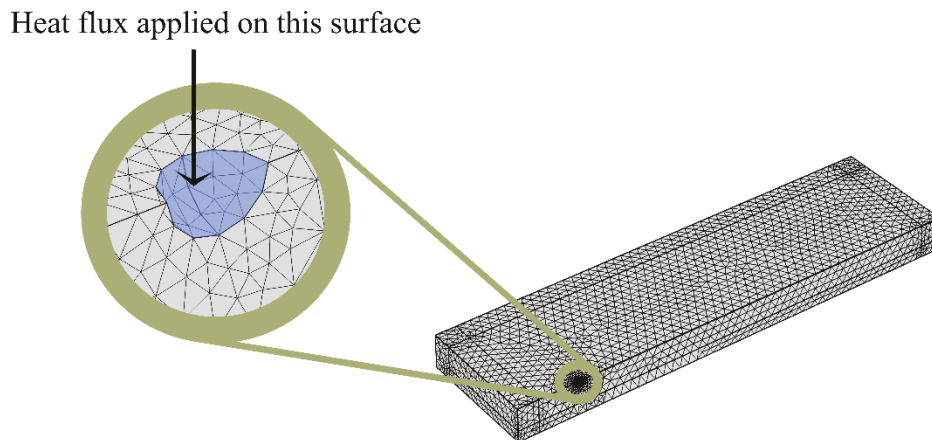


Figure 3.6: Mesh generated when a hemisphere, 0.1 mm in radius, is removed from the geometry at the position of the point source.

The temperature profile generated using this approach is available in Figure 3.7. The color range is cropped at 1800 K to make the profile more legible. The minimum temperature reached is 205 K which is close to 293.15 K. On the picture the isotherms display smooth edges, which are more physically acceptable than what a simple point source yields. The problem relative to the lowest and the highest temperatures still remains. The absolute relative difference in percent with Rosenthal approach is reported in Figure 3.8. The color range is cropped by 50% to allow for comparison with the previous case considered. Here the error with Rosenthal's solution is much smaller than before, with the biggest discrepancies localized at the interface between the domain with common tetrahedral elements and the domain meshed using infinite elements.

3.2.1.4. Conclusions regarding a single point source:

From the above, it is clear that Rosenthal's results can be reproduced with the software with fairly good agreement. Also, the software allows for the same boundary conditions as the ones used by Rosenthal. It is important to note that the introduction of a hemispherical irregularity is an easy way to help the meshing program to generate a more efficient mesh. When the irregularity was introduced, better results were achieved with half the number of elements. The irregularity also removes the part of the geometry which goes to the infinity due to the singularity.

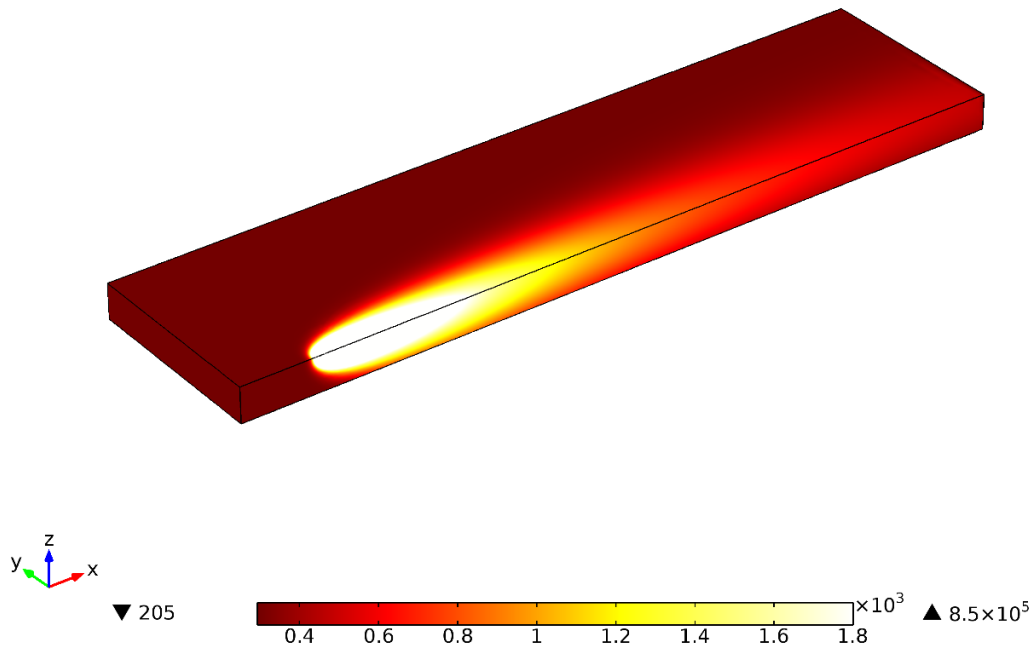


Figure 3.7: Temperature profile generated using a spherical irregularity at the surface.

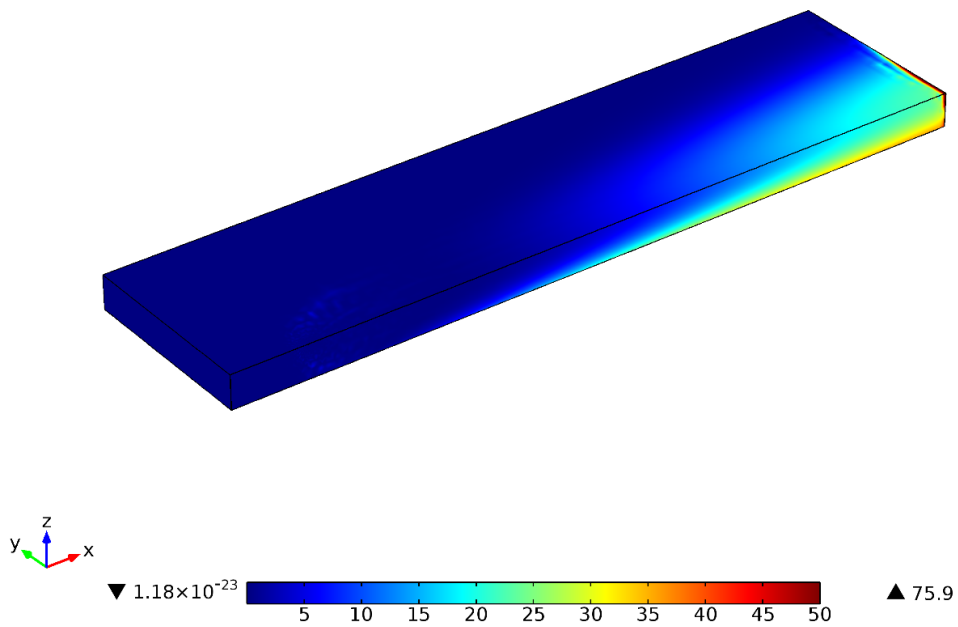


Figure 3.8: Difference of the temperature profile reported in Figure 3.7 with Rosenthal's solution when a hemispherical irregularity is introduced.

3.2.2. Two point sources:

For quick calculations on welding operations with two electrodes, it is of interest to see to what extent it is possible to use point sources and to go beyond them.

First, the possibility to extend Rosenthal's results for two sources is investigated. Then a simulation with two hemispherical surface sources is performed and compared with the extension of Rosenthal's solution.

3.2.2.1. Extension of Rosenthal's solution to two sources:

As stated in the Introduction, multiple electrode welding processes are often used in industry. The most commonly used among these processes uses two electrodes. Tandem SAW process, in which two sources are controlled independently, is of interest in this work.

Equation (3.6) is the solution of Equation (3.5) when the Rosenthal's assumption are applied (see Section 3.2.1.1). Under these assumptions Equation (3.5) is a linear PDE. Therefore, if the boundary conditions are linear, which is the case here as the Dirichlet boundary condition is linear, the superposition principle can be applied.

H is defined as an operator:

$$H = k\vec{\nabla}^2 + \rho C_p v \frac{\partial}{\partial x} \quad (3.10)$$

If

$$HT_1 = -Q_1 \quad (3.11)$$

and

$$HT_2 = -Q_2 \quad (3.12)$$

then

$$H(T_1 + T_2) = -(Q_1 + Q_2) \quad (3.13)$$

Equation (3.13) shows that the temperature profile when two sources are used is the superposition of the solution with each source considered alone. So, considering (x_1, y_1, z_1) and R_1 to be, respectively, the Cartesian and the radial components of the spherical coordinate system centred

on the first source, and (x_2, y_2, z_2) and R_2 to be, respectively, the Cartesian and the radial component of the spherical coordinate system centred on the second source, the temperature profile generated by two point sources is given in Equation (3.14).

$$T = T_0 + \frac{P_1}{2\pi k} e^{-\lambda v x_1} \frac{e^{-\lambda v R_1}}{R_1} + \frac{P_2}{2\pi k} e^{-\lambda v x_2} \frac{e^{-\lambda v R_2}}{R_2} \quad (3.14)$$

This is of interest for industry people to have a quick way to assess the temperature profile during tandem SAW operations knowing that the limitations are the same as for the classical Rosenthal's solution. It also gives another way to check numerical results with analytical ones.

3.2.2.2. Simulation using two hemispherical surface sources:

The same power for the lead and the trail source are used. This is closer to an operation of twin-wire SAW. The power is delivered by 550 A and 28 V yielding 15.4 kW with an arc efficiency of 95% for each source. The two sources are separated by 23 mm. Each source is represented by a hemispherical indent as explained before. Figure 3.9 shows the mesh used to solve the problem. The settings used to produce the mesh are discussed in Section 3.1.2.1. It shows, as before, a higher element density around the sources. The total number of elements is 45,976. Therefore, adding another source using this technique only adds 3224 elements in this case³. The temperature profile obtained is shown in Figure 3.10. The color range is cropped at 1800 K. The difference between the calculated temperature profile and the one obtained using Equation (3.14) is reported in Figure 3.11. The color range is cropped by 50% for ease of comparison. It shows good agreement as in most of the space the difference is lower than 4%.

³ Only 7.5% increase in number of elements.

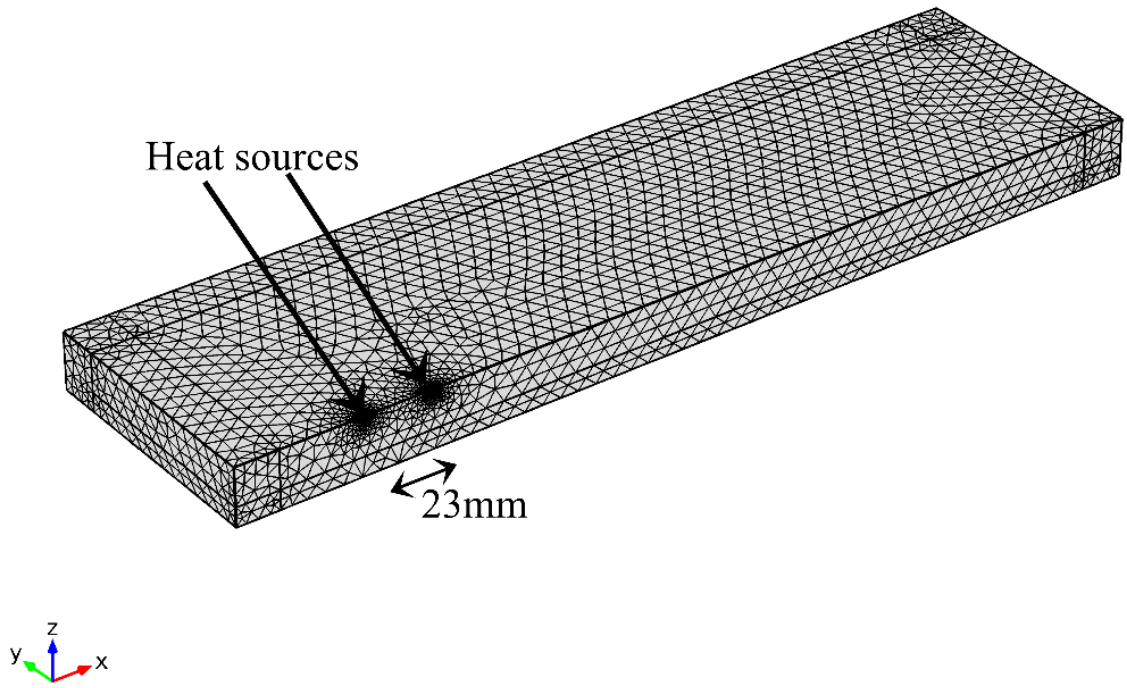


Figure 3.9: Mesh used to simulate two point sources separated by 23mm.

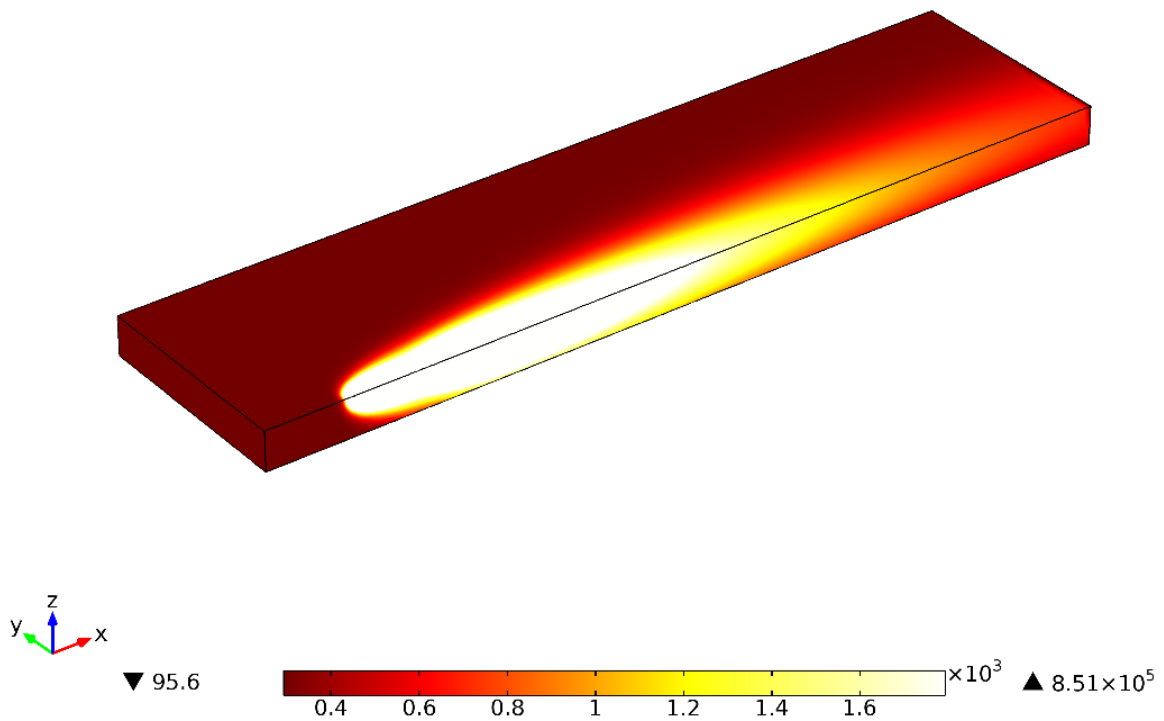


Figure 3.10: Temperature profile obtained with two point sources.

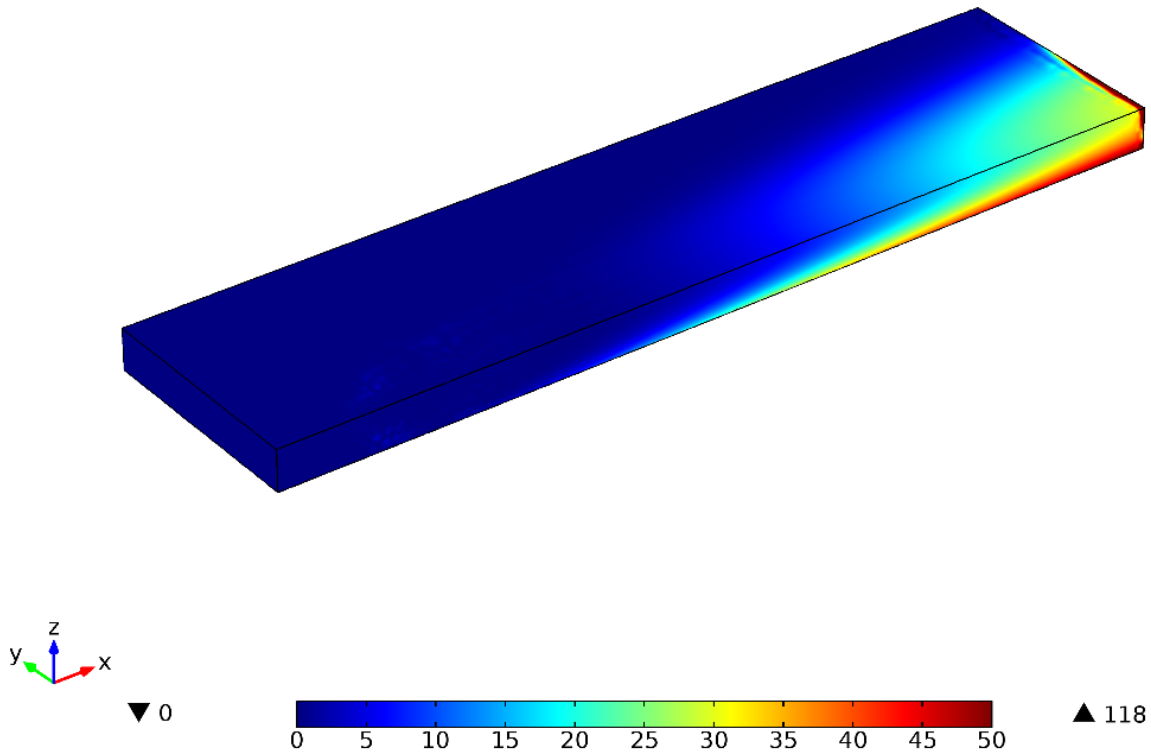


Figure 3.11: Difference with Rosenthal's solution of the temperature profile when two spherical irregularities are used.

This work gave confidence in the capabilities in the software and also provided the following information:

- As anticipated, the tetrahedral elements give good results for heat transfer in the case studied here.
- It is possible to reproduce Rosenthal's results using FEM.
- Using a small hemispherical irregularity to apply the flux is a much better solution than a simple point when dealing with numerical solutions.
- The superposition principle is confirmed by the simulation, revealing no major flaw in the method when expanding the results to two sources.
- An estimate of the temperature profile for one and two source welding is provided.

3.3. Mixed boundary conditions:

One of the major assumptions in Rosenthal's work is the absence of boundary conditions other than the "no flux" boundary condition. This is obviously far from reality. Even if the software gives tools to simulate an infinite body, this is neither physical, nor good for the simulation. It requires convoluted manipulations and can sometimes require tuning in the solving of the matrix equations for convergence.

To use better boundary conditions, it is imperative to first define where they should be applied. The problem is that a part of the workpiece is covered by a blanket of powder. Therefore, there are two cases, either the new boundary condition is applied on the surface under the flux or this surface is considered to be thermally insulated. This requires a change in geometry.

First, a change in the geometry is proposed. Then the mixed boundary condition is presented. After that, the results for the two cases considered here are presented. Finally, conclusions obtained from this work are presented.

3.3.1. Geometry:

The geometry must change to better approximate reality. The geometry used in this section is shown in Figure 3.12. Infinite elements are still used in the welding direction, as welds done by SAW on pipes are often long enough to consider infinite extension in this direction. Therefore, the temperature at both ends in the welding direction is fixed to ambient temperature. The same logic applies to the width as the diameters of pipes are much larger than the width of base metal considered here. In addition, a surface is covered by the flux. The width of this surface corresponds to half the width of the flux dam used, which measures 7.62 cm (3 inches). As shown in Figure 3.12 one source was used to first introduce the boundary condition before increasing the complexity.

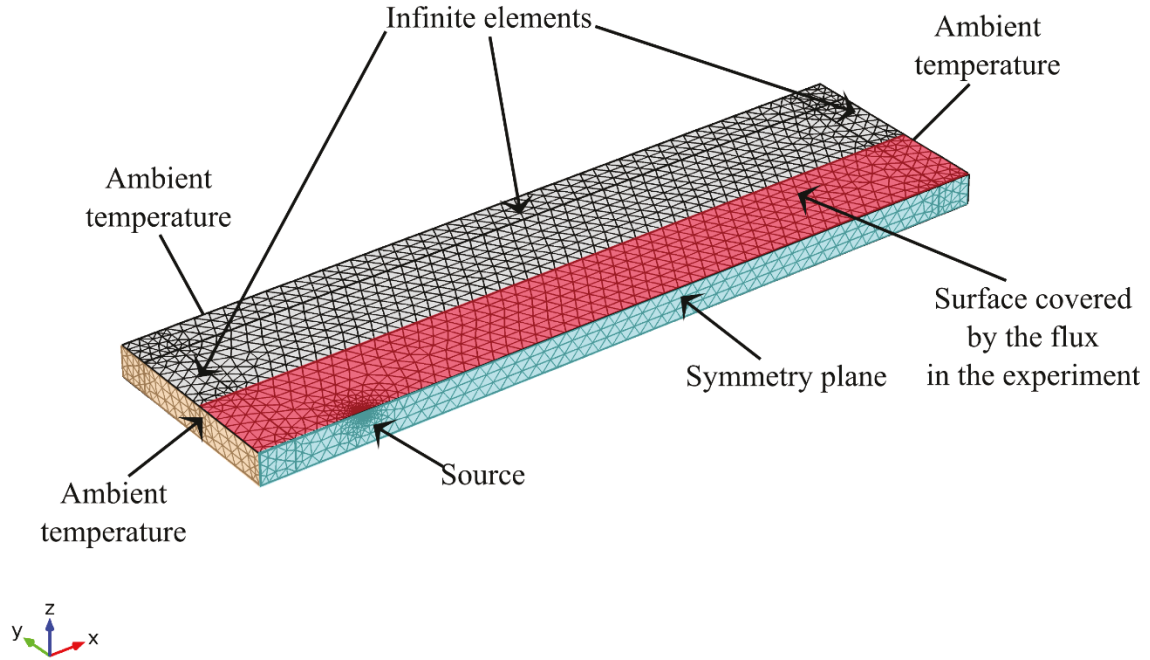


Figure 3.12: Geometry and mesh used for a point source and mixed boundary conditions.

3.3.2. Boundary conditions considered:

Two types of boundary conditions are used. One is a Dirichlet boundary condition at the end of the infinite domains where the temperature is fixed at ambient temperature. The surface covered by the flux is ignored. The remaining surfaces are subjected to convective and radiative boundary conditions. The general formulas for the convective and radiative boundary conditions are presented, respectively, in Equation (3.15) and Equation (3.16).

$$q_{conv} = -k \frac{dT}{dr} = h(T - T_{\infty}) \quad (3.15)$$

$$q_{rad} = -k \frac{dT}{dr} = \varepsilon\sigma(T^4 - T_{\infty}^4) \quad (3.16)$$

It is possible to use these equations, but often [10, 57-59] Equation (3.15) is used alone with a coefficient called h_{comb} which is lumped together for the effect of convection and radiation. This

coefficient varies with temperature. The actual formula corresponding to the boundary condition used is available in Equation (3.17) and Equation (3.18) gives the expression for h_{comb} .

$$q_{comb} = h_{comb}(T) \cdot (T - T_{\infty}) \quad (3.17)$$

$$h_{comb}(T) = 24.1 \cdot 10^{-4} \varepsilon T^{1.61} \quad (3.18)$$

The classical approach consists of using both Equation (3.15) and Equation (3.16) for the boundary conditions for open surfaces. To assess the reliability of the approach using Equations (3.17) and (3.18), it is necessary to compare the evolution of the heat flux crossing a surface with temperature in both cases. Figure 3.13 shows the heat flux predicted by the classical approach in blue and the heat flux which uses Equation (3.17) in dashed red. For the calculations the convective coefficient was equal to 15 W/Km^2 and ε was equal to 0.9 [59]. It is interesting to see that these two curves are close to each other. The variation is similar in both cases. This means that Equation (3.17) does not show any unrealistic behavior. Equation (3.17) is used in this project. In this study ε is taken to be equal to 0.9.

The other boundary conditions are Neumann boundary conditions, where the flux is fixed. The symmetry boundary condition and the boundary condition on the surface of the hemispherical irregularity are no flux boundary conditions.

The last surface to address is the one covered by the flux. The problem is that it is often assumed [59] that the surface directly on top of the source is insulated and the other surfaces are subjected to the boundary conditions mentioned above. In the case of a point source, the surface directly on top of the source is either zero if the source is an actual point or insignificant in the case of a spherical notch, which is the case studied here. Therefore, not knowing whether insulation should be assumed or not, simulations were done using both.

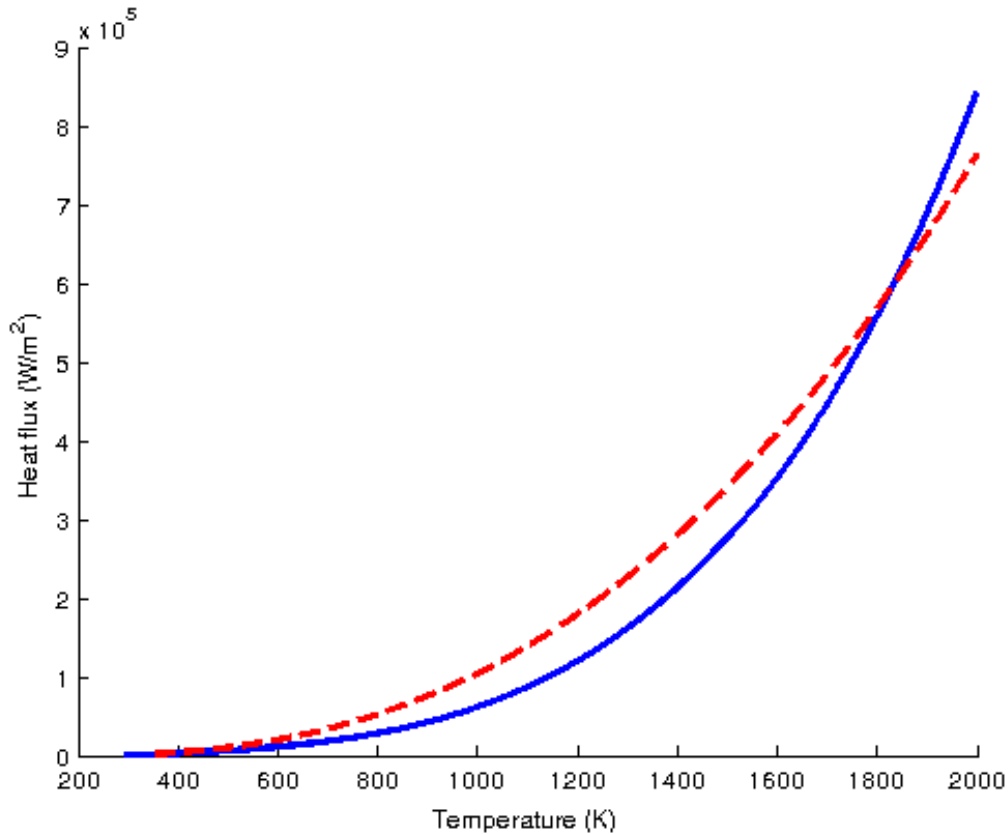


Figure 3.13: Heat flux calculated using two different methods for the boundary conditions. The blue curve corresponds to the addition of Equation (3.15) and Equation (3.16). The red dashed curve corresponds to the heat flux calculated using Equation (3.17).

3.3.3. Results:

One problem is to determine where to apply each boundary condition. As shown before, the geometry is divided into two parts. One is covered by the flux while the other one is not. Two scenarios are considered here. Figure 3.14 shows the boundary conditions used in the two scenarios. In the first case, a mixed boundary condition is used on the surface under the flux. In the second case the surface under the flux is considered to be thermally insulated.

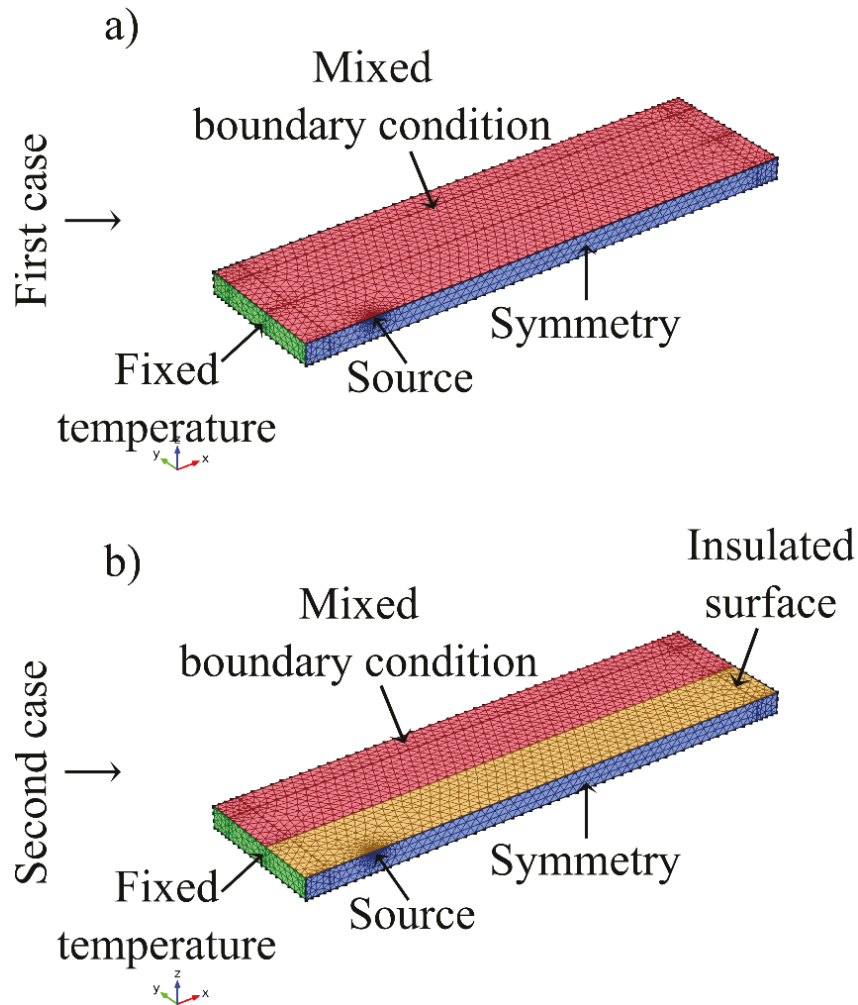


Figure 3.14: Boundary conditions used in the both cases studied. a) corresponds to the first case, while b) corresponds to the second one.

The results of the two approaches are then compared to each other and to Rosenthal's solution. This is useful to assess the validity of using real boundary conditions on different parts of the geometry. Figure 3.15 shows the temperature profile at the surface of the geometry for the two cases considered here. In both cases the maximum temperature is of the order of magnitude of 1.10^5 K, which is too high. This problem is the same as before and is certainly due to the source and data used. For both cases the minimum temperature is equal to the initial one. The temperature profile for the second case is similar to the one presented in Section 3.2.1.3, while the temperature profile in the first case is drastically different. The part of the metal which is molten, represented in white, is significantly smaller. The molten pool is too small compared to the bead shape data

analyzed (Appendix A). The molten pool would be almost round which is in disagreement with experiments.

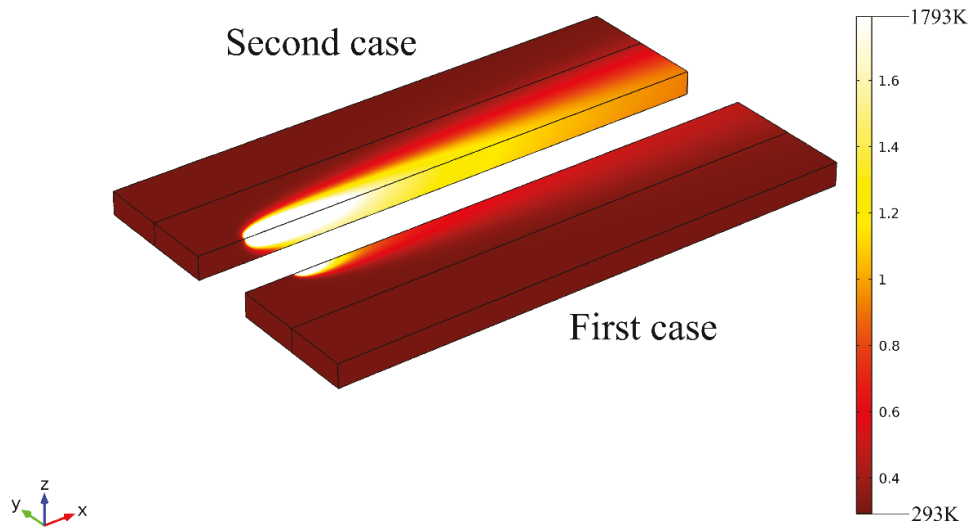


Figure 3.15: Temperature profiles generated by the two cases considered in this work.

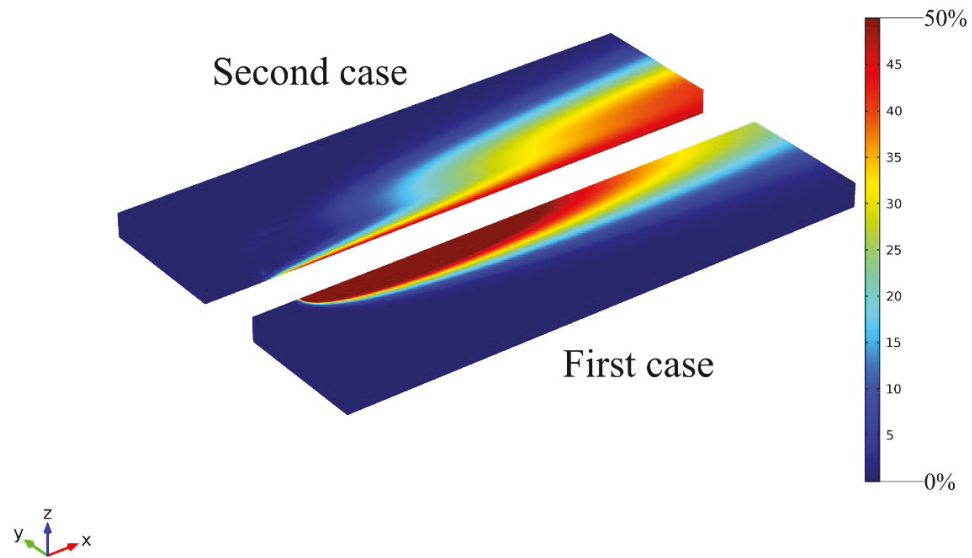


Figure 3.16: Comparison of the temperature profiles obtained for both cases considered in this work.

Comparisons with Rosenthal’s model for both cases are shown in Figure 3.16. The second case is closer to Rosenthal’s solution than the first one. For the first case, the temperature profile around

the source is greatly affected and a deviation from Rosenthal of more than 50% occurs. The deviations on the top surface for the second case are minor and take place away from the source.

3.3.4. Conclusions:

The introduction of realistic boundary conditions did not significantly improve the simulations involving point sources. For the part of the top surface not covered by the flux, the use of realistic boundary conditions is not crucial. However, applying mixed boundary conditions for the entire surface covered by the flux drains too much power from the source for a point heat source. For the bottom surface, changes in temperature exist and do not show any unrealistic behavior, meaning they are progressive and follow the diffusion front. This means that to use realistic boundary conditions, an approach between the two cases studied here must be used. For a point heat source, using realistic boundary conditions is not crucial.

The problem encountered while using realistic boundary conditions with a point source is that the surface directly on top of the molten pool should be considered insulated, and to apply this condition with a point source requires trial and error efforts to determine the correct shape of the surface above the melting temperature of the metal. In addition, this work can only be done with temperature variable thermal properties that account for melting, which is not the case in this work. If one wants to do quick calculation using a point source, it is recommended to consider the top surface as being insulated.

To improve the results, the only approach is to use better heat sources like the double ellipsoidal approach proposed by Goldak [10].

3.4. Double ellipsoid source:

Based on work done previously (see Section 2) one of the best sources to model deep penetration arc welding is the double ellipsoid source proposed by Goldak [10]. Some sources may be better, like the egg-shaped source [51], but using them requires information that is difficult to obtain. Therefore, in this project the double ellipsoid source is used.

In this section the source and the change in geometry it induces are first presented. Then the boundary conditions adapted to the new geometry are discussed. The resolution of some of the issues that arise with the increase in complexity of the model is done by using numerical transient

calculations. The results obtained using constant thermal properties are then discussed. This is followed by the results obtained using thermal properties which vary with temperature. Finally, the simulation of welding with two sources using the double ellipsoid model for the source and varying thermal properties is attempted.

3.4.1. Presentation of the source and geometry:

First, the double ellipsoid volumetric heat source is presented. Second, the geometry of the source and the plate are presented.

3.4.1.1. Equations related to the distribution of the source:

In the double ellipsoid model, the power transferred by the electrode to the plate is spread throughout a double ellipsoidal volume. The spreading is done assuming a Gaussian distribution. The equations and developments presented here are based on the book written in 2005 by Goldak and Akhlaghi [10]. If the power is spread throughout a single ellipsoid with its centre at (0,0,0) and semi-axes (a, b, c), the spreading of the power, noted Q , can be written as follows:

$$q(x, y, z) = q(0)e^{-Ax^2}e^{-By^2}e^{-Cz^2} \quad (3.19)$$

The notation q refers to the power density; expressed in W/m^3 . To determine the expressions for A, B and C , it is considered that at the border of the ellipsoid the power density falls by 5% of the maximum power density. This gives Equations (3.20), (3.21) and (3.22).

$$A = \frac{\ln(20)}{a^2} \quad (3.20)$$

$$B = \frac{\ln(20)}{b^2} \quad (3.21)$$

$$A = \frac{\ln(20)}{c^2} \quad (3.22)$$

Using the principle of conservation of energy on an ellipsoid gives Equation (3.23).

$$q(0) = \frac{2Q\sqrt{ABC}}{\pi\sqrt{\pi}} \quad (3.23)$$

The double ellipsoid model uses two ellipsoids with two different power distributions based on what was developed previously in this work. Only one fourth of each ellipsoid is considered and the ellipsoids are stitched together at their centre. The heat deposited in each ellipsoid is considered to be different. Therefore, the fractions, f_f for the front ellipsoid and f_r for the rear one, are introduced. They must satisfy Equation (3.24).

$$f_f + f_r = 2 \quad (3.24)$$

A value of 0.6 was chosen for f_f [59]. The power density applied for the front ellipsoid is reported in Equation (3.25) and the one applied on the rear ellipsoid is reported in Equation (3.26). Equations (3.25) and (3.26) are expressed in the same reference system which is independent of the reference system of the plate. In this reference system the zero of the axes is the point on the top surface which is beneath the electrode. To implement these equations in the model some translation terms were added to x , y and z to express them in the reference system of the plate.

$$q(x, y, z) = \frac{2Qf_f\sqrt{ABC}}{\pi\sqrt{\pi}} e^{-Ax^2} e^{-By^2} e^{-Cz^2} \quad (3.25)$$

$$q(x, y, z) = \frac{2Qf_r\sqrt{ABC}}{\pi\sqrt{\pi}} e^{-Ax^2} e^{-By^2} e^{-Cz^2} \quad (3.26)$$

3.4.1.2. Geometry of the plate and the source:

The choice was made to use a geometry more similar to the experiments that will be conducted than to the actual welding of a pipe. That is why infinite elements were only used in the welding direction. This also reduces the number of elements used in the simulation, making it faster. Figure 3.17 shows a schematic of the geometry used for the simulation of one electrode welding using

Goldak's double ellipsoid approach. A 45° bevel is taken into account. It has a depth of 0.51 cm and a width of 0.51 cm. The geometry is partitioned where the bevel is. It can be used to take into account the change in composition between the base metal and the deposited metal, but this case is not studied here. The part of the bevel in front of the source is removed to decrease the number of elements in the simulation and because in the reality the bevel is empty in front of the arc. Also the symmetry of the problem is used to advantage. The system is cut in half, which reduces the number of elements used in the study by 50%.

The source is an important feature of the geometry. The electrode is placed at 12 cm from the centre of the top surface of the plate to be welded. A close up of the source is available in Figure 3.18. On this picture are reported the four parameters used to define the two ellipsoids. The semi-axes of each ellipsoid are noted a_x in the "x" direction, b_y in the "y" direction and c_z in the "z" direction. In addition the subscript "f" is used to refer to the front ellipsoid and the subscript "r" is used to refer to the rear one. For each heat source, which is composed of two ellipsoids, front and rear, the two ellipsoids must have common points of intersection between them. To do so, Equations (3.27) and (3.28) must be met. For b_y and c_z the subscripts "r" or "f" are omitted as they are equal for both front and rear ellipsoid.

$$b_{yf} = b_{yr} \quad (3.27)$$

$$c_{zf} = c_{zr} \quad (3.28)$$

To determine the other parameters, data on the bead shape of the weld are used. The relations shown in Appendix A are used. The parameter b_y corresponds to half of the bead width. The parameter c_z corresponds to the penetration depth. The parameter a_{xf} corresponds to half the bead width while a_{xr} corresponds to twice the bead width according to Goldak's model. It is recommended to use parameters for the source slightly smaller than the parameters of the bead. The reduction factor is determined by trial and error. It is often taken as 10%, but here this was not considered. This is a matter of adequacy of the results compared with the experiments which is discussed in Section 5. The parameters used to obtain the source shown in Figure 3.18 are available in Table 3.2. In this simulation the bevel is considered filled with metal from the start of the heat

source to the end of the geometry. The simulation is started with the entire geometry, including the bevel and the source, considered to be at a constant temperature of 293.15 K.

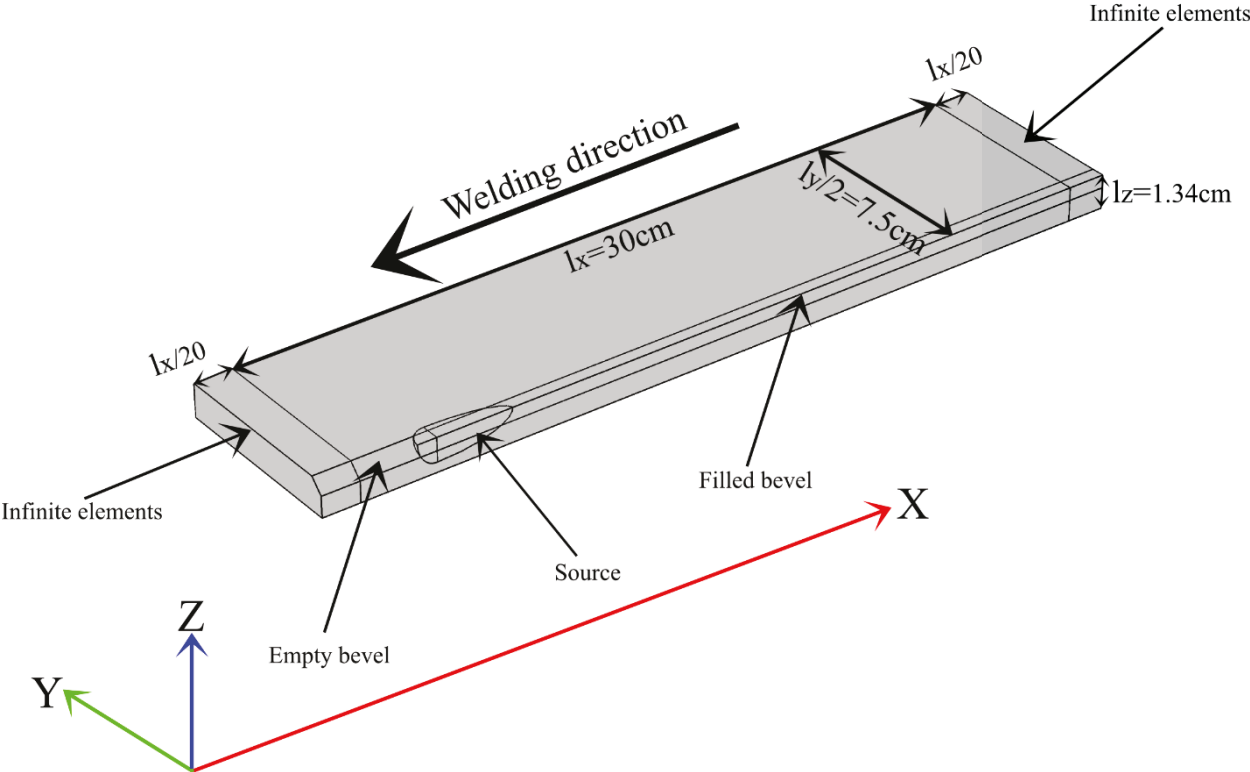


Figure 3.17: Schematic of the geometry used for one double ellipsoidal source simulation.

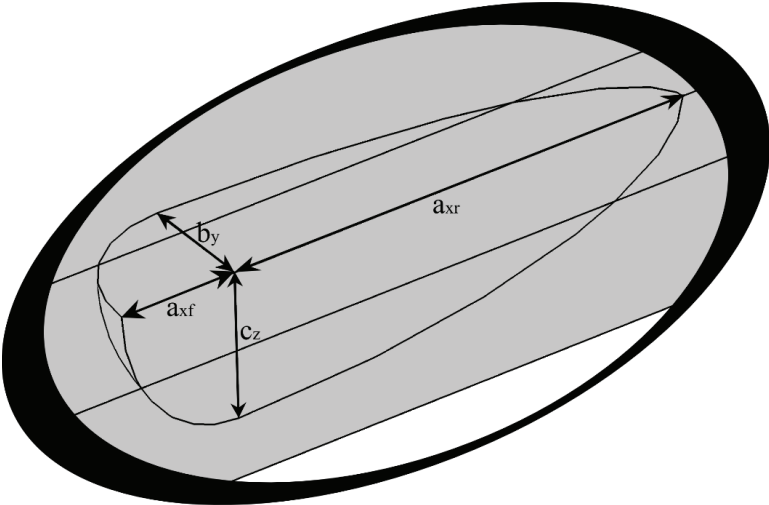


Figure 3.18: Close up of the double ellipsoidal source with the parameter notations characterizing the source.

Table 3.2: Parameters used to calculate the dimensions of the source presented in Figure 3.18.

Parameter	Value
Current (A)	700
Voltage (V)	32
Travel Speed (mm/s)	8.9
Frequency (Hz)	60
Balance (%)	50
Offset (%)	0
Bead width (mm)	15.1
Penetration depth (mm)	9.5
f_f	0.6
f_f	1.4

3.4.2. Boundary conditions:

In this model three different boundary conditions are considered in four different situations. The temperature is fixed at ambient temperature at both ends of the geometry in the welding direction. The surface atop the source is considered insulated as is the surface of the empty bevel. A symmetry boundary condition is used where the geometry is cut in half. The mixed boundary condition presented in Section 3.3 is used for all the other surfaces. Figure 3.19 shows where the different boundary conditions are applied.

3.4.3. Numerical transient calculations:

This was not addressed before, as a steady state calculation was used to get the quasi-steady state results. However, the complexity of the geometry and the source is such that the solver does not converge if a steady state calculation is done. This means that the initial condition used to start the steady state calculation is too far away from the actual solution.

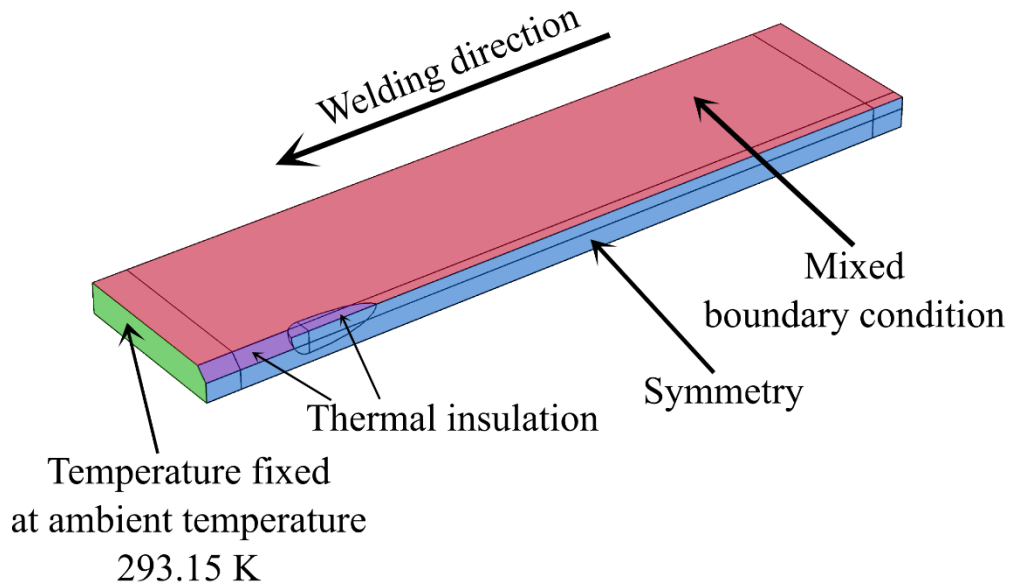


Figure 3.19: Geometry and boundary conditions used for the simulation with one double ellipsoidal source.

To overcome this problem it was decided to start the simulation with the geometry presented in Figure 3.19 at a uniform temperature of 293.15 K. Then the system was allowed to evolve with time step by step using Equation (3.4), which is the transient form of the heat equation in the moving coordinate system considered here. After a certain time the system reached steady state, which is what was desired. The time it takes the simulation to reach steady state was determined to be 60 s. It was determined by trial and error. This is a numerical trick and the time in this transient calculation does not correspond to the actual time during the welding operation.

3.4.4. Simulation with constant thermal properties:

First, the mesh was generated using the settings discussed in Section 3.2.1.2. The number of elements generated is 74,161. A picture of the mesh is shown in Figure 3.20. The mesh density is higher around the source and on the filled part of the bevel. This is explained by the irregularities in the geometry that are the double ellipsoid and the bevel. A higher element density is beneficial around the source as this is where the gradient is the largest and the equation to be solved is the most complex, as this is where a source term is used. The higher density in the filled bevel is also beneficial as most of the change in temperature occurs in this direction due to the use of a moving coordinate system.

A surface plot of the temperature profile is shown in Figure 3.21. The infinite element domains are not considered, as they are used as computational tools and the temperatures in these domains are neither meaningful nor useful for analysis of the process. The color range was cropped at 1793 K which is the liquidus temperature of the steel considered here (Appendix C). The minimum temperature is 293.15 K and the maximum temperature is 4905 K. The minimum temperature is equal to the initial one. On the other side, the maximum temperature is higher than what is expected [10]. This is certainly due to the use of constant thermal properties, which *de facto* leaves out the influence of phase changes on the temperature profile.

The use of a double ellipsoidal source is a big improvement from the point source. The minimum temperature is not below the initial one. The maximum temperature is lower, even if it still is higher than what is expected. The smoother handling of the source makes it easier, for the software, to handle the temperature gradients.

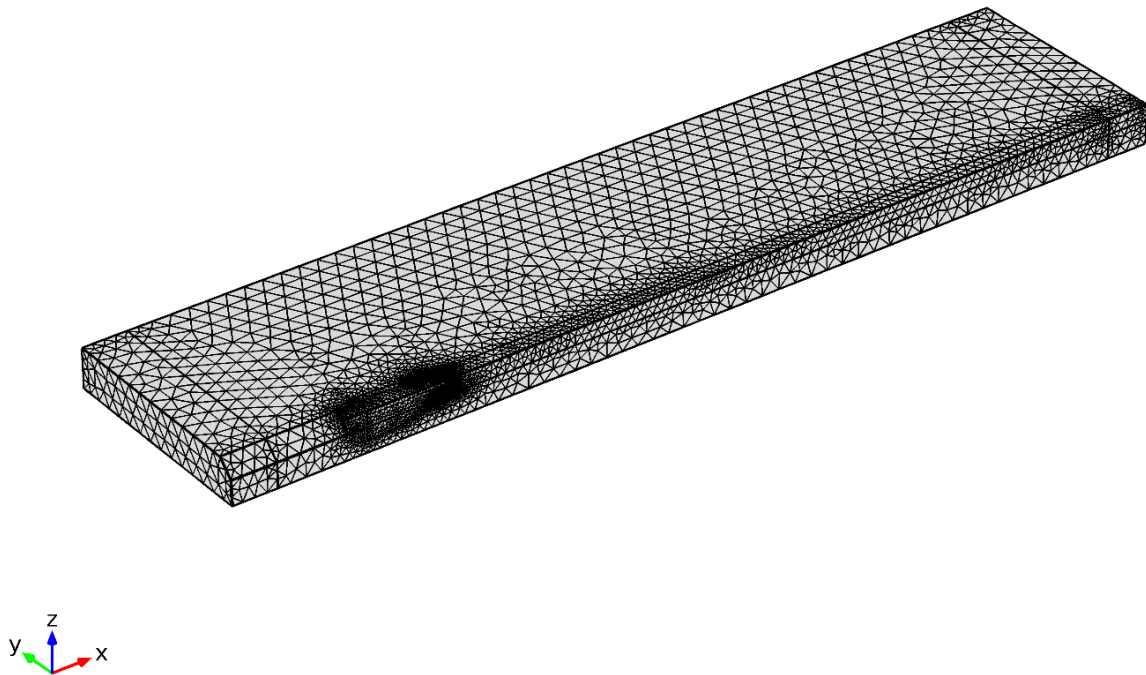


Figure 3.20: Mesh used to carry out the calculations with a single double ellipsoidal source and fixed thermal properties. 74,161 tetrahedral elements were used.

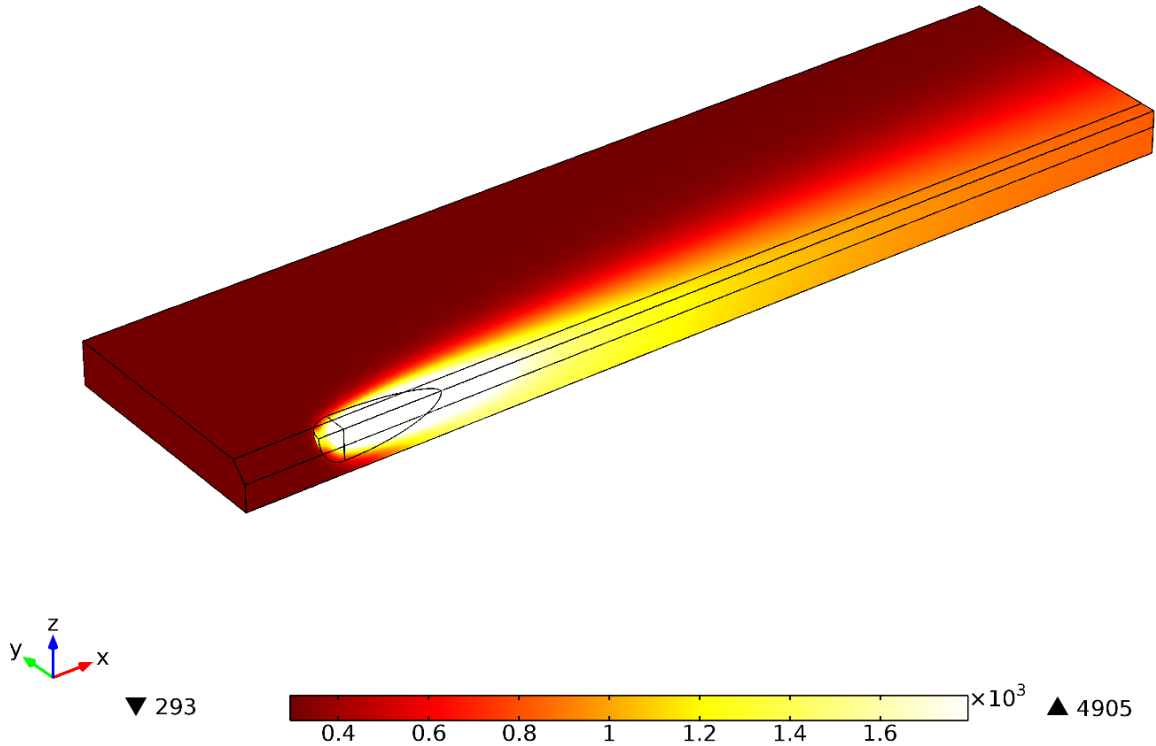


Figure 3.21: Temperature profile generated with a double ellipsoidal source and an input current of 700 A and an input voltage of 32 V.

3.4.5. Simulation with temperature dependent thermal properties:

To get even closer to reality, the next major step is the use of temperature dependent thermal properties. The parameters used are presented in Appendix C. The introduction of a variation in the thermal properties with temperature greatly increases the computational time. With constant thermal properties, the computational time is 7 min and 6s. With varying thermal properties, the computational time is 1 day, 4 h, 23 min and 31 s, or 240 times slower⁴.

The temperature profile obtained when using varying thermal properties is reported in Figure 3.22. The minimum temperature is 255 K which is below the initial one but it is still close to the initial one of 293.15 K. The maximum temperature is now 2531 K compared with 4905 K for the preceding case. According to Goldak, measurements have shown that the peak temperature in the weld pool is between 300 K and 500 K above the melting temperature of the material [10]. The

⁴ The hardware used for the two calculations is the same.

liquidus temperature is 1793 K. This was determined using Thermo-Calc[®] (Appendix C). Therefore, the maximum temperature of the weld pool should be between 2093 K and 2293 K. The peak temperature is 237 K more than what was expected. This can be explained by the fact that the movement in the weld pool is not directly taken into account here. A reduction in the peak temperature was expected due to the introduction of melting in the modelling. The molten pool, which corresponds to the white part in Figure 3.22, is longer and narrower than when the thermal properties are considered constant.

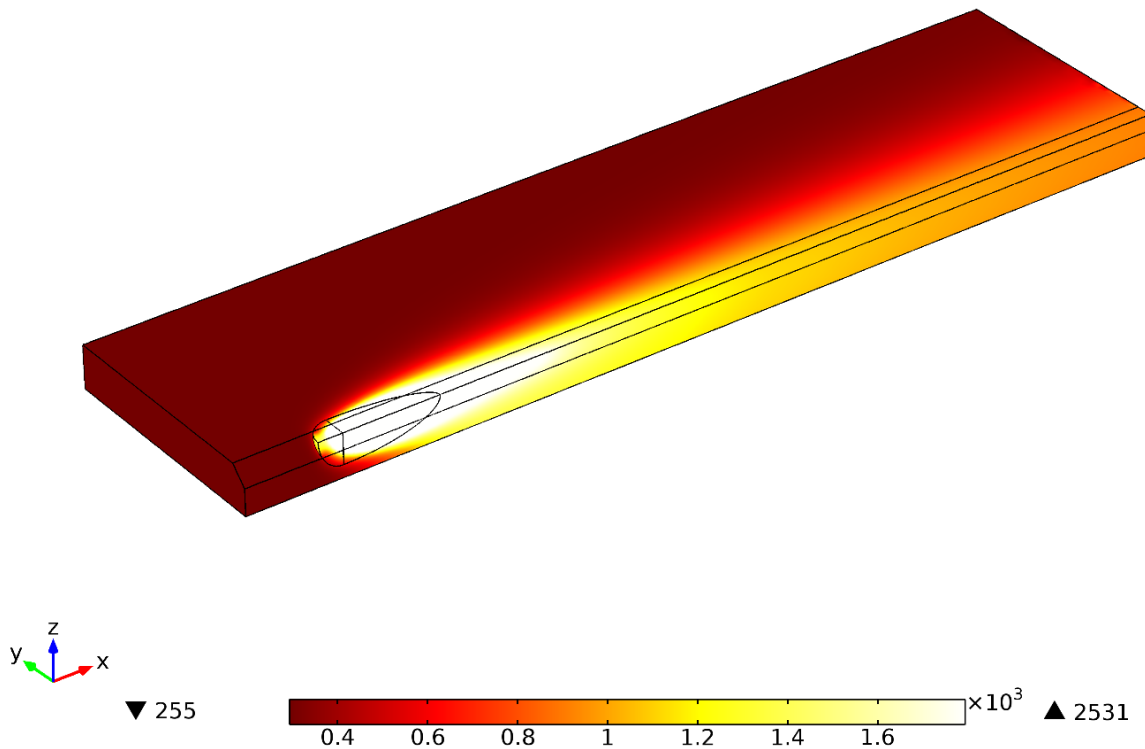


Figure 3.22: Temperature profile generated using a double ellipsoid source and varying thermal properties.

There are differences between the results obtained with and without varying thermal properties, but they are not as striking and directional as before where these were clear. Therefore, Equation (3.9) was used to compare the two results. Figure 3.23 shows the difference between these two approaches on the surface of the geometry. The minimum difference is 0% and the maximum is 67%. Differences above 10% are concentrated in the vicinity of the source. So the color range is cropped by 10% in these figures. The second place where the discrepancies are ~10% is the end of the centerline. This suggests that using varying thermal properties has an effect on the predicted

cooling of the weld. Another striking feature is the fact that no clear trend in the deviation occurs. Therefore, it is difficult to actually foresee the error made if a simulation is done using constant thermal properties. So for a simulation made using constant properties, a margin of error of at least 10% must be considered for the computed temperature profile.

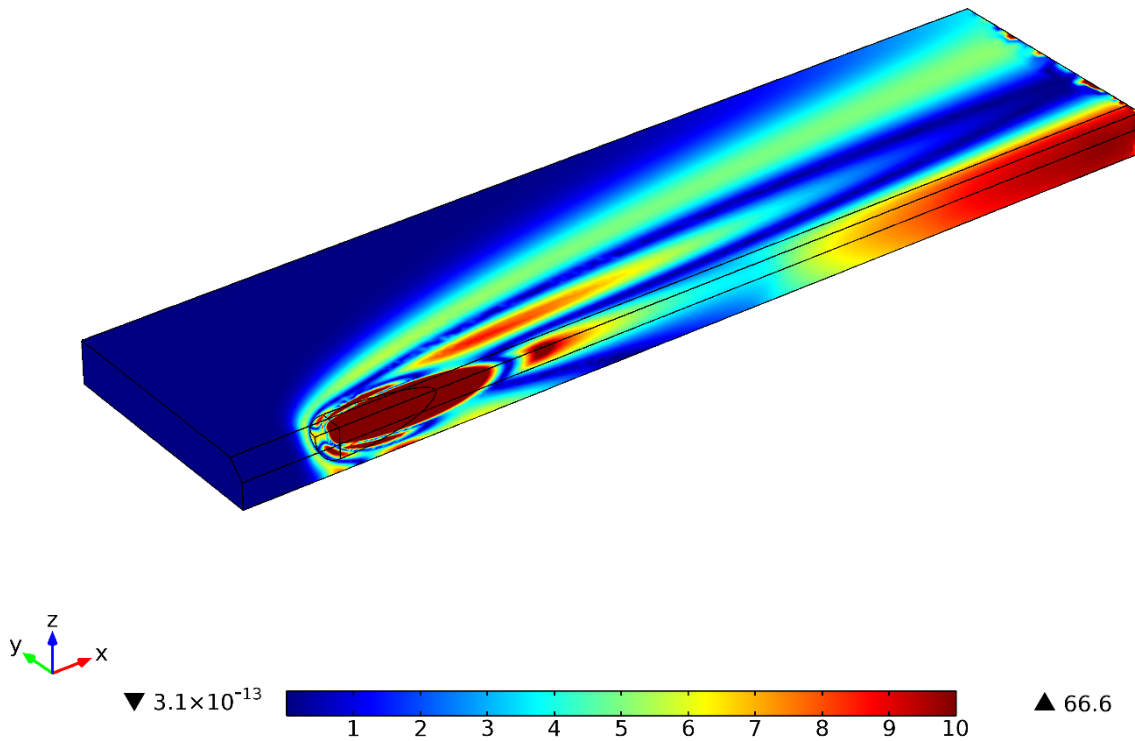


Figure 3.23: Percentage of difference between the temperature profiles generated using fixed and varying thermal properties.

3.4.6. Simulation with two sources:

Here two similar heat sources are used. The same power and geometry are used for both sources and are the same as before. The travel speed is also considered to be the same as before. The two sources are separated by 4 cm. The importance of this simulations is to determine the numerical problems that can arise due to the presence of a second source when using double ellipsoid heat sources.

First, the boundary conditions must be changed to take into account the presence of the second source. Figure 3.24 shows the geometry and the different boundary conditions used. The top

surface of the bevel lying between the two sources is considered to be insulated. The entire surface that is between the two sources in the x direction should be considered insulated. This surface should have the same width as the source. The problem is that the surface of the ellipsoid being curved if the top surface is partitioned to be able to single out the surface in-between the two sources, then the meshing produces bad quality elements. This is due to the curvature of the double ellipsoid and the straight line delimiting the surface to be considered insulated. The space between the line and the ellipsoid become infinitely small, which leads to the formation of highly deformed elements and even some inverted elements. It was tried to insulate a wider surface but the problem still remained.

The expression for the mixed boundary coefficient was changed. Because of the high power input and the use of quadratic shape functions, it is possible for the code to give negative temperatures. This is not physically correct, but it is due to some numerical errors close to the source and at the interface between the regular tetrahedral elements and the infinite elements. Therefore, in the expression for the mixed boundary condition coefficient, the absolute value of the temperature was used instead of the temperature.

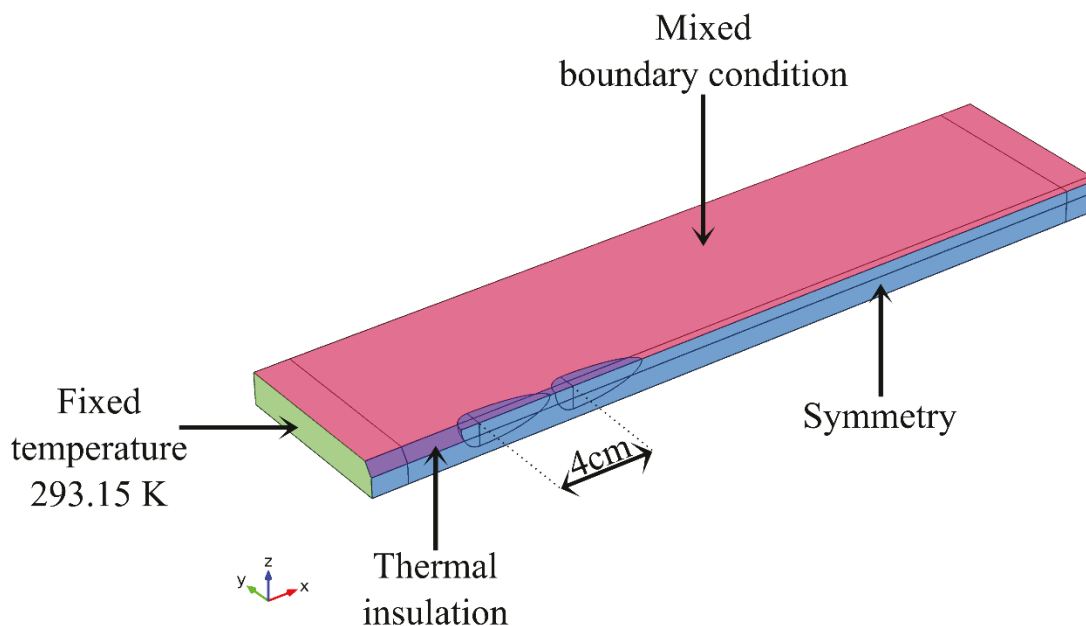


Figure 3.24: Geometry used for the simulation with two double ellipsoid sources. On this schematic the different boundary conditions used are noted.

The mesh density considered here was drastically reduced, because the introduction of a second source increases the computational time. The mesh used is reported in Figure 3.25 and consisted of 6011 elements. It was generated using the “Fine” setting in COMSOL Multiphysics®.

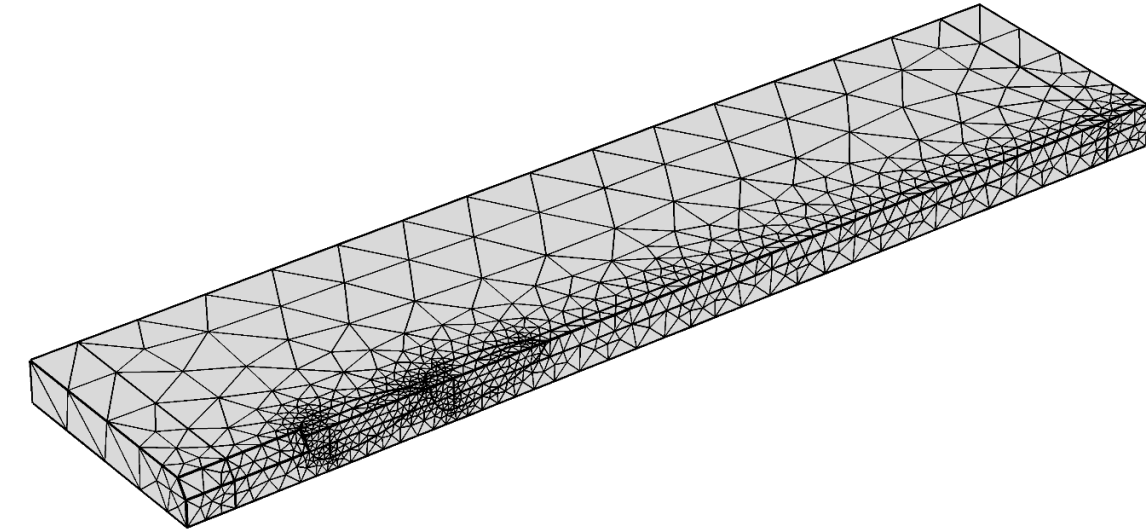


Figure 3.25: Mesh used to carry out the calculations with two double ellipsoidal sources.

The temperature profile generated by the simulation with two ellipsoid sources with varying thermal properties is shown in Figure 3.26. The minimum temperature is negative, which is a numerical mistake because no temperatures below the initial one should be encountered. However, the elements returning negative values are located at the interface between an infinite elements domain, which is only used as a numerical trick and on which the temperature cannot be analyzed, and the Cartesian domain. The maximum temperature is 2885 K. This maximum is around 600 K above the maximum temperature that is expected in the weld pool, but an operation with two sources is considered. This may also be due to the low element density. However, the peak temperature is only 400K higher than the maximum witnessed for the simulation performed with one electrode. So, the simulation does not give incoherent results for the peak temperature. Looking at the temperature profile, the simulation predicts burn through. This means that the parameters used are not optimal. The run was stopped before 60 s because the calculation of the mixed boundary condition coefficient failed. It stopped at 58.3 s, which was enough to reach a

steady-state. The failure to compute h_{comb} is certainly due to the numerical errors which led to the appearance of temperatures close to 0 K. Therefore, for the simulation of a welding operation involving more than one electrode the classical approach should be used for the boundary conditions rather than the mixed boundary conditions.

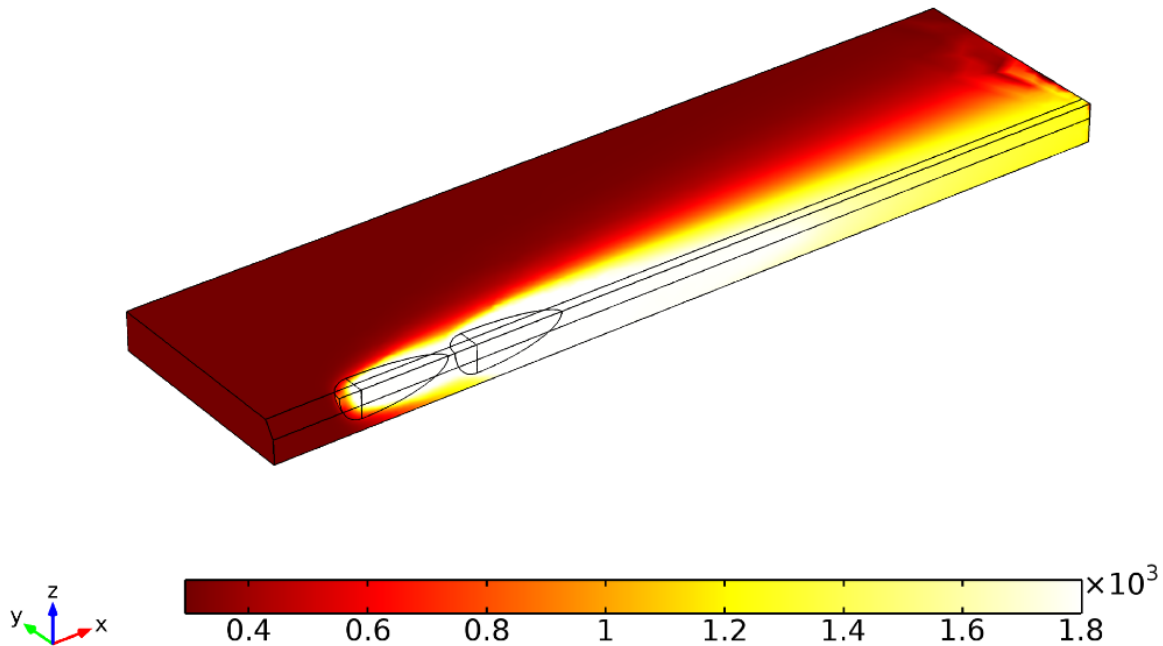


Figure 3.26: Temperature profile generated using a two double ellipsoid source and varying thermal properties.

The simulation using two ellipsoid sources highlighted several problems which arise when going from one to two sources when using double ellipsoid sources. The first is that even if the surface between the two electrodes are considered as insulated, doing so leads to numerical problems as it impacts drastically the mesh quality. Also, due to concentration of power, the risk of having unrealistic temperature in the calculations, while the solver is trying to find a solution, increases and it is therefore better to avoid using the mixed boundary conditions approach.

Another major problem when addressing tandem SAW is that one needs to assess the geometry of both sources as they are not given by the bead shape anymore. The bead shape is the result of the use of two electrodes, so the parameters of one of the two sources cannot be singled out. Therefore, the simulation done is closer to the twin SAW process than the tandem one.

3.5. Conclusions:

This study showed that results similar to the ones obtained by Rosenthal can be obtained using FEM software. The best way to approach the problem is to apply the HI on the surface of a hemispherical irregularity removed from the top surface. To consider boundary conditions that are closer to reality, it is advised to use a heat source other than the point source. The heat source investigated here, i.e., the double ellipsoid, makes it easier to introduce these different boundary conditions, especially the thermal insulation atop the molten pool. It also improved the temperature profiles obtained. The maximum and minimum temperatures are closer to what is expected. This source also makes it easier to consider varying thermal properties as the temperature gradients are lower and smoother. Using varying thermal properties improves the peak temperature. The change in the temperature profile due to the introduction of this variation is reduced by 67% and is around 10% in most of the volume.

When going from one to two sources several problems arise. Those are:

- The surface between the two sources cannot be considered insulated even if it should.
- The use of the mixed boundary conditions is not recommended.
- It is not possible to determine the source geometry based on bead shape analysis.
- The simulations done here are closer to a process for twin-wire SAW.

4. Instrumented welds:

Due to time constraints, only SAW operations with one wire were performed. The parameters used were chosen from the work of Pepin [11] for bead on plate (BOP) SAW. These parameters are reported in Table 4.1.

Table 4.1: Parameters used for the experiments.

Parameter	Value
Frequency (HZ)	60
Balance (%)	50
Offset (%)	0
Current (A)	700
Voltage (V)	32
Travel speed (mm/s)	8.9
Electrode diameter (mm)	4

Based on regression analysis of Pepin's data, a formula (available in Appendix B) to calculate the WFS was developed. Used in conjunction with some basic geometry, this formula gave the deposited area. Based on the same regression analysis, a formula to calculate the bead width was determined (available in Appendix A).

- Deposited area: 45.48 mm².
- Bead width: 15.1 mm.

These results will be compared with the data on the bevel:

- Cross sectional area of the bevel: 26 mm².
- Largest opening of the bevel: 10.2 mm.

The cross sectional area and the bead width predicted are larger than the dimensions of the bevel. This means that there should be no problem for the weld to fill and cover the bevel. No undercuts should be seen.

The welding device⁵ used for this study was operated in constant current mode. This means that the welder tries to keep the current as stable as possible and will do so by adjusting other parameters like the voltage.

Four welds were performed. A summary of the differences in these experiments and their success is reported in Table 4.2. The order of the tests presented in this table follow the partitioning chosen in this section. When thermocouples were used, the available information is reported in Table 4.2. A value reported in bold is a measured value; a value not in bold corresponds to the nominal placement of the thermocouple. For the column labeled “Success”, “Yes” means, when no thermocouples were used, that the weld showed consistent bead shape and no significant defects. When thermocouples are used, “Yes” means that the temperature profile generated by this thermocouple is usable. When “Destroyed” is specified in the “Success”, field it means that the thermocouple was destroyed, which triggered some instabilities in both the weld and the data acquisition system. A comparison between the measurements, which are reported in bold in Table 4.2, and the targeted values, which are described in Section 4.2, shows that the thermocouples were placed close to the specified location.

In Table 4.2 is also reported the nomenclature used for the different thermocouples. This nomenclature is detailed in Section 4.2.

In this section, first, the BOP weld is presented. Then, the weld performed on machined plates is discussed. This is followed by presentation of the experimental set up with both type K and type B thermocouples. Then, the experiment conducted with only type K thermocouples is presented. Finally, the conclusions drawn from the work presented here are reported.

For more details see Appendix D.

⁵ The welding device is called the welder in this document.

Table 4.2: Summary of the four different welds performed and their results.

Test	Machined	Zone	Thermocouples / Nomenclature	Depth (mm)	Distance from the centre of the plate (mm)	Success	
1	No	-	-	-	-	Yes	
2	Yes	-	-	-	-	Yes	
3	Yes	Z1	B / R1BZ1	5.1	6.4	Destroyed	
			K / R1KaZ1	5.1	8.4	No	
			K / R1KbZ1	4.98	12.71	Yes	
		Z2	-	-	-	-	-
			K / R1KaZ2	5.1	8.4	No	
			K / R1KbZ2	5.1	12.4	No	
		Z3	B / R1BZ3	5.1	6.4	Destroyed	
			K / R1KaZ3	5.1	8.4	No	
			K / R1KbZ3	5.13	11.88	Yes	
4	Yes	Z1	-	-	-	-	
			K / R2KaZ1	4.78	7.98	Yes	
			K / R2KbZ1	4.75	12.33	Yes	
		Z2	-	-	-	-	
			K / R2KaZ2	5.27	7.85	Yes	
			K / R2KbZ2	5.14	11.97	Yes	
		Z3	-	-	-	-	
			K / R3KaZ3	5.1	8.4	No	
			K / R3KbZ3	5.1	12.4	No	

4.1. Bead on plate weld:

In this section the BOP weld performed using the parameters reported in Table 4.1 is analyzed. The bead shape is first analyzed. This is followed by an analysis of the stability of the process via the output of the welder. Finally, the conclusions relative to this weld are presented.

4.1.1. Bead shape analysis:

A picture of the BOP weld is shown in Figure 4.1. For this weld no irregularities or bead inconsistencies were seen. The reinforcement is regular and constant. This weld is acceptable and corresponds to what is expected for a good weld.



Figure 4.1: Picture of the BOP weld.

4.1.2. Welding stability:

The welder was equipped with an instrumentation device recording the current, the voltage and the WFS throughout the experiment. Table 4.3 shows the average values and the standard deviations of the parameters given by the welder. The table also shows the intended values for the current and the voltage. For the WFS, the intended value is based on calculations from the developments available in Appendices A and B. The values reported in Table 4.3 show that the

welder is able to maintain the current and voltage at the intended values. The WFS is close to what was calculated from the statistical relationships available in Appendices A and B.

Table 4.3: Average values and standard deviations of the parameters given by the welder reported along with the intended values.

Parameter	Average	Standard deviation	Aim
Current (A)	700	2.47	700
Voltage (V)	31.9	0.53	32
Wire feed speed (mm/s)	32.9	0.7	32.2

4.1.3. Conclusions:

This weld was mainly performed to ascertain the choice of parameters made. The bead shape shows no instabilities or defects. This means that a good weld can be performed with the parameters chosen. In addition, the outputs of the welder do not significantly deviate from the intended values. They deviate by one standard deviation at most. As such, the weld was performed with the desired parameters and was a good weld.

4.2. Weld on machined plate without thermocouples:

For each weld performed on machined plates, two plates of X70 steel were welded together. One run out tab was placed at each end to make sure the start and the end of the weld did not occur on the plate. One of these two plates was adapted to allow for the embedment of thermocouples. Figure 4.2 shows the dimensions of the plate in which the thermocouples were embedded. The positions and nomenclature of the different thermocouples in the different zones are reported in Figure 4.3.

In general to refer to a thermocouple its name as given in Figure 4.3 is used followed by the letter “Z” and the number of the zone the thermocouple is in. For instance to refer to the thermocouple Ka in zone 2 KaZ2 is used and for thermocouple B in zone 3 BZ3 is used.

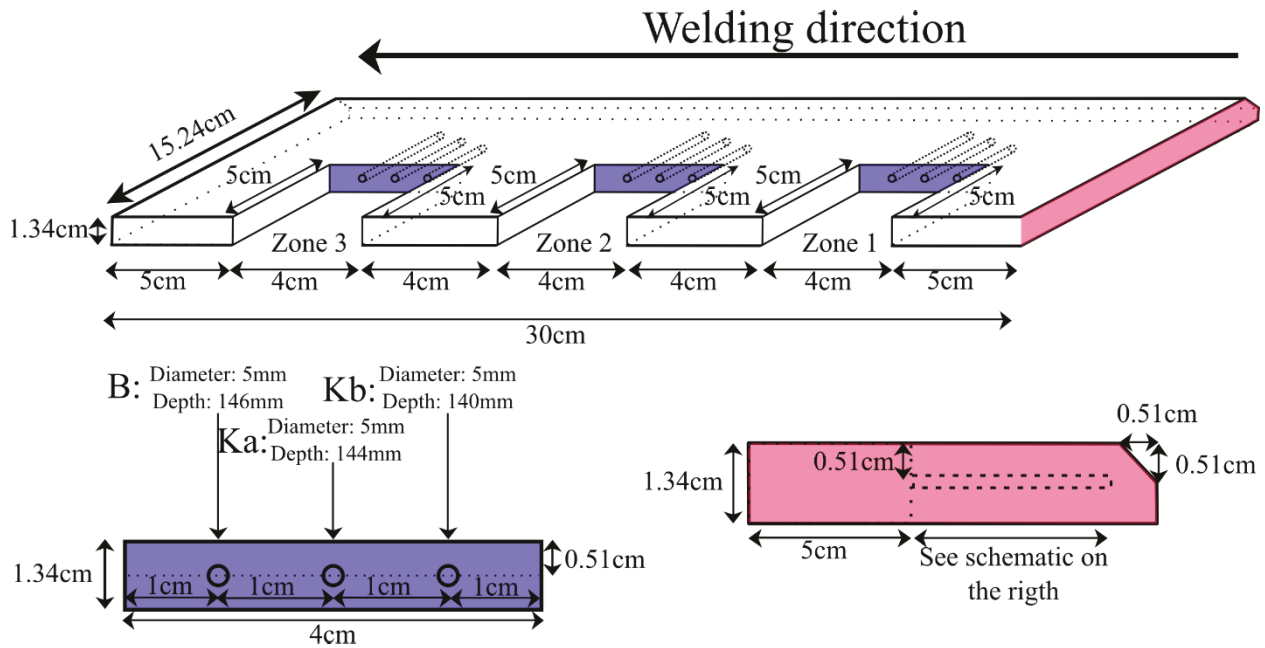


Figure 4.2: Geometry of the machined plates.

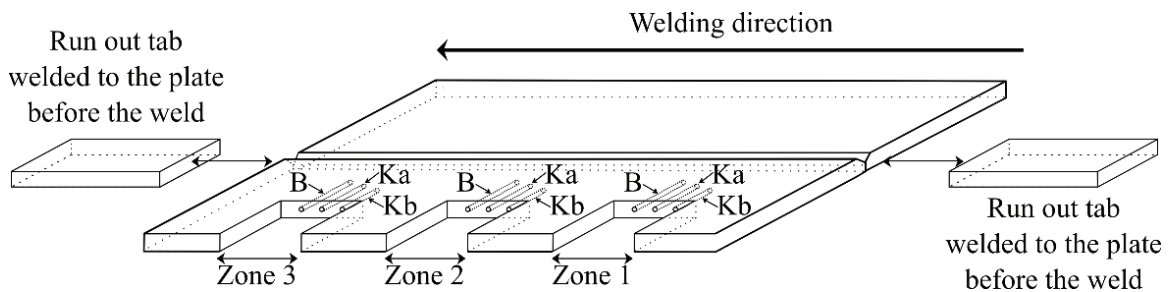


Figure 4.3: Description of the plate in place for welding, with the positions of the thermocouples.

4.2.1. Bead shape analysis:

In this section, the first part is dedicated to analysis of the physical appearance of the weld. In the second section the cross-sections of the weld taken at the location of each thermocouple are discussed.

4.2.1.1. Physical appearance of the weld:

Since the BOP weld was good, the next step was to see if the weld was still good when machined plates are used. One concern was the presence of the holes machined for the thermocouples.

An image of the weld, after the first cut was done, is shown in Figure 4.4. As with the BOP weld, this one does not show any visible defects. In addition, no burn through was noticed in the side holes. This confirmed the decision to use the parameters detailed in Table 4.1 for the instrumented welds.



Figure 4.4: Image of the weld performed on the machined plate without thermocouples.

4.2.1.2. Cross-sections of the weld:

The physical appearance of the weld is interesting, but to assess the quality of a weld taking cross-sections gives better information. A cross-section was taken perpendicular to the weld direction at the position of each thermocouple.

To carry out the analysis, the samples were cut and polished. The final polishing and the etching⁶ were done at the EVRAZ Inc. Research and Development Centre in Regina. This decision was taken because they have a microscope capable of taking pictures of polished samples with a large field of view⁷.

Image of the nine cross-sections are shown in Figure 4.5. The bead width, maximum reinforcement height, maximum penetration depth and the distance between the centre of the plate and the centre weld are reported in Table 4.4. The distance between the centre of the plate and the centre of the

⁶ Etching was done using 2% Nital.

⁷ The microscope used was a Keyence VHX-600 digital microscope.

weld is taken as positive if the centre of the weld is closer to the thermocouple than the centre of the plate. A table listing all the bead shape measurements done is available in Appendix E.

Both Figure 4.5 and Table 4.4 show that the 9 cross-sections are similar and no significant deviation is seen. The welds are symmetric. The distance between the centre of both the plate and the weld is less than 1 mm and the mean is 0.23 mm. Therefore, it is safe to say that the weld is centred with the plate. The predicted parameters are also close to the measured values.

The experiments confirm the choices made for the parameters used. In addition, the presence of the holes for thermocouple insertion does not disturb the weld significantly.

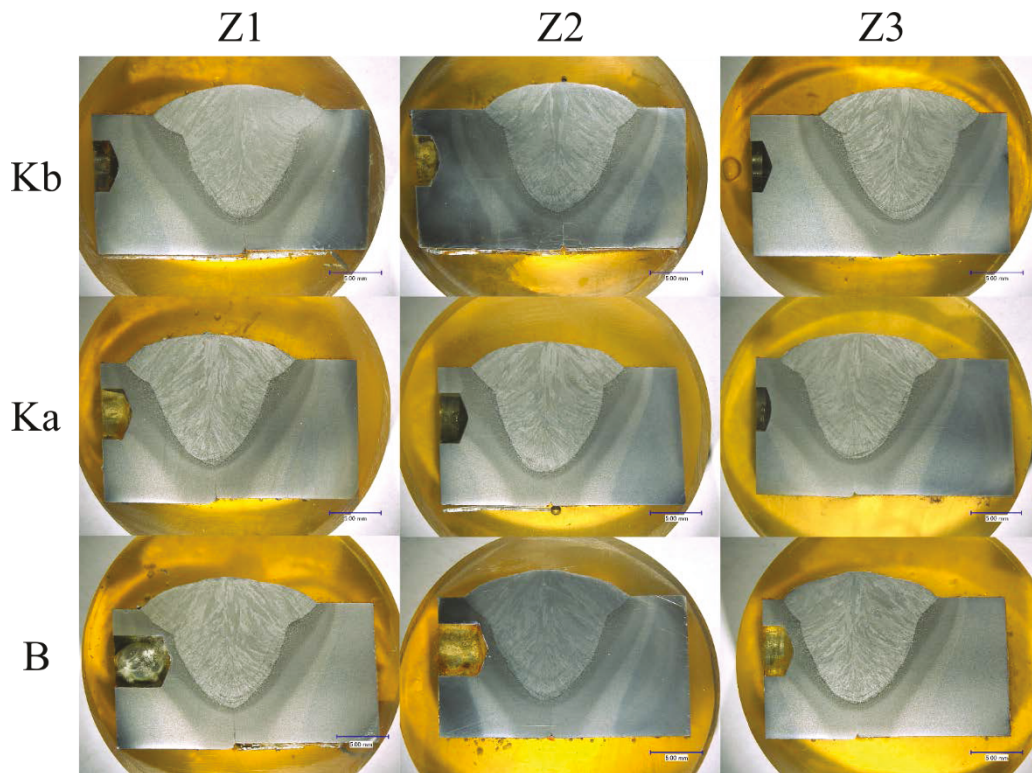


Figure 4.5: Polished and etched cross-sections taken at different thermocouple positions along the welding direction. The blue line is 5 mm long.

Table 4.4: Main bead shape parameters measured from the cross-sections.

Parameter	Minimum	Mean	Maximum	Prediction
Bead width (mm)	14.97	15.84	17.08	15.08
Maximum reinforcement height (mm)	2.52	2.76	3.13	3.92
Maximum penetration depth (mm)	9.58	9.93	10.03	9.47
Difference between plate and weld centre (mm)	-0.27	0.23	0.89	/

4.2.2. Welding stability:

The average current, voltage and WFS delivered by the welder are reported in Table 4.5, along with the intended values and the standard deviations. The average value is equal to the intended value for the current and the voltage. However, the WFS increases by 2 mm/s compared with the BOP weld. In this experiment, the plates were beveled which means an increase in stick-out inducing a higher melting rate of the electrode. This explains the increase in WFS. The standard deviations are the same for the BOP weld and the one conducted on machined plates without thermocouples. For the WFS, the standard deviation is higher than for the BOP weld.

Table 4.5: Average values and standard deviations for the parameters given by the welder along with the intended values.

Parameter	Average	Standard deviation	Aim
Current (A)	700	2.46	700
Voltage (V)	32	0.50	32
Wire feed speed (mm/s)	33.9	0.9	32.2

4.2.3. Conclusions:

The appearance of the weld performed on a machined plate, without the presence of thermocouples, was good with no defects. The quality of the weld was further confirmed by the cross-section images taken at the location of each thermocouple. The images showed a symmetric bead shape, which stayed consistent throughout the length of the weld. The current and voltage delivered by the welder were equal to the intended values. There was an increase in the WFS due to the presence of the bevel. The machining of the plates does not significantly impact the weld.

4.3. Weld with type B and type K thermocouples:

Here the experiment conducted on machined plates with 2 type B thermocouples and 6 type K thermocouples embedded is discussed. First, the thermocouples were connected to the data acquisition system and then they were spot-welded at the end of the holes. The experimental plan involved 9 thermocouples but one of the type B thermocouples was damaged beyond repair while it was spot-welded; before the actual experiment. One of the two wires of the thermocouple touched the base metal and melted to an extent that it became too small to be placed at the end of the hole. The missing thermocouple is the type B thermocouple, which should have been in zone 2.

4.3.1. Bead shape analysis:

The physical appearance of the weld performed using two type B thermocouples and six type K is first discussed. Then the cross-sections taken at the location of each hole drilled in the side of the plate are analyzed.

4.3.1.1. Physical appearance of the weld:

A picture of the weld is shown in Figure 4.6. The first striking feature is that the weld can be divided in two parts based on its appearance. From the beginning to approximately the end of zone 1, the reinforcement has the same morphology as the one performed with no embedded thermocouples. The weld looks acceptable with no apparent defects. Then, the reinforcement takes a shape similar to what is seen when arc blow occurs during the process. The weld bead became erratic after the first block and the type B thermocouples were disabled.

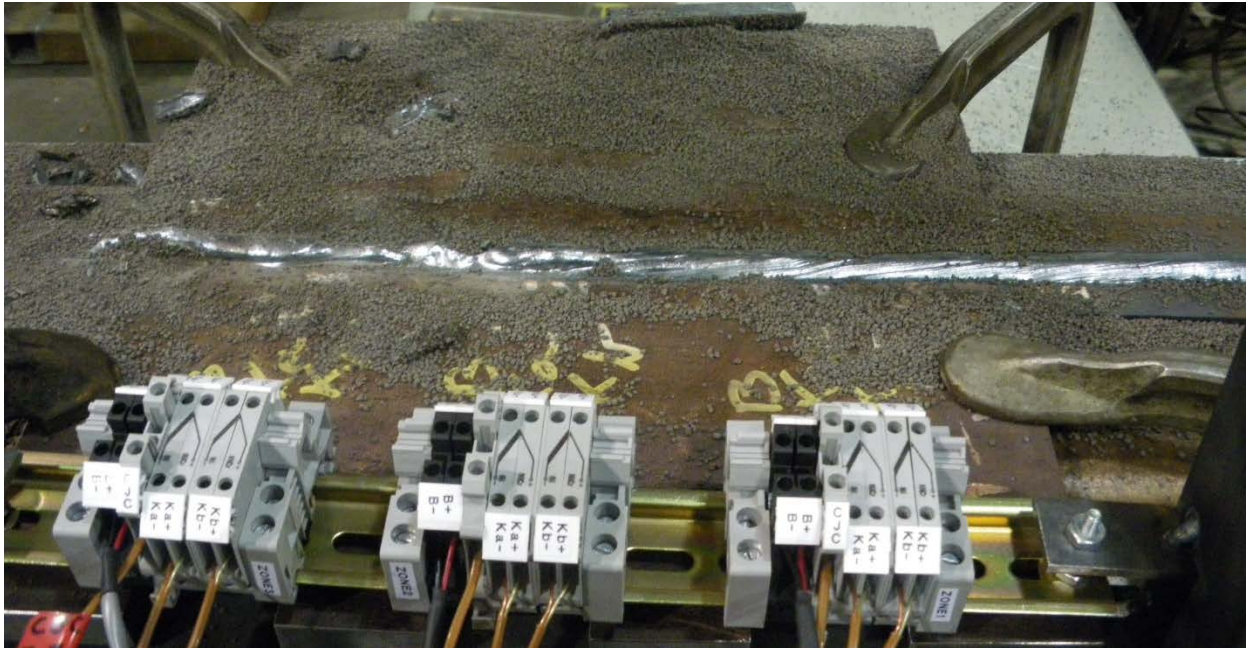


Figure 4.6: Image of the weld performed with 8 thermocouples embedded in the plate.

4.3.1.2. Cross-sections of the weld:

The way the cross-section were obtained is presented in Section 4.2.1.2. The parameters chosen to perform the weld were also validated in Section 4.2.1.2. This means that any changes here are likely coming from the introduction of thermocouples.

Images of the etched cross-sections are shown in Figure 4.7. The first striking thing is that the welds are no longer symmetric. The bead shapes are slanted and they are all shifted toward the side where the thermocouples were embedded. The high electrical conductivity of the type B thermocouples can have disturbed the electromagnetic fields in the piece to be welded. This may be an explanation for the shift of the bead shapes. They have disturbed the electromagnetic environment of the arc, while it traveled through the piece to be welded. Also, the reinforcement is displaced toward the side of the thermocouple. One feature that appeared, which was not witnessed for the experiment without thermocouples, is burn through. For thermocouples Ka and Kb liquid metal flowed in the holes with the thermocouples. For thermocouple BZ2 the hole was empty when the experiment was carried out. This explains why the flow of metal was more important for the hole drilled for thermocouple BZ2. A change in geometry of the reinforcement occurs between zone 1 and zone 2.

Table 4.6 shows the minimum, average and maximum values obtained for the bead width, the maximum reinforcement height, the maximum penetration depth and the distance between the centre of the plate and the centre of the weld. The welds are slanted and, therefore, it is difficult to define a centre. In this case, the centre of the weld was considered to be the vertical projection line of the deepest point of the fusion zone. A table listing all the bead shape measurements is available in Appendix E.

Compared with the experiments conducted with no embedded thermocouples, the bead width is roughly the same. The penetration depth is higher. There is also a large increase in the maximum reinforcement height. This is in part due to the change in geometry of the reinforcement between zone 1 and zone 2. The largest increase occurs for the distance between the centre of the plate and the centre of the weld. No weld has the same centre as the plate and no weld has its centre on the opposite side from the thermocouple. This provides support for the hypothesis that the weld was attracted toward the side where the thermocouples were embedded.

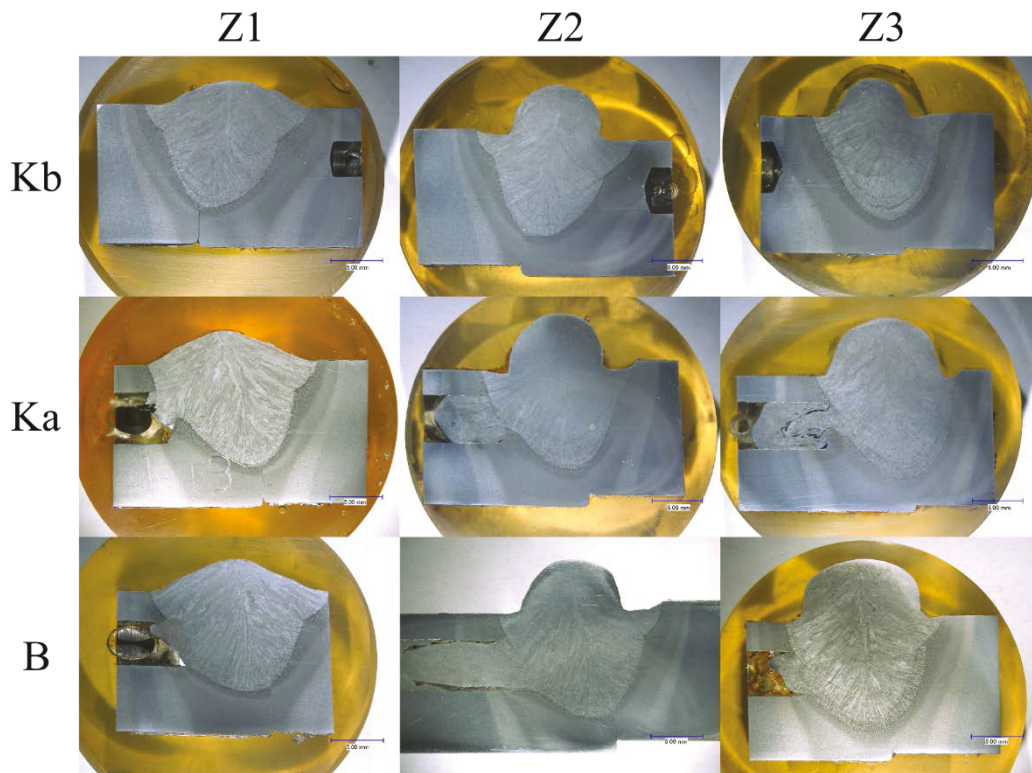


Figure 4.7: Polished and etched cross-sections taken at the different positions of the thermocouples along the welding direction. The blue line is 5 mm long.

Table 4.6: Main bead shape parameters measured from the cross-sections.

Parameter	Minimum	Mean	Maximum	Prediction
Bead width (mm)	13.59	15.38	17.01	15.08
Maximum reinforcement height (mm)	2.29	4.39	6.23	3.92
Maximum penetration depth (mm)	9.48	10.15	10.81	9.47
Difference between plate and weld centre (mm)	1.01	1.66	2.59	/

4.3.2. Welding stability:

The current, voltage and WFS recorded by the welder are reported in Table 4.7. The average current is not significantly different from the intended value. The same can be said for the voltage and the WFS. However, the standard deviations of these parameters is significantly higher than the standard deviations for the welds performed with no embedded thermocouples.

Table 4.7: Average values and standard deviations of the parameters given by the welder reported along with the intended values.

Parameter	Average	Standard deviation	Aim
Current (A)	701	4.27	700
Voltage (V)	32.2	0.60	32
Wire feed speed (mm/s)	32.7	1.43	32.2

4.3.3. Temperature profiles:

During this weld, the type B thermocouples came in contact with some molten metal. They were destroyed and triggered significant disturbances in the output signals of the other thermocouples. Therefore, to overcome this problem and get rid of any other disturbance the outputted text files were passed through a Matlab[®] code. This code removed the data out of the temperature range of interest, which is 0°C to 1600°C, and puts aside the points which are such that the derivative of the temperature with respect to time at this point exceeds a value inputted by the operator. Figures 4.8 and 4.9 show the superposition of raw data obtained for R1KaZ1 and R2KaZ1 in red and treated data as black circles. The treated data were reported at a rate of one point every 0.2 s for legibility

sake. One can see in Figure 4.8 that the two big artefacts introduced by the destruction of the type B thermocouples were filtered out. Also one can notice that there is much less noise in the experiment in which no type B thermocouples than when type B thermocouples are used.

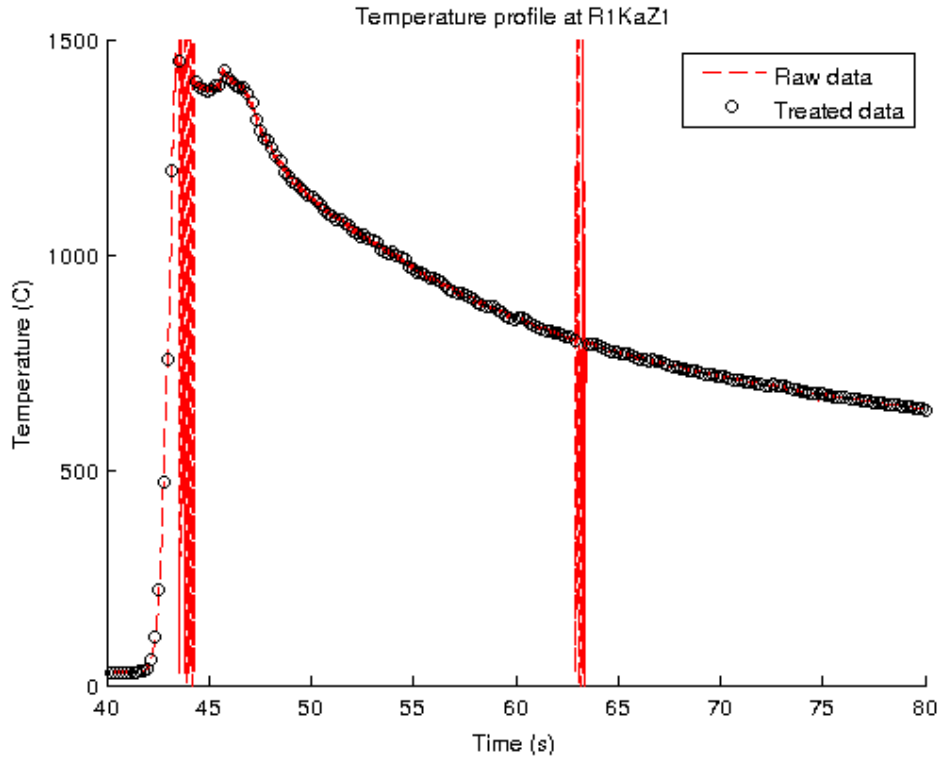


Figure 4.8: Superposition of the raw data obtain for R1KaZ1 (red line) and the processed data (black circles). The treated data were reported as discreet circles, at a rate of one every 0.2 s, for legibility sake.

Only the temperature profiles acquired from the Kb thermocouples are presented for this experiment as burn through occurred for the other thermocouples

The three temperature profiles produced by the three Kb thermocouples are plotted in Figure 4.10. The starting times for the different temperature profile were manipulated to make the three curves start at roughly the same time. The red curve corresponds to the signal of KbZ2 but shifted 9 s to the left and the blue one corresponds to the signal of KbZ3 but shifted 19 s to the left. The

maximum derivative used to remove the outliers from the data is 4000 K/s for KbZ1 and KbZ2 and 5000 K/s for KbZ3.

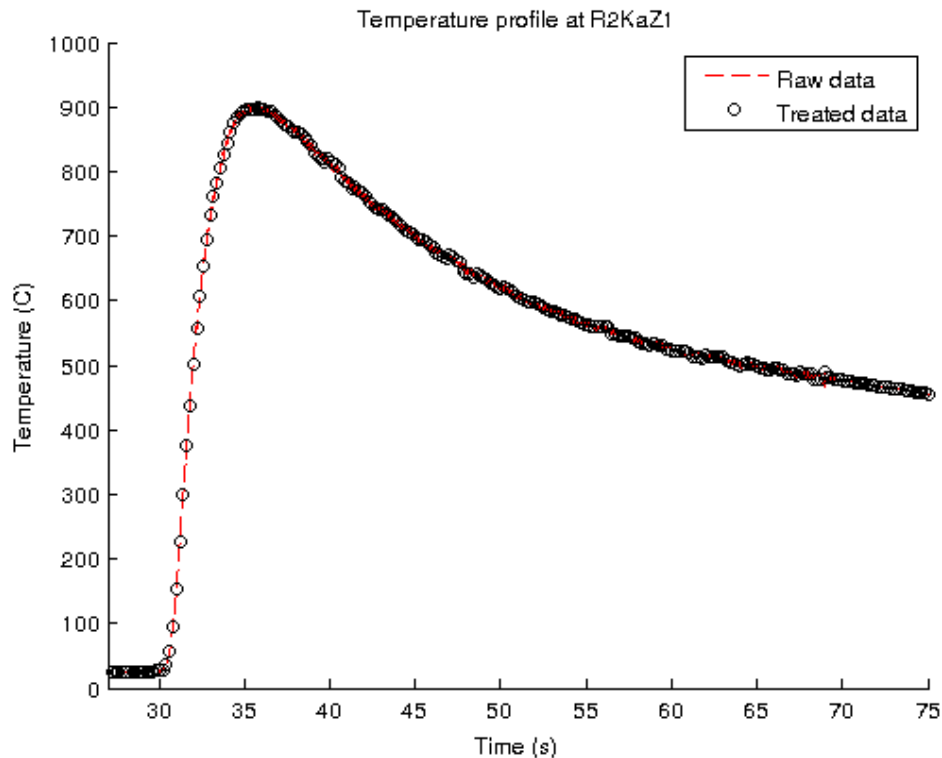


Figure 4.9: Superposition of the raw data obtain for R2KaZ1 (red line) and the processed data (black circles). The treated data were reported as discreet circles, at a rate of one every 0.2 s, for legibility sake.

The first striking feature is that the three curves have the same starting gradient. Then the temperature profile recorded by KbZ2 (red) shows a behavior that does not match the others and displays a plateau. There is no reason for a plateau in temperature to occur. It is possible that the spot-weld, which was holding the thermocouple in place, broke and that some spring load, introduced when the thermocouple was put in place, moved it away from its original position. The red curve follows the blue curve up to when the plateau forms. The higher maximum temperature for KbZ3 (blue) can be explained by the fact that the weld is closer to the thermocouple than it is for KbZ1 (black). The peak temperature increase as the weld is performed.

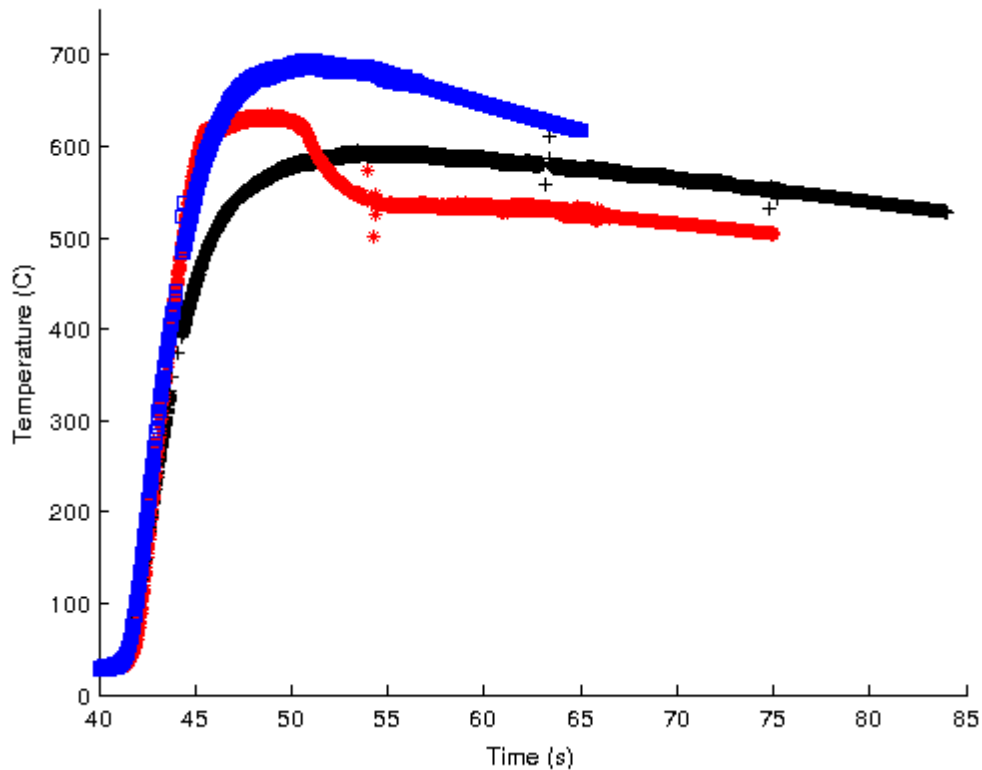


Figure 4.10: Signals for three Kb thermocouples. The black points corresponds to zone 1, the red ones to zone 2 and the blue ones to zone 3. The time display was manipulated to superimpose the three graphs.

4.3.4. Conclusions:

Based on the results of Sections 4.1 and 4.2 it is possible to say that the parameters chosen for the welds were good. However, the first instrumented weld which used two type B thermocouples and six type K ones was not good. The bead was inconsistent and major defects were found. Therefore, the presence of the thermocouples linked to the data acquisition system disturbed the weld. The weld bead was slanted and displaced toward the side where the thermocouples were embedded. Also, the stability was not as good as for the weld performed without thermocouples. The variability in the current voltage and WFS all increased. However, even if the bead shape was different, especially the reinforcement, it was still similar to the weld performed without thermocouples but slanted. Therefore, it could still be analyzed.

Burn through occurred from the side of the holes for the two B thermocouples and the three Ka ones. Therefore, the temperature profiles recorded by the thermocouples embedded in these hole were not usable.

Among the Kb thermocouples, only two were usable since the temperature profile recorded by KbZ2 was irregular. The thermocouples that will later be used for comparison in Section 5 are KbZ1 and KbZ3.

4.4. Weld with only type K thermocouples:

It was decided to conduct another experiment to determine if the disturbances were caused by the presence of the type B thermocouples and if it was possible to improve the results obtained. Also, the holes where the B thermocouples were supposed to be, were plugged with metal wire. This was decided to avoid any burn through like what happened for thermocouple BZ2 in the experiment in which B thermocouples are used.

4.4.1. Bead shape analysis:

First, the physical appearance of the weld performed using only six type K thermocouples is analyzed. Then, the cross-sections taken at the locations of each hole drilled are discussed.

4.4.1.1. Physical appearance of the weld:

As can be seen in Figure 4.11 the bead, like previously, begins well then undercut and inconsistency are observed for the reinforcement. The consistent and acceptable part of the weld last until just after the first zone.

This being said, the disturbances observed are less erratic than what was observed for the experiment conducted with B thermocouples embedded. Instead of what was noticed when B thermocouples were used, the weld bead does not seem preferentially attracted on either side. This backs the proposition that the highly electrically conductive nature of type B thermocouple being place this close to the weld adds some disturbances, but this is not the only reason for the disturbances. The type K thermocouples also seem to disturb the arc. Therefore, the fact that some thermocouples are embedded seems to disturb the weld independently of the type of thermocouple used.



Figure 4.11: Instrumented weld produced with only 6 type K thermocouples embedded.

4.4.1.2. Cross-sections of the weld:

The procedure for producing cross-sections is presented in Section 4.2.1.2. The cross-sections obtained are compared to the cross-sections obtained for the experiment with no thermocouples (Section 4.2) and the experiment with 8 thermocouples embedded (Section 4.3).

Images of the 9 cross-sections taken are shown in Figure 4.12. The images show bead shapes that are skewed for thermocouple BZ1 and the thermocouples of zone 2. However, these bead shapes are less skewed than the ones seen in the experiment in which six type K and two type B thermocouples were used. The other bead shapes are not slanted and are symmetric. A change in the reinforcement occurs from zone 1 to zone 2. Also, a second change seems to occur between zone 2 and zone 3. In this experiment no burn through were witnessed. Looking closely at the images, it is probable that plugging the empty holes prevented molten metal to flow in them. Avoiding burn through from the holes for the thermocouples certainly contributed to better welds than for the experiment in which six type K and two type B thermocouples were used.

Table 4.8 shows the minimum, average and maximum values for the bead width, the maximum reinforcement height, the maximum penetration depth and the distance between the centre of the plate and the centre of the weld. The bead width is lower than for the experiment without thermocouples. The maximum penetration depth is slightly larger than for the experiment conducted without thermocouples. The maximum reinforcement height is similar to the results obtained for the experiment conducted with 8 thermocouples. The distance between the centre of the plate and the centre of the weld is closer to the results obtained for the experiment without thermocouples than the one obtains for the experiment with 8 thermocouples. The best improvement in the results is the fact that the weld was more symmetric and aligned with the centre of the plate. A table listing all the bead shape measurements done is available in Appendix E.

Table 4.8: Main bead shape parameters measured from the cross-sections.

Parameter	Minimum	Mean	Maximum	Prediction
Bead width (mm)	13.37	14.64	15.51	15.08
Maximum reinforcement height (mm)	2.92	4.27	5.65	3.92
Maximum penetration depth (mm)	9.72	10.61	11.59	9.47
Difference between plate and weld centre (mm)	0.24	0.77	1.07	/

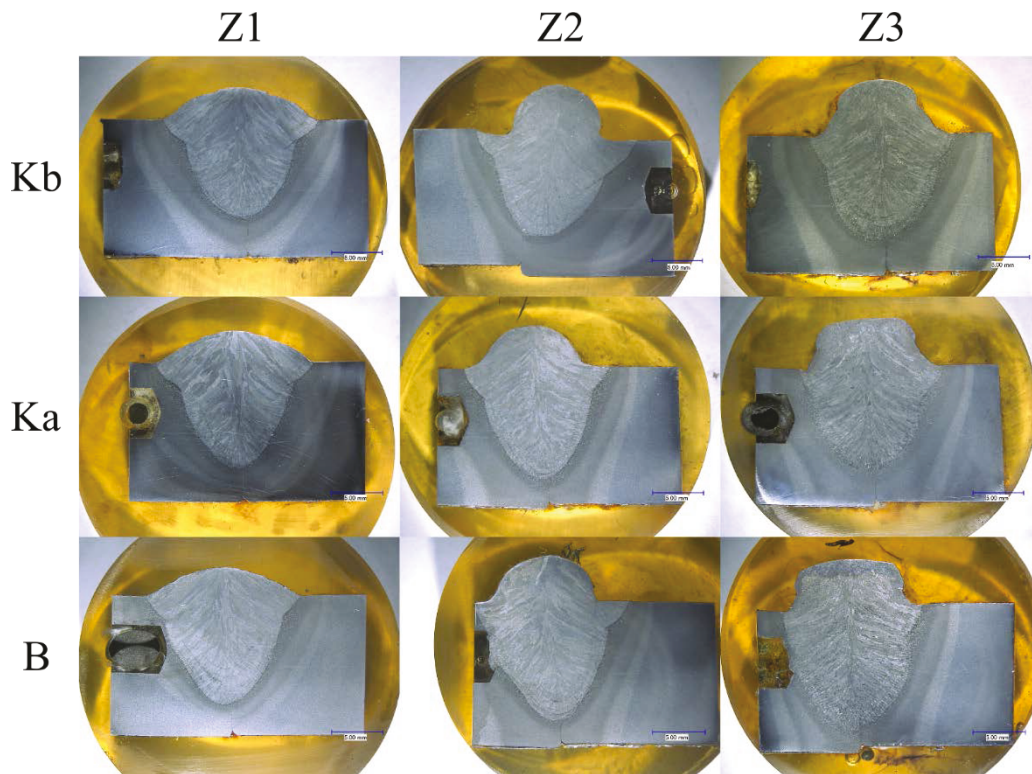


Figure 4.12: Polished and etched cross-sections taken at the different positions of the thermocouples along the welding direction. The blue line is 5 mm long.

4.4.2. Welding stability:

The average value and the standard deviation of the parameters recorded by the welder are reported in Table 4.9. The average value of the current and the voltage are not significantly different from the intended values. The standard deviation calculated for the current is between the value found for the welds performed with no thermocouples and the experiment performed using two type B and six type K thermocouples. Therefore, removing the type B thermocouples improved the

stability of the current. However, the variability of the voltage is higher than for the experiment involving type B thermocouples. The process was operated in constant current mode. Therefore, current stability is more important voltage stability. The average WFS and its standard deviation are the highest recorded among the experiments performed.

Table 4.9: Average values and standard deviations of the parameters given by the welder reported along with the intended values.

Parameter	Average	Standard deviation	Aim
Current (A)	701	3.94	700
Voltage (V)	31.7	1.19	32
Wire feed speed (mm/s)	34.9	2.13	32.2

4.4.3. Temperature profiles:

Based on the analysis of the cross-sections (Section 4.4.1.2) the temperature profile for all Kb and Ka thermocouples must be investigated. The temperature profiles for the Kb thermocouples are presented first, followed by the profiles for the Ka thermocouples.

4.4.3.1. Kb thermocouples:

The temperature profiles for all three Kb thermocouples are superimposed in Figure 4.13. The time scales for the KbZ2 and KbZ3 thermocouples were manipulated to make the three curves start at the same time. The manipulation consisted of a shift of 9 s to the left for KbZ2 and 18 s to the left for KbZ3. The maximum derivative used to remove the outliers from the data is 1000 K/s all three thermocouples.

The heating rate for the three curves is similar. No significant deviation occurs on heating part except for the maximum temperature. The peak temperature for the first two zones (black and red) are similar, while on the cooling side zone 2 (black) and zone 3 (blue) are the closest and have similar asymptotes. The cooling part of zone 1 (black) is consistent with the other two zones (blue and red). The peak temperatures are reached at roughly the same time.

These curves can be analyzed in conjunction with Figure 4.11, showing a top view image of the weld. One can see, on this figure, a crater that can come from short-circuit within the third zone.

This crater indicates that a part of the molten liquid was pushed away. Therefore, the energy inputted around this crater was lower. This can lead to a decrease in peak temperature.

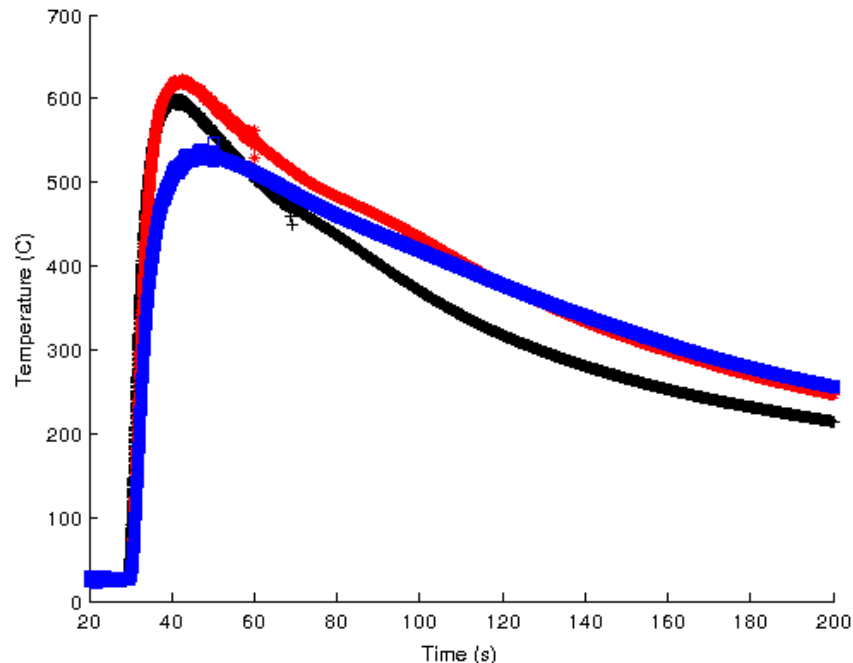


Figure 4.13: Superposition of the three temperature profiles recorded by the Kb thermocouples. The black curve corresponds to zone 1. The red one to zone 2 shifted 9 s to the left and the blue plot shows the temperature for zone 3 shifted 18 s to the left.

4.4.3.2. Ka thermocouples:

Figure 4.14 displays the superposition of the three temperature profiles for the Ka thermocouples. The time scales of the temperature profiles for KaZ2 and KaZ3 were manipulated to allow for superposition of the three curves. The manipulation consisted of a shift of 9 s to the left for KaZ2 and 18 s for KaZ3. The maximum derivative used to remove the outliers from the data is 4000 K/s for KbZ1 and KbZ2 and 5000 K/s for KbZ3.

The peak temperature for zone 1 (black) and zone 3 (blue) are close while the peak temperature for zone 2 is lower. The heating parts for the three curves are similar and follow each other closely. The cooling parts of the curves for zones 2 (red) and 3 (blue) are similar and have the same asymptote while the cooling part for zone 1 (black) shows lower temperatures but a similar trend.

An unexpected variation is witnessed on the temperature profile recorded by KaZ3. This is correlated to the image available in Figure 4.11. There is a crater in the reinforcement of the weld in front of the holes where those thermocouples were placed. This means that at this spot there was less metal in the molten weld. Therefore, the energy transferred from the molten pool by conduction was lower which accounts for the lower peak temperature for kbZ3. If this crater is due to short-circuiting, it may have removed a part of the metal which was initially present. The effect of this disturbance then fades away by the effect of the surrounding material which would tend to smooth the rapid variations. When looking closely at the evolution of the current with time, a surge is seen at the time when the electrode is in zone 3. The variation is fast for KaZ3 as it is closer and can benefit from the input of metal which comes after the disturbance, while the variation for KbZ3 is slow because it is further away. Therefore, the temperature profiles recorded by the thermocouples positioned in zone 3 will be excluded from further comparisons (Section 5).

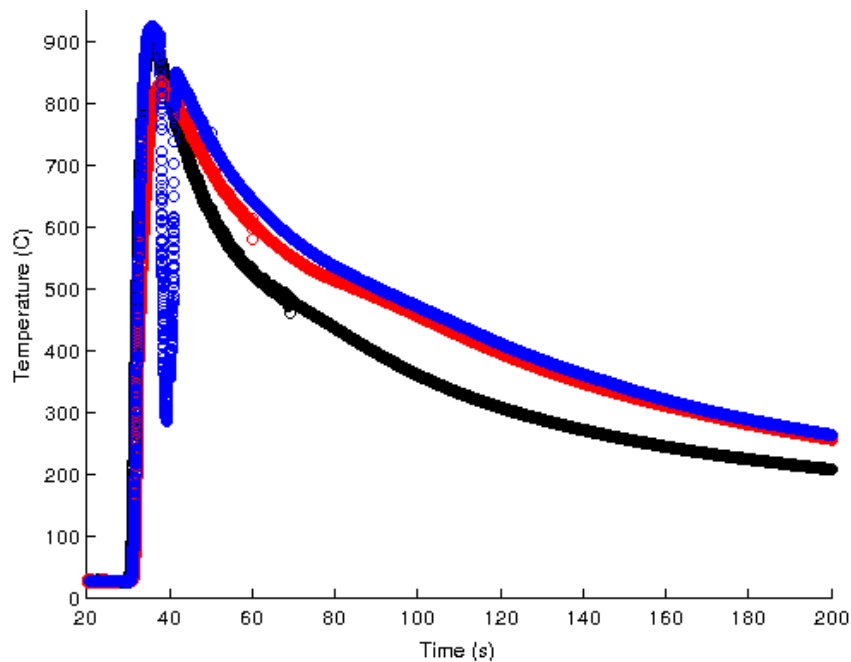


Figure 4.14: Superposition of the three temperature profiles recorded by the Ka thermocouples. The black curve corresponds to zone 1 with. The red one corresponds to zone 2 shifted 9 s to the left and the blue plot shows the temperature for zone 3 shifted 18 s to the left.

4.4.4. Conclusions:

The bead shape is not as good as for the welds performed without embedded thermocouples, but is better than for the experiment in which B thermocouples were used. The cross-sections show bead shapes that are less displaced toward the thermocouples and are more symmetric. Based on the analysis conducted, it is safe to say that the results obtained in this experiment are better. Therefore, removing the type B thermocouples and filling the holes led to better results. However, some disturbances occurred.

The variability observed in the data extracted from the welder was higher than before, suggesting that the removal of the B thermocouples does not affect the variability in the data. This is shown by the maximum derivatives used for the removal of the outliers, which were lower for this experiment. This does not affect the validity of the data but shows that the simple fact of adding thermocouples adds noise in the output of the welder and this is independent from the type or location of the thermocouple.

The analysis of the bead shape and the temperature profiles showed that the outputs for KbZ1, KaZ1, KbZ2 and KaZ2 can be used for comparison. The results given by thermocouples KbZ3 and KaZ3 are debatable and should not be used.

4.5. Conclusions:

The first conclusions coming from the two preliminary experiments are that the parameters chosen and presented in Section 2 are correct and produce good welds when the thermocouples are not inserted. This means that the changes recorded or witnessed in the other experiments likely come from the insertion of thermocouples.

The other two experiments were conducted with the presence of the thermocouples to record the temperature profiles. In these experiments inconsistency in the bead shapes of the welds produced was noted. This means that the introduction of the thermocouples influenced the temperature profiles and this is something that needs to be taken into account while later comparing the results with the simulation. The cooling parts of the temperature profiles for the Kb thermocouples, except for KbZ2, are similar in both experiments.

In the first experiment the thermocouples KbZ1 and KbZ3 gave usable results that can be used for comparison. In the experiment described in Section 4.5 the thermocouples KbZ1, KaZ1, KbZ2 and KaZ2 gave results that can be used for comparison with the model.

5. Comparison between simulation and experiments:

First, a general presentation of the subject is given to provide information that applies to the entire section. Then, comparisons between the simulations and experiments are discussed for each thermocouple considered. After that, a sensitivity analysis is presented. Finally, the conclusions of this section are presented.

5.1. General presentation:

Not all the simulations are used for comparison. The ones used are: the point source applied to the surface of a hemisphere (Section 3.2.1.3), the double ellipsoid source with constant thermal properties (Section 3.4.4) and the double ellipsoid source with varying thermal properties (Section 3.4.5).

The temperature profiles used for comparison are reported in Table 5.1, along with the measured positions of the thermocouples which recorded the profiles. An example of a line from which the calculated temperatures are extracted from the model is reported in Figure 5.1.

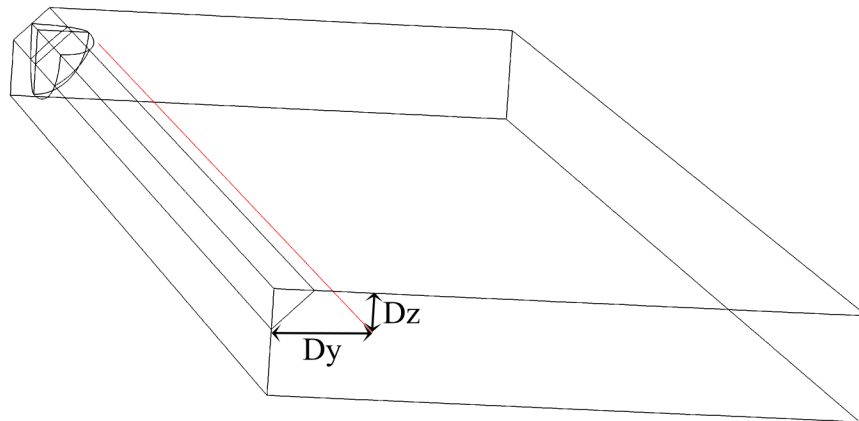


Figure 5.1: Example of line on which the calculated temperature profile is extracted.

Table 5.1: Position of different thermocouples in the plane (z,y). Parameters Dz and Dy are the ones shown in Figure 5.1.

Run	Zone	Dz (mm)	Dy (mm)	Thermocouple
With 8 thermocouples	1	4.98	12.71	R1KbZ1
With 8 thermocouples	3	5.35	11.88	R1KbZ3
With 6 thermocouples	1	4.75	12.33	R2KbZ1
With 6 thermocouples	2	5.14	11.97	R2KbZ2
With 6 thermocouples	1	4.78	7.98	R2KaZ1
With 6 thermocouples	2	5.27	7.85	R2KaZ2
Nominal placement	-	5.1	Ka: 8.4 Kb: 12.4	-

In the legends of the pictures, the following nomenclature is used:

- T_{measured} : measured temperature profile.
- T_{ps} : temperature profile generated using the point heat source discussed in Section 3.2.1.3.
- $T_{\text{ellipsoid-CT}}$: temperature profile generated using the double ellipsoid heat source with constant thermal properties discussed in Section 3.4.4.
- $T_{\text{ellipsoid}}$: temperature profile generated using the double ellipsoid heat source with varying thermal properties discussed in Section 3.4.5.

To compare the results from the simulations and the results from the experiments, it is necessary to change the coordinate system of the simulation. One needs to convert the results of the simulation, which are obtained in the coordinate system (x,y,z), to the coordinate system of the

thermocouples used in the experiments, i.e., (t,y,z). To do so, Equation (5.1) is used where “ lx ” is the length of the plate in the “ x ” direction and v is the travel speed. This relation depends on where the origin of the axes is chosen. In this project, the origin of the axes is chosen at the middle of the block modelling the base metal.

$$t = \frac{x + lx/2}{v} \quad (5.1)$$

Also to compare the temperature profiles, an offset is added to the time of the temperature profiles generated by the simulations.

5.2. Comparison for each thermocouple:

The experimental temperature profiles are compared with the simulations in the following order: R1KbZ1, R1KbZ3, R2KbZ1, R2KbZ2, R2KaZ1 and R2KaZ2.

The data acquisition system recorded the temperatures at a rate of 100 points per second. However, in the figures the measured temperatures are reported at a rate of two points per second.

5.2.1. R1KbZ1:

The different temperature profiles coming from the simulations and the experiment are available in Figure 5.2. The three models are able to model the starting part of the heating phase. This means that accurate calculations of the initial heating rate are possible and can be done using any of the three models.

Going from a point source to a double ellipsoid source with constant properties improves the prediction of the time at which the peak is reached and the cooling portion of the temperature profile. Also, the temperature profile predicted using a double ellipsoid heat source follows the heating part better. Further improvements are obtained when variation in the thermal properties is taken into account. This model is the one that predicts the peak temperature the best.

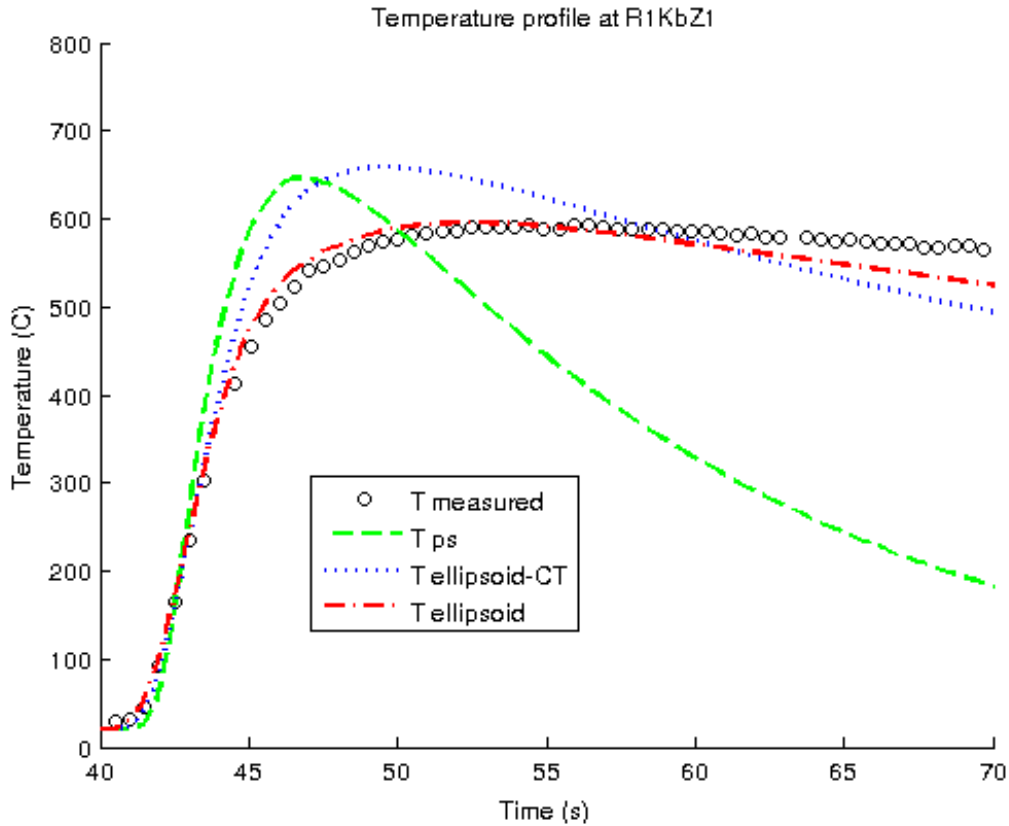


Figure 5.2: Experimental temperature profile for R1KbZ1 along with temperature profiles generated by a point source (green), a double ellipsoid source with constant properties (blue) and a double ellipsoid source with varying thermal properties (red).

5.2.2. R1KbZ3:

The different temperature profiles considered here are available in Figure 5.3. The three models predict the heating part of the temperature profile correctly. Using a double ellipsoid heat source does not improve the match between the measurements and the calculations, which is different from the result for R1KbZ1. However, the double ellipsoid source improves the prediction of both the time at which the peak temperature is reached and the cooling part of the profile.

Using varying thermal properties does not give temperatures closer to the measurement values, but the variations it predicts are closer to the measurement values. Therefore, this model is better to predict the peak temperature. However, none of the models exactly matches the recorded temperature profile. It is possible that the thermocouple was not exactly positioned where it was

assumed to be. Also, a surge in WFS occurs when the electrode enters this zone of the weld (Appendix D).

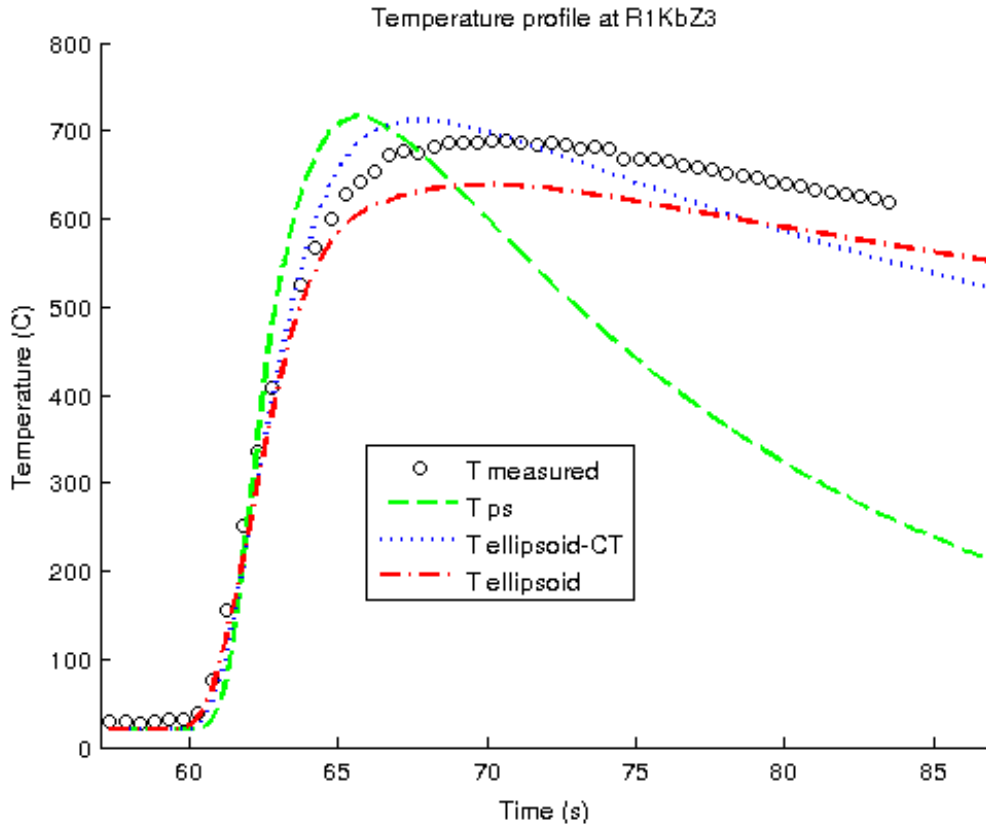


Figure 5.3: Experimental temperature profile for R1KbZ3 along with temperature profiles generated by a concentrated heat source (green), a double ellipsoid source with constant properties (blue) and a double ellipsoid source with varying thermal properties (red).

5.2.3. R2KbZ1:

The temperature profiles compared here are reported in Figure 5.4.

The heating part of the curve is predicted well by all three models. The best fit is the model using a double ellipsoid heat source and varying thermal properties.

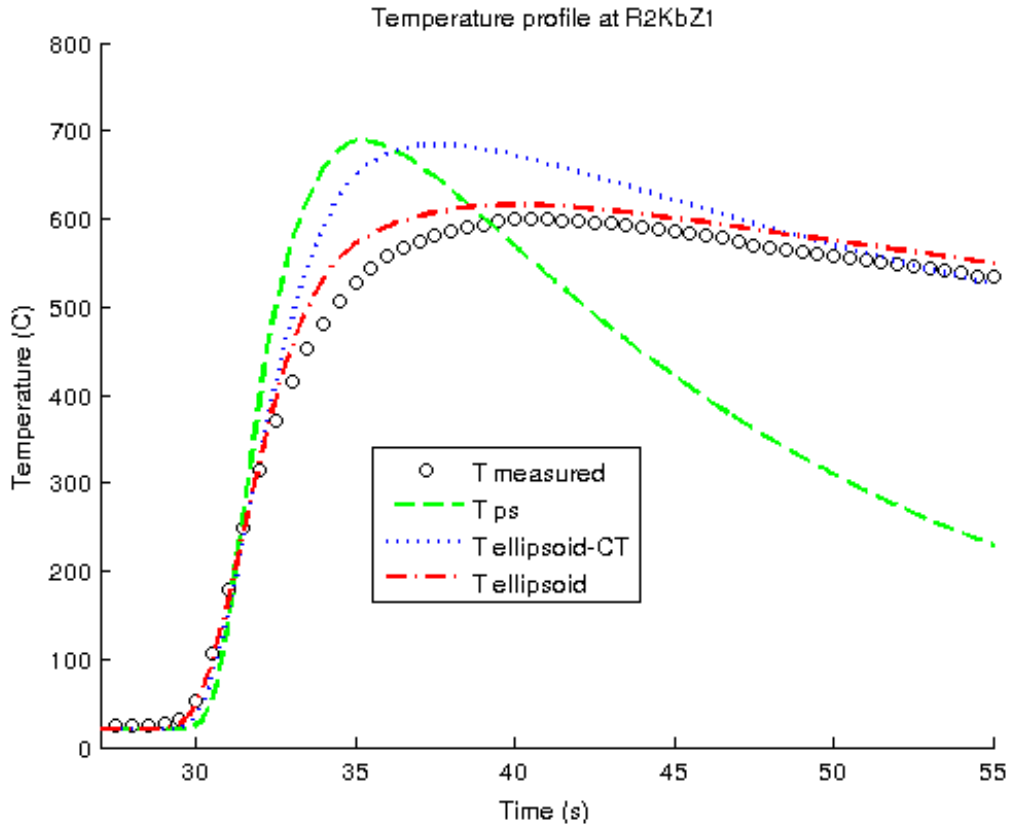


Figure 5.4: Experimental temperature profile for R2KbZ1 along with temperature profiles generated by a concentrated heat source (green), a double ellipsoid source with constant properties (blue) and a double ellipsoid source with varying thermal properties (red).

5.2.4. R2KbZ2:

The various temperature profiles considered are reported in Figure 5.5.

The three models can predict the heating portion. The double ellipsoid approach also predicts the cooling phase and the peak time. Taking into account variation in the thermal properties with the temperature improves the prediction of both the peak temperature and the cooling portion.

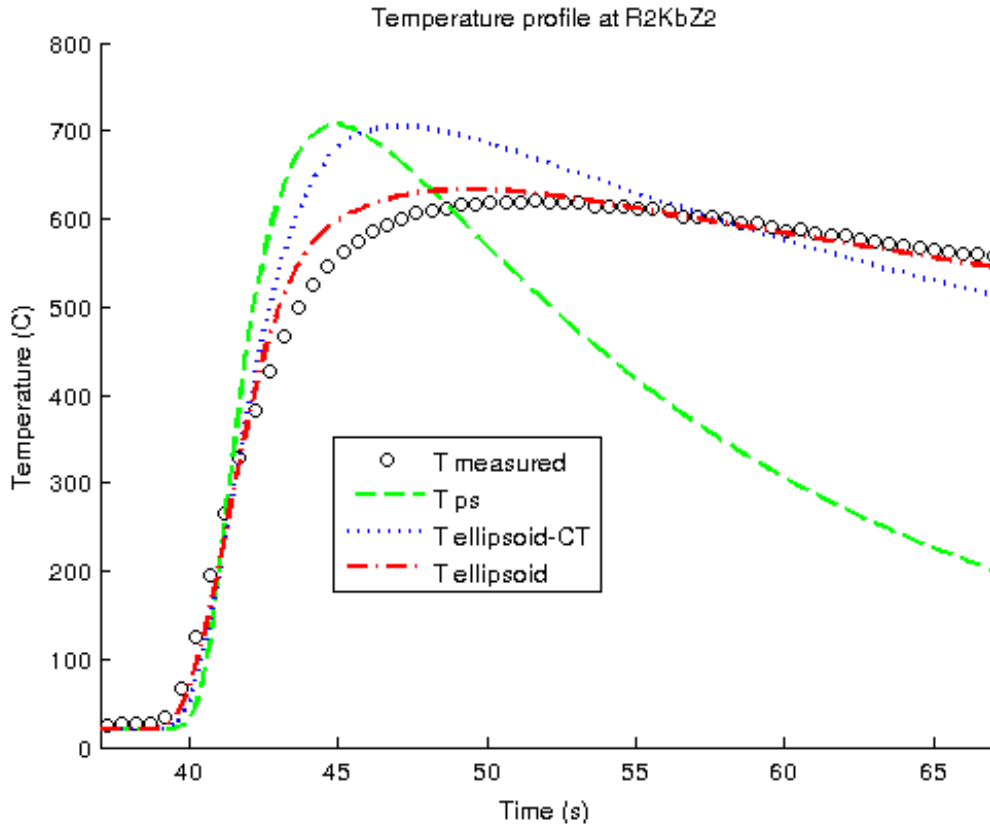


Figure 5.5: Experimental temperature profile for R2KbZ2 along with temperature profiles generated by a concentrated heat source (green), a double ellipsoid source with constant properties (blue) and a double ellipsoid with varying thermal properties (red).

5.2.5. R2KaZ1:

The thermocouple considered here is closer to the fusion line than the ones discussed previously. The temperature profiles are available in Figure 5.6.

The point source does not predict the measured temperature profile well even for the heating part, where it predicts a steeper increase in temperature.

The double ellipsoid approach improves the prediction for both the heating and the cooling parts. Accounting for variations in the thermal properties with temperature improves the prediction of the cooling rate, but does not improve the prediction of the temperature itself. None of the three models predicts the peak temperature correctly. It is possible that the thermocouple was not placed exactly at the bottom of the hole. This can explain the differences.

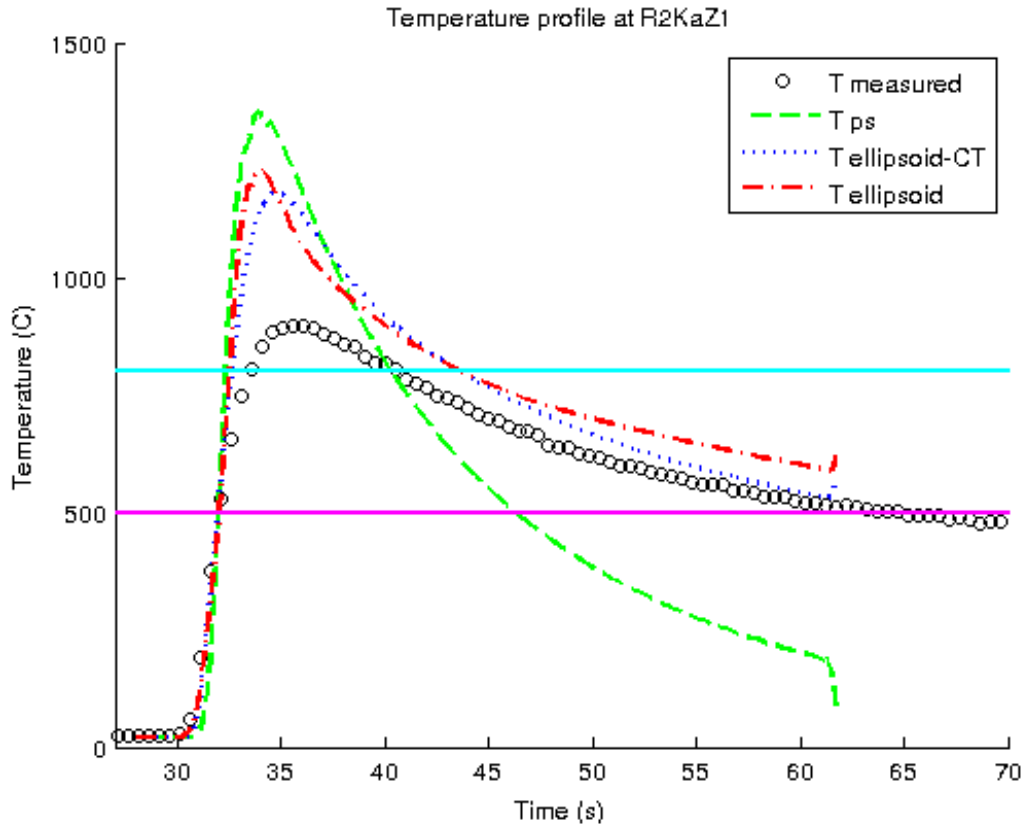


Figure 5.6: Experimental temperature profile for R2KaZ1 along with temperature profiles generated by a concentrated heat source (green), a double ellipsoid source with constant properties (blue) and a double ellipsoid source with varying thermal properties (red). The cyan line corresponds to 800°C the magenta one corresponds to 500°C.

Among the interesting feature that a model can yield there is the $t_{8/5}$ which corresponds to the time that a point takes to go from 800°C to 500°C. To calculate this time Rosenthal's solution is often used. Two equations are often used to work out this parameters, one is for thick plates the second one is for thin plates. They are reported in [60] and give around 8 s for a thick plate and around 36 s for a thin plate. For R2KaZ1 the $t_{8/5}$ was measured at 23 s which is really different from the one calculated based on Rosenthal's solution. The plate was 1.34 cm thick. The point source model gives 6 s which is close to the one calculated for thick plates. For the other two models the time at which 500°C was reached was computed using linear interpolation beginning at the end of the curve. This gave a $t_{8/5}$ of 23 s for the model with a double ellipsoid heat source and constant thermal properties and 29 s for the one which use a double ellipsoid heat source,

varying thermal properties and considers phase changes. Therefore the models which use double ellipsoid heat source give $t_{8/5}$ that are closer to the reality than the equations based on Rosenthal's solution.

5.2.6. R2KaZ2:

The temperature profiles studied here are available in Figure 5.7. The number of points per second represented was multiplied by five. A break is present in the data and is indicated on the figure. The curve is not differentiable at the break point. This is not physical. This means that something unexpected happened. The break may be due to slight movement of the thermocouple, which may have broken free from the spot-weld but still remained close to its initial position.

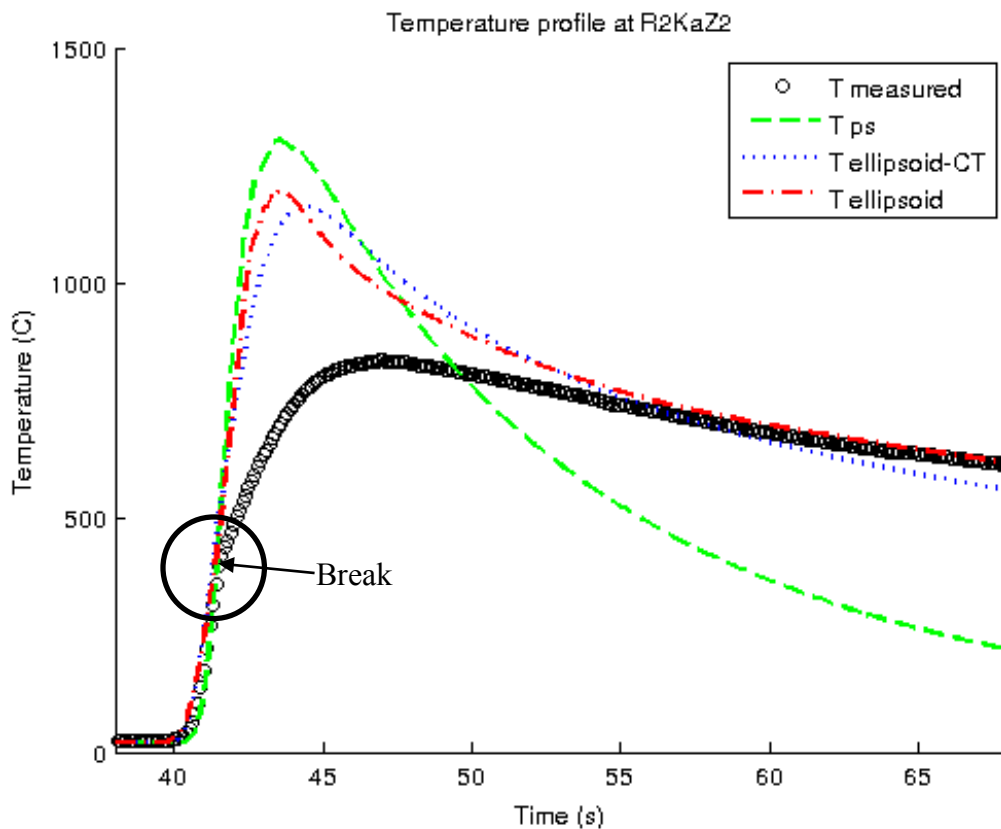


Figure 5.7: Experimental temperature profile for R2KaZ2 along with temperature profiles generated by a concentrated heat source (green), a double ellipsoid source with constant properties (blue) and a double ellipsoid with varying thermal properties (red).

The three temperature profiles generated by simulation follow the heating part up to the break in the curve. Then the same remarks as for the previous Ka thermocouple can be drawn, except that the cooling phase is very well predicted by the simulation using a double ellipsoid heat source with varying thermal properties.

5.2.7. Conclusions:

The comparisons between the measurements done and the simulations with a point source, a double ellipsoid source and a double ellipsoid source with varying thermal properties are reported in Table 5.2. Three symbols are used to describe the accuracy of the models. These are:

- - : the model does not match the measured data at all.
- + : the model shows variations and temperatures that are comparable with measurements.
- ++ : the model gives results that are quite close to the measurements.

Table 5.2: Strengths and weaknesses of the three models compared with measurements.

Model	Heating		Peak position		Peak temperature		Cooling	
	Kb	Ka	Kb	Ka	Kb	Ka	Kb	Ka
Point source	+	-	-	-	-	-	-	-
Double ellipsoid	+	+	+	+	-	-	+	+
Double ellipsoid varying properties	++	+	++	-	++	-	++	+

The positions of the different thermocouples were determined by measurements done on cross-sections taken assuming that the thermocouples were spot-welded at the end of the hole. It is possible that the thermocouples were not precisely in the assumed positions.

Also the $t_{8/5}$ was better predicted by the models using a double ellipsoid heat source.

5.3. Sensitivity analysis:

First, the sensitivity of both the density and the specific heat is studied. Then the sensitivity of the thermal conductivity is discussed. After that, the parameter f_r from the double ellipsoid model is studied. This is followed by the study of the mixed boundary condition coefficient. The effect of the uncertainty on the thermocouple placement is also investigated through two examples. Finally, the conclusions are presented.

The goal is to determine which parameters affect the temperature profiles and among these which ones are the most important. The approach chosen is to report the scaled sensitivity coefficient (Equation 5.1) [61] throughout the geometry. In this expression, θ refers to a parameter and θ_0 to the nominal value used for the simulations. The expression of the scaled sensitivity coefficient is reported in Equation (5.1). The derivative is calculated numerically using Equation (5.2). The value of the offset “ h ” is determined using Equation (5.3).

$$T_\theta = \theta_0 \frac{\partial T}{\partial \theta} \quad (5.1)$$

$$\frac{\partial T}{\partial \theta} = \frac{\Delta T}{\Delta \theta} = \frac{T(\theta_0 + h) - T(\theta_0 - h)}{2h} \quad (5.2)$$

$$h = 0.05 \times \theta_0 \quad (5.3)$$

According to Section 5.2, the best model is the one with a double ellipsoid heat source with varying thermal properties. However, the model which used a double ellipsoid source and constant thermal properties gives comparable results shows roughly the same trend as the one which uses varying thermal properties. Due to the increased computational time induced by using varying thermal properties, it was decided to carry out the sensitivity analysis on the model which uses a double ellipsoid source and constant thermal properties.

5.3.1. Density and specific heat:

Density is one of the three thermal properties which has been varied with temperature. However, since density was varied at the same time as the other parameters its influence could not be isolated. The density and the specific heat appear in the same term in the heat equation. The density only appears because the weight specific heat is used. Therefore, a disturbance applied on either of those parameters will have the same effect on the temperature profile. This is also witnessed when the scaled sensitivity parameters are calculated. This means the model gives coherent results.

Therefore, only the distribution of the scaled sensitivity parameter for the density is reported here. This distribution is available in Figure 5.8. For better legibility, the color range in the figure is cropped at -700 K and 0 K. The minimum value of the scaled sensitivity coefficient is -2395 K, and the maximum is 0 K. The scaled sensitivity coefficient is significantly different from 0 K; therefore the density and the specific heat are sensitive parameters. The negative sign of the scaled sensitivity parameters means that an increase in either the density or the specific heat will reduce the temperature predicted by the model. Therefore, if the formation of a phase is not taken into account at high temperature, the model may overestimate the temperature at the location where the temperature would allow for this phase to form. This can explain some of the discrepancies between the predicted and the measured temperatures for the Ka thermocouples.

An interesting feature of note is the evolution of the scaled sensitivity parameter throughout the geometry. This evolution is not isotropic. It also does not follow a simple pattern like a paraboloid shape. This means that the sensitivity for the density and the specific heat is not the same everywhere. This is important when assessing the reliability of the data from modelling.

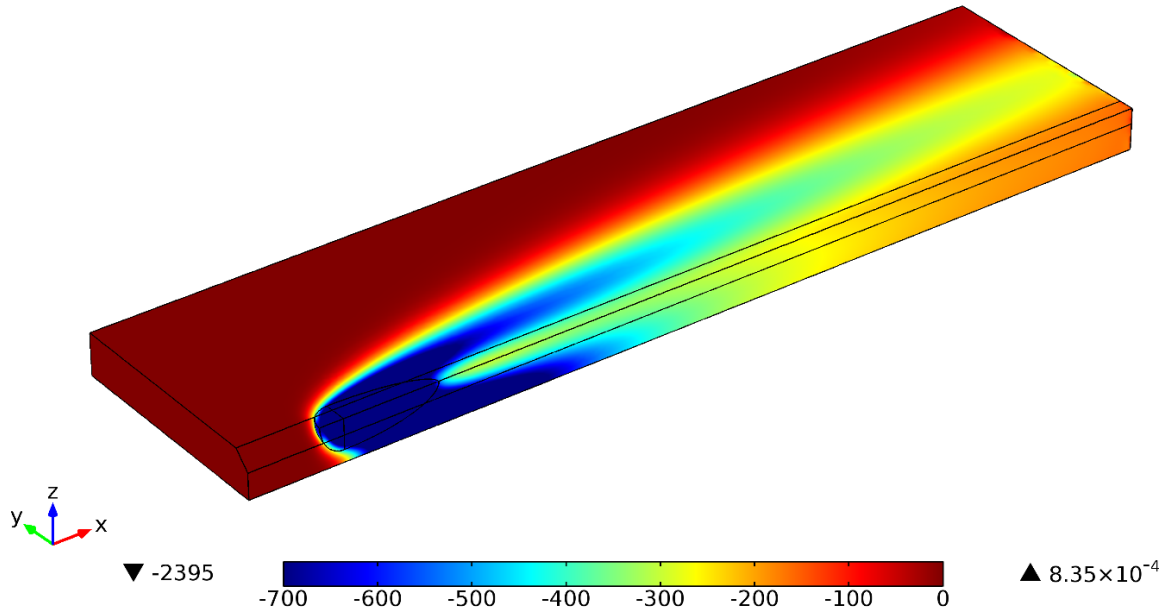


Figure 5.8: Distribution of the scaled sensitivity coefficient for density.

5.3.2. Thermal conductivity:

The thermal conductivity is one of the major parameters affecting the temperature profile in heat transfer. The distribution of the scaled sensitivity coefficient for the thermal conductivity is reported in Figure 5.9. For clarity the color range in the figure is cropped at -700 K and 200 K. The minimum value of the scaled sensitivity coefficient is -2633 K and the maximum is 508 K. One of the benefits of using scaled sensitivity coefficients is the fact that the sensitivity of different coefficients is directly comparable. Therefore, looking at both the range of variation and the maximum values for the density and the thermal conductivity, it is possible to conclude that the thermal conductivity is more sensitive. The distribution of the scaled sensitivity coefficient is also different than the one for the density. This can be explained by the fact that the density and the specific heat represent obstacles for heat diffusion while thermal conductivity quantifies how well the material conducts heats. Therefore, these parameters complement each other and this is best described by the diffusivity. However, the diffusivity is only usable when constant properties are considered.

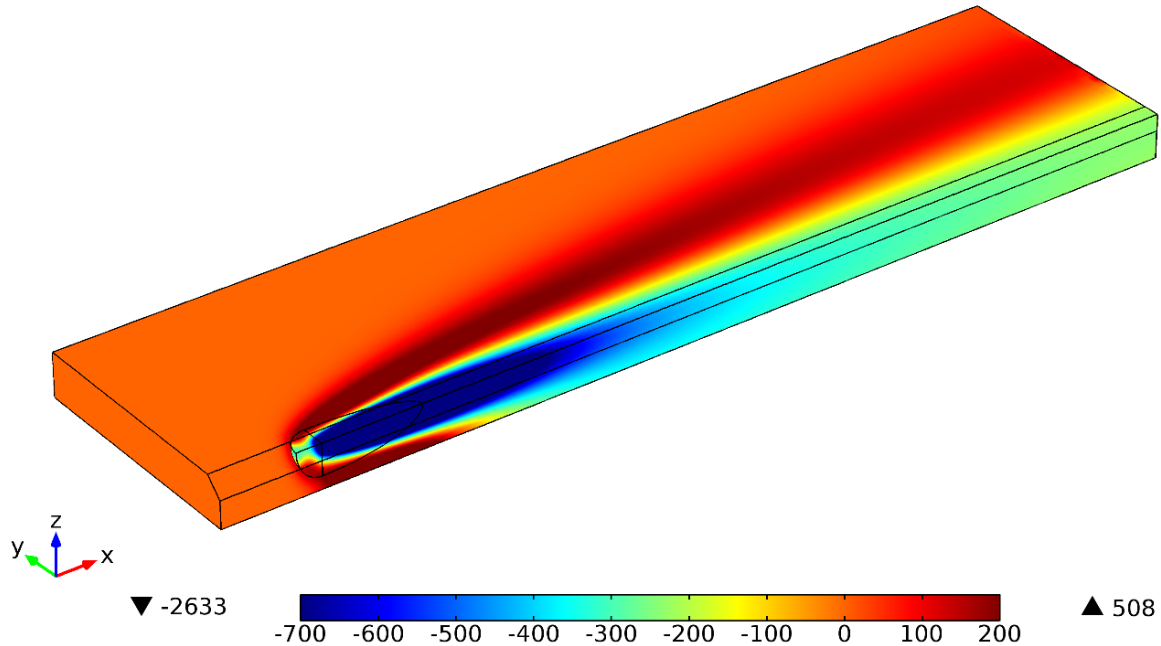


Figure 5.9: Distribution of the scaled sensitivity coefficient for thermal conductivity.

5.3.3. F_f parameter:

In the double ellipsoid model a parameter is used to partition the heat in the two ellipsoids. This parameter is f_f . The distribution of the scaled sensitivity coefficient for the f_f coefficient is reported in Figure 5.10. For clarity the color range in the figure is cropped at -100 K and 100 K. The minimum value of the scaled sensitivity coefficient is -413 K and the maximum is 2845 K.

The maxima are comparable to the ones for the scaled sensitivity coefficient of density and thermal conductivity. However, looking at Figure 5.10 the absolute values of the scaled sensitivity coefficient above 100 is only located close to the source. Therefore, this parameter can be considered sensitive. However, the volume over which it significantly impacts the temperature profile is narrower than for the thermal conductivity and the density or the specific heat. Even more than for the other parameters studied, the position of the temperature profile is important.

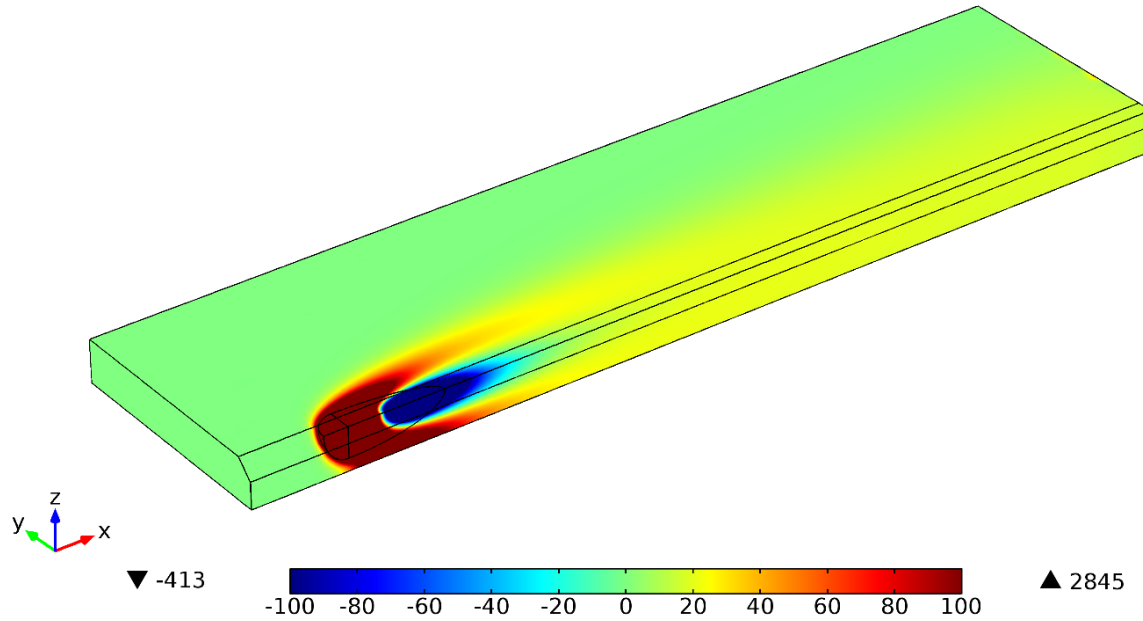


Figure 5.10: Distribution of the scaled sensitivity coefficient for the f_f coefficient in the double ellipsoid source.

5.3.4. Mixed boundary condition coefficient:

The boundary conditions are necessary and the data available to assess them come from correlations. Someone may wonder whether it is of interest to get better data. That is why the sensitivity of the mixed boundary coefficient is studied (Equation (3.17)). Since this coefficient depends on temperature, it was decided to multiply the coefficient presented in Equation (3.18) by either 1.05 or 0.95 for the sensitivity analysis, instead of adding a fixed quantity.

The distribution of the scaled sensitivity coefficient for the mixed boundary condition coefficient is available in Figure 5.11. For clarity the color range in the figure is cropped at -30 K and 0 K. The minimum value of the scaled sensitivity coefficient is -72.1 K and the maximum is 160 K. The evolution of the scaled sensitivity coefficient does not show anything surprising. The range of values taken for this coefficient is significantly smaller than for the f_f parameter, the thermal conductivity and the density or the specific heat. Therefore, it is, among the parameters studied, the least sensitive.

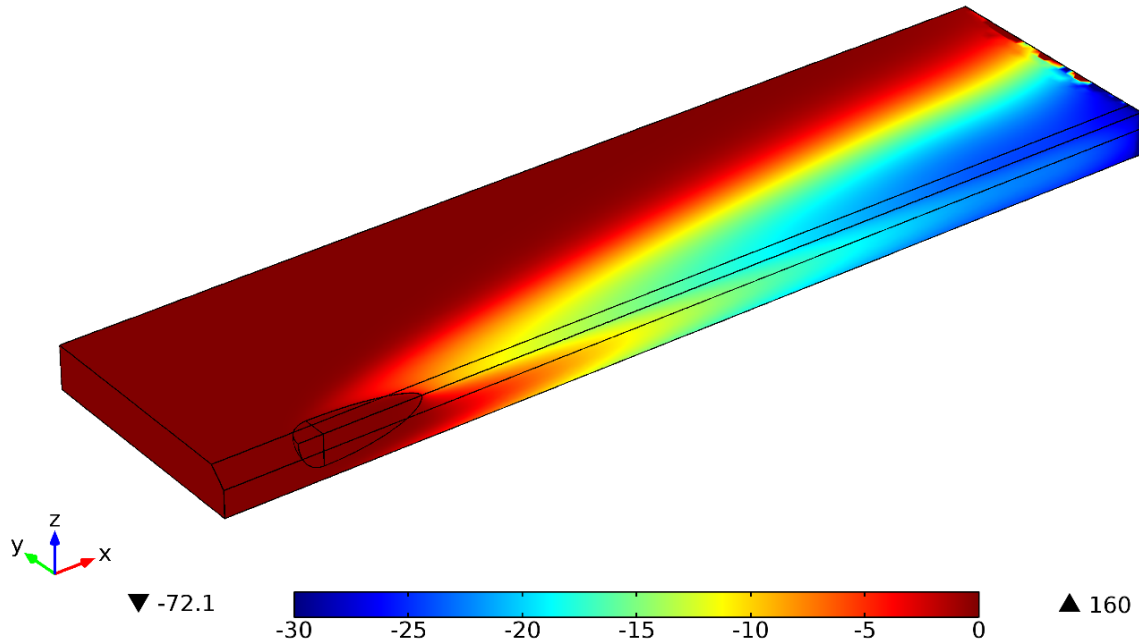


Figure 5.11: Distribution of the scaled sensitivity coefficient for the mixed boundary coefficient.

5.3.5. Effects of the uncertainties on the location of the thermocouples:

One of the major uncertainties in the comparisons carried out in Section 5.2 is the exact position of the thermocouple. The importance of the location of the thermocouple is studied for two cases. These cases correspond to thermocouple R2KbZ1, and thermocouple R2KaZ1 (see Section 4.2). The reason why these two thermocouples were chosen is that they are located at different distances from the centre of the plate.

Here scaled sensitivity coefficients are not used. Instead it was deemed more interesting to report the measured temperature with the results given by the simulation at both the location that was specified beforehand when the experiments were set up and the location measured afterward on the cross-sections.

First, the case of thermocouple R2KbZ1 is studied. The temperature measured by the thermocouple is reported on Figure 5.12 as black circles. Also two temperature profiles obtained by simulation are reported as a blue and a red curve. The reference simulation used a double ellipsoid source, varying thermal properties and phase changes. To obtain the blue curve the thermocouple was assumed to be where it was specified to be in Figure 4.2. To obtain the red one the thermocouple

was assumed to be at the measured location. Both the nominal and measured locations of R2KbZ1 are reported in Table 5.1.

The difference in percent between the two locations studied is calculated using Equation (5.4) for each direction, “z” and “y” (see Section 5.1). For R2KbZ1 the differences in percent between the two locations are of 0.6% in the depth and 7% in the “y” direction. Therefore, the two locations are relatively close. The maximum temperature of the red curve is 616°C and 588°C for the blue one. The difference is 4.6% and the shape of the two temperature profiles are similar. Therefore for R2KbZ1 the uncertainty on the thermocouple location is not a problem

$$Diff\% = 200 \cdot \left| \frac{D_{specified} - D_{Measured}}{D_{specified} + D_{Measured}} \right| \quad (5.4)$$

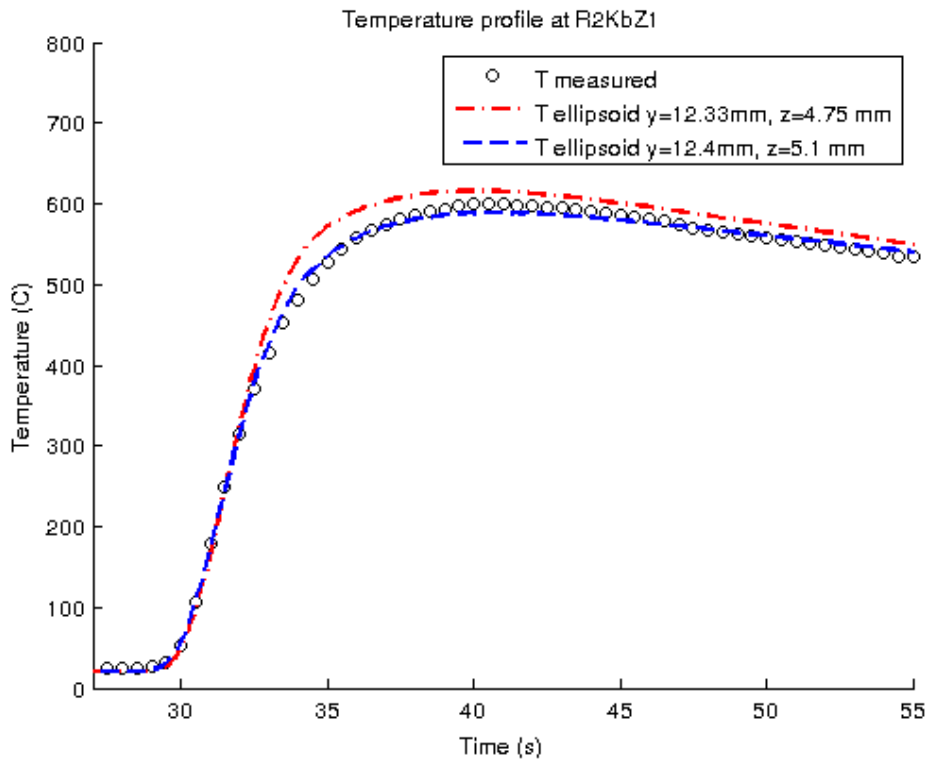


Figure 5.12: Temperature profile measured by R2KbZ1 (black circles). The other two curves are the profiles extracted assuming two different positions for the thermocouple. The thermocouple was assumed to be at the specified location for the blue curve while for the red curve its position was determined by measurements.

Then it is interesting to see what happens for R2KaZ1 which is closer to the centre of the plate. As before the black circles correspond to the measured temperature profile while the blue curve and red curves correspond to the temperature profile extracted from simulation at the expected location and the measured one. Both the nominal and measured location of R2KaZ1 are reported in Table 5.1.

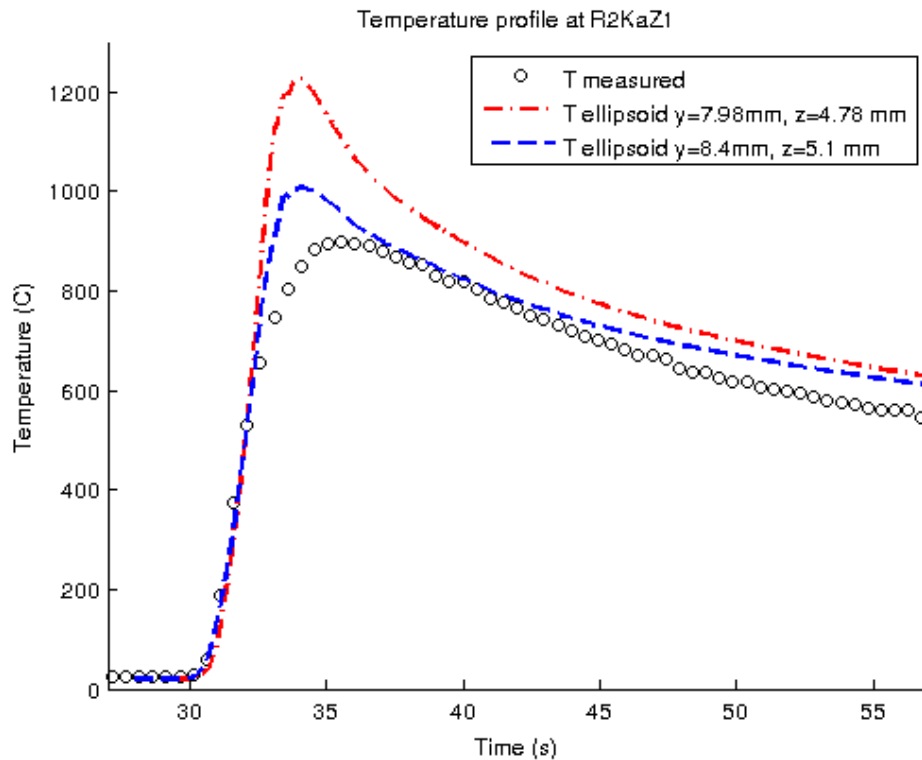


Figure 5.13: Temperature profile measured by R2KaZ1 (black circles). The other two curves are the profiles extracted assuming two different positions for the thermocouple. The thermocouple was assumed to be at the specified location for the blue curve while for the red curve its position was determined by measurements.

The difference in percent between the specified and the measured positions is 6% in depth and 5% in the “y” direction (see Section 5.1). Therefore, the difference is the same for the depth as for R2KbZ1 and is larger in the “y” direction. However, even if the deviation is larger than for R2KbZ1 it is still small; a 5% of error in placement is easy to obtain. The maximum temperature reached by the red curve is 1226°C while it is 1008°C for the blue one. This is a difference of 19.5%. The difference in maximum temperature is significant while the difference in location is

not. The maximal temperature is used to assess the size of the HAZ for instance. It is therefore, an important data to have. Also the shape of the temperature profile change drastically between the two locations. One has almost the same shape as the measurement while the other one is far from it. This shows that at locations close to R2KaZ1 the temperature profile is really sensitive to the location at which it is recorded.

Considering these two examples it is possible to say that the temperature profile is not sensitive to the exact placement of the thermocouple when the measurement is taken away from the source (here 12.4 mm at a depth of 5.1 mm). However, as the measurements are taken closer to the source the temperature profile becomes more sensitive to the location at which it was taken. This is logical but one needs to take care as the sensitivity increases really fast, it does not increase linearly as the measurements are taken closer to the source and even a difference of 5% can lead to drastic change in the temperature profile.

5.3.6. Conclusions on the sensitivity of the studied parameters:

The sensitivity analysis showed that not all parameters have the same importance on the temperature profiles. In increasing order of importance the parameters can be sorted as follows:

- The constant coefficient in the expression of h_{comb} .
- The f_f parameter.
- Density and specific heat.
- Thermal conductivity.

Density and specific heat are multiplied in the heat equation. Therefore, even if they are less sensitive than the thermal conductivity they must be looked at closely as they are more prone to error propagation. The errors in density will be multiplied by the ones for specific heat. The f_f parameter is not as significant as the thermal parameters, but it should be studied as too few studies were conducted [62] on it.

In addition the temperature profile is sensitive to the location of the thermocouple which is recording it when it is close to the source and even small deviations in the placement can lead to big errors.

5.4. Conclusions:

Among the three models that were compared with the measured temperatures, i.e., the concentrated heat source, the double ellipsoid source with constant properties and the double ellipsoid source with varying properties, the one that fits the best is the double ellipsoid model with varying thermal properties. If using varying thermal properties is too cumbersome, it has been noticed that the model using a double ellipsoid source and constant thermal properties gives results that are compatible with the measurements. Care must be taken when using the point source model because deviations from measurement values is significant and it only gives meaningful results for the heating part of the temperature profiles. When the thermocouples were close to the source no model predicted the peak temperature correctly. However, the double ellipsoid model with varying thermal properties still gave results close to the measurements for the heating and cooling part.

Also the models using double ellipsoid predicts the $t_{8/5}$ better than the equations based on Rosenthal's solution.

Several explanations can be put forward to explain the differences between the experimental results and the simulations. The main suspected source of errors is the uncertainty in the actual placement of the thermocouples. They were spot-welded at the end of their holes, but the exact location is unknown.

To determine which parameters are critical for the simulations and to also further investigate errors, a sensitivity analysis was performed. Based on the comparisons, it was decided to perform the sensitivity analysis on the model using a double ellipsoid heat source and constant thermal properties. This analysis was performed on the density, the specific heat, the thermal conductivity, the f_r parameter used in Goldak's approach and the mixed boundary coefficient. The most sensitive parameters are the thermal properties⁸. The next most sensitive parameter, f_r , appears in the formulation of the double ellipsoid model. Only one paper [62] was found discussing this parameter, while a lot more work has been done on thermal properties. The sensitivity of the mixed boundary condition is minor especially considering the sensitivity of the other parameters studied here. Therefore, getting precise data on the boundary conditions is not crucial.

⁸ The density and the specific heat are exactly the same for the sensitivity analysis.

Knowing the exact position of the thermocouples is crucial when measurements are done close to the source. When a thermocouple is embedded far away from the source its exact position is not crucial. There is a drastic surge in sensitivity of the temperature profile with respect to the thermocouple location when one tries to take measurements close to the source.

6. Conclusions and future work:

The conclusions drawn from the work presented in this thesis are presented followed by future developments that are worth undertaking.

6.1. Conclusions of this work:

From this study the following were concluded.

1. The results obtained by Rosenthal can be obtained using FEM software.
2. To simulate a point source, it is easier to apply the power on the surface of a hemisphere removed from the surface; this improves the mesh and the results.
3. It is possible to extend Rosenthal's solution to multiple sources and to obtain the same results with FEM software (two sources).
4. To take realistic boundary conditions into account, it is advised to use sources like a double ellipsoid on top of which the surface can be considered as insulated.
5. The results obtained using the double ellipsoid heat source are more realistic and smoother than the ones obtained using a point source.
6. Going from one to two heat sources via a double ellipsoid source gives rise to some problems:
 - a. The surface between the two sources should be considered insulated, but partitioning the geometry to do so makes it more difficult for the software to create a correct mesh and it can produce inverted elements.
 - b. The numerical errors, which can occur when the software is finding a solution, can produce negative temperatures⁹ which makes it impossible to evaluate the mixed boundary coefficient used.
 - c. The parameters of the heat source are determined by bead shape measurement, but when two sources are considered it is impossible to determine the parameters of the heat sources by bead shape measurements only. Therefore, only twin-wire SAW can really be modelled that way as both sources are the same.
7. The parameters chosen to produce the weld studied in this thesis are correct and produce a good weld.

⁹ The negative temperature are not physically meaningful and are numerical errors.

8. Machining of the plate does not disturb the weld.
9. The use of thermocouples at the selected distances disturbs the weld. In particular, the weld tends to be slanted and attracted toward the thermocouples.
10. Even if the weld reinforcement was erratic, the cross-section images showed that the data collected by some thermocouples was still usable.
11. At a distance of around 12 mm from the center of the plate:
 - a. The point source describes correctly the heating phase only.
 - b. The double ellipsoid source with constant properties give results closer to reality, but tends to overestimate the peak temperature and the cooling rate.
 - c. The double ellipsoid with varying thermal properties provides the best fit and gives results which are close to the measurement results.
12. At a distance of around 8.4 mm from the center of the plate:
 - a. The point source is not reliable.
 - b. The double ellipsoid with constant temperature gives better results, but completely misses the peak in the temperature profile and overestimates the cooling rate.
 - c. The double ellipsoid with varying thermal properties give results which are close for the heating portion and the cooling portion, but misses completely the peak of the temperature profile.
13. The use of a double ellipsoid heat source improves the prediction of the $t_{8/5}$.
14. The thermal properties are the most sensitive.
15. The parameter f_r used in Goldak's approach is sensitive and there is a lack of study focusing on it.
16. The Neumann boundary conditions are not sensitive parameters.
17. Knowing the exact position of a thermocouple is crucial when measurements are done close to the heat source.

6.2. Future developments:

In Goldak's approach the parameters of the heat source are determined from the bead shape parameters by measurement on the cross-sections. This is not possible for tandem SAW as the bead shape is the result of the action of two sources. The development of a method to determine the parameters of the double ellipsoid heat sources which should be used to model a tandem SAW process would be a big improvement in the simulation of these processes.

In the variation of thermal conductivity with temperature, a parameter was used to simulate convective mixing in the liquid. This parameter was considered constant and its value was kept low to avoid having a step in the thermal data, which would have a similar effect on the simulation as a discontinuity. However, it is argued that this parameter should not be kept constant [63] and also the value used was determined for the casting of steel. Therefore, the effect of a change in this parameter should be studied in this context. Also, this could be done by taking the movement in the weld pool into account.

To improve the experiments, similar tests to the ones presented here should be done but with thermocouples embedded further away from the weld. If bead inconsistency still happens the set up itself should be checked to see if there are any problems with it, like bad contact between the plate to be welded and the copper plate used as a ground. If the weld still becomes erratic then the use of a laptop running on a battery may be a problem and the use of a desktop computer with an insulated transformer should be considered.

It would be of interest to see the change in the temperature profile when going from a single electrode to a double electrode welding process to a process with two electrodes with power and one without.

To expand the validity of this work, the experiments and the comparison done here should be repeated for different conditions. The higher the HI the stronger the electromagnetic fields are. Therefore, the experiments should be repeated with different HI to see if this has an effect on the quality of the weld and on the comparison with the simulations. One also may want to redo the experiments with other steels and different thicknesses. This could also be used to further prove that the use of a double ellipsoid heat source in modelling improves the prediction of the $t_{8/5}$ when compared to models and solutions based on a point heat source.

The sensitivity analysis unveiled the sensitivity of the f_r parameter used in Goldak's double ellipsoid model. Therefore, better ways to determine this parameter should be used.

When temperature measurements are taken close to the heat source in SAW one should know precisely where the thermocouples were embedded. This also means that one should ensure that the thermocouples do not move during the experiment. Therefore, other experiments with the same parameters used here and some others, as discussed before, should be done but some compressive spring load should be put in the thermocouple to ascertain that they stay at the bottom of their holes. Also, more a powerful spot-welder should be used but one should take care that the spot-welder is not too powerful to avoid melting the bead of the thermocouple too much.

References:

- [1] The James F. Lincoln Arc Welding Foundation, "Historical development of fusion joining," in *The Procedure Handbook of Arc Welding*, 14th ed. Cleveland, OH: The James F. Lincoln Arc Welding Foundation, 2000, ch. 1, sec. 1, pp. 1-10.
- [2] A. F. Manz, "Tracing Our Welding Genealogy," *Weld. J.*, vol. 93, pp. 72-75, Jun. 2014.
- [3] R. Cazes, "Soudage à l'arc soudage sous flux en poudre," Tech. Ing., Saint-Denis, France, Tech. Rep. b616P2, 1990.
- [4] The James F. Lincoln Arc Welding Foundation, "Welding carbon and low-alloy steels with the submerged-arc process," in *The Procedure Handbook of Arc Welding*, 14th ed., Cleveland, OH: The James F. Lincoln Arc Welding Foundation, 2000, ch. 6, sec. 3, pp. 1-72.
- [5] H. K. Narang, M. M. Mahapatra, P. K. Jha and I. Mukherjee, "Modelling and predicting the effects of submerger arc weldment process parameters on weldment characteristics and shape profiles," *Proc. Inst. Mech., Part B*, vol. 226, no.7, pp. 1230-1240, Jul. 2012.
- [6] W. D. Callister, "Applications and processing of metal alloys," in *Materials Science and Engineering an Introduction*, 6th ed. Hoboken, NJ: John Wiley & Sons, 2003, ch. 11, pp. 332-382.
- [7] S. Kyriakides and E. Corona, "Pipe and tube manufacturing processes," in *Mechanics of Offshore Pipelines, Volume I: Buckling and Collapse*, 1st ed. Amsterdam, Netherlands: Elsevier, 2007, ch. 3, pp. 59-88.
- [8] J. A. Goldak and M. Akhlaghi, "Introduction," in *Computational Welding Mechanics*. New York, NY, USA: Springer, 2005, ch. 1, pp. 1-15. [Online]. Available: <http://link.springer.com/book/10.1007%2Fb101137>
- [9] J. H. Argyris, J. Szimmat, and K. J. Willam, "Computational aspects of welding stress analysis," *Comput. Meth. Appl. Mech. Eng.*, vol. 33, pp. 635-665, Sep. 1982. [Online]. Available: <http://www.sciencedirect.com/science/article/pii/0045782582901268>
- [10] J. A. Goldak and M. Akhlaghi, "Computer simulation of welding processes," in *Computational Welding Mechanics*. New York, NY, USA: Springer, 2005, ch. 2, pp. 16-69. [Online]. Available: <http://link.springer.com/book/10.1007%2Fb101137>
- [11] J. T. Pepin, "Effects of Submerged Arc Weld (SAW) Parameters on Bead Geometry and Notch-Toughness for X70 and X80 Linepipe Steels," M.S. thesis, Chem. and Mat. Eng. Dept., Univ. Alberta, Edmonton, Canada, 2009.

- [12] American Welding Society A2 Committee on Definitions and symbols, "Terms and definitions," in *Standard Welding Terms and Definitions*, 12th ed. Miami, FL, USA: American Welding Society, 2009, ch. 4, pp. 2-49.
- [13] P. T. Houldcroft, "Origins and development," in *Submerged-Arc Welding*, 2nd ed. Cambridge, England: Woodhead Publishing, 1989, ch. 1, pp. 9-18. [Online]. Available: <http://www.sciencedirect.com/science/article/pii/B9781855730021500044>.
- [14] C. L. Jenney and A. O'Brien, "Survey of joining, cutting, and allied processes," in *Welding Handbook, Volume 1 - Welding Science and Technology*, 9th ed. Miami, FL, USA: American Welding Society, 2001, ch. 1, pp. 1-50.
- [15] Canadian Centre for Occupational Health and Safety. *Welding - Fumes and Gases*. (2012) [Online]. Available: http://ccohs.ca/oshanswers/safety_haz/welding/fumes.html, Accessed on: Apr. 03, 2016.
- [16] N. Christensen, V. Davies, and K. Gjermundsen, "Distribution of Temperatures in Arc Welding," *Br. Weld. J.*, vol. 12, pp. 54-75, Feb. 1965.
- [17] L. E. Allgood, "Submerged arc welding." in *ASM Handbook, Volume 06A - Welding Fundamentals and Processes*, T. J. Lienert, S. S. S. Babu, A. A. Thomas and L. Viola, Eds. Materials Park, OH, USA: ASM International, 2011, ch. 35, pp. 335-343.
- [18] D. V. Kiran, B. Basu, and A. De, "Influence of process variables on weld bead quality in two wire tandem submerged arc welding of HSLA steel," *J. Mater. Process. Technol.*, vol. 212, no. 10, pp. 2041-2050, Oct. 2012.
- [19] R. Cazes, "Soudage à l'arc," Tech. Ing., Saint-Denis, France, Tech. Rep. b7730, 1995.
- [20] ASM Committee on Submerged Arc Welding of Steel, "Submerged-arc welding," in *METALS HANDBOOK Welding and Brazing*, 8th ed., ASM Handbook Committee, Ed. Materials Park, OH : ASM International, 1971, pp. 46-77.
- [21] D. V. Kiran and S.-J. Na, "Numerical Studies on Submerged Arc Welding Process," *Journal of Welding and Joining*, vol. 32, no. 4, pp. 339-347, Aug. 2014.
- [22] K. Weman, "Arc welding: An overview," in *Welding Processes Handbook*, 2nd ed. Cambridge, England: Woodhead Publishing, 2012, ch. 4, pp. 31-50.
- [23] R. S. Chandel and L. Malik, "Relationship between Wire Feed Speed and Submerged-Arc-Welding Parameters," in *Proc. Int. Conf. Welding for Challenging Environments*, (Toronto, Ontario, Canada) , 1986, pp. 245-251.
- [24] S. Jindal, R. Chhibber, and N. P. Mehta, "Effect of welding parameters on bead profile, microhardness and H₂ content in submerged arc welding of high-strength low-alloy steel," *Proc. Inst. Mech., Part B*, vol. 228, no. 1, pp. 82-94, Jan. 2014.

- [25] D. V. Kiran, B. Basu, A. K. Shah, S. Mishra, and A. De. "Probing influence of welding current on weld quality in two wire tandem submerged arc welding of HSLA steel," *Sci. Technol. Weld. Joining*, vol. 15, no. 2, pp. 111-116, 2010. [Online]. Available: <http://dx.doi.org/10.1179/136217109X12518083193432>
- [26] L. J. Yang, R. S. Chandel, and M. J. Bibby, "The effects of process variables on the bead width of submerged-arc weld deposits," *J. Mater. Process. Technol.*, vol. 29, no. 1-3, pp. 133-144, Jan. 1992.
- [27] R. V. Rao and V. D. Kalyankar, "Experimental investigation on submerge arc welding of Cr-Mo-V steel," *Int. J. Adv. Manuf. Technol.*, vol. 69, no. 1-4, pp. 93-106, Oct. 2013.
- [28] S. Shen, I. N. A. Oguocha, and S. Yannacopoulos, "Effect of heat input on weld bead geometry of submerged arc welded ASTM A709 Grade 50 steel joints," *J. Mater. Process. Technol.*, vol. 212, no. 1, pp. 286-294, Jan. 2012.
- [29] D.-W. Cho, W. Song, M.-H. Cho, and S.-J. Na, "Analysis of submerged arc welding process by three-dimensional computational fluid dynamics simulations," *J. Mater. Process. Technol.*, vol. 213, no. 12, pp. 2278-2291, Dec. 2013.
- [30] The James F. Lincoln Arc Welding Foundation, "The submerged arc process," in *The Procedure Handbook of Arc Welding*, 14th ed., Cleveland, OH: The James F. Lincoln Arc Welding Foundation, 2000, ch. 5, sec. 2, pp. 1-7.
- [31] D. V. Kiran, D.-W. Cho, W. H. Song, and S.-J. Na, "Arc behavior in two wire tandem submerged arc welding," *J. Mater. Process. Technol.*, vol. 214, no. 8, pp. 1546-1556, Aug. 2014.
- [32] F. Cardarelli, "Ferrous metals and their alloys," in *Materials Handbook*, 2nd ed., London, England: Springer, 2008, ch. 2, pp. 59-157.
- [33] É. Tocqué and C. Travers, "Pétrole," *Tech. Ing.*, Saint-Denis, France, Tech. Rep. be8520, 2010.
- [34] D. K. Banerjee, "Transportation of heavy oil/bitumen," in *Oil Sands, Heavy Oil and Bitumen - from Recovery to Refinery*, Tulsa, OK, USA: PennWell, 2012, ch. 6, pp. 71-81.
- [35] B. White, "North Slope Gas Pipeline Challenge: 'Goldilocks' Effect Of Permafrost," *Pipe. Gas j.*, vol. 241, no. 1, pp. 54-60, Jan. 2014.
- [36] M. D. Herynk, S. Kyriakides, A. Onoufriou, and H. D. Yun, "Effects of the UOE/UOC pipe manufacturing processes on pipe collapse pressure," *Int. J. Mech. Sci.*, vol. 49, no. 5, pp. 533-553, May 2007.
- [37] D. Rosenthal, "The theory of moving sources of heat and its application to metal treatments," *Trans. A.S.M.E.*, vol. 68, pp. 849-866, Nov. 1946.

- [38] N. D. Malmuth, "Temperature Field of a Moving Point Source with Change of State," *Int. J. Heat Mass Transfer*, vol. 19, no. 4, pp. 349-354, Apr. 1976.
- [39] L. Wenji, L. Liangyu, Y. Jianfeng, L. Haihua, and Y. Lei, "A kind of analytical model of arc welding temperature distribution under varying material properties," *Int. J. Adv. Manuf. Technol.*, vol. 81, no. 5, pp. 1109-1116, Nov. 2015.
- [40] T. W. Eagar and N.-S. Tsai, "Temperature fields produced by traveling distributed heat sources," *Weld. J.*, vol. 62, no. 12, pp. 346-355, Dec. 1983.
- [41] S. K. Jeong and H. S. Cho, "An analytical solution to predict the transient temperature distribution in fillet arc welds," *Weld. J.*, vol. 76, pp. 223-232, Jun. 1997.
- [42] A. Ghosh and S. Chattopadhyaya, "Analytical solution for transient temperature distribution of semi-infinite body subjected to 3-D moving heat source of submerged arc welding process," in *2010 2nd Int. Conf. Mechanical and Electrical Technology*, (Singapore), pp. 733-737.
- [43] A. Ghosh and H. Chattopadhyay, "Mathematical modeling of moving heat source shape for submerged arc welding process," *Int. J. Adv. Manuf. Technol.*, vol. 69, no.9, pp. 2691-2701, Dec. 2013.
- [44] C. Zhangxin, "Elementary Finite Elements," in *Finite Element Methods and their Applications*, Berlin, Germany: Springer, 2005, ch. 1, pp. 1-85. [Online]. Available: <http://link.springer.com/book/10.1007/3-540-28078-2>
- [45] D. G. Pavlou, "An overview of the finite element method," in *Essentials of the Finite Element Method - for Mechanical and Structural Engineers*, London, England: Academic Press, 2015, ch. 1, pp. 1-18. [Online]. Available: <http://www.sciencedirect.com/science/article/pii/B9780128023860000013>
- [46] A. Lecoanet, D. G. Ivey, and H. Henein, "Simulation of the temperature profile during welding with COMSOL multiphysics® software using Rosenthal's approach," in *Proc. 2014 COMSOL Conf. Boston*, (Boston, MA, USA), 2014. [Online]. Available: https://www.comsol.com/paper/download/194353/lecoanet_paper.pdf
- [47] J. Ascough, "A single step finite element analysis of the temperature distribution around a moving laser heat source," *Opt. Lasers Eng.*, vol. 6, no. 3, pp. 137-143, 1985.
- [48] W. Perret, C. Schwenk, and M. Rethmeier, "Comparison of analytical and numerical welding temperature field calculation," *Comput. Mater. Sci.*, vol. 47, no. 4, pp. 1005-1015, Feb. 2010.
- [49] Z. Paley and P. D. Hibbert, "Computation of Temperatures in Actual Weld Design," *Weld. J.*, vol. 54, pp. 385-392, Nov. 1975.
- [50] J. Goldak, A. Chakravarti, and M. Bibby, "A new Finite Element Model for Welding Heat Sources," *Metall. Trans. B*, vol. 15, no. 2, pp. 299-305, Jun. 1984.

- [51] N. Yadaiah and S. Bag, "Development of egg-configuration heat source model in numerical simulation of autogenous fusion welding process," *Int. J. Therm. Sci.*, vol. 86, pp. 125-138, Dec. 2014.
- [52] A. Sharma, N. Arora, and S. R. Gupta, "Investigation into Arc Behavior during Twin-Wire Submerged Arc Welding," *Mater. Manuf. Processes*, vol. 25, no. 8, pp. 873-879, Sep. 2010. [Online]. Available: <http://www.tandfonline.com/doi/pdf/10.1080/15394450902996593>
- [53] D.-W. Cho, D. V. Kiran, W.-H. Song, and S.-J. Na, "Molten pool behavior in the tandem submerged arc welding process," *J. Mater. Process. Technol.*, vol. 214, no. 11, pp. 2233-2247, Nov. 2014.
- [54] A. Degiovanni, "Transmission de l'énergie thermique - conduction," Tech. Ing., Saint-Denis, France, Tech. Rep. be8200, 1990.
- [55] E. Saadjan, "Transfert de chaleur par conduction," in *Les Bases de la Mécanique des Fluides et des Transferts de Chaleur et de Masse pour L'Ingénieur*, 1st ed. Boulogne, France: Les Editions Sapiaientia, 2009, ch. 4, pp. 105-138.
- [56] COMSOL Multiphysics®, "Definitions," in *COMSOL Multiphysics® Reference Manual Version 4.3b*, Stockholm, Sweden: COMSOL AB, 2013, ch. 4, pp. 207-346.
- [57] H. G. Fan, H. L. Tsai, and S. J. Na, "Heat transfer and fluid flow in a partially or fully penetrated weld pool in gas tungsten arc welding," *Int. J. Heat Mass Transfer*, vol. 44, no. 2, pp. 417-428, Aug. 2001.
- [58] E. A. Bonifaz, "Finite element analysis of heat flow in single-pass arc welds," *Weld. J.*, vol. 79, no. 5, pp. 121-125, May. 2000.
- [59] E. Nart and Y. Celik, "A practical approach for simulating submerged arc welding process using FE method," *J. Constr. Steel Res.*, vol. 84, pp. 62-71, May. 2013.
- [60] K. Poorhaydari, B. M. Patchett, and D. G. Ivey, "Estimation of Cooling Rate in the Welding of Plates with Intermediate Thickness," *Weld. J.*, vol. 84, no. 10, pp. 149-155, Oct., 2005.
- [61] K. J. Dowding and B. F. Blackwell, "Sensitivity Analysis for Nonlinear Heat Conduction," *J. Heat Transfer*, vol. 123, no. 1, pp. 1-10, Feb. 2001.
- [62] G. Fu, J. Gu, M. I. Lourenco, M. Duan, and S. F. Estefen, "Parameter determination of double-ellipsoidal heat source model and its application in the multi-pass welding process," *Ships Offshore Struct.*, vol. 10, no. 2, pp. 204-217, 2015. [Online]. Available: <http://dx.doi.org/10.1080/17445302.2014.937059>
- [63] S. Kasap and D. Tonchev, "Thermal properties and thermal analysis: Fundamentals, Experimental Techniques and Applications," in *Springer Handbook of Electronic and Photonic Materials*, S. Kasap and P. Capper, Eds. Boston, MA, USA: Springer, 2007, ch. 19, pp. 385-408.

- [64] S. Manoharan, "Arc welding processes," in *Welding Technology for Engineers*, R. Baldev, V. Shankar, and A. K. Bhaduri, Eds. New Dehli, India: Narosa, 2006, pp. 116-156.
- [65] J. Pepin, H. Henein, D. G. Ivey, and M. Yarmuch, *MANIPULATING THE SAW VOLTAGE AND CURRENT WAVEFORMS TO CONTROL WELDING PRODUCTIVITY AND QUALITY*. Edmonton, AB, Canada: PCL Construction, 2014. [Online]. Available: <http://www.pcl.com/Services-that-Deliver/Industry-Leadership/Leadership-Articles/Documents/Manipulating-the-SAW-Voltage-and-Current-Waveforms.pdf>
- [66] J. Pepin, *et al.*, "Using semipenetration ratio to characterise effects of waveform variables on bead profile and heat affected zone with single electrode submerged arc welding," *Can. Metall. Q.*, vol. 51, no. 3, pp. 284-293, 2012. [Online]. Available: <http://dx.doi.org/10.1179/1879139512Y.0000000018>
- [67] B. A. Ogunnaike, "Regression Analysis," in *Random Phenomena: Fundamentals of Probability and Statistics for Engineers*, Boca Raton, FL, USA: CRC Press, 2010, ch. 16, pp. 643-726.
- [68] D. C. Montgomery and G. C. Runger, "Multiple Linear Regression," in *Applied Statistics and Probability for Engineers*, 5th ed. Hoboken, NJ, USA: Wiley, 2011, ch. 12, pp. 449-512.
- [69] Materials Algorithms Project. *Program MAP_STEEL_THERMAL10*. (2010) [Online]. Available: <http://www.msm.cam.ac.uk/map/steel/programs/thermalmodel10.html>, Accessed on: Mar. 10, 2016.
- [70] M. J. Peet, H. S. Hasan, and H. K. D. H. Bhadeshia, "Prediction of thermal conductivity of steel," *Int. J. Heat Mass Transfer*, vol. 54, no. 11-12, pp. 2602-2608, May 2011.
- [71] D. Ceotto, "Thermal diffusivity, viscosity and prandtl number for molten iron and low carbon steel," *High Temp.*, vol. 51, no. 1, pp. 131-134, Jan. 2013.
- [72] J. Miettinen and S. Louhenkilpi, "Calculation of Thermophysical Properties of Carbon and Low-Alloyed Steels for Modeling of Solidification Processes," *Metall. Mater. Trans. B*, vol. 25, no. 6, pp. 909-916, Dec. 1994.
- [73] J. Miettinen, S. Louhenkilpi, H. Kytönen, and J. Laine, "IDS: Thermodynamic–kinetic–empirical tool for modelling of solidification, microstructure and material properties," *Math. Comput. Simul.*, vol. 80, no. 7, pp. 1536-1550, Mar. 2010.
- [74] P. A. Nikrityuk, "Mathematical Description of Physical Phenomena in Thermofluid Dynamics," in *Computational Thermo-Fluid Dynamics in Materials Science and Engineering*, Weinheim, Germany: Wiley, 2011, ch. 2, pp. 7-38.
- [75] J. Miettinen, "Calculation of solidification-related thermophysical properties for steels," *Metall. Mater. Trans. B*, vol. 28, no. 2, pp. 281-297, Apr. 1997.

[76] I. L. Yakovleva, T. I. Tabatchikova, N. A. Tereshchenko, A. N. Makovetskii, and D. A. Mirzaev, "Kinetics of austenite decomposition upon cooling of low-alloy pipe steel from the intercritical temperature range," *Bull. Russ. Acad. Sci.: Phys.*, vol. 77, no. 11, pp. 1373-1377, Nov. 2013.

[77] P. Oksman, S. Yu, H. Kytönen, and S. Louhenkilpi, "The Effective Thermal Conductivity Method in Continuous Casting of Steel," *Acta Polytech. Hung.*, vol. 11, no. 9, pp. 5-22, 2014. [Online]. Available: http://uni-obuda.hu/journal/Oksman_Yu_Kytonen_Louhenkilpi_55.pdf

Appendices:

A. Statistical Analysis Results:

The data and method used to obtain the results presented here are detailed in the next appendix (Appendix B).

It is important to note that the data used were generated by PEPIN for his Master of Science thesis [11] and that the experiments used here, were bead on plate (BOP) welds with an electrode diameter of 3.2 mm and AC polarity.

In this appendix the correlation used to compute the WFS is first presented along with the formula used to convert the results obtained on one diameter of electrode to another one. Then the results of the statistical analysis for the reinforcement area, the maximum reinforcement height, the bead width, the penetration area, and the maximum penetration depth. To account for the presence of the bevel a way to calculate the maximum penetration depth from the penetration area is presented in the part relative to the maximum penetration depth.

A.1. Wire feed speed:

Here a way to take into account the change in diameter of the electrode is presented.

The statistical analysis gave the following formula¹⁰ for the WFS in the situation of a BOP one wire SAW and an electrode diameter of 3.2 mm.

$$WFS \left(\frac{mm}{s} \right) = 0.090 I(A) - 0.2 B(\%) - 0.06 O(\%) - 0.3 TS \left(\frac{mm}{s} \right) \quad (A.1)$$

The electrode can have different diameters. To account for this, the WFS can be interpreted as a flow of matter.

For two electrodes 1 and 2 it is possible to write:

$$\rho_1 H_1 \frac{WFS_1 \pi D_1^2}{4} = \rho_2 H_2 \frac{WFS_2 \pi D_2^2}{4} \quad (A.2)$$

¹⁰ For more details see appendix B.

where:

- ρ : the density in kg/m^3 .
- H : the weight enthalpy considered constant in J/kg.
- D : the diameter of the electrode in mm.

If the properties of the two electrodes are assumed equal Equation (A.2) becomes:

$$WFS_2 = WFS_1 \left(\frac{D_1}{D_2} \right)^2 \quad (A.3)$$

A.2. Reinforcement area:

This parameter is not used in the present project but has a practical interest. The equation given by the analysis algorithm is the following.

$$RA = -4.8 \cdot 10^{-2}F - 1.57 \cdot 10^{-1}B - 1.23 \cdot 10^{-1}O + 2.22 \cdot 10^{-1}I - 1.68 U - 1.89 \cdot 10^{-4}I^2 + 1.81 \cdot 10^{-2}HI \quad (A.4)$$

The half-width of the confidence interval around each variable in Equation (A.4) is given in Table A.1.

Table A.1: Half-width of the confidence intervals for the regression of the reinforcement area.

Variable	Half-width of the confidence interval
Frequency (F) in Hz	$4.1 \cdot 10^{-2}$
Balance (B) in %	$5.2 \cdot 10^{-2}$
Offset (O) in %	$8.2 \cdot 10^{-2}$
Current (I) in A	$4.9 \cdot 10^{-2}$
Voltage (U) in V	$4.0 \cdot 10^{-1}$
Square of the current (I^2) in A^2	$4.7 \cdot 10^{-5}$
Heat input (HI) in W/mm	$2.1 \cdot 10^{-3}$

The coefficient of determination is;

$$R^2 = 0.92 \quad (\text{A.5})$$

The ratio of the theoretical F statistic over the calculated one is lower than 4%.

$$\frac{F_{theoretical}}{F_{calculated}} = \frac{2.38031}{62.1091} = 3.8\% \quad (\text{A.6})$$

Finally no outlier was detected. So, based on Equation (A.5) and (A.6) it is safe to say that the regression is significant. Also, one can notice by comparing Table A.1 and Equation (A.4) that except for the frequency, the half-width of the confidence interval for each parameter is one order of magnitude lower than the parameter itself. Observing the parity plot available in Figure A.1 one can note that no trend in the deviation from the ideal case (black line) is apparent. An interesting thing to note is that the square of the current is significant which is explained by the fact that the reinforcement depends on the melting rate which depends on Joule heating.

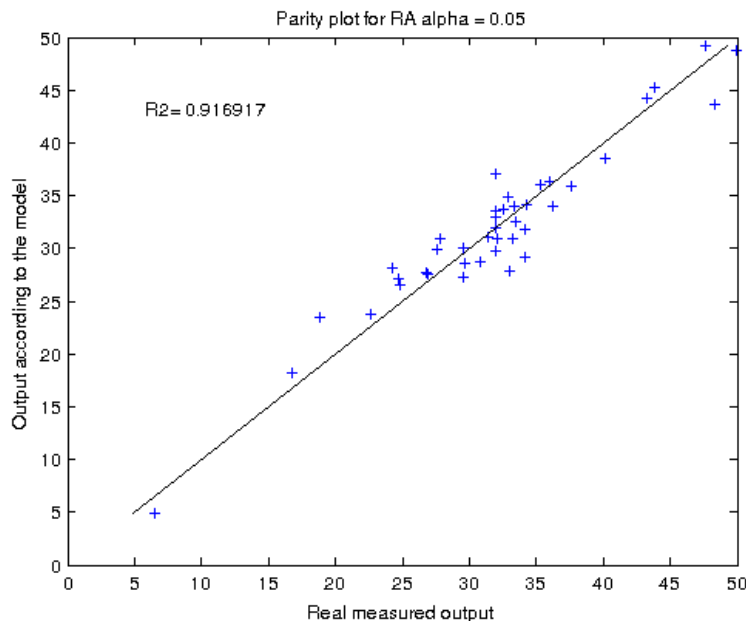


Figure A.1: Parity plot representing the calculated reinforcement area against the measured one. The black curve is the function "y=x".

A.3. Maximum reinforcement height:

This parameter is not used in the present project but has a practical interest. The equation given by the analysis algorithm is the following.

$$MRH = -1.38 \cdot 10^{-2}B + 1.94 \cdot 10^{-2}I - 1.17 \cdot 10^{-1}U - 1.42 \cdot 10^{-5}I^2 + 6.9 \cdot 10^{-4}HI \quad (A.7)$$

The half-width of the confidence interval around each variable in Equation (A.7) is given in Table A.2.

Table A.2: Half-width of the confidence intervals for the regression of the maximum reinforcement height.

Variable	Half-width of the confidence interval
Balance (B) in %	$6.2 \cdot 10^{-3}$
Current (I) in A	$5.6 \cdot 10^{-3}$
Voltage (U) in V	$4.8 \cdot 10^{-2}$
Square of the current (I^2) in A^2	$5.4 \cdot 10^{-6}$
Heat input (HI) in W/mm	$2.5 \cdot 10^{-4}$

The coefficient of determination is;

$$R^2 = 0.72 \quad (A.8)$$

The ratio of the theoretical F statistic over the calculated one is lower than 12%.

$$\frac{F_{theoretical}}{F_{calculated}} = \frac{2.63353}{23.5308} = 11.2\% \quad (A.9)$$

No outlier was found for this analysis. The coefficient of determination (Equation (A.8)) and the ratio of the F statistics reported in Equation (A.9), show that the regression picks up a significant part of the variation in the data on maximum reinforcement height, but it does not account for all the variability in the data. As Table A.2 shows, the half-width of the confidence intervals of the parameters are one order of magnitude lower than the parameter itself except for the HI, which means that those parameters are certainly significant. The parity plot available in Figure A.2 however makes it hard to rule out the possibility of a trend in the deviation with the ideal case and therefore the possibility that some correlations were ignored or that some of the parameters found significant are actually not is real and must be taken into account.

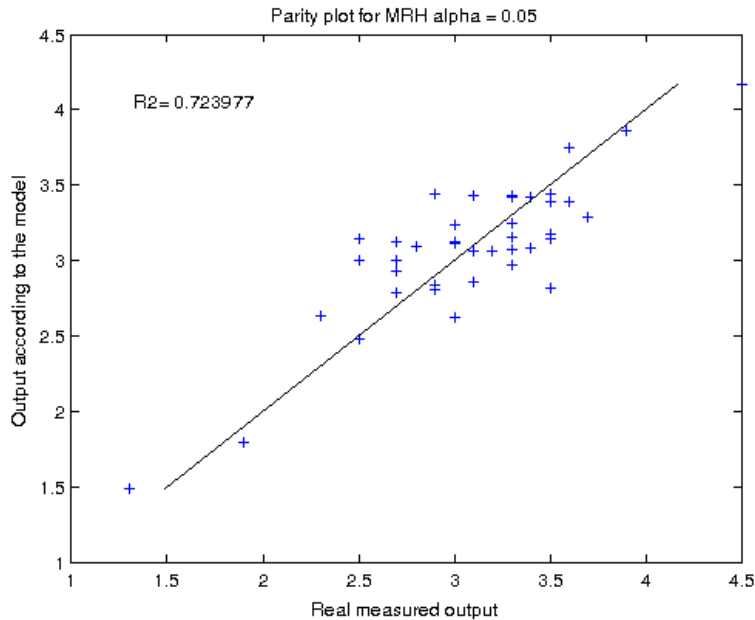


Figure A.2: Parity plot representing the calculated maximum reinforcement height against the measured one. The black curve is the function "y=x".

A.4. Bead width:

The bead width is an important input for this project as it dictates the width of the heat source used to model the welding process.

The equation given by the analysis algorithm is the following.

$$\begin{aligned}
 BW = & 1.9 \cdot 10^{-2}B + 5.4 \cdot 10^{-2}I - 4.6 \cdot 10^{-1}U - 9.2 \cdot 10^{-5}I^2 \\
 & + 8.9 \cdot 10^{-4}P + 6.46 \cdot 10^{-3}HI
 \end{aligned}
 \tag{A.10}$$

The half-width of the confidence interval around each variable in Equation (A.10) is given in Table A.3.

Table A.3: Half-width of the confidence intervals for the regression of the bead width.

Variable	Half-width of the confidence interval
Balance (B) in %	$1.4 \cdot 10^{-2}$
Current (I) in A	$1.4 \cdot 10^{-2}$
Voltage (U) in V	$2.5 \cdot 10^{-1}$
Square of the current (I^2) in A^2	$2.8 \cdot 10^{-5}$
Power (P) in W	$5.9 \cdot 10^{-4}$
Heat input (HI) in W/mm	$5.5 \cdot 10^{-4}$

The coefficient of determination is;

$$R^2 = 0.95 \tag{A.11}$$

The ratio of the theoretical F statistic over the calculated one is lower than 2%.

$$\frac{F_{theoretical}}{F_{calculated}} = \frac{2.49362}{128.366} = 1.94\% \tag{A.12}$$

Finally only one outlier was detected and removed to obtain these results. So, based on Equation (A.11) and (A.12) it is safe to say that the regression is significant. Also, based on the comparison of Table A.3 and Equation (A.10), it is possible to say that the most significant variable for this regression is the HI. The parity plot which corresponds to the correlations reported in Equation (A.10) is available in Figure A.3. The points one the parity plot are close to the black line and the

distance by which they deviate seems random. Therefore, the parity plot shows that the correlation does not omit important parameters.

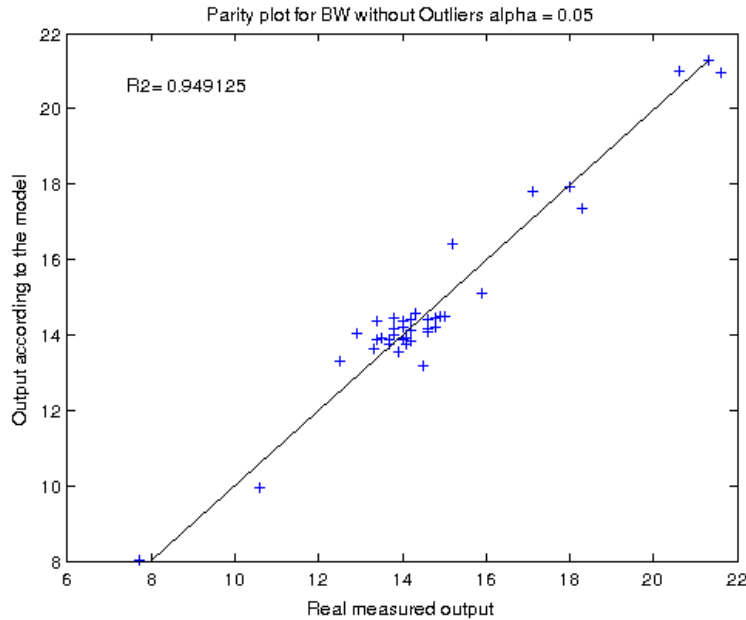


Figure A.3: Parity plot representing the calculated bead width against the measured one. The black curve is the function "y=x".

A.5. Penetration area:

This parameter is not directly used in this project but indirectly it can be used to calculate either the bead width or the penetration depth knowing one of those parameters and assuming an ellipsoidal shape for the part of the weld in the base metal. This will be addressed in the following sections. The equation given by the analysis algorithm is the following.

$$\begin{aligned}
 PA = & 1.49 \cdot 10^{-1}B + 3.12 \cdot 10^{-1}I + 4.9 U - 1.51 TS \\
 & + 6.6 \cdot 10^{-4}I^2 - 7.6 \cdot 10^{-3}P
 \end{aligned}
 \tag{A.13}$$

The half-width of the confidence interval around each variable in Equation (A.13) is given in Table A.4.

Table A.4: Half-width of the confidence intervals for the regression of the penetration area.

Variable	Half-width of the confidence interval
Balance (B) in %	$6.9 \cdot 10^{-2}$
Current (I) in A	$7.5 \cdot 10^{-2}$
Voltage (U) in V	1.2
Travel speed (TS) in mm/s	$3.8 \cdot 10^{-1}$
Square of the current (I^2) in A^2	$1.4 \cdot 10^{-4}$
Power (P) in W	$2.8 \cdot 10^{-3}$

The coefficient of determination is;

$$R^2 = 0.94 \quad (\text{A.14})$$

The ratio of the theoretical F statistic over the calculated one is lower than 3%.

$$\frac{F_{theoretical}}{F_{calculated}} = \frac{2.50264}{109.327} = 2.3\% \quad (\text{A.15})$$

For this analysis two outliers were identified and removed from the batch of data. The coefficient of determination (Equation (A.14)) and the ratio of F statistics (Equation (A.15)) indicates that the correlation which corresponds to Equation (A.13) accounts for most of the variability in the data. The half-width of the confidence intervals (Table A.4) of the parameters reported in Equation (A.13) are one order of magnitude lower than themselves except for the voltage and the square of the current. The parity plot (Figure A.4) shows points close to the ideal case (black line) and no clear trend in the deviation from the ideal line.

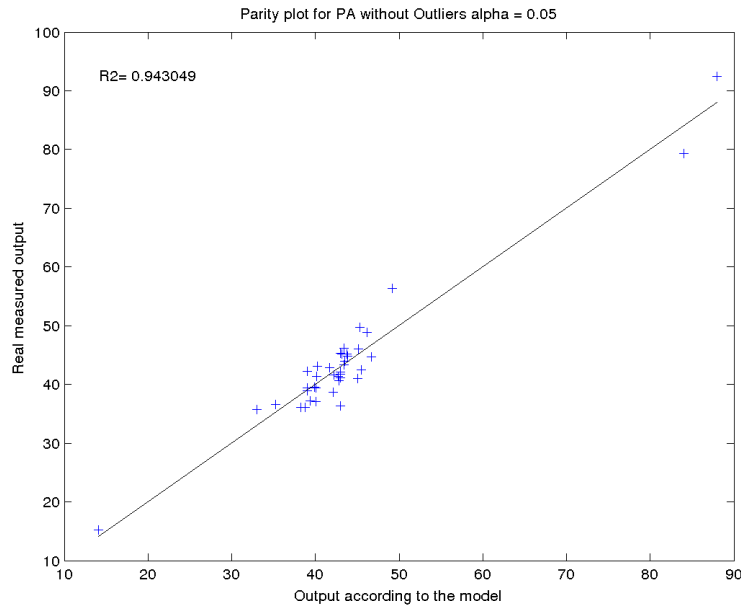


Figure A.4: Parity plot representing the calculated penetration area against the measured one. The black curve is the function "y=x".

A.6. Maximum penetration depth:

The maximum penetration depth is an important input for this project as it dictates the depth of the heat source used to model the welding process. The problem with the data used for this analysis is that the experiments were BOP welds and most of the welding operations studied here use a bevel which will *de facto* increase the maximum penetration depth.

The equation given by the analysis algorithm is the following.

$$\begin{aligned}
 MPD = & 1.5 \cdot 10^{-2}B - 3.3 \cdot 10^{-2}I - 6.3 \cdot 10^{-1}U - 1.6 \cdot 10^{-1}TS \\
 & + 8.2 \cdot 10^{-5}I^2 - 1.05 \cdot 10^{-3}P - 1.1 \cdot 10^{-3}HI
 \end{aligned}
 \tag{A.16}$$

The half-width of the confidence interval around each variable in Equation (A.16) is given in Table A.5.

Table A.5: Half-width of the confidence intervals for the regression of the penetration area.

Variable	Half-width of the confidence interval
Balance (B) in %	$1.1 \cdot 10^{-2}$
Current (I) in A	$1.4 \cdot 10^{-2}$
Voltage (U) in V	$2.8 \cdot 10^{-1}$
Travel speed (TS) in mm/s	$1.3 \cdot 10^{-1}$
Square of the current (I^2) in A^2	$2.8 \cdot 10^{-5}$
Power (P) in W	$5.4 \cdot 10^{-4}$
Heat input (HI) in W/mm	$1.0 \cdot 10^{-3}$

The coefficient of determination is;

$$R^2 = 0.89 \quad (\text{A.17})$$

The ratio of the theoretical F statistic over the calculated one is lower than 6%.

$$\frac{F_{theoretical}}{F_{calculated}} = \frac{2.39908}{42.874} = 5.6\% \quad (\text{A.18})$$

The coefficient of determination (Equation (A.17)) and the ratio of the F statistics (Equation (A.18)) shows that the correlation obtained (Equation (A.16)) explains a big part of the variability in the data but the coefficient of determination is little bit weak as it is under 90 %. Also the half-widths of the confidence intervals are close to the values of the parameters themselves. This means that the possibility that some other dependencies were missed and that some considered here significant can actually not be, cannot be ruled out. The parity plot (Figure A.5) shows points close to the ideal case (black line) and no clear trend in the deviation of the points from the ideal case can be pointed out.

The maximum penetration depth (MPD) is influenced by the presence of a bevel. Therefore, Equation (A.16) must be modified to account for the bevel as the data used here were generated with BOP welding operations. To do so three hypothesis are posed:

- The bead width is the same in both cases.
- The area of base metal melted are the same in both cases.
- The penetration area of a weld has an ellipsoidal shape.

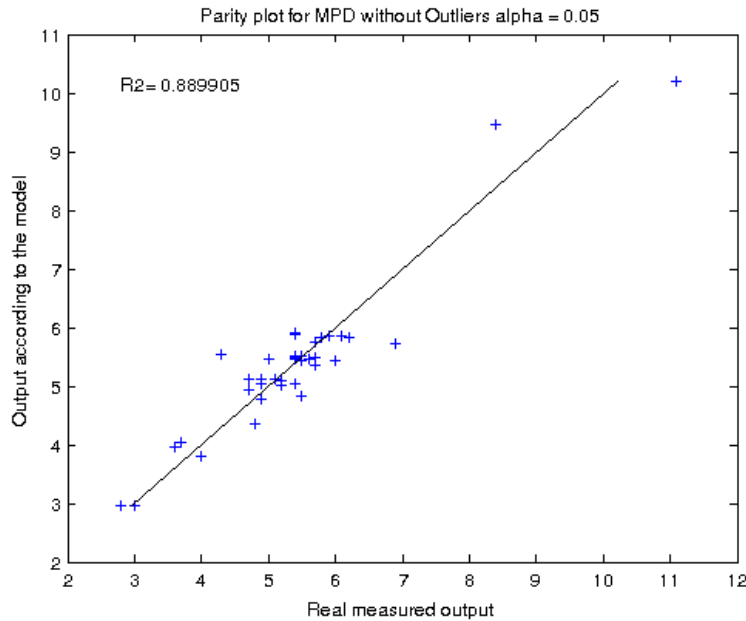


Figure A.5: Parity plot representing the calculated maximum penetration depth against the measured one. The black curve is the function "y=x".

Figure A.6 shows the differences between a weld generated with a BOP operation and one generated with a beveled plate. The penetration area in the case of a weld on a beveled plate is equal to the area of base metal melted plus the area of the bevel. This is given in Equation (A.19) using the notation used in Figure A.6 for the bevel.

$$PA_B = PA_{BOP} + h \cdot l \quad (A.19)$$

Assuming an ellipsoidal shape for the penetration area and assuming that the bead width is the same in both cases, it is possible to write Equation (A.20).

$$PA_B = \frac{\pi}{4} BW \cdot MPD_B \quad (A.20)$$

A way to calculate the maximum penetration depth for a weld on a beveled plate based on the penetration area is obtained by combining Equations (A.19) and (A.20). Also, the statistics calculated on the correlation obtained on the penetration area are better than the one obtained on the maximum penetration depth for a BOP weld. Equation (A.21) is the one used throughout this project.

$$MPD_B = \frac{4}{\pi} \frac{PA_{BOP} + h \cdot l}{BW} \quad (A.21)$$



Figure A.6: Schematic illustrating the difference between a BOP weld (left) and a beveled one. The green parts corresponds to the material added during the operation while the red ones corresponds to the material melted.

B. Statistical Analysis of Wire Feed Speed During Submerged Arc Welding:

An Empirical Model for the Wire Feed Speed in One Wire Submerged Arc Welding of X70 Steel with AC Polarity

This appendix is a project of paper thus the special presentation

A. Lecoanet^{1*}, J. T. Pepin², H. Henein¹, D.G. Ivey¹

¹Department of Chemical & Materials Engineering, University of Alberta, Edmonton, AB, Canada

²PCL Industrial Constructors Inc., Edmonton, AB, Canada

*lecoanet@ualberta.ca

B.1. Abstract:

Some data previously generated on the wire feed speed (WFS) during submerged arc welding (SAW) were analyzed. The variables tested were: frequency (Fq), balance (B), offset (O), current (I), voltage (U), and travel speed (TS). Multiple linear regression (MLR) was used for analysis. Due to the presence of significant uncertainty, a method was developed to remove the outliers. Also, insignificant parameters were automatically suppressed and the regression was rerun without them to achieve better accuracy. The outcome of the regression was analyzed via hypothesis testing. A Student-t test was used to assess the significance of the parameters. An F-test was used to determine the significance of the overall regression. These tests, as well as a coefficient of determination of 94.4%, showed the regression to be accurate and reliable for the set of data used. A large dataset of 41 points was used, which indicates that the model developed is reliable outside of the dataset as well.

$$WFS(mm/s) = -0.20 B(\%) - 0.06 O(\%) + 0.090 I(A) - 0.3 TS(mm/s)$$

$$WFS(inch/s) = -7.8 \times 10^{-3} B(\%) - 2.3 \times 10^{-3} O(\%) + 3.56 \times 10^{-3} I(A) - 0.3 TS(inch/s)$$

B.2. Introduction:

The SAW process is one of the most effective and used processes to weld piping. Its automation makes it possible to use significantly higher wire feed speeds (WFS) to achieve faster production. Also, the flux covering the weld makes the process safer by masking the arc and blocking the fumes [20, 64]. The flux makes it more difficult to know what is happening during the welding operation and increases the number of parameters to control. During constant current operation of the SAW process the WFS is controlled indirectly [20, 64]. It is changed so that the current stays the same throughout the operation. Thus, the distance between the tip of the electrode and the work piece stays constant.

The WFS is a crucial variable as it is a measure of productivity, in combination with travel speed. It is, therefore, critical to develop equations to predict it. The method utilized to regress, especially the part dealing with the removal of the outliers, is also presented because the lack of literature on how to automate this procedure was striking.

This problem was first studied by Chandel and Malik [23], but the waveform variables were not taken into account. This question has not been addressed for several decades until recently when some studies on the effect of the waveform variables were qualitatively carried out [11, 65].

In this work it is further demonstrated that the input parameters affecting the WFS are mostly the waveform variables, which confirm previous studies [11, 65], keeping in mind that the diameter of the wire has not been changed which could have an effect [23]. The goal of the present study is to build on the work previously done by Pepin et al. [11, 65, 66] on linking the settings of one wire SAW with constant current operation to the WFS¹¹ by applying the multiple linear regression (MLR) method as well as hypothesis testing to check the relevance of each parameter and the

¹¹ Since the WFS is controlled to give a constant arc length, this is equivalent to linking these parameters to the arc length.

entire regression. The SAW data has significant noise and some outliers may be present. A method is developed to remove the outliers.

The list of the symbols and the acronyms used in this appendix and their signification are available in Table B.3 and B.4. Also the list of the data utilized is available in Table B.5.

B.3. Inputs:

B.3.1. Parameters:

The input parameters taken into account are the following:

- Fq: frequency (Hz)
- B: balance (%)
- O: offset (%)
- I: current (A)
- U: voltage (V)
- TS: travel speed (mm/s)

No constant was considered as it is not physically meaningful here.

B.3.2. Data:

The data used here have been generated previously by Pepin et al. [11, 65]. For this work only the welds performed with one wire were considered. The welds with inconsistent bead shape have been removed before analysis. The ranges of variation of the input data are presented in Table B.1. The data regressed are available in Table B.5. The diameter of the wire used was fixed at 3.2 mm and the flux used was basic.¹²

¹² To grasp the effect of a change in diameter one can look into the literature [23].

Table B.1: Range in variables for analysis.

Parameters	Minimum	Maximum
Fq (Hz)	30	90
B (%)	25	75
O (%)	-15	15
I (A)	385.3	700.6
U (V)	27.3	35.3
TS (mm/s)	4.3	22.6

B.4. Methods used:

To carry out this work an MLR procedure was coded in MATLAB[®]. The different methods used during this study are developed here¹³ [67, 68].

B.4.1. Multiple Linear Regression:

The basic equations used for MLR are as follows:

$$\Phi^T \Phi \hat{\theta} = \Phi^T y \quad (\text{B.1})$$

$$\hat{\theta} = (\Phi^T \Phi)^{-1} \Phi^T y \quad (\text{B.2})$$

Φ is the matrix that is equal to $\Psi(X)$ when the problem is written as follows:

$$\hat{y} = \Psi(X) \hat{\theta} \quad (\text{B.3})$$

¹³ These methods also stem from the course given by J.P. Corriou at E.N.S.I.C. (École Nationale Supérieure des Industries Chimiques), France, within 2012/2013.

X is the matrix of inputs, \hat{y} is the output estimated by the regression to approach the real one (y), and $\hat{\theta}$ are the parameters estimated by the regression.

Both Equations (B.1) and (B.2) can be used. Equation (B.1) can be solved by an algorithm without inverting a matrix. This would allow one to avoid the conditioning problem that can arise in these kinds of situations. However, to determine the confidence intervals, as will be presented in Section 3.2, the inverse of $\Phi^T \Phi$ is required. So Equation (B.2) was used in this study.

B.4.2. Statistical tests:

The variables were recorded from a series of experiments, so some noise is expected. To differentiate noise from real information, confidence intervals were needed for each parameter. In fact, one needs to determine if a parameter is meaningful. This corresponds to the following hypothesis testing:

$$\begin{aligned} H_0 : \theta_i &= 0 \\ H_a : \theta_i &\neq 0 \end{aligned} \tag{B.4}$$

This is a two sided test and a rejection zone needs to be defined. Assuming that the estimators of the parameters $\hat{\theta}_i$ are unbiased and follow a normal distribution, the variance in the parameters is estimated as [68]:

$$\hat{\sigma}^2(\theta_i) = s_{\theta_i}^2 = c_{ii} s_y^2 \tag{B.5}$$

where c_{ij} are the elements of $(\Phi^T \Phi)^{-1}$ and s_y^2 is an estimator of the variance in the studied output variable. The following estimator has been chosen for s_y^2 :

$$s_y^2 = \frac{1}{m-n} \sum_{i=1}^m (y_i - \hat{y}_i)^2 \tag{B.6}$$

where m is the number of data points and $(m - n)$ represents the degrees of freedom for the regression. The confidence interval at a significance level, α , for each parameter is given by the following relation:

$$\hat{\theta}_i - t_{\frac{\alpha}{2},(m-n)}s_{\theta_i} < \theta_i < \hat{\theta}_i + t_{\frac{\alpha}{2},(m-n)}s_{\theta_i} \quad (\text{B.7})$$

If the interval:

$$\left[\hat{\theta}_i - t_{\frac{\alpha}{2},(m-n)}s_{\theta_i} ; \hat{\theta}_i + t_{\frac{\alpha}{2},(m-n)}s_{\theta_i} \right] \quad (\text{B.8})$$

does not include zero, this means that the value obtained for θ_i is statistically different from 0 at a level of significance α . Therefore, H_0 is rejected. For this study, the standard value of 5% has been chosen for α .

B.4.3. F-test:

The F-test is a test of the variance [68]. If the value of the F statistic for the regression is higher than the theoretical one, F_{α, ν_1, ν_2} with $\alpha=5\%$, $\nu_1 = n - 1$, and $\nu_2 = m - n$, then the model explains a significant part of the variance in y , at a level of significance α . As more of the variance is explained, the value of the F statistic increases. The F statistic is worked out in the following way:

$$F = \frac{SS_R/(n - 1)}{SS_E/(m - n)} \quad (\text{B.9})$$

$$SS_R = \sum_{i=1}^m (\hat{y}_i - \bar{y})^2 \quad (\text{B.10})$$

$$SS_E = \sum_{i=1}^m (y_i - \hat{y}_i)^2 \quad (\text{B.11})$$

where y_i is the actual value of y measured for the data point i , \hat{y}_i is the value according to the model, and \bar{y} is the mean of the output y . The regression is considered significant if

$$F_{\alpha, \nu_1, \nu_2} < F \quad (\text{B.12})$$

In terms of hypothesis testing this can be written as:

$$\begin{aligned} H_0 &: \forall i \in \llbracket 1, n \rrbracket \theta_i = 0 \\ H_a &: \exists i \in \llbracket 1, n \rrbracket \mid \theta_i \neq 0 \end{aligned} \quad (\text{B.13})$$

H_0 is rejected when $F_{\alpha, \nu_1, \nu_2} < F$.

B.4.4. Coefficient of determination R^2 :

The coefficient of determination value is a measure of how much of the variability in the data is explained by the model [67]. Its value is bounded by 0 and 1 and was calculated using the following formula:

$$R^2 = 1 - \frac{SS_E}{S_{yy}} \quad (\text{B.14})$$

$$S_{yy} = \sum_{i=1}^m (y_i - \bar{y})^2 \quad (\text{B.15})$$

where y_i is the actual value of y measured for the data point i , \hat{y}_i is the value according to the model, and \bar{y} is the mean of the output y . If the model is perfect, $SS_E = 0$ and $R^2 = 1$.

B.4.5. Outliers:

When experiments are carried out sometimes problems in measurements or unexpected events can generate data which do not represent reality. They corrupt the analysis and must be removed.

A way to determine whether a data point is an outlier is to form the vector of the residuals e^0 . This is the vector of the differences between the model and the actual data. Then one can mean-centred standardize the vector using the following formula for every element of e^0 :

$$e_i = \frac{e_i^0 - \bar{e}}{s_e} \quad (\text{B.16})$$

The mean-centred normalized residuals are then assumed to follow a normal distribution centred on 0 with a variance of 1. For such a distribution, the probability that this random variable has a value outside of $[-3,3]$ is 0.0027. This point is likely to be an outlier and must be removed and the regression performed again.

One could argue that the mean of the residuals should be equal to zero and, therefore, the data point should not be removed from the residuals. The choice has been made to keep the data point to make the outliers analysis more independent from the regression to avoid error propagation.

B.5. Implementation:

The next step was to implement the methods previously described into MATLAB[®] commercial software to perform the actual calculation. A simplified schematic of the overall procedure used is shown in Figure B.1.

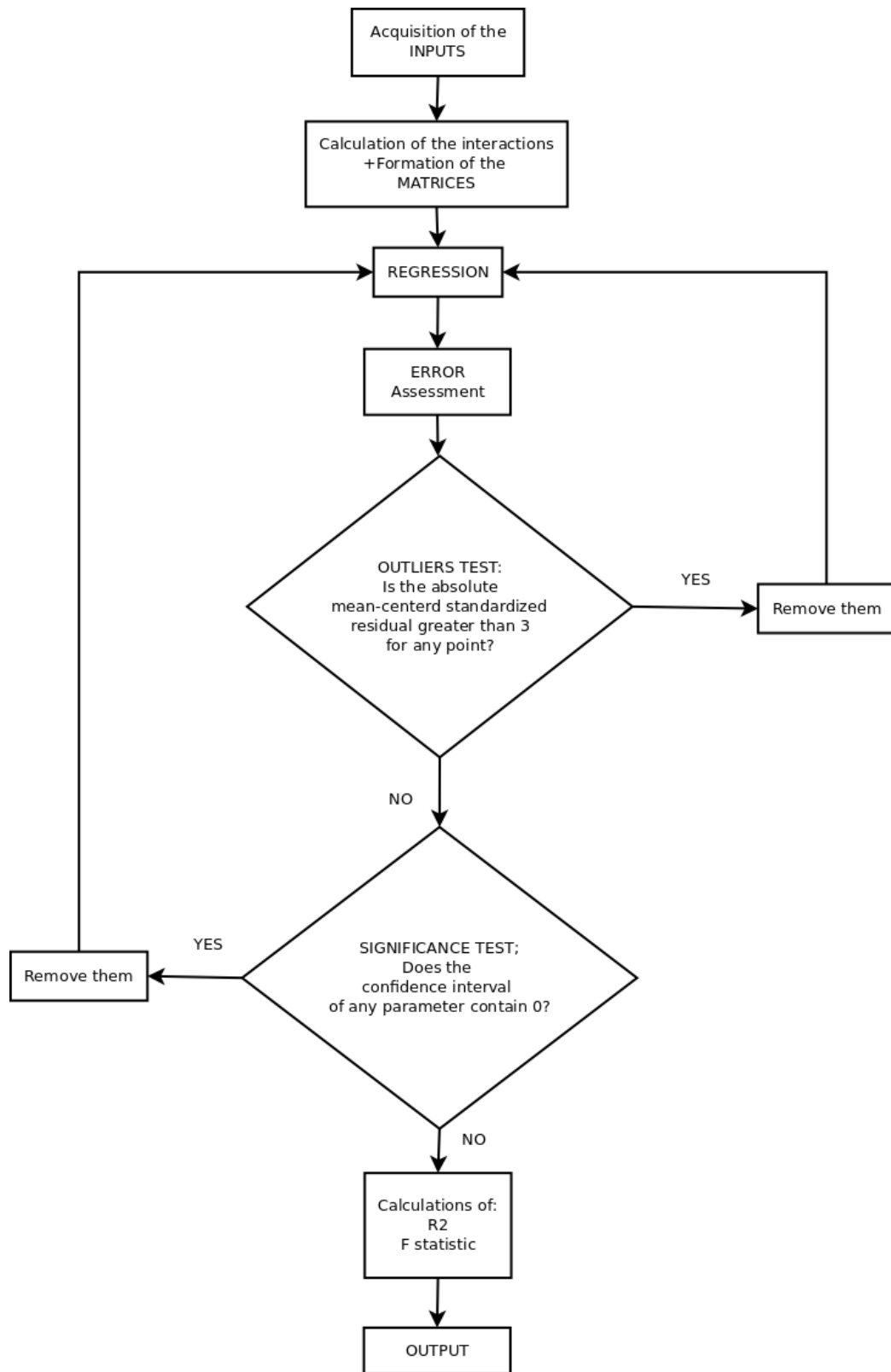


Figure B.1: Schematic description of the algorithm used.

B.6. Results & Discussion:

The regression gave Equations (B.17) and (B.18), in SI units, with a coefficient of determination of 94.4%. The value of the F-statistic is 188.7, which is compared with the theoretical value, 2.866. One outlier was found within the 41 data points and removed.

$$WFS(mm/s) = -0.20 B(\%) - 0.06 O(\%) + 0.090 I(A) - 0.3 TS(mm/s) \quad (B.17)$$

$$WFS\left(\frac{inch}{s}\right) = -7.8 \times 10^{-3} B(\%) - 2.3 \times 10^{-3} O(\%) + 3.56 \times 10^{-3} I(A) - 0.3 TS(inch/s) \quad (B.18)$$

B.6.1. Hypothesis testing analysis:

The value of the determination coefficient means that the regression agrees pretty well with the experiments. The F-statistic value is much higher than the theoretical one, which indicates that a major part of the variation in the data is captured by the regression. This further reinforces what the value of the coefficient of determination shows.

The values of the half-width of the confidence interval are reported in Table B.2. The half-widths are one order of magnitude lower than the parameters for the balance and the current. This is a measure of the accuracy of the value of the parameter. The smaller the width of the confidence interval, the more accurate is the value of the parameter. For the offset and the travel speed, the width of the confidence interval is of the same order of magnitude as the parameter. This can be explained from the number of different values used for the experiments. For the balance three values were used (25%, 50%, 75%). The value of the travel speed was changed more, but it was kept constant at ~10.6 mm/s for half of the experiments.

Table B.2: Half width of the confidence intervals, for the significant variables.

Parameters	½ width of confidence interval
B	0.031
O	0.056
I	0.0049
TS	0.21

B.6.2. Parity plot analysis:

If all variations¹⁴ of the experimental data are captured by the regression, the points of the parity plot would align perfectly with the bisector of the graph. Due to the noise intrinsic to every experiment, some scatter is expected. If the model used to regress the data is good, which means it accounts for all the major processes occurring, the scatter should be evenly spread around the bisector and follow a normal distribution. This assumption has been used before to remove the outliers. Also, if a trend is visible in the residual¹⁵ it means that a process, via a parameter, was omitted and must be accounted for.

In Figure B.2 the points are evenly distributed around the black line, except at the beginning of the curve. Due to the small number of points in this region (7) and the even smaller number of points away from the line (3), it is impossible to determine if a process with a minor effect has been omitted. Therefore, the parity plot shows that it is likely that all relevant parameters have been taken into account and that the regression seems to correctly describe the process.

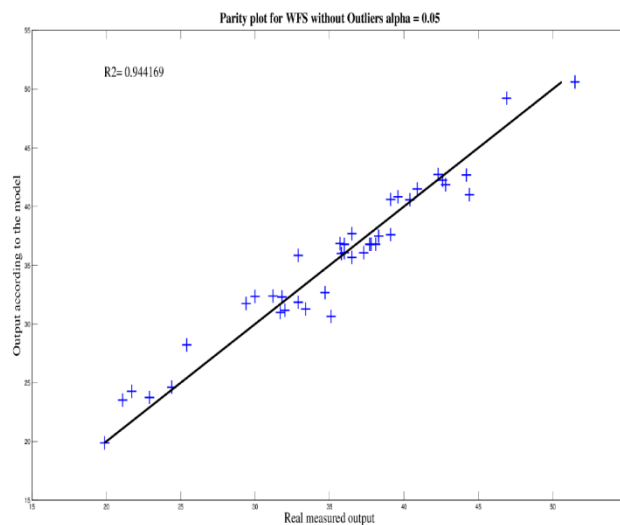


Figure B.2: Parity plot representing the output according to the model versus the real measured one. The black curve is the function "y=x".

¹⁴ Including the errors.

¹⁵ This can be seen on a parity plot when the points seem to follow a line, which crosses the line corresponding to the bisector.

B.6.3. Analysis of the trends:

Since the coefficient of determination is above 90%, there is little chance that it could be improved. Also, the first order parameters likely have the largest effect on the process. To be sure some interactions were tried ($O \times B, I^2, U \times I, \frac{U \times I}{TS}$). They were not shown to be significant and turned the Fisher information matrix into a singular one, making it impossible to solve the problem within the scope of the methods used here.

One outlier was removed. It changed the R^2 significantly but increased the F-statistic by 42. Removing this outlier changed the value of the estimator of the parameter in front of the travel speed, by a factor of two, and did not significantly change the other ones. This is an indication that the experiments were conducted correctly because only one out of the 41 points was considered as an outlier in this study.

It is generally agreed that a Direct Current Electrode Negative (DCEN) melts more electrode wire, while a Direct Current Electrode Positive (DCEP) melts more base metal [11, 23]. Figure B.3 shows a schematic of this concept.

BALANCE: Equation (B.17) shows that the balance has a negative effect on the WFS. The higher the balance, the longer the system stays in DCEP mode compared with DCEN mode. This is represented in Figure B.4. As stated before, the DCEN mode increases melting of the wire [23]. Therefore, as balance increases the WFS decreases. This is consistent with previous work [65].

CURRENT: An increase in current was shown [23] to increase the melting rate of both the electrode and the base metal. Joule heating is a phenomenon which can explain an increase in melting rate when the current increases, but it is proportional to the square of the current. The fact that the current was significant but not its square may be due to the noise. Therefore, this trend is consistent with the literature.

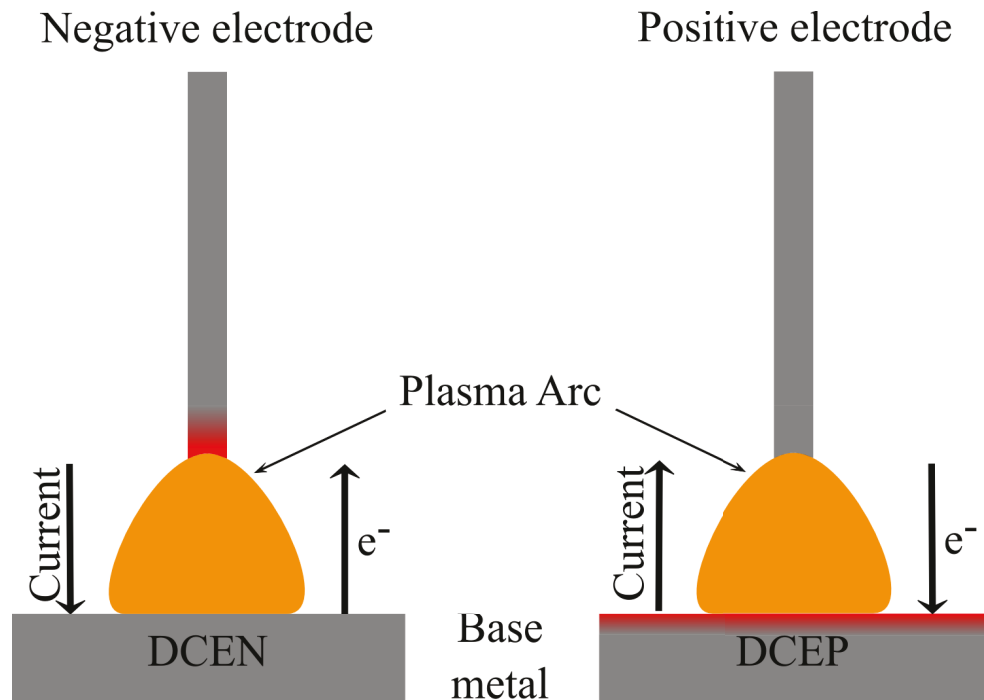


Figure B.3: Schematic showing the effect of the polarity on the melting of both the base metal and the electrode. Inspired by [11].

OFFSET: Equation (B.17) also shows that offset has a negative effect on the WFS. As the offset increases the current decreases during the DCEN mode (Figure B.5). As stated before, a higher current increases the melting rate and since a higher offset means a lower current in DCEN it decreases the melting rate of the electrode and, therefore, decreases the WFS.

TRAVEL SPEED: Equation (B.17) shows that travel speed has a negative effect on the WFS. As such, a higher travel speed results in less melting of the electrode wire. The slower the travel speed the longer the electrode stays at the same point and the hotter the base metal and the flux becomes, which provides additional energy back to the electrode through radiation or conduction.

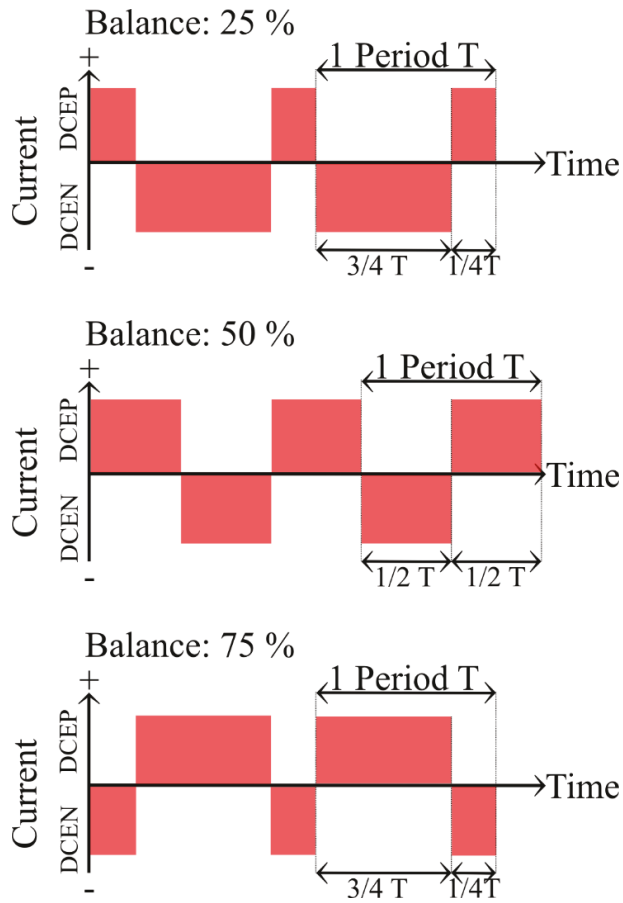


Figure B.4: Schematic explaining how the balance effects the electrical signal. Inspired by [11].

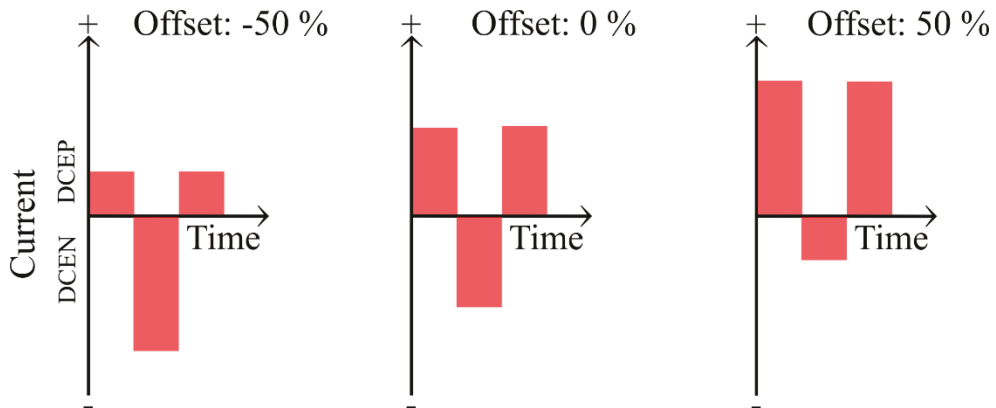


Figure B.5: Schematic explaining how the offset effects the electrical signal. Inspired by [11].

B.7. Insignificant variables:

Among the first order variables only two were shown to be insignificant, i.e., frequency and voltage. This confirms Chandel and Malik's results [23] for the voltage and the analysis by Pepin et al. [11].

The frequency is the number of times the polarity shifts from one polarity to the other. If the polarity stays too long positive or negative, then this is equivalent to having a succession of different welds. This would cause welds with irregular penetration and reinforcement, as each polarity melts preferentially either the base metal or the electrode (Figure B.3). Also, when the shift between polarities occurs, the current stays for some time at 0. If the current stays there for too long the arc will stop. So, if the shift takes too long the arc will constantly stop and will restart just after short-circuiting when the electrode touches the molten pool. For these reasons modern power supplies try to make the shift as fast as possible, but they have limitations. Therefore, above a given frequency an alternating current square signal (AC-SQ), such as the one used in the experiments, will turn into a triangular one, which results in a different effective HI. If the experiment is done at a frequency high enough to prevent the arc from stopping, but low enough to maintain a correct AC-SQ signal, then no effect is expected which is the case for this study.

B.8. Link with properties:

The speed at which welding is carried out, while an important issue of productivity, has to be balanced with the ability to produce a sound metallurgical weld of high quality. Equation B.3 suggests that one can improve productivity using a high current. However, this is not limitless. A sufficiently high current could lead to a significant coarse grain heat affected zone and, thus, poor fracture toughness values. Recent work by Pepin [11] addressed the issue of the relationship between current and fracture toughness, as measured using the Charpy test, for one electrode SAW.

Pepin [11] introduced a parameter, termed SP ratio, to describe the shape of a weld bead. This ratio compares the full width to the width at half (or semi) penetration (i.e., "w2/w1") and is illustrated in Figure B.6.

BOP samples used in the regression described in this paper were machined and Charpy tests evaluated¹⁶. The Charpy results for the single electrode tests as a function of SP ratio for two different electrode currents is shown in Figure B.7. This figure clearly illustrates that for both current values, an increase in SP ratio will yield higher SS-CVN fracture energy values. Additionally, as current is increased, the trend line is shifted to the right. As a result, if a larger current value is used, a higher SP ratio is required to achieve the same SS-CVN fracture energy values. As a result, if two beads have comparable SP ratio values, the bead produced using a larger current likely has lower notch-toughness. However, for two beads produced using different currents to have the same SP ratio, it would be necessary to modify voltage and travel speed. Thus, maximizing WFS, as outlined by the regression presented here, can be achieved when combined with the shape of the weld and its metallurgical properties.



Figure B.6: Schematic explaining how the semi-penetration ratio can help characterize a weld. Inspired by [11].

¹⁶ For details see [11].

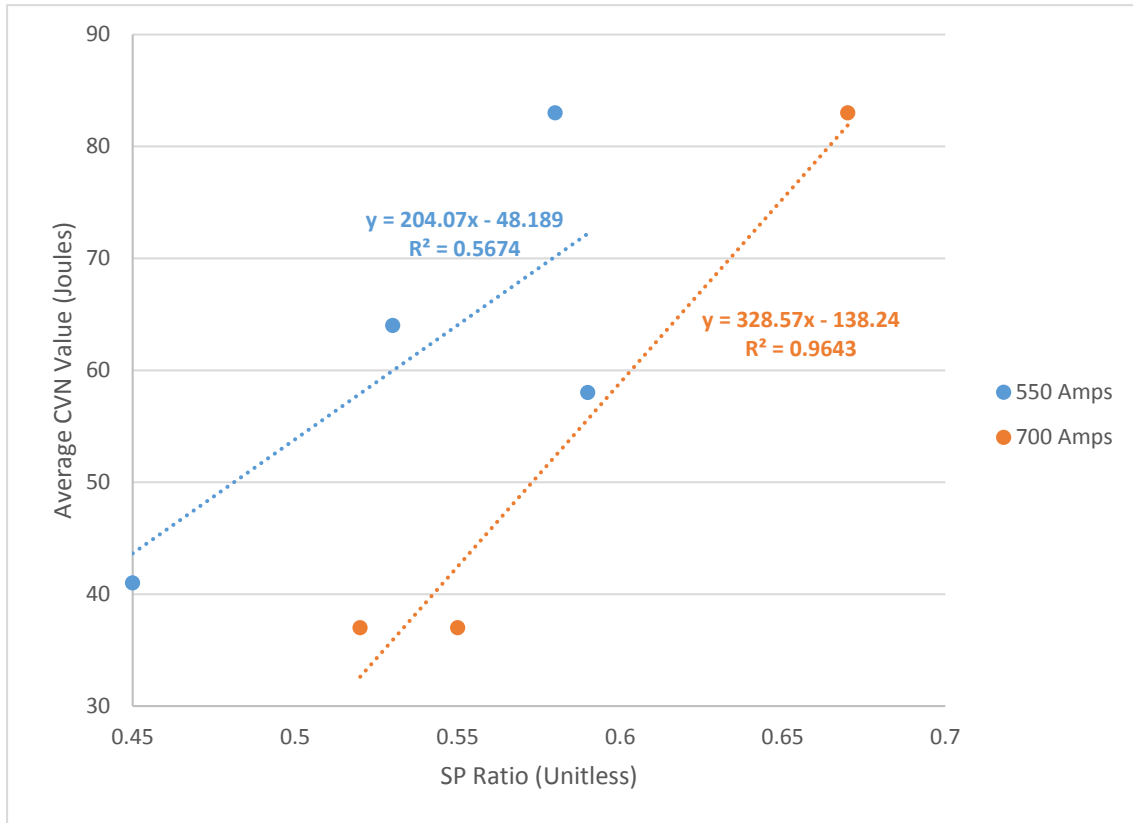


Figure B.7: Effect of the semi-penetration ratio on the average SSCVN fracture energy for two different currents.

B.9. Conclusions:

Throughout this work a reliable and efficient way to predict the WFS during SAW was developed. Also a way to remove the outliers has been proposed. This is important when a lot of data is analyzed together and in noise prone environments like welding. Removing outliers improves the coefficient of determination, but more importantly it gives more accurate values for the parameters. The results were analyzed and compared with previous studies and showed good agreement, which further justifies the approach taken. The relationship developed can be used for production purposes even if it does not account for changes in wire diameter. In addition, the mechanism for welding stainless steel or aluminum can be quite different. The trends for steels other than carbon steel may also differ.

From this study the following conclusions can be drawn:

- The frequency and the voltage are not significant in assessing WFS.
- An accurate and reliable functional relationship was developed to link the WFS to the operational parameters.
- The first order variables are sufficient to predict the WFS¹⁷.

It is possible to apply the method shown to other outputs and in other domains. The approach provides a rapid answer and also frees the operator of most of the burden, which is to go through several models by systematically removing the insignificant parameters. The approach is easy to implement and gives information which cannot be easily assessed otherwise.

B.10. Acknowledgements:

The authors are grateful to the Natural Sciences and Engineering Research Council (NSERC) of Canada and to the following companies for providing research funding: Evraz Inc. NA, TransCanada Pipelines Ltd., Enbridge Pipelines Inc., UT Quality Inc. and Alliance Pipeline Ltd.

The authors would also like to acknowledge Alberta Innovates - Technology Futures (AITF) for providing the facilities and equipment necessary to further investigate and analyze the completed welds. Finally, the authors would like to acknowledge PCL Industrial Constructors Inc. for supporting the analysis.

¹⁷ No interactions needed.

B.11. Symbols and Acronyms:

Table B.3: List of symbols and acronyms used (Latin alphabet).

Acronym / Symbol	Full Name	Units/ Value
AC	Alternating current	-
AC-SQ	Alternating current Square signal	-
B	Balance	%
c_{ij}	Elements of $(\Phi^T \Phi)$	-
DCEN	Direct current electrode negative	-
DCEP	Direct current electrode positive	-
e	Normalized residuals	-
e^0	Residuals	-
\bar{e}	Mean of the residuals	-
F	Experimental F statistic	-
F_{α, ν_1, ν_2}	Theoretical F statistic	-
Fq	Frequency	Hz
I	Current	A
m	Number of data points	41
MLR	Multiple linear regression	-
n	Number of parameters	-
O	Offset	%
R^2	Coefficient of determination	-
SAW	Submerged arc welding	-
SI	Système International	-
SP	Semi Penetration	-
SS-CVN	Sub-Size Charpy V-Notch	-
s_e	Standard deviation of the residuals	-
s_y^2	Estimator of the variance in y	-

$s_{\theta_i}^2$	Estimator of the variance in the parameters values	-
$t_{\frac{\alpha}{2}, (m-n)}$	Theoretical student-t statistic	-
TS	Travel speed	mm/s
U	Voltage	V
WFS	Wire feed speed	mm/s
X	Matrix of the inputs	-
y	Experimental output	mm/s
\bar{y}	Mean of the output	mm/s
\hat{y}	Output according to the model	mm/s

Table B.4: List of symbols and acronyms used (Greek alphabet).

Acronym/ Symbol	Full Name	Units/ Value
α	Level of significance	5%
θ	Real parameter	-
$\hat{\theta}$	Estimator of the parameter	-
Φ	Matrix of inputs transformed according to the model	-
Ψ	Operator defining the model	-

B.12. Data used for processing:

Table B.5: Data utilized.

Frequency (Hz)	Balance (%)	Offset (%)	Current (A)	Voltage (V)	Travel speed (mm/s)	Wire feed speed (mm/s)
60	50	0	398.4	31.5	22.6	19.9
60	50	0	400.3	29.4	7.3	21.7
60	50	0	385.3	28.1	4.3	22.9
60	50	0	395.6	35.0	8.5	21.1
60	50	0	397.3	34.1	5.1	24.4
60	50	0	548.9	31.5	10.6	36.0
60	50	0	523.4	28.8	6.3	36.5
60	50	0	542.8	35.3	12.0	32.9
60	50	0	538.6	34.4	7.0	35.7
60	50	0	700.6	31.3	8.0	60.2
60	50	0	699.5	34.8	14.8	46.9
60	50	0	696.4	35.0	8.8	51.5
60	50	0	442.8	32.1	6.9	25.4
60	50	0	490.7	31.6	7.5	31.2
60	50	0	549.3	32.2	10.7	37.8
60	50	15	550.9	30.2	10.7	36.0
60	50	-15	549.5	29.9	10.7	36.5
60	75	0	549.3	29.6	10.7	32.9
60	75	15	550.9	28.9	10.6	32.0
60	75	-15	548.3	31.0	10.6	34.7
60	25	0	541.0	31.9	10.6	44.4
60	25	15	545.9	31.9	10.6	40.4
60	25	-15	550.0	32.6	10.6	44.2
30	50	0	548.9	32.2	10.6	37.7
30	50	15	550.5	31.0	10.6	37.3
30	50	-15	548.3	32.2	10.6	39.1
30	75	0	535.5	29.8	10.6	35.1
30	75	15	552.2	30.8	10.6	33.4
30	75	-15	544.8	28.9	10.6	30.0
30	25	0	550.4	32.0	10.6	42.8
30	25	15	548.6	31.8	10.6	39.6
30	25	-15	545.0	33.4	10.6	42.6

90	50	0	549.0	31.2	10.6	38.1
90	50	15	549.9	31.3	10.6	35.8
90	50	-15	547.0	31.9	10.6	38.3
90	75	0	547.7	27.3	10.6	29.4
90	75	15	549.0	27.7	10.6	31.7
90	75	-15	544.2	30.8	10.6	31.8
90	25	0	546.4	31.8	10.6	40.9
90	25	15	546.2	31.8	10.6	39.1
90	25	-15	550.5	32.2	10.6	42.3

C. Thermo-physical properties:

The thermo-physical properties are one of the most important input for every numerical study involving heat transfer. Good properties are required to get good results but do not warrant them. They can also play a significant part in the difficulty, for numerical software, to obtain results. That is why two batches of thermo-physical data have been used in this study to go from constant ones to some varying with the temperature.

C.1. Constant thermo-physical properties:

The simplest way to get a first insight in the welding process is to assume constant thermal properties. So when the thermal properties were considered constant, the following values were chosen and are based on the literature for mild steel [59].

- Specific heat: $C_p = 600 \text{ (J/kg K)}$
- Thermal conductivity $k = 40 \text{ (W/m K)}$
- Density $\rho = 7870 \text{ (kg/m}^3\text{)}$

C.2. Thermo-physical properties varying with the temperature:

First, a global overview presenting which parameters are needed and how to obtain them. Then, the data derived from the thermodynamic are discussed. After that a special section is dedicated to the thermal conductivity.

C.2.1. Global overview:

The properties needed for the simulation are the following:

- The density.
- The enthalpy.
- The thermal conductivity.

The first two can be derived directly from thermodynamic. One is a thermodynamic variable the other one is a function of the lattice parameters specific to the different phases present at a given temperature, which is given by thermodynamic. Therefore, to assess the variation of those two variable with the temperature Thermo-Calc[®] software was used.

The thermal conductivity is not easily derived from thermodynamic and Thermo-Calc[®] does not give it. So, another approach was used. A software giving the evolution of the thermal conductivity with the temperature for steels was developed by the materials algorithms project (MAP) which is affiliated to the University of Cambridge [69, 70]. It is used for the solid state. For the liquid state the Wiedemann-Franz-Lorenz law is applied [71]. The values for the transition zone are given by the addition of those two approach weighed by the liquid fraction. The convective mixing was simulated by multiplying the liquid thermal conductivity by a factor found in the literature [72].

C.2.2. Thermodynamic related properties:

The first part of this section is dedicated to a general presentation. Then the determination of the density and its variation is discussed. This is followed by a part discussing the specific heat and the enthalpy.

C.2.2.1. Foreword:

This section presents the work done, using Thermo-Calc[®], to obtain the data on the density, the enthalpy, and the phases amount. The first step is to define the system. In this software it means to specify the database and the elements used. The TCFE6 database was used. The elements taken into account are the following.

- Iron
- Carbon
- Chromium
- Manganese
- Niobium
- Aluminum
- Silicon
- Titanium
- Vanadium
- Nickel
- Copper
- Molybdenum

Taking more elements into account does not change significantly the results but can make it harder for this numerical software to give correct and coherent results.

A constant pressure of 101325 Pa was assumed and the quantity of matter of the system was fixed at 1 mole. The temperature on which the calculations were carried out ranged from 293 K to 3000 K. This range is wider than the actual range of temperatures that should be encountered in SAW operations. This is done on purpose to give a margin to the finite elements analysis software which will use those data for its calculations.

C.2.2.2. Density:

The quantity of matter in the system was fixed at 1 mole. The software does not give the density directly but it gives the mass and volume of the system. Therefore, the density was calculated within the software by defining a function giving the ratio between the mass and the volume of the system. The evolution of the density with the temperature given by Thermo-Calc[®] with a maximum step size of 0.5 K is reported in Figure C.1. The list of the phases appearing on the graph, according to Thermo-Calc[®], is given in Figure C.2.

Figure C.3 is a close up on the part of the graph where the evolution of the density with the temperature changes. The phases present for this interval of temperature are also reported on the graph too. This explains why the change occurs. Within this interval first a structure transformation from BCC, which is non-compact, to a FCC structure, which is a compact structure, occurs. A more compact phase occupies less space but still weights the same. Therefore, this increase in density is coherent with the other outputs of the software. The second drastic evolution in the density evolution with temperature comes from the inverse change in structure (from FCC to BCC) followed by the melting of the alloy.

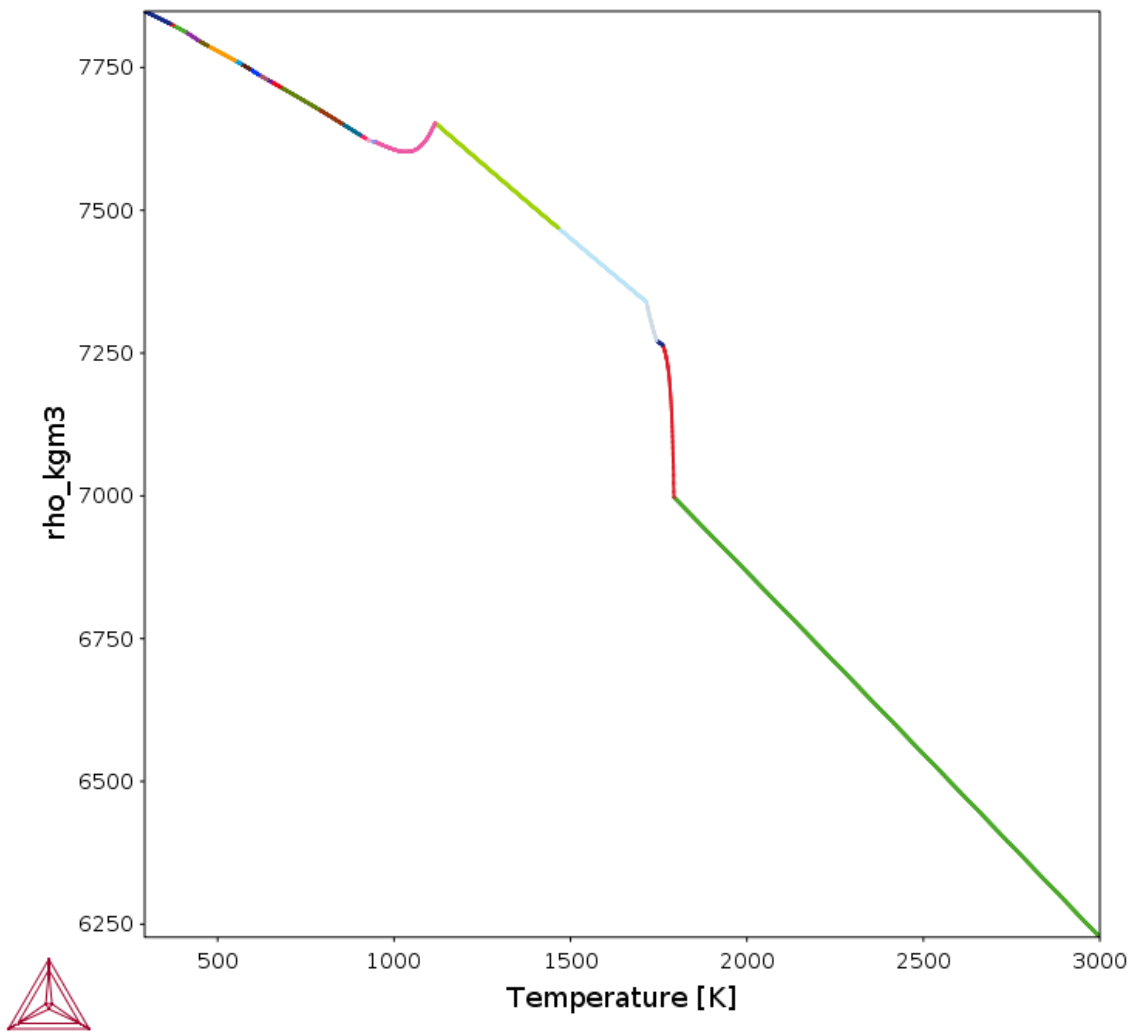


Figure C.1: Density as a function of temperature given by Thermo-Calc[®] for the bulk material and a maximum step size of 0.5 K.

It is interesting to also compare those results with some other results available in the literature. In the Materials Handbook [32] the density reported for HSLA is 7750 kg/m³. The maximum density given by the calculation is 7848 kg/m³ for 20 °C (the lowest temperature in the calculation). A density of 7750 kg/m³ is reached at 308°C. Therefore, as the temperature at which the book gives the density is not reported the results obtained by Thermo-Calc[®] seem to fit the ones from the Materials Handbook. Also a paper reported the same trend [73] as the one shown in Figure C.1 but the temperature at which the transition from BCC to FCC occurs is different in this paper. The steel considered in this paper is different and they were considering cooling with the production

of meta-stable phases like martensite. This means that there is no obvious mistake or unrealistic results in the output given by Thermo-Calc® for the density.

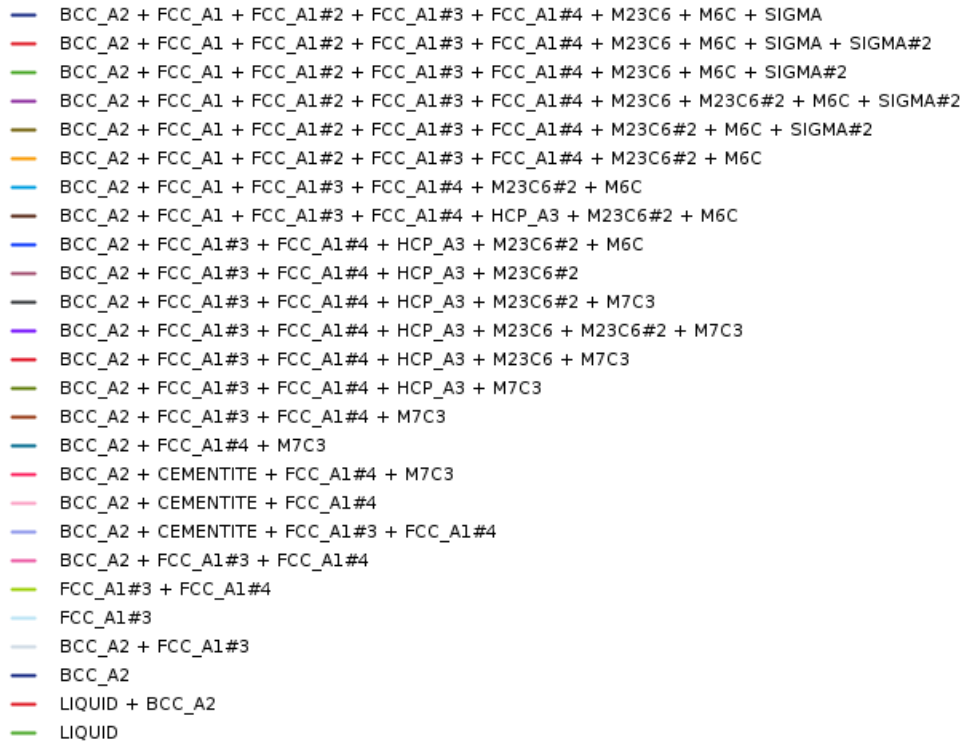


Figure C.2: Color legend of the phases present as a function of temperature.

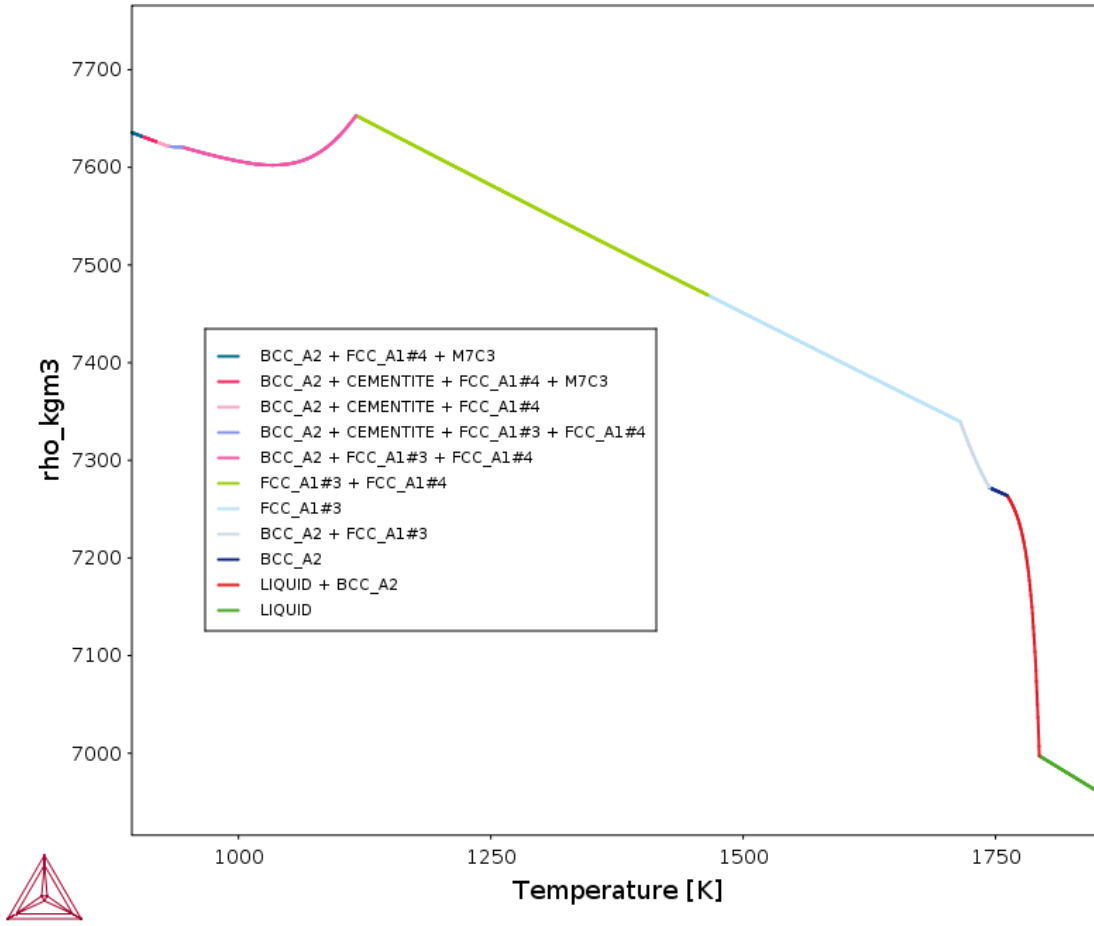


Figure C.3: Zoom on the parts of the density curves where a change in evolution is witnessed.

C.2.2.3. Specific heat and enthalpy:

The heat equation for a solid with no sources can be written as [74]:

$$\rho \frac{\partial h}{\partial T} \frac{\partial T}{\partial t} = \vec{\nabla} \cdot (k \vec{\nabla} T) \quad (C.1)$$

when discarding the phase changes it is possible to write:

$$c_p = \left(\frac{\partial h}{\partial T} \right)_p \quad (C.2)$$

this leads to the common formulation of the heat equation when no phase change occurs:

$$\rho c_p \frac{\partial T}{\partial t} = \vec{\nabla} \cdot (k \vec{\nabla} T) \quad (\text{C.3})$$

Various methods were developed to take the latent heat of fusion into account in the formulation of the c_p [74] but as the software directly gives the enthalpy it is more logical, and convenient, to use Equation (C.1) rather than using an apparent c_p .

The derivative of the enthalpy with respect to the temperature was used in this project. A custom function giving this derivative was used in the software. At the phase change the derivative changes really fast. The peak in the derivative was changing with the maximum step size chosen. This is certainly due to the fast change and a difficulty for the software to adapt its mesh correctly to it. Therefore, the maximum step size was reduced up to 0.1 K and the main peak of the derivative stabilized at a maximum step-size of 0.5 K as the peak derivative for this maximum step size was the same as for a maximum step size of 0.1 K.

For a maximum step-size of 0.5 K the evolution of the derivative of the enthalpy with the temperature is reported in Figure C.4. Every peak and break in the line corresponds to a phase change.

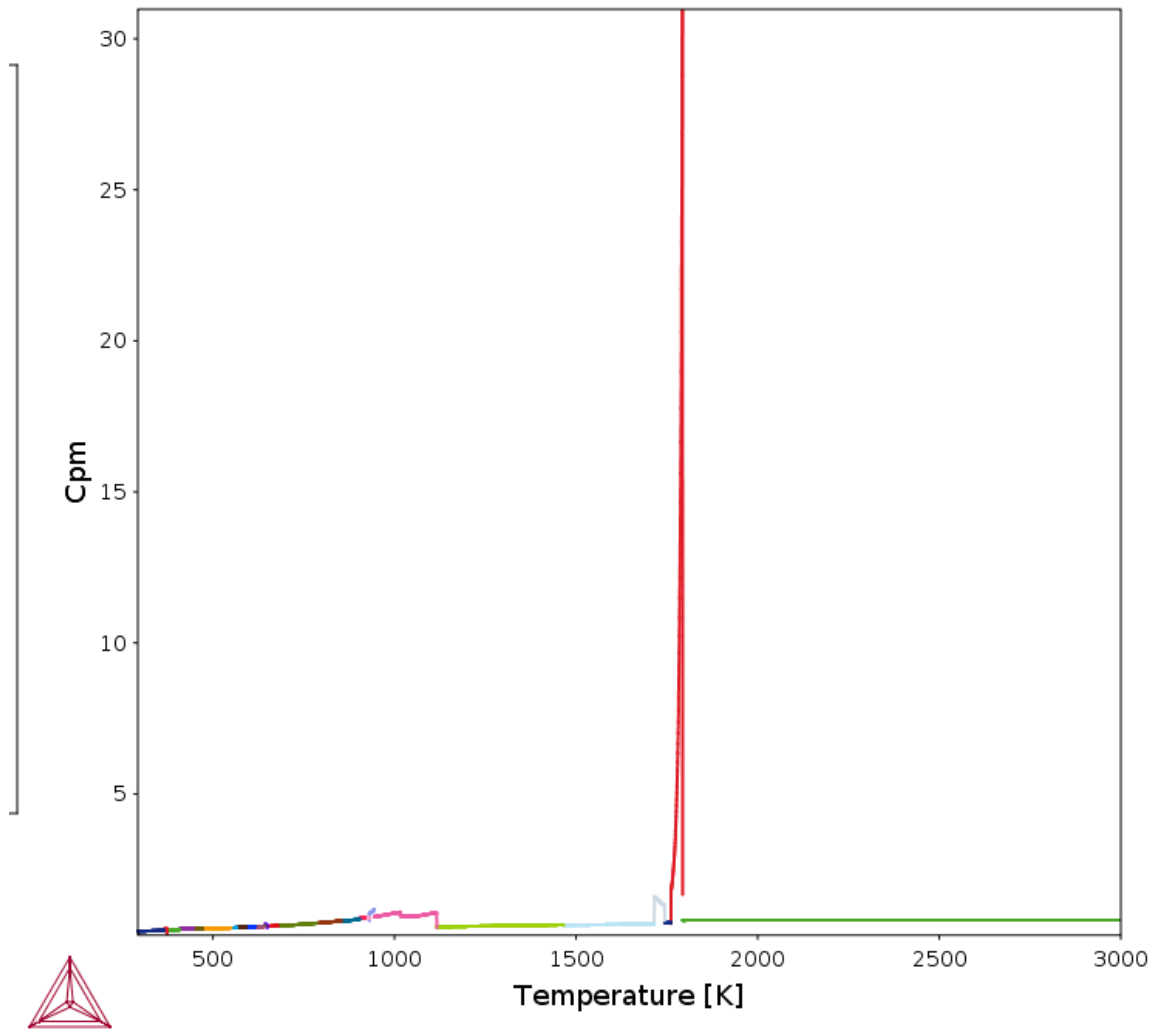


Figure C.4: Evolution, with the temperature, of the derivative of the enthalpy with respect to the temperature in J/g.K using a maximum step-size of 0.5 K.

C.2.3. Thermal conductivity:

This section is divided in three parts. They correspond to the determination of the thermal conductivity in solid state, in liquid state, and in the mushy zone.

C.2.3.1. In solid state:

For the solid state a program developed by the MAP is used. This program needs, as an input, the elements, and the temperature. The elements possible to take into account in this software are the following:

- **Carbon**
- **Manganese**
- **Nickel**
- **Molybdenum**
- **Vanadium**
- **Chromium**
- **Copper**
- **Aluminum**
- **Niobium**
- **Silicon**
- Tungsten
- **Titanium**
- Cobalt
- **Phosphorus**
- **Sulfur**

The elements in bold are the ones used in the program of the MAP. The underlined ones are the ones used for the second approach used to compare and ascertain the reliability of the results given by the program of the MAP.

The thermal conductivity is calculated at the same temperature on which the other properties have been computed by Thermo-Calc[®]. The evolution of the thermal conductivity with the temperature given by the program of the MAP is available in Figure C.5.

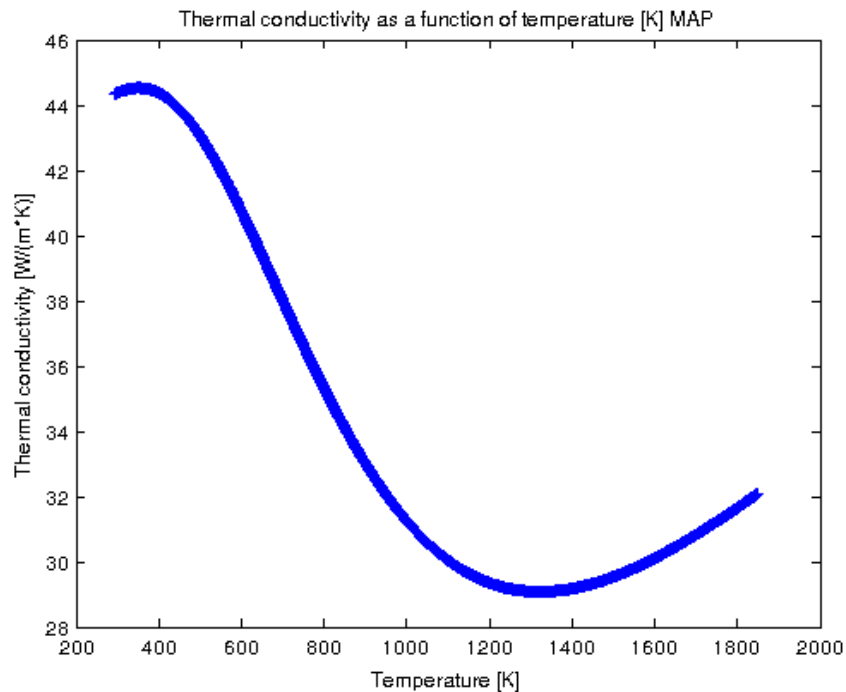


Figure C.5: Evolution of the thermal conductivity with the temperature in solid phase.

It is interesting to compare those results to some other results reported in the literature. Miettinen proposed a way to calculate the variation of the thermal conductivity with the temperature [75]. In

this method, Equation (C.4) is used from the solidus temperature down to the austenite decomposition temperature, it is the green points on Figure C.6. Then, three equations give the thermal conductivity for three different temperatures, Equation (C.5) for 400 °C, Equation (C.6) for 200 °C, and Equation (C.7) for 25 °C, these three points are displayed as red stars on Figure C.6. The “S” superscript means “solid”. The evolution of the thermal conductivity with the temperature given by this method is represented as a black line in Figure C.6. The austenite decomposition temperature is here considered to be 865°C based on a paper on pipe-steel [76].

It is really important to precise that Equation (C.4) is not the same as the one reported in the paper cited [75]. The reason is that, after email communication with Miettinen J., it was noted that there is a mistake in the equation numbered 66 in the paper. The term “ $-0.009T$ ” should be replaced by “ $+0.009T$ ”.

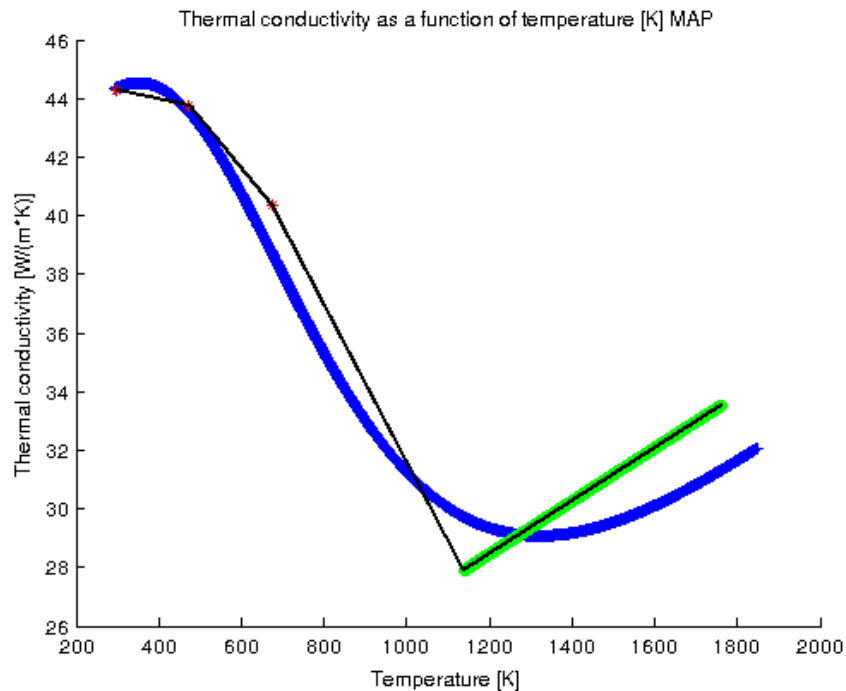


Figure C.6: Evolution of the thermal conductivity with the temperature according to the program of the MAP (blue) and according to Miettinen (black line). The red and the green points are part of the calculation for Miettinen's approach.

When comparing the two approaches (Figure C.6) one can see that they give results close to each other. The results given by the program of the MAP show a first increase in the thermal

conductivity when the temperature increases and then a decrease. This is not what the other approach shows here but this possibility is clearly considered by this approach too in the paper. The trends are the same for both methods and the first two points are on the results given by the MAP. Miettinen's approach is rougher but still matches the MAP results. The MAP approach's is better for the simulation because the evolution is smoother which makes the calculations easier.

$$\begin{aligned}
k^S &= 20.76 + 0.009 T - 3.2627 C_C^S + \\
&(0.0124 - 2.204 \cdot 10^{-4} T + 1.078 \cdot 10^{-7} T^2 + 7.822 \cdot 10^{-4} C_{Cr}^S - 1.741 \\
&\cdot 10^{-7} T C_{Cr}^S) C_{Cr}^S \\
&+ (-0.5860 + 8.354 \cdot 10^{-4} T - 1.368 \cdot 10^{-7} T^2 + 1.067 \cdot 10^{-2} C_{Ni}^S - 1.504 \\
&\cdot 10^{-5} T C_{Ni}^S) C_{Ni}^S - 0.7598 C_{Si}^S - 0.1432 C_{Mn}^S - 0.2222 C_{Mo}^S
\end{aligned} \tag{C.4}$$

$$\begin{aligned}
k^S(400^\circ C) &= 50.3 - 13.67 C_C^S + 5.245 C_C^{S^2} \\
&- 6.863 C_{Si}^S + 1.409 C_{Si}^{S^2} \\
&- 3.996 C_{Mn}^S + 0.188 C_{Mn}^{S^2} \\
&- 3.199 C_{Cr}^S + 0.141 C_{Cr}^{S^2} \\
&- 3.307 C_{Mo}^S + 3.174 C_{Mo}^{S^2} \\
&- 1.251 C_{Ni}^S + 0.014 C_{Ni}^{S^2}
\end{aligned} \tag{C.5}$$

$$\begin{aligned}
k^S(200^\circ C) &= 63.5 - 22.70 C_C^S + 9.612 C_C^{S^2} \\
&- 17.45 C_{Si}^S + 6.060 C_{Si}^{S^2} \\
&- 7.694 C_{Mn}^S + 0.419 C_{Mn}^{S^2} \\
&- 4.812 C_{Cr}^S + 0.216 C_{Cr}^{S^2} \\
&- 9.745 C_{Mo}^S + 8.388 C_{Mo}^{S^2} \\
&- 2.305 C_{Ni}^S + 0.040 C_{Ni}^{S^2}
\end{aligned} \tag{C.6}$$

$$\begin{aligned}
k^S(25^\circ C) = & 80.5 - 45.03C_C^S + 21.85 C_C^{S^2} \\
& -31.69C_{Si}^S + 11.57C_{Si}^{S^2} \\
& -15.32C_{Mn}^S + 0.959C_{Mn}^{S^2} \\
& -8.091C_{Cr}^S + 0.452C_{Cr}^{S^2} \\
& -4.674C_{Mo}^S + 0.204C_{Mo}^{S^2} \\
& -3.780C_{Ni}^S + 0.084C_{Ni}^{S^2}
\end{aligned} \tag{C.7}$$

C.2.3.2. In liquid state:

In the liquid state the Wiedemann-Franz-Lorenz law is used. This relation is based on the existing correlation between electrical and thermal conductivity in metals. It gives good results for liquid pure metals [63]. It can be used because the steel considered is a microalloyed steel in which the proportion of the main alloying element (carbon) is lower than 0.25 w%. Also Miettinen reported that the effect of those alloying elements in microalloyed steel on the thermal conductivity at high temperature is small [75]. The Wiedemann-Franz-Lorenz law depends on the material. Therefore some correlation are needed. Equation (C.8) and Equation (C.9) [71] are used. The temperature in the expression of the thermal conductivity (Equation (C.8)) is in Kelvin while the one in the expression of the electrical resistivity (Equation (C.9)) is in Celsius. Figure C.7 shows the evolution of the thermal conductivity with the temperature in the liquid.

$$k^L = \frac{2.445 \cdot 10^{-8}T}{\rho_e} \tag{C.8}$$

$$\rho_e = 0.0154T + 112.3 \tag{C.9}$$

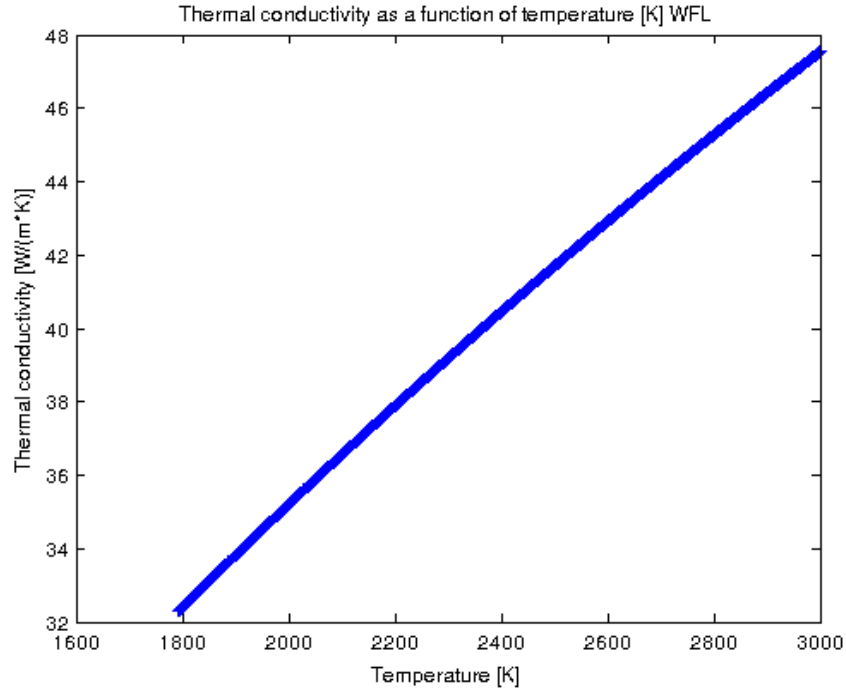


Figure C.7: Thermal conductivity in the liquid as predicted using the Wiedemann-Franz-Lorenz law.

C.2.3.3. Mushy zone and convection:

The way the thermal conductivity is computed in the solid and liquid zones were presented. These approaches need to be merged to take into account the mushy zone. To do so Equation (C.10) is used. The two thermal conductivities are multiplied by the fraction of phase they correspond to. “L” means liquid, “S” means solid.

$$k = f^L k^L + f^S k^S \quad (\text{C.10})$$

This equation is the actual global equation used to compute the thermal conductivity. In fact only the fraction of liquid is used. It is determined using Thermo-Calc[®]. So Equation (C.11) is used.

$$k = f^L k^L + (1 - f^L) k^S \quad (\text{C.11})$$

Equation (C.11) gives Figure C.8 on which you can see that the two sets of results are coherent because the last value from the solid state is less than 1 W/mK away from the first point of the liquid state.

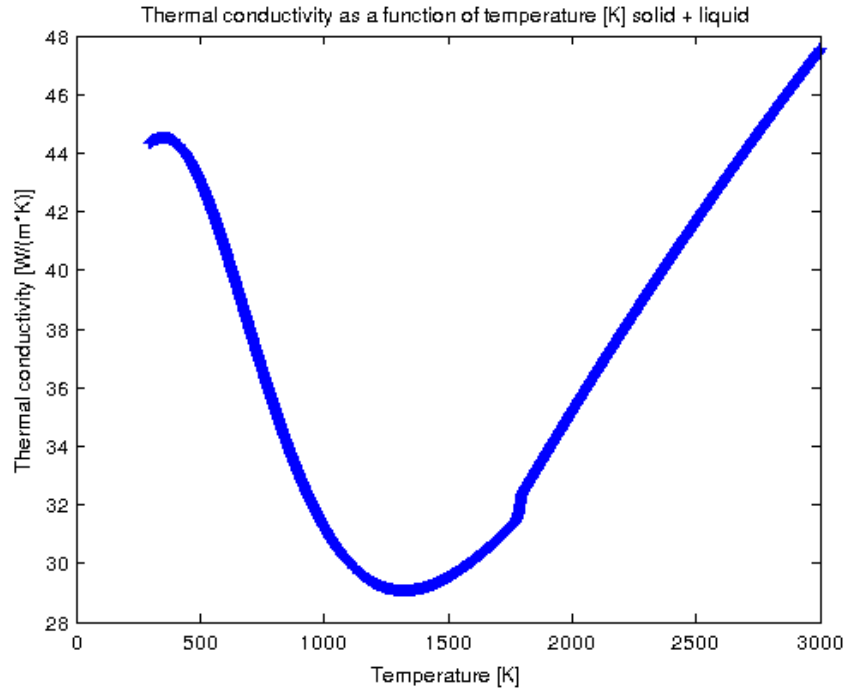


Figure C.8: Thermal conductivity computed using Equation (C.11).

In addition to the thermal conductivity it is possible to take into account the convection by adding a factor accounting for it in the expression of the thermal conductivity. In this case Equation (C.12) is used. The new term represent the convection stirring effect.

$$k = (1 + A_{mix})f^L k^L + (1 - f^L)k^S \quad (C.12)$$

The problem is to find the value of A_{mix} . For continuous casting some recommend values between 4 and 6 [72], while it is also argued that different A_{mix} should be used at different temperatures [77]. The problem is the lack of correlation between the A_{mix} and the temperature. Also the process studied here is welding which is different from continuous casting. The stirring is higher but also the molten zone is much smaller. These data are used by a numerical software. So, even

if a high value of A_{mix} could be closer to the reality to avoid discontinuity in the input, which would make it harder for the FEM software to solve the problem, a value 5 was chosen for A_{mix} .

Figure C.9 shows the thermal conductivity used for the calculations in this project.

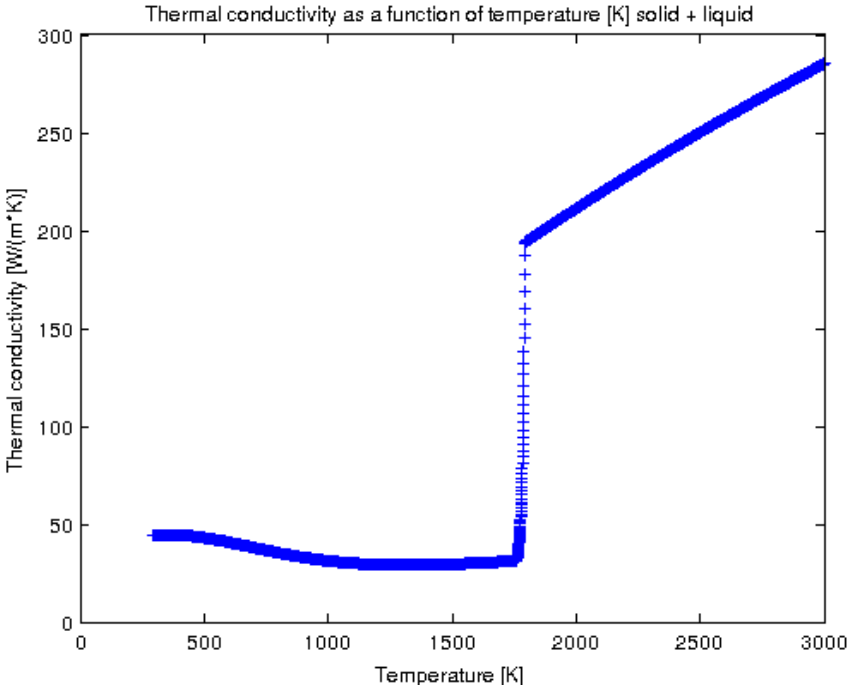


Figure C.9: Thermal conductivity computed using Equation (C.12) and an A_{mix} of 5.

D. Additional information on the experiments:

In this section the temperature profiles recorded are presented first. Then the output given by the welder are discussed.

D.1. Temperature profiles:

The measurements done with two type B and six type K thermocouples are presented first. Then, the experiment conducted with six type K thermocouples is presented.

D.1.1. Experiment with 8 thermocouples (2B,6K):

Here the temperature profiles obtained for thermocouples Ka and Kb are compared zone by zone.

Zone 1:

This zone is the first one encountered by the arc. It is also the one which corresponds to the good part of the weld. The signal given by the type B thermocouple is not exploitable. Therefore, the analysis will be focused on the other two thermocouples. The time scale has been reduce to the interval [40 s-85 s] to focus on the interesting part of the curve. The maximum derivative fixed for the removal of the outlier is 4000 K/s.

The first temperature profile, available in Figure D.1, corresponds to the thermocouple KbZ1. The maximum temperature reached at this point is 594°C. This temperature profile is constituted of two parts, a steeper part due to the heat of the arc being transferred by diffusion to the thermocouple and a second part which is the cooling of the point by diffusion in the parts of the bulk which are further away from the source. The evolution is smooth and no sharp peak is present.

The second temperature profile exploitable in the first zone, available in Figure D.2, corresponds to the thermocouple KaZ1. This temperature profile shows a sharp increase followed by a plateau then the profile ends with a smooth cooling. The first part is explained by the heating due to the arc and the melting of the metal. The problem is the plateau in the middle. The height of the plateau is signified by the red line which corresponds to 1450°C which is the maximum operational temperature indicated by the supplier, OMEGA[®]. This maximum operational temperature for a thermocouple corresponds to the lower melting point of the two materials constituting of the thermocouple. The maximum recorded temperature is 1455°C. Therefore, a part of the thermocouple melted. This explains the plateau.

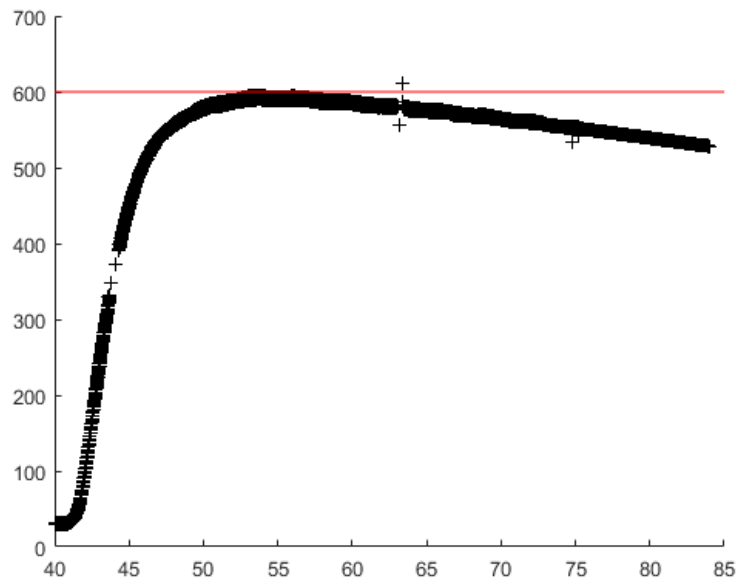


Figure D.1: Temperature profile recorded by the thermocouple KbZ1. The red line corresponds to 600°C.

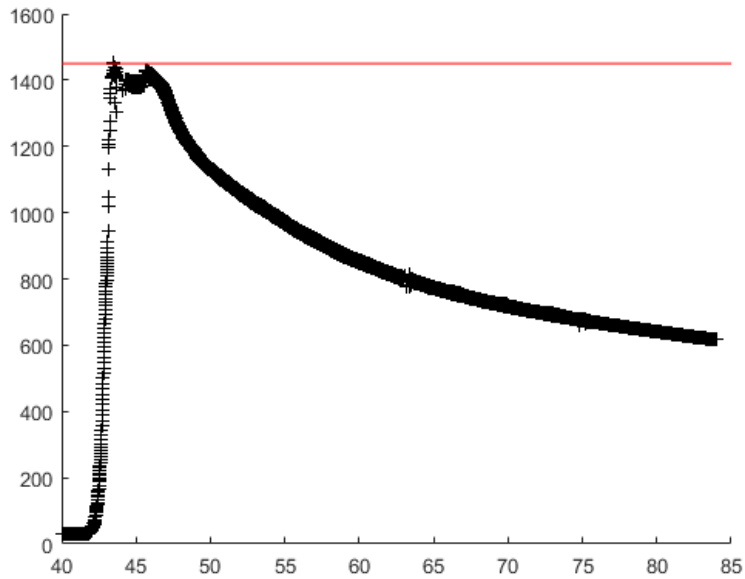


Figure D.2: Temperature profile reported by the thermocouple KaZ1. The red line corresponds to 1450°C.

Zone 2:

This zone is the one where no type B thermocouple was embedded. Also, the hole drilled for this thermocouple was kept empty. This is the first zone where the reinforcement of the weld begins to show instabilities. To focus on the relevant information the time scale is here reduced to the interval [49s-85s]. The maximum derivative used for the removal of the outliers is here 4000 K/s.

The temperature profile corresponding to KbZ2 is available in Figure D.3. The maximum temperature on the curve is 634°C. The first feature to be noted is that the maximum reached here is higher than the one reached by KbZ1. Also the evolution of the temperature is different than in zone 1. In this curve four zones are identified. The first one is a surge in temperature followed by a plateau and an exponential decay ended by another slower decay. The first and last part can easily be explained as before by the diffusion of the heat coming from the arc and by the cooling due to diffusion. The other parts can be explained by a displacement of the thermocouple during the recording.

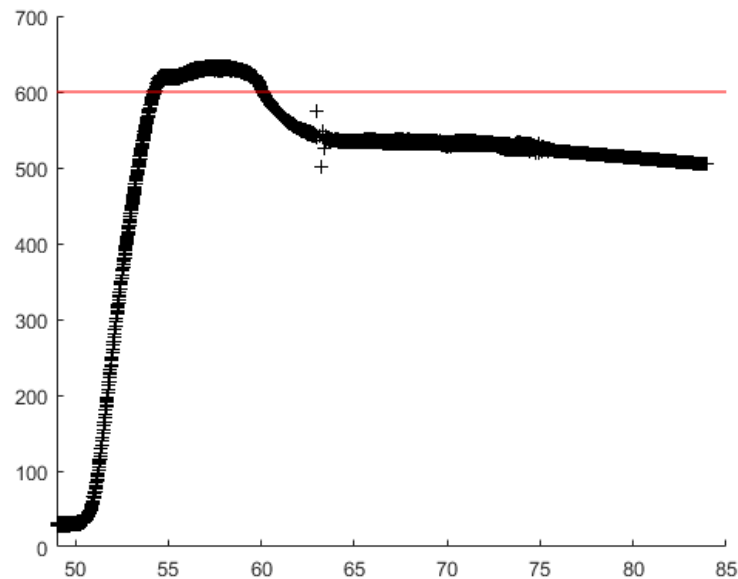


Figure D.3: Temperature profile recorded by the thermocouple KbZ2. The red line corresponds to 600°C.

The temperature profile given by KaZ2 is available in Figure D.4. The curve is similar to the one recorded for KaZ1 but the plateau is inexistent. The maximum temperature is 1454°C. The peak is

narrower and the lack of plateau seems to indicate that the actual temperature was close to the one indicated by the thermocouple at the peak. This indicates that the maximum temperature at the location of this thermocouple was lower than the one at the location of its equivalent in zone 1. This seems in contradiction with what KbZ2 shows but the bead shape is slanted. Some molten metal flowed in the hole where the thermocouple was placed. It explains why the temperature reaches the melting point of the thermocouple. Due to the melting of the steel the thermocouple which was spot-welded to the thermocouple can have moved pushed by the molten metal or due to some spring load coming from the installation of the thermocouple.

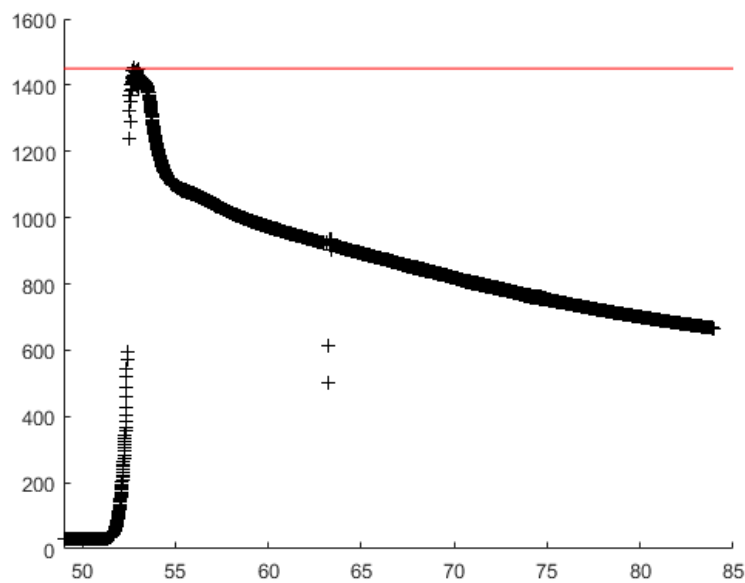


Figure D.4: Temperature profile reported by the thermocouple KaZ2. The red line corresponds 1450°C.

Zone 3:

This is the furthest zone from the starting point of the weld. This is the zone where the disturbances seen in the reinforcement are the biggest. The time scale is reduced to [59s-85s]. In the following graphs the maximum derivative used in the removal of the outliers is 5000 K/s.

On the graph representing the temperature profile recorded by KbZ3 (Figure D.5) the blue line corresponds to 700°C. The maximum temperature recorded is 694°C. The shape of the graph is the same as the one observed for KbZ1. The big difference with the profile of KbZ1 is the maximum,

as here the maximum is 100°C higher than for KbZ1. This was not foreseen, as the deportation of the bead is the same for KbZ1 and KbZ3. This can be due to burn through.

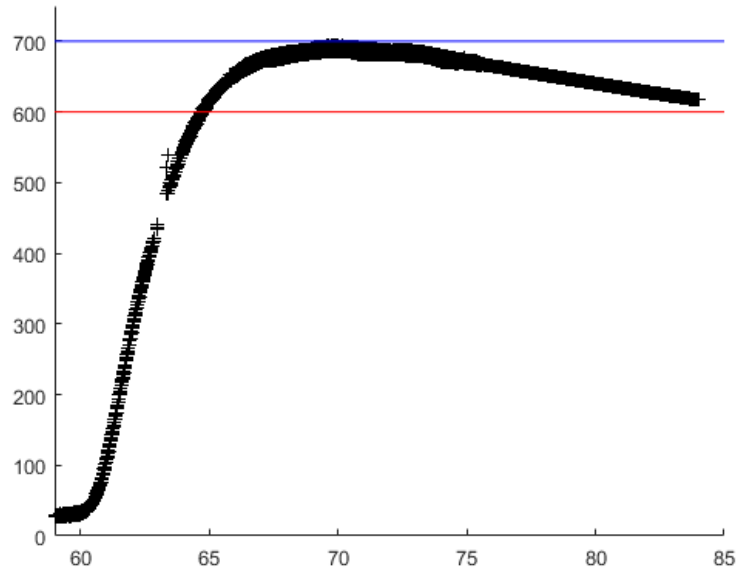


Figure D.5: Temperature profile recorded by the thermocouple KbZ3. The red line corresponds to 600°C. The blue one corresponds to 700°C.

Figure D.6 reports the temperature profile of KaZ3. The graph is similar to the one of KaZ2. The maximum temperature reached is 1405°C. This is lower than KaZ2. On KaZ1 a plateau is present while on KaZ2 a smaller part at the peak of the curve does not match exactly the cooling trend and is flatter than the rest of the curve. On KaZ3 no phenomenon like these ones are witnessed while the peak temperature is clearly under 1450°C. Burn through happened for this thermocouple. The fact that the reading does not go up to 1450°C indicates certainly that the thermocouple moved out of his position when the metal it was spot-welded to melted due to some spring load introduced while placing it.

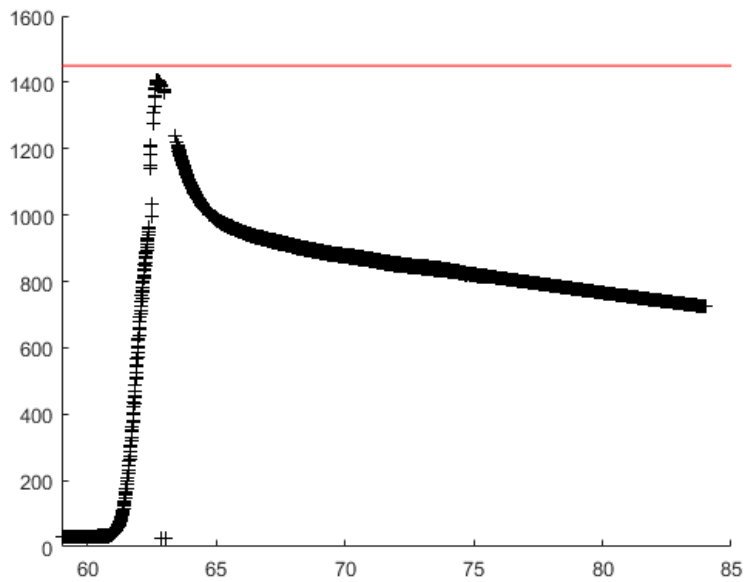


Figure D.6: Temperature profile reported by the thermocouple KaZ3. The red line corresponds 1450°C.

D.1.2. Experiment with 6 K thermocouples:

Here the temperature profiles recorded are analyzed zone by zone.

Zone 1:

The temperature profile corresponding to KbZ1, available in Figure D.7, is smoother than its equivalent in the experiment conducted with 8 thermocouples embedded. The maximum temperature is 600°C. The maximum derivative used for the removal of outliers is 1000K/s.

In Figure D.8 the temperature profile obtained for KbZ1 during the experiment which used type B thermocouples with a shift of 11.5 s to the left is superposed to the one available in Figure D.7. The shift has been decided to superpose the two curves. The heating parts of the two curves are similar and the heating rate are close to each other. A minor difference is seen at the peak which comes a little bit later. Instead, the cooling parts of the curve are different. Indeed, the cooling rate is, at first faster, for the present experiment compared to the previous one. Then, both temperature profiles seem to admit parallel asymptotes.

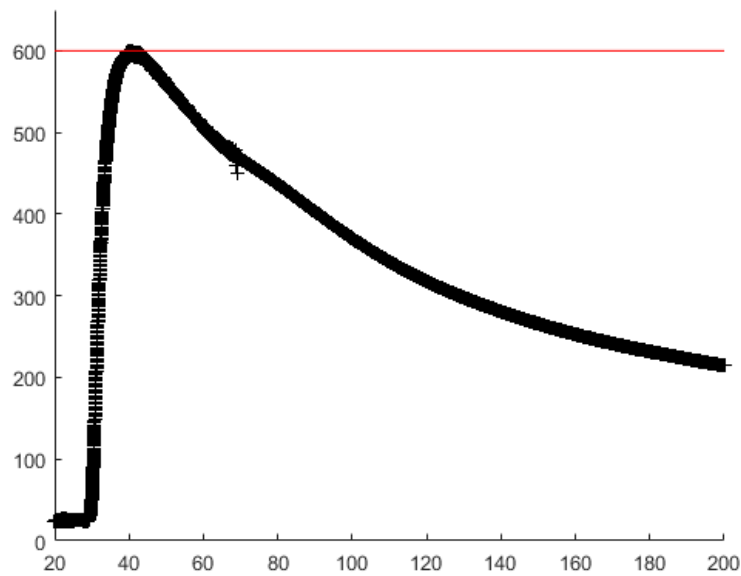


Figure D.7: Temperature profile recorded by the thermocouple KbZ1. The red line corresponds to 600°C.

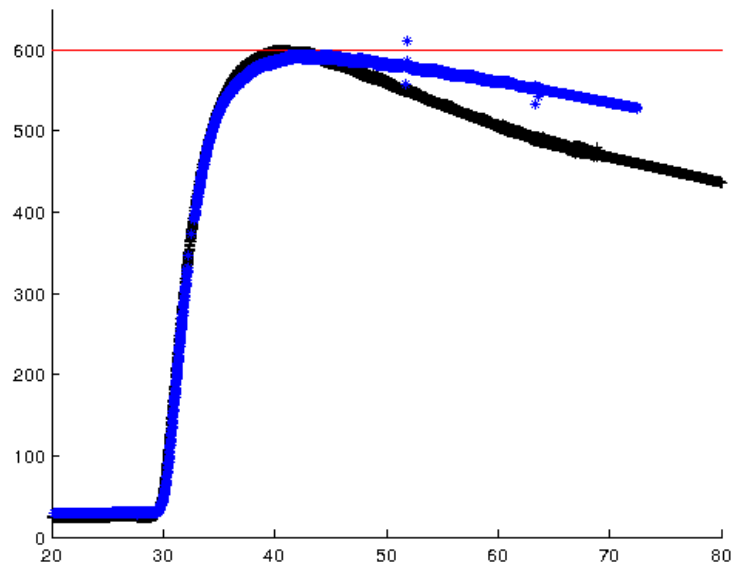


Figure D.8: The black curve corresponds to the temperature profile recorded by the thermocouple KbZ1. The blue one corresponds to the temperature profile generated with 8 thermocouples with a shift of 11.5s to the left. The red one corresponds to 600°C.

The temperature profile corresponding to KaZ1 is available in Figure D.9. In this case the maximum temperature reached is 902°C. The shape of the temperature profile, instead of what has been recorded before, only has two parts, a heating and a cooling regime.

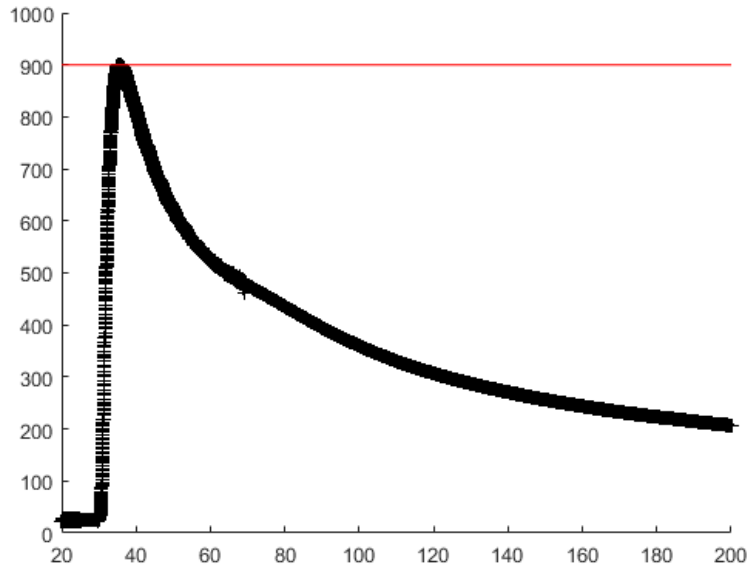
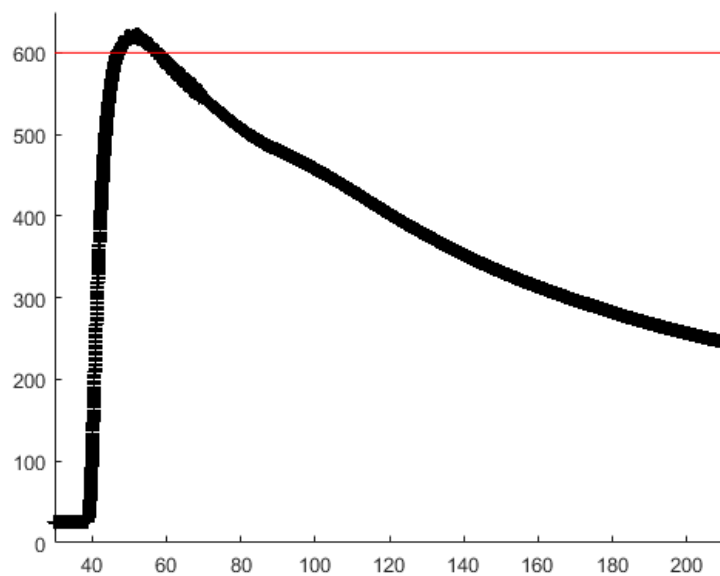


Figure D.9: Temperature profile recorded by the thermocouple KaZ1 after smoothing. The red line correspond to 900°C.

Zone 2:

The temperature profile in Figure D.10 corresponds to the one recorded by KbZ2. The maximum temperature recorded here is 623°C. The maximum derivative used for the removal of the outliers is 1000K/s. The temperature profile reported in Figure D.11 corresponds to KaZ2. The maximum recorded temperature is 833°C. The maximum temperature is lower than for KaZ1. Otherwise the evolution of the curve is similar to KaZ1.



**Figure D.10: Temperature profile recorded by the thermocouple KbZ2 after smoothing.
The red line corresponds to 600°C.**

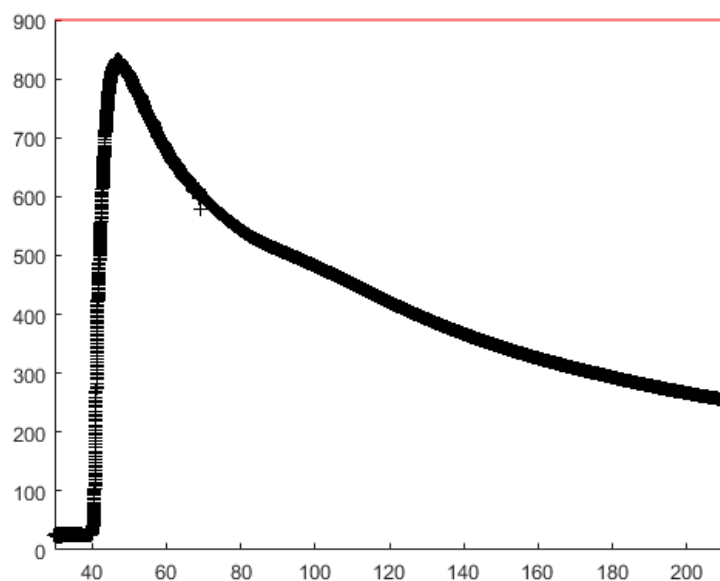


**Figure D.11: Temperature profile recorded by the thermocouple KaZ2. The red line
corresponds to 900°C.**

Zone 3:

Figure D.12 shows the temperature profile which corresponds to KbZ3. The maximum temperature derivative used for the removal of the outliers is still 1000K/s. The maximum temperature recorded here is 539°C

A comparison with the temperature profile recorded by the thermocouple KbZ3 in the experiment in which type B thermocouples were embedded is available in Figure D.13. Once again the heating slopes are sensibly different. The maximum temperature is also not reached at the same time.

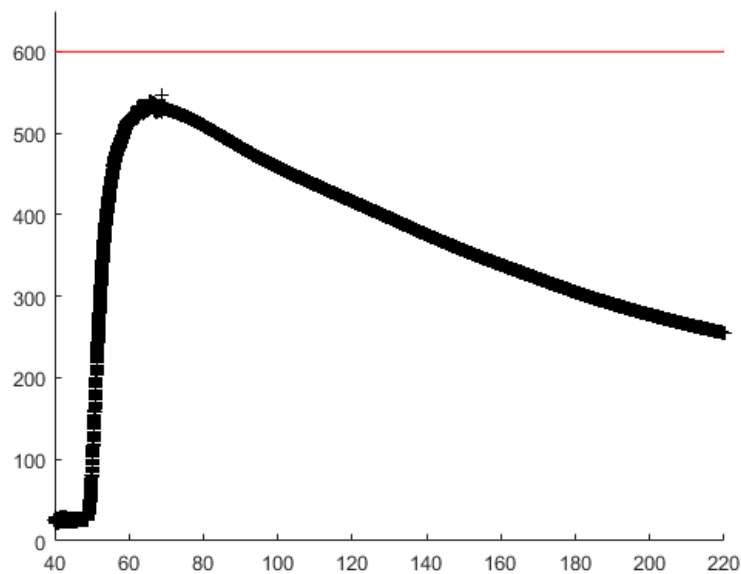


Figure D.12: Temperature profile recorded by the thermocouple KbZ3. The red line corresponds to 600°C.

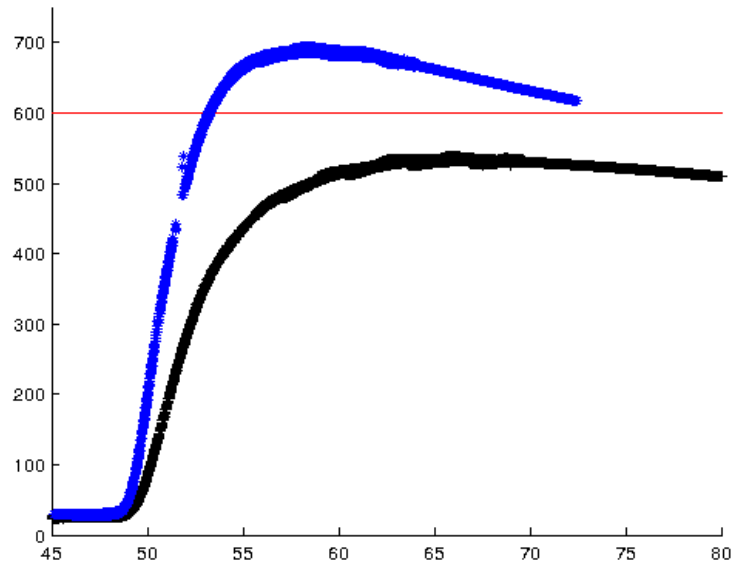


Figure D.13: The black curve corresponds to the temperature profile recorded by the thermocouple KbZ3. The blue one corresponds to the temperature profile generated with 8 thermocouples and with a shift of 11.5s to the left. The red one corresponds to 600°C.

The data produced by KaZ3 is reproduced in Figure D.14. The maximum temperature reached is 922°C. It is the highest peak among the Ka thermocouples for this experiment. An artefact is present just after the peak where the temperature drops then goes back up again. This can be explained by some local disturbances in the weld above the measured point.

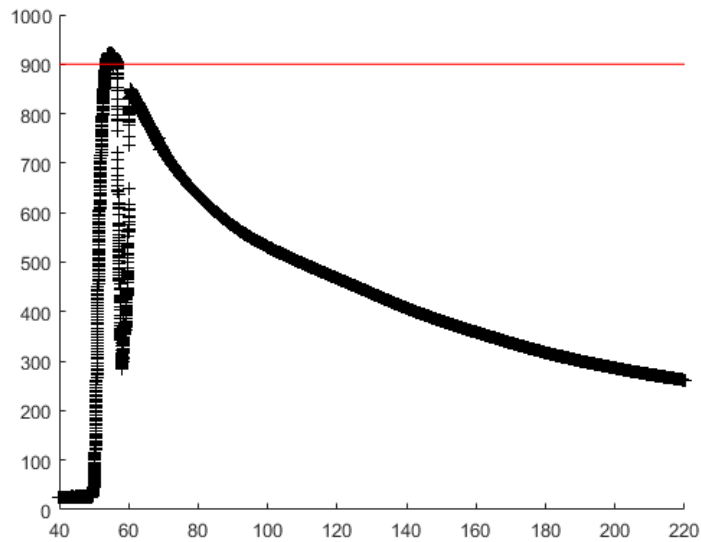


Figure D.14: Temperature profile recorded by the thermocouple KaZ3. The red line corresponds to 900°C.

D.2. Output of the welder:

The output recorded by the welder for the BOP weld is first presented. Then, the one recorded while a weld was performed on a machined plate with no thermocouples embedded is discussed. After that the output recorded when two type B and six type K thermocouples were embedded is presented. Finally, the data recorded by the welder when six type K thermocouples were embedded are reported.

D.2.1. Bead on plate experiment:

The welder was equipped with an instrumentation device recording the current, the voltage and the WFS throughout the experiment. The first, and last, six points were removed to get rid of the starting and stopping phases, without suppressing the meaningful data, which are outside the scope of the quasi-steady state.

D.2.1.1. Current:

The evolution of the current with time is available in Figure D.15. The average current value is 700A (red line) while the standard deviation is 2.47A. Visually no patterns are noticed in the

deviation of these points from the mean. The mean value corresponds to the value specified for the experiment.

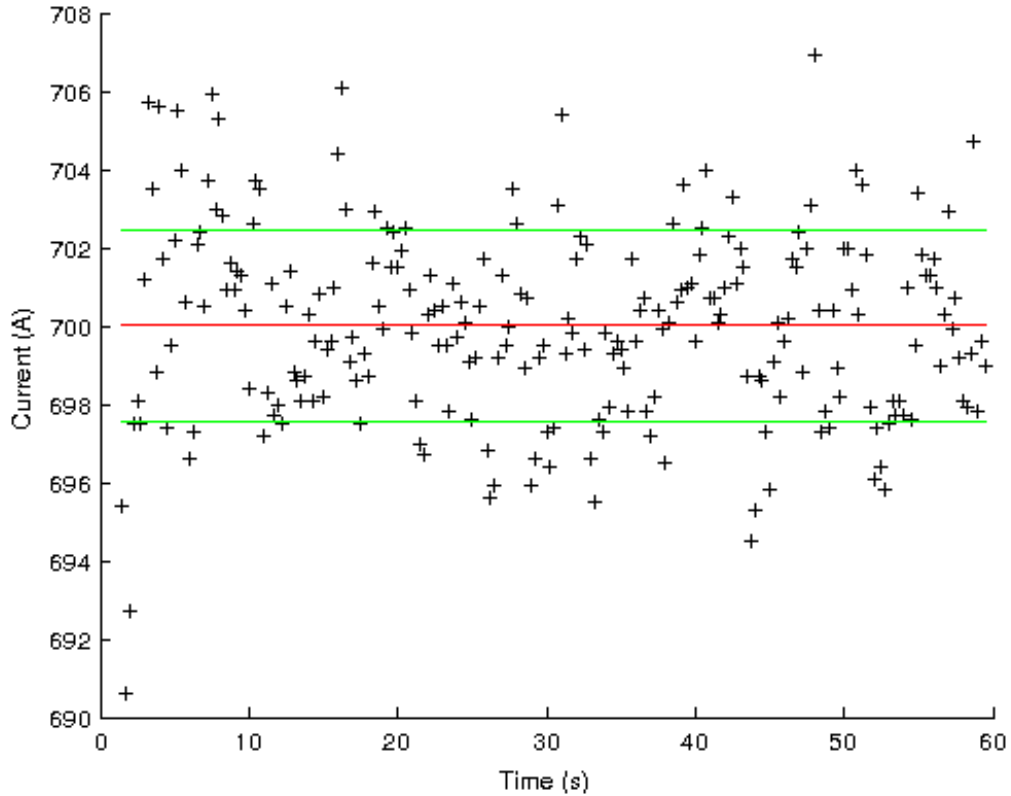


Figure D.15: Current recorded by the welder during the BOP experiment. The red line corresponds to the mean value (700 A) and the two green ones correspond to the mean plus or minus the standard deviation (2.47 A).

D.2.1.2. Voltage:

The evolution of the voltage with time during the experiment is available in Figure D.16. The observed mean value is 31.9 V; which is really close to the aim (32 V). The standard deviation is 0.53 V. No patterns are distinguishable in the distances of the points from the mean (red line).

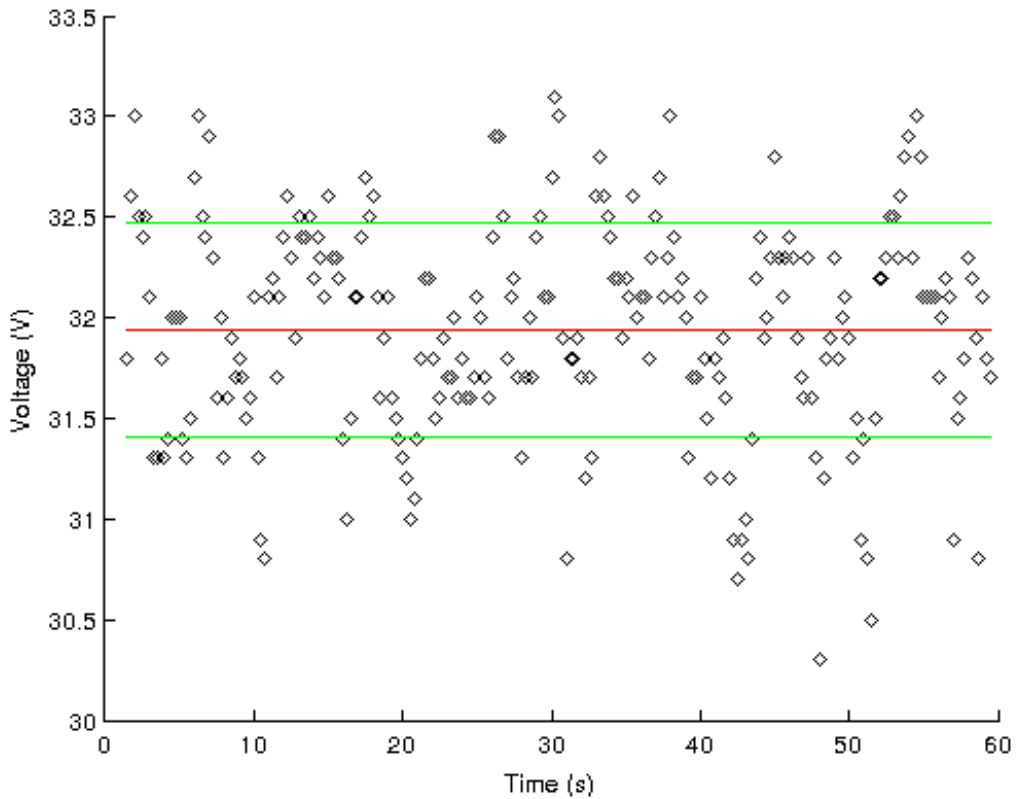


Figure D.16: Voltage evolution throughout the BOP experiment. The red line corresponds to the mean (31.9 V) and the green line corresponds to the mean plus or minus the standard deviation (0.53 V).

D.2.1.3. Wire feed speed:

The WFS is an important data for productivity assessment. Its evolution with time is available in Figure D.17. On this figure are superimposed to the actual recording a red line showing the mean (32.9mm/s) and two green lines corresponding to the mean plus or minus the standard deviation (0.70 mm/s). The WFS calculated using the equations developed in Appendix C is also reported in the figure, as blue stars for the calculations using the actual current recording and as a black line when the aim current is used for the calculation.

No patterns can be seen in the data deviation from the average. The WFS calculated using the recorded current is close to the value calculated with the aim current. The relative absolute difference between the calculated WFS using the aim parameters and the data average is 2.26%. It is calculated using the formula reported in Equation (D.1).

$$ERR\% = 200 \cdot \left| \frac{WFS_{Experiment} - WFS_{Calculated}}{WFS_{Experiment} + WFS_{Calculated}} \right| \quad (D.1)$$

The graph available in Figure D.17 shows that the chosen parameters give results close to the one calculated in this case.

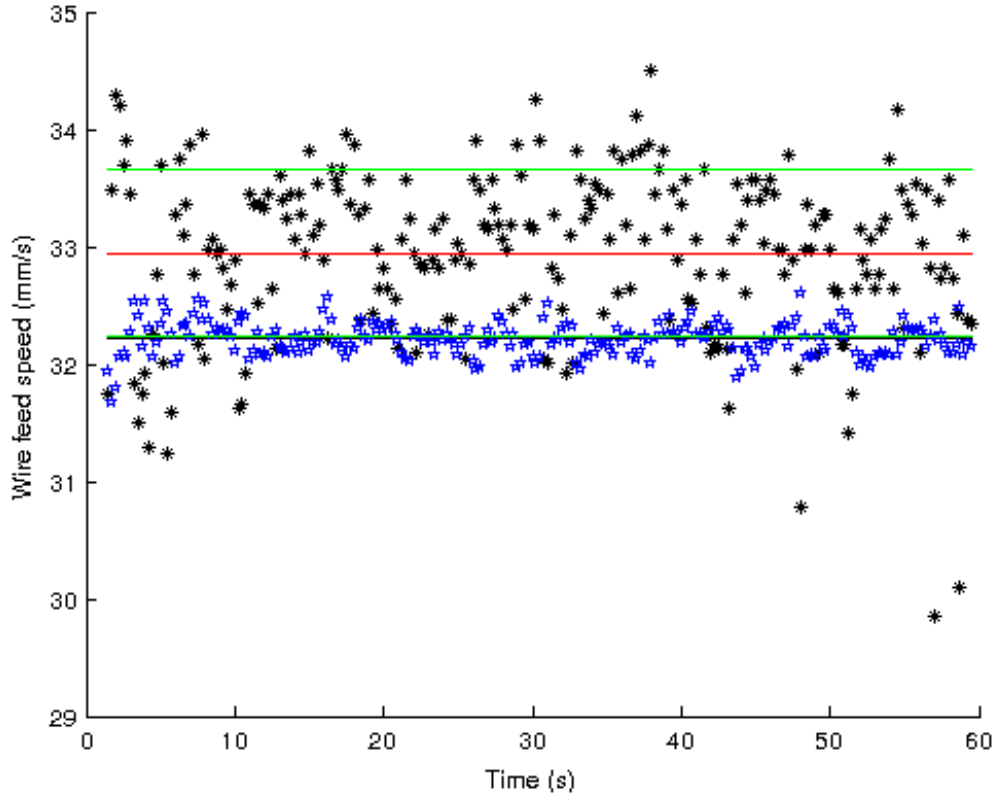


Figure D.17: The black stars represent the recorded evolution of the WFS during the BOP experiment. The red line shows the mean (32.9 mm/s) and the green ones represent the mean plus or minus the standard deviation (0.70 mm/s). The blue stars correspond to the WFS calculated from the method presented in Appendix A and the recorded current. The black line corresponds to the WFS calculated using the aim current (32.2 mm/s). It is under the lower green line.

D.2.2. Weld on machined plate without thermocouples:

The first and last six point have been removed on the outputs of the welder to remove the starting and stopping phase which are of no interest for the present work. The outputs analyzed here are: the current, the voltage, and the WFS.

D.2.2.1. Current:

The evolution of the current with time for the experiment carried out without thermocouples but on a machined plate is available in Figure D.18. The average current recorded is 700 A and the standard deviation is 2.46 A. No deviation patterns are witnessed from the average. This is the same as what was witnessed for the BOP experiment. Therefore, it advocates toward the hypothesis that the machining of the plates does neither change nor disturb significantly the current inputted and its regulation system.

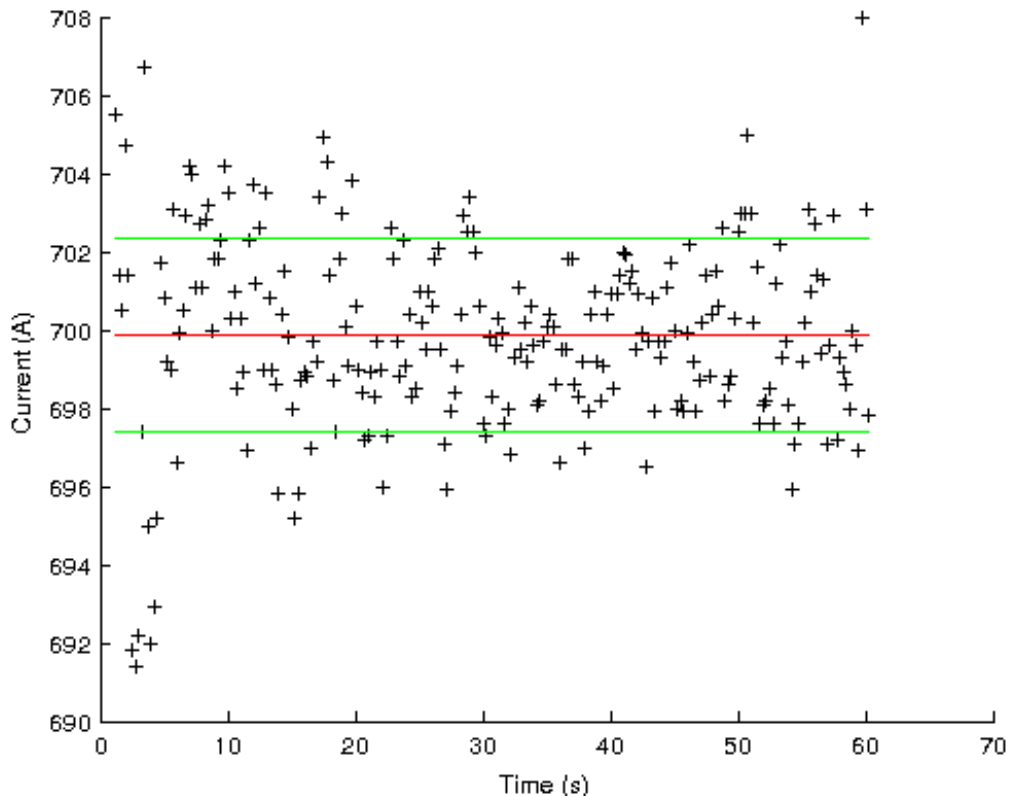


Figure D.18: Evolution of the current during the welding operation carried out on a machined plate with no thermocouples embedded. The red line corresponds to the average (700 A), the green lines to the mean plus or minus the standard deviation (2.46 A).

D.2.2.2. Voltage:

Figure D.19 shows the evolution of the voltage during the experiments. It also shows the average voltage (32 V) and its standard deviation (0.50 V). This graph is similar to the one recorded for the BOP weld except that more points are located below the lower green line at the beginning and the end of the graph. This trend is not strong enough to challenge the assumption that the voltage is not affected by the change in geometry of the plate to be welded. Otherwise, no clear deviation patterns from the average are seen. This tends to prove that the machining of the plate does not have bearing on the voltage regulation.

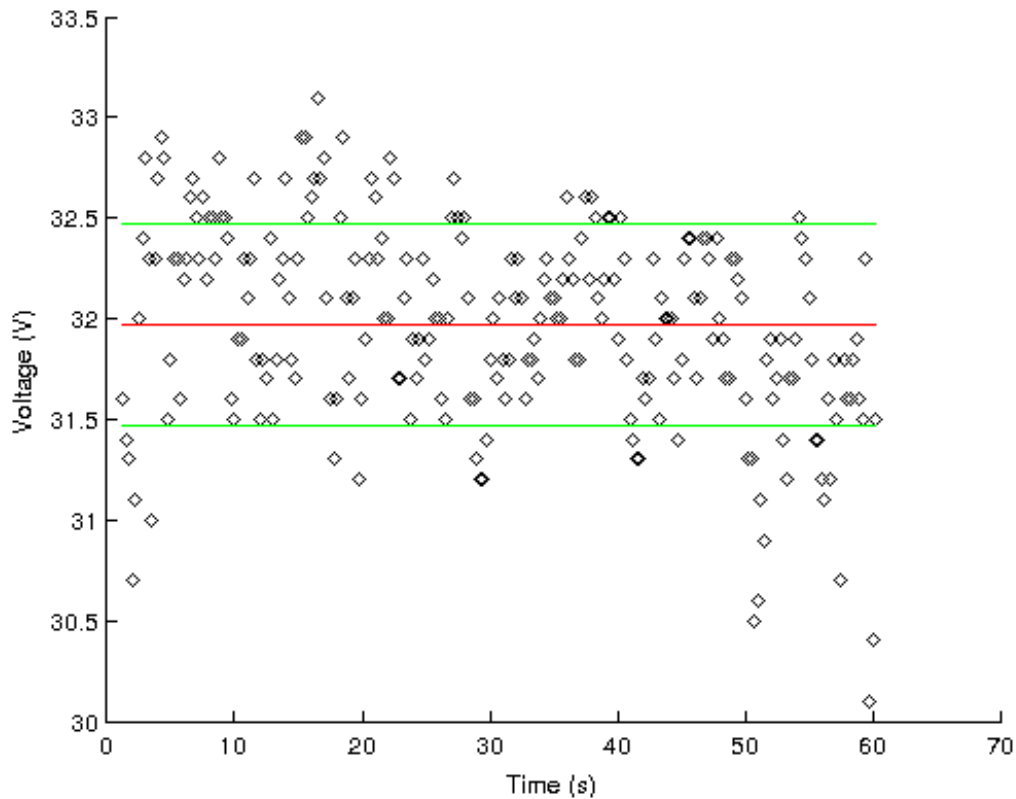


Figure D.19: Evolution of the voltage during the welding operation carried out on machined plate with no thermocouples embedded. The red line corresponds to the average (32 V), the green lines to the mean plus or minus the standard deviation (0.50 V).

D.2.2.3. Wire feed speed:

One concern about the change in geometry comes from the bevel as it needs to be filled. The contact tip to work distance increases due to the depth of the bevel. Therefore, an increase in WFS is foreseen.

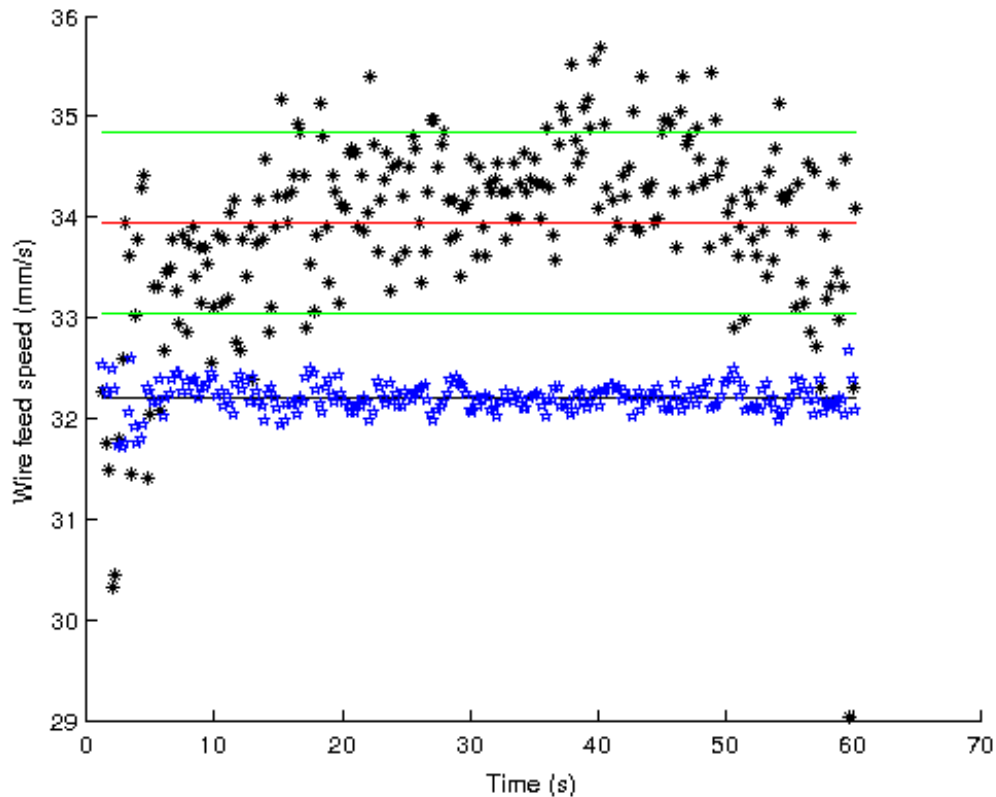


Figure D.20: The black stars represent the recorded evolution of the WFS for a weld performed on a machined plate without thermocouples. The red line shows the mean (33.9 mm/s) and the green ones represent the mean plus or minus the standard deviation (0.90 mm/s). The blue stars correspond to the WFS calculated from a formula obtained via regression using the recorded current and the black line corresponds to the WFS calculated using the aim current (32.2 mm/s).

The recorded WFS is available in Figure D.20. As described in the BOP section the recorded WFS is represented along with some calculated values. The average WFS is 33.9 mm/s with a standard deviation of 0.90 mm/s. The calculated WFS based on the aim parameters is 32.2 mm/s. The

deviation from the calculated value of the experimental average is 5.23 %. Therefore, the WFS is still close to what was calculated. The average value is higher than for the BOP experiment.

The change of geometry, from BOP to the machined plate, seems to have an effect on the variability of the data and the starting and ending phases. Otherwise, no major changes are witnessed. Therefore, this does not jeopardize the experiments and its data.

D.2.3. Experiment with 8 thermocouples (2B,6K):

After the analysis carried out on the experiments without thermocouples this one is centred on the comparison with these analysis. The time when the data acquisition system was started and the time when the data from the welder began are different. The data from the welder begin at the same time as the weld, while the data acquisition system was started before. The hypothesis that the noise produced by the arc is responsible for the part of the variability of the data which stop suddenly at approximately 75 s in this experiment is posed. This is based on the sudden reduction in thickness of the graph due to the reduction of scatter and that no other process in the experiment can affect all the thermocouples at the same time. If this hypothesis is accepted, then it is possible to calculate the difference in time between the start of the data acquisition system and the start of the arc. This difference is 20 s.

D.2.3.1. Current:

The change in current during the experiment is available in Figure D.21. The average current is 701 A while the standard deviation is 4.27 A. The average value and the standard deviation show that from an overall point of view the command system works well as the average is close to the inputted parameter.

The analysis before showed that the system had no problems to give 700 A but here at the beginning the system gives current that are above the mean plus three times the standard deviation indicating that these points are not generated by random error. Therefore, there is a real trend at the beginning of the signal. The delay between the starting times being 20 s this surge should not affect the temperature profile.

Around 25 s and 43 s the scatter in the data increase. These times correspond to when the two type B thermocouples were put out of order. Based on the standard deviation the presence of the thermocouples here seems to increase the variability in the data.

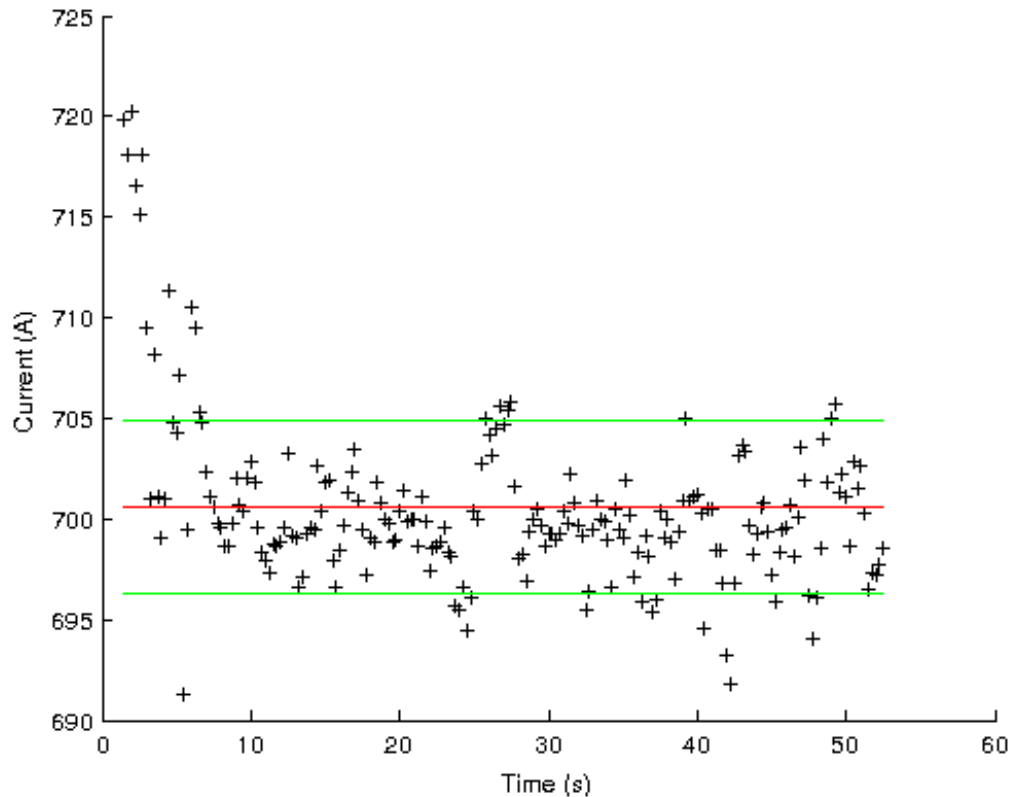


Figure D.21: Evolution of the current during the welding operation carried out with eight thermocouples embedded. The red line corresponds to the average (701 A), the green lines to the mean plus or minus the standard deviation (4.27 A).

D.2.3.2. Voltage:

The voltage change during the experiment is available in Figure D.22. The average voltage delivered in the experiment is 32.2 V. The standard deviation is 0.60 V. The average voltage is still close to the aim value.

On the graph showing the voltage (Figure D.22) two small peaks in scatter are present. Likewise, here two peaks in the data are located at around 25 s and around 43 s. This backs up the idea that the delay between the two starts is 20 s. Also this participates to the scatter in the data and can explain a part of the increase in standard deviation.

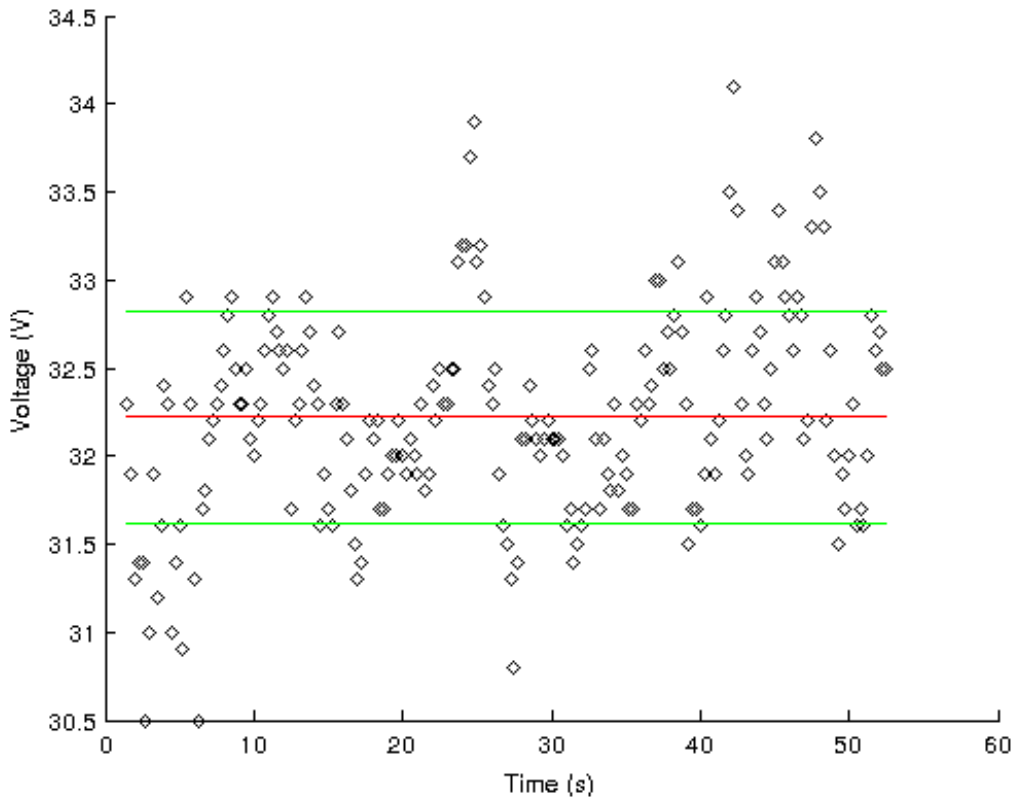


Figure D.22: Evolution of the voltage during the welding operation carried out with eight thermocouples embedded. The red line corresponds to the average (32.2 V), the green lines to the mean plus or minus the standard deviation (0.60 V).

D.2.3.3. Wire feed speed:

The evolution of the WFS with time is shown in Figure D.23 as black stars. The blue stars correspond to the calculated values of the WFS based on the current recorded by the welder. The black line corresponds to the WFS calculated with the aim parameters. The red line shows the average (32.7 mm/s) and the green lines show the mean plus or minus the standard deviation (1.43 mm/s).

Here, even if the values of the average and the standard deviation shows that the output is not far from the aim, some new feature are encountered. The points begin by showing a downward trend crossing the black line. Then a clear rising trend is witnessed. By looking at the blue stars one can deduce that the downward trend at the beginning could be explained by the surge in current at the beginning of the process. Afterward, except at 25 s where there is a peak certainly caused by BZ1

being destroyed, the trend seems to come from another phenomenon. One of the hypothesis put forward just after the experiment is that the piece would not be correctly grounded. The problem is that the plate was grounded with a copper electrode and four clamps which is the same as before when this trend was not witnessed.

The only remaining factor that can explain this is the presence of the thermocouples. However, the process by which they affect the WFS is not clear.

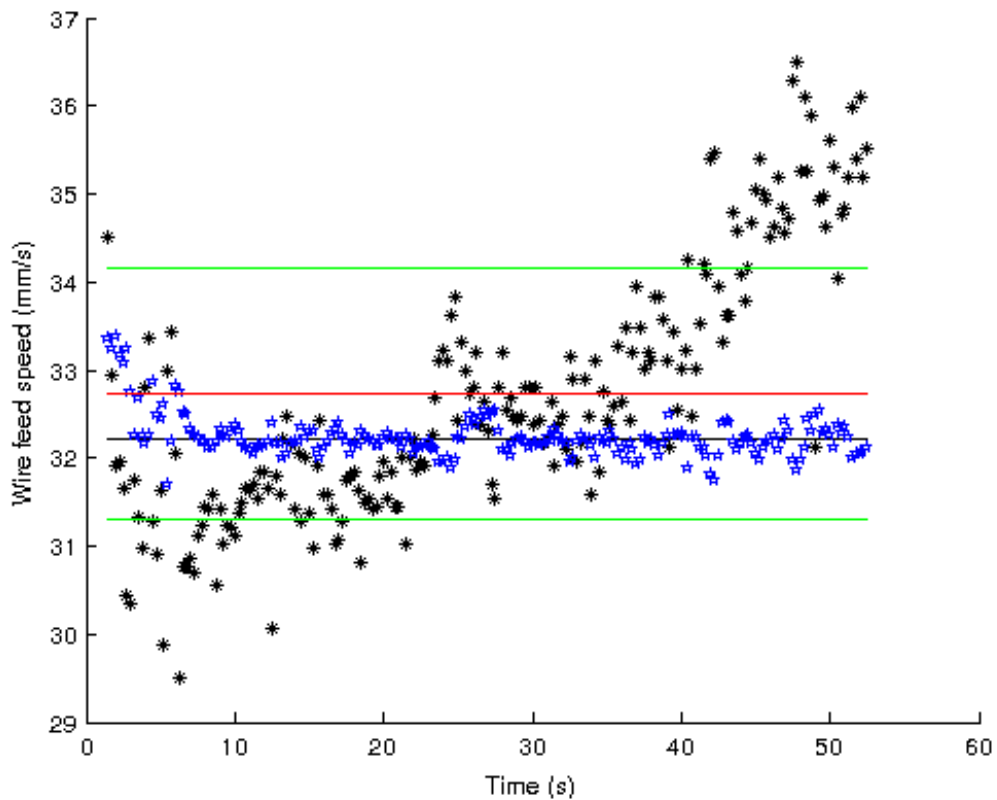


Figure D.23: The black stars represent the recorded evolution of the WFS during the experiment with eight thermocouples. The red line shows the mean (32.7 mm/s) and the green ones represent the mean plus or minus the standard deviation (1.43 mm/s). The blue stars correspond to the WFS calculated from a formula obtained via regression using the recorded current and the black line corresponds to the WFS calculated using the aim current (32.2 mm/s).

D.2.4. Experiment with 6 K thermocouples:

Following the same reasoning as previously the delay between the start of the data acquisition system and the start of the welding device is around 13s. The reduction in thickness in the data of the thermocouples occurs roughly 70s after the start of the weld and the weld lasted 57 s according to the data of the welder.

Here is presented the evolution of the current, the voltage, and the WFS throughout the experiment.

D.2.4.1. Current:

The recording of the change in current during the experiment is available in Figure D.24. The average current is 701 A which is close to the aim. The standard deviation is 3.94 A.

As noticed in the previous analysis here a surge in current is witnessed at the beginning of the weld. This can be interpreted as an elongation of the starting process. This phase comes to an end within the first 10 s of the experiment while the first signal recorded by the first thermocouple starts after 15 s from the start of the weld. Therefore, this surge should not have a direct effect on the weld. The points between 40 s and 50 s tends to be higher than the other ones and form a second peak in the data. This range of time corresponds to the time when the artefact in the signal KaZ3 occurs. This backs up the idea that a problem in the arc occurred at this time. A common problem that can explain the shape of the reinforcement as well as the surge in current is short-circuit. When short-circuit occurs the resistance of the system drops drastically thus increasing the current.

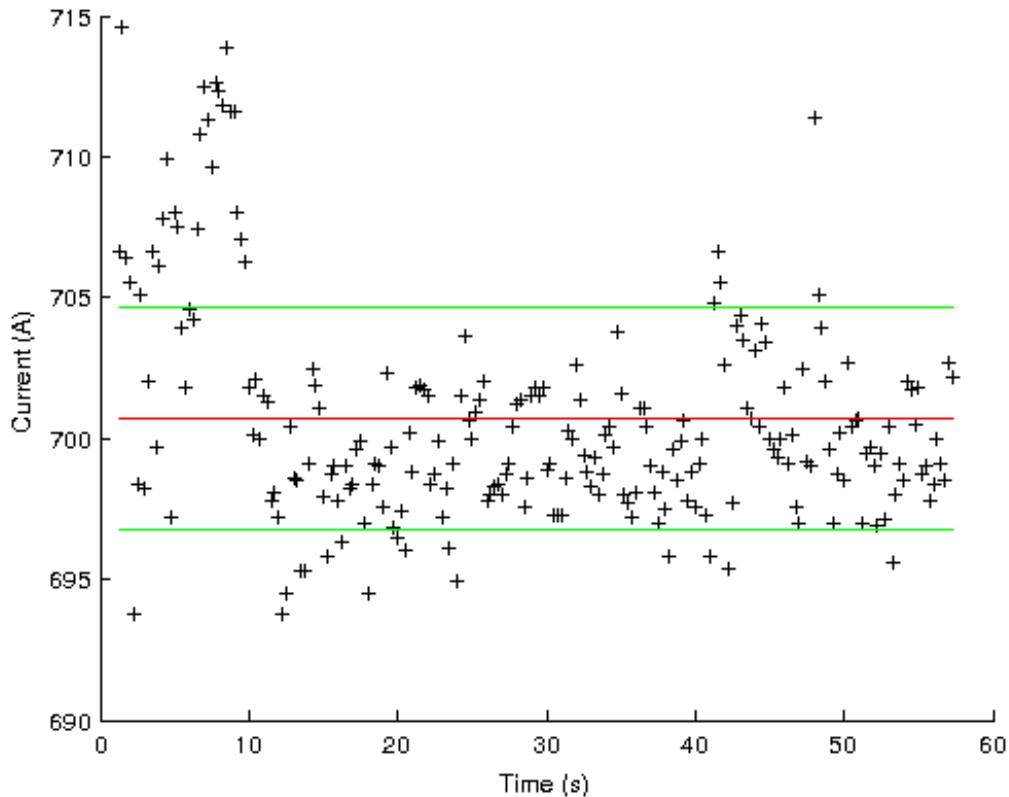


Figure D.24: Evolution of the current during the welding operation carried out with six thermocouples embedded. The red line corresponds to the average (701 A), the green lines to the mean plus or minus the standard deviation (3.94 A).

D.2.4.2. Voltage:

The evolution of the voltage throughout the experiment is reported in Figure D.25. The average voltage recorded is 31.7 V which is close to the aim of 32 V. The standard deviation is 1.19 V.

In the beginning of the signal a surge followed by a decrease in the signal is witnessed. The surge can be explained by the starting phase. The decrease can be explained by the fact that the system was operated in a constant current mode. Therefore, the welder tried to keep the current as stable as possible and did so by adjusting other parameters like the voltage. So, the association of the two peaks is certainly generated by the regulation process. The disturbance lasts longer for the voltage which is logical as the system was operated in constant current mode. This association of two peaks is also present between 40 s and 50 s which is approximately the time when the artefact for KaZ3 is recorded.

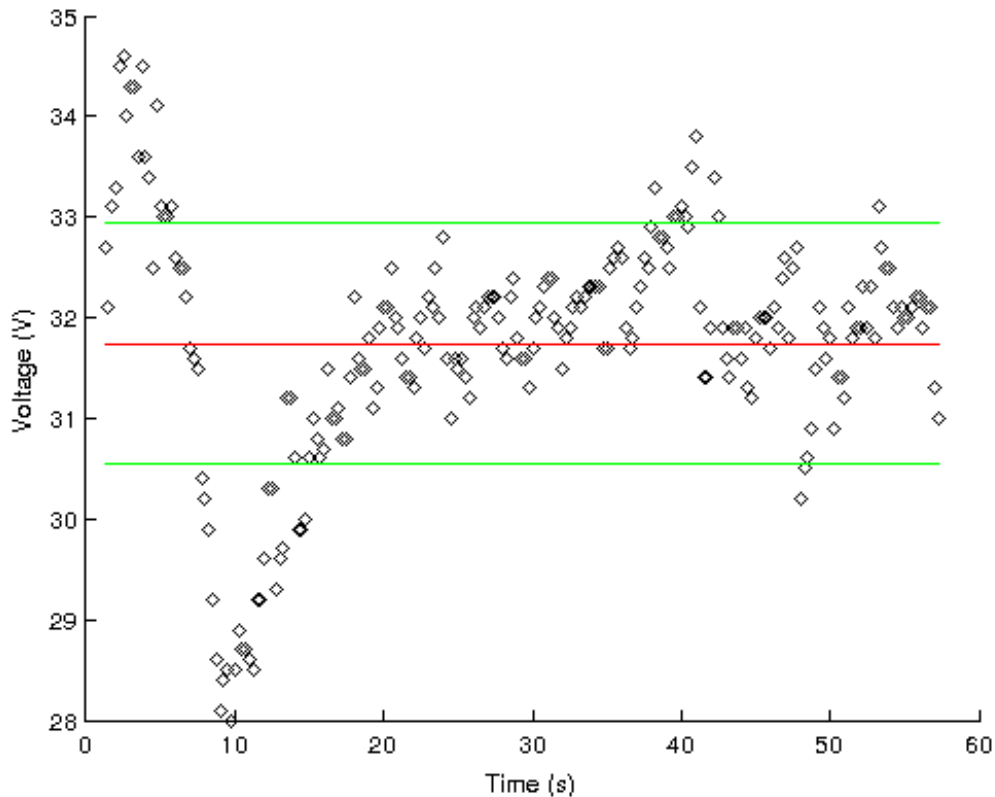


Figure D.25: Evolution of the voltage during the welding operation carried out with six thermocouples embedded. The red line corresponds to the average (31.7 V), the green lines to the mean plus or minus the standard deviation (1,19 V).

D.2.4.3. Wire feed speed:

The evolution of the WFS during the process is reported in Figure D.26. It shows a higher average WFS of 34.9 mm/s, which is higher than for the last experiment, and a deviation of 8.1 %, according to Equation (D.1), with the WFS calculated with the formula coming from regression. The standard deviation is of 2.13 mm/s which is higher than for the previous experiment but still two orders of magnitude lower than the average value.

The surge at the beginning of the signal certainly explain a significant part of the increase in average and standard deviation. This surge comes partially from the surge in current which increase the melting rate of the electrode by Joule's effect. This is shown by the increase of the values of the WFS calculated using the actual current recording (blue stars). The WFS is then

stable until 30 s. Then, it increases until around 40 s where a peak is recorded. This peak corresponds to the peak in current and can be explained as before by Joule's heating.

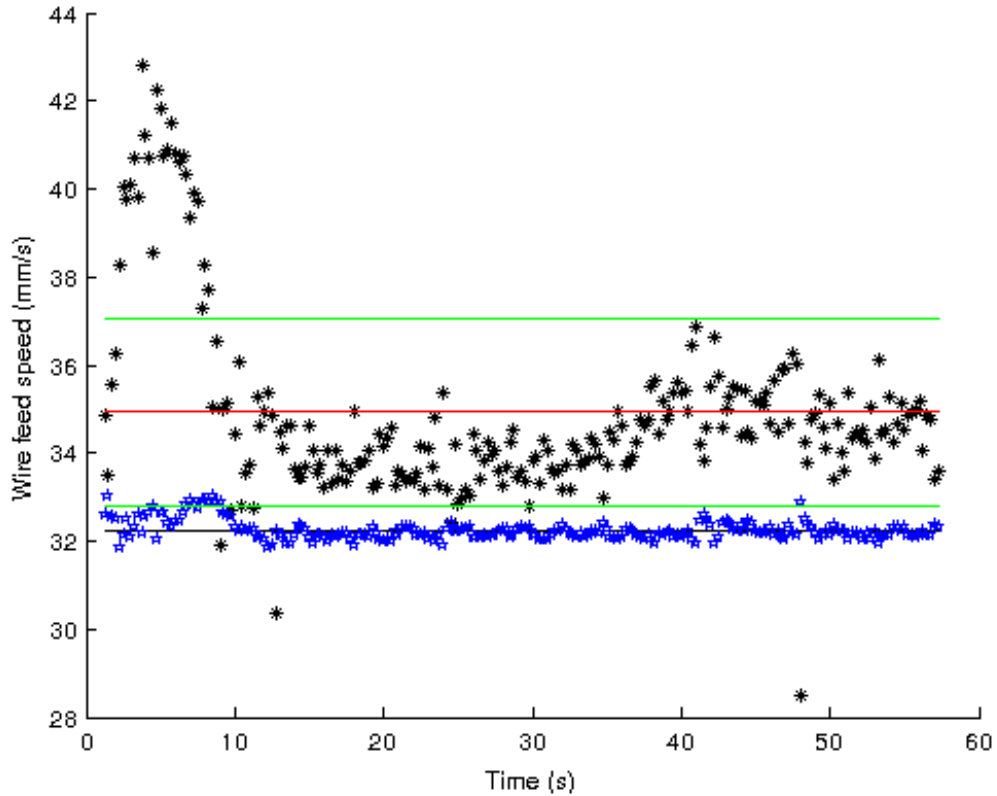


Figure D.26: The black stars represent the recorded evolution of the WFS during the experiment with six thermocouples. The red line shows the mean (34.9 mm/s) and the green ones represent the mean plus or minus the standard deviation (2.13 mm/s). The blue stars show the values of the WFS calculated by using the current recorded. The black one shows the WFS calculated with the aim parameters only (32.2 mm/s).

E. Bead shape measurements:

Here is reported a table giving all the bead shape parameters measured on the cross-sections done for the experiment without thermocouples, the one conducted with eight thermocouples embedded, and the one carried out with six embedded thermocouples.

Table E.1: Bead shape parameters measured on the cross-sections.

Exp.	Z	TC	BW (mm)	MRH (mm)	MPD (mm)	Centre Distance (mm)	
Experiment without thermocouples	Z1	B	17.08	3.13	9.58	0	
		Ka	16.68	2.83	9.94	0	
		Kb	16.48	2.89	9.93	0.25	
	Z2	B	15.99	2.70	9.87	0.89	
		Ka	15.16	2.52	10.30	0.43	
		Kb	14.97	2.64	9.92	0.54	
	Z3	B	15.15	2.80	10.01	0.25	
		Ka	15.70	2.63	9.83	0	
		Kb	15.35	2.66	10.03	-0.27	
	Average			15.84	2.76	9.93	0.23
	Experiment with 8 thermocouples (2B,6K)	Z1	B	17.01	3.17	9.48	2.59
			Ka	16.17	3.30	9.75	1.01
			Kb	16.14	2.29	9.96	1.04
Z2		B	15.80	5.19	10.15	2.56	
		Ka	14.68	5.72	9.84	1.28	
		Kb	15.85	4.56	10.49	1.69	
Z3		B	15.49	6.23	10.76	2.59	
		Ka	13.59	5.90	10.18	1.07	
		Kb	13.72	3.15	10.81	1.08	
Average			15.38	4.39	10.15	1.66	
E x p		Z1	B	14.90	2.92	10.41	0.80

		Ka	15.37	3.14	10.30	0.64
		Kb	15.51	3.30	9.72	0.24
	Z2	B	14.65	4.41	11.42	0.66
		Ka	14.20	4.27	10.84	0.76
		Kb	15.18	4.63	11.09	1.02
	Z3	B	13.37	5.03	11.59	1.07
		Ka	14.30	5.08	10.03	0.90
		Kb	14.29	5.65	10.14	0.88
	Average		14.64	4.27	10.61	0.77

The columns of the table correspond, from the left to the right, to the experiment from which the cross-section was taken, the zone where the thermocouple was embedded, the thermocouple considered¹⁸, the bead width, the maximum reinforcement height, the maximum penetration depth, and the distance between the centre of the plate and the centre of the weld. This distance is considered positive if the centre of the weld is closer to the thermocouple than the centre of the plate. For slanted bead the centre of the weld was considered to be the vertical line projection of the point where the bead reaches its maximum penetration depth.

¹⁸ For the correspondence between the name given to the thermocouple and its position see Figures 4.2 and 4.3.